DOCTOR OF ENGINEERING (ENGD)

Mapping and Optimising A Mixed Flow Turbocharger Turbine Under Unsteady Flow Conditions

Liu, Zheng

Award date:
2020

Awarding institution:
University of Bath

Mapping and Optimising A Mixed Flow Turbocharger Turbine Under Unsteady Flow Conditions

Zheng Liu

Department of Mechanical Engineering

University of Bath

This dissertation is submitted for the degree of

Doctor of Philosophy

January 2020

DECLARATION

Zheng Liu

January 2020

ABSTRACT

The performance of a turbocharger turbine is important to down-sized engines. The pulsating flow nature of exhausted flows arises the uncertainties when designing and matching the turbine to an engine, since turbocharger turbines are commonly designed and tested under steady-state flow conditions. To overcome this difficulty, this PhD work carried out both experimental and numerical study for better understanding the turbine characteristics under pulsating flow conditions.

A new method for mapping radial turbines will be demonstrated, which can utilize unsteady experimental data to create a turbine characteristic map, namely the unsteady turbine map. Compared with the standard steady-state gas-stand mapping approach, the unsteady turbine map reveals the energy conservation of turbine under pulsating flow conditions, providing a better opportunity of matching a turbocharger to an engine during the engine development process. In order to generate realistic pulsating flows in a laboratory environment, a pulsation generator, modified by a three-cylinder engine, was designed in the University of Bath with the capability of blocking the air flow path of one cylinder for studying the effects of cylinder deactivations on the turbine unsteady performance. Compared with the standard mapping method, the negative turbine power was measured during the trough of a pulse, indicating that both turbine and compressor absorb energy from the rotating inertial during that period, and negative efficiency was produced. An extrapolation method was developed, based on the modifications of nozzled turbine model and mean-line model, to overcome the inability of conventional extrapolation model that lacks of predicting negative efficiency. This study found the negative turbine work can take up approximately 15% of turbine net work under 20 Hz pulses. This percentage is even more when there exists a large period of blank pulse, corresponding to the effects due to cylinder deactivations. This study utilizes the unsteady

turbine map for simulation and shows a general improvement for the prediction of compressor power, especially under low pulse frequency conditions.

In order to seek the optimal aerodynamic design of a radial flow turbine under pulsating flow conditions, the present research utilizes CFD method to optimize the blade shape of a small-scale mixed flow turbine under 50 Hz pulses, corresponding to 2000 rpm of a three-cylinder engine. To understand how a less computationally intensive, steady-state optimization compares, the blade shape was also optimized using the peak power point of the pulse. The optimization was carried out using a CFD-GA coupled approach, targeting at maximizing both energy-weighted efficiency and energy output during a predefined pulse period. To ensure that the new design maintains a similar matching to the engine, the maximum deviation of turbine swallowing capacity is controlled to be similar as the baseline turbine. This study found the unsteady optimization method can produce a higher cycle-averaged efficiency over a pulse and better off-design performance, whilst the single point optimization can achieve a higher efficiency at the design point.

This study also studied the influence of the optimization algorithm in the turbine optimization applications. A novel optimization algorithm based on Kriging surrogate (KS) model was developed, and compared with the genetic algorithm (GA). Both the volute and rotor are optimized simultaneously for the peak point of the pressure pulse (2.4 bar). The KS algorithm shows a higher converging rate compared with the GA. The turbine efficiency was improved by 3 percentage points (pp) with the using the genetic algorithm, and an improvement of 3.65 pp was achieved by using the KS algorithm. Although the optimized turbine has a lower peak efficiency, the optimal velocity ratio of optimized design shifted to a lower value, implying a better performance will be achieved under high loading conditions. The improvement of the turbine performance is attributed to a better blade loading in the 0.2-0.4 stream-wise location. The elementary effectiveness has been studied, and the camber-line distributions of the rotor is found to be the most influential factor on the turbine performance.

ACKNOWLEDGEMENTS

And I would like to express my deepest acknowledgement and appreciation to my supervisor Dr. Colin Copeland for long-term supervision, encouragement and guidance throughout the course of this study.

I must also thanks Dr. Ramkumar Vijayakumar in his considerable technical assistance in helping me to operate the turbocharger test-rig during my first year. I am also grateful to other colleagues Yang Liu, Haizhu Wang, and Stefan Tuechler. Their companion makes me feel at home. It has been a great pleasure working with you all.

Finally, this thesis is especially dedicated to my parents. Their unconditional support and love have endowed me with the strength to complete this study.

TABLE OF CONTENTS

LIST OF FIGURES

LIST OF TABLES

NOMENCLATURE

Acronyms

MSt	modified strouhal number	
EET	elementary effects method	
IBC	inverted brayton cycle	
MFT	mixed flow turbine	
OAT	one at a time	
ORC	organic rankine cycles	
PR	pressure ratio	
RFT	radial flow turbine	
RN	degree of reaction	
SP	single passage or speed parameter	$\mathrm{rev\,min^{-1}\,K^{-0.5}}$
A	amplitude	
ANN	artificial neural network	
DE	differential evolution	

DNS direct numerical simulations

EGR entropy generation rate or exhaust gas recirculation

FR full rotor

FVM finite volume method

GA genetic algorithm

GUI graphical user interface

Hex hexahedron

KS Kriging surrogate

lb lower bound

LE leading edge

MFP mass flow parameter $\mathrm{kg\,s^{-1}\,\sqrt{K}\,kPa^{-1}}$

MSTD moving standard dedeviation

NA natural aspired

OF objective function

pp percentage point

PDE partial differential equation

Pri prism

Pyr pyramid

RANS Reynold Averaged Navier-Stokes

RMS root mean square

SM sliding mesh

TE trailing edge

TT total time

up upper bound

VGT variable geometry turbine

Greek Symbols

α absolute flow angle

β relative flow angle

β_B blade angle

ε turbulent kinetic energy dissipation rate W

η efficiency

γ ratio of specific capacity **or** blade cone angle

Λ	Lambda number	
λ	thermal conductivity	$\mathrm{W\,m^{-1}\,K^{-1}}$
μ	dynamic viscosity	$\mathrm{N\,s\,m^{-2}}$
ν	kinematic viscosity	$\mathrm{m^2\,s^-1}$
Φ	entropy generation rate per unit volume	$\mathrm{W\,m^{-3}\,K^{-1}}$
ϕ	camber angle	
ϕ_β	camber angle in β criteria	
ϕ_θ	camber angle in θ criteria	
Π	normalized pulse amplitude	
τ	blade torque	$\mathrm{N\,m}$
φ	effective pulse fraction	

Roman Symbols

$\dot{m}$	mass flow rate, $\mathrm{kg\,s^{-1}}$	
$\dot{S}$	entropy rate	$\mathrm{W\,K^{-1}}$
$\dot{W}$	power	W
a	speed of sound	$\mathrm{m\,s^{-1}}$

C	absolute velocity, $\mathrm{m\,s^{-1}}$	
c_p	specific heat at constant pressure	$\mathrm{J\,kg^{-1}\,K^{-1}}$
D	blade diameter	mm
f	frequency	Hz
H	enthalpy	$\mathrm{kJ\,kg^{-1}}$
I	momentum of inertia	$\mathrm{kg\,m^2}$
i	incidence angle	$^\circ$
L	length	m
N	rotational speed	$\mathrm{rev\,min^{-1}}$
P	pressure	Pa
R	gas constant	$\mathrm{J/kg}$
S	entropy	$\mathrm{J\,K^{-1}}$
S	swirl coefficient	
s	specific entropy	$\mathrm{J\,kg^{-1}\,K^{-1}}$
T	temperature	K
u	gas velocity	$\mathrm{m\,s^{-1}}$

W	relative flow velocity	$\mathrm{m\,s^{-1}}$
Z	number of blades	

Superscripts

$\bar{}$	averaged value
$crit$	critical condition

Subscripts

0	stagnation conditions
1	volute inlet section
2	volute outlet section
3	rotor inlet section
4	turbine outlet section
$\parallel$	parallel
$\perp$	perpendicular
θ	tangential component
B	blockage factor
b	body

c	compressor
h	hub
in	inlet
ise	isentropic
m	meridional
$mech$	mechanical
opt	optimum
out	outlet
r	rotor
s	shroud
s	surface
t	turbine
tc	turbocharger
w	wall

CHAPTER 1

INTRODUCTION

1.1 Background

In an internal combustion engine (ICE) of an automotive vehicle, exhaust gases normally contain 30-40 percent of the chemical energy released by the combustion [1]. The large portion of heat energy loss from the engine exhaust will not only result in high fuel consumption, it also leads to excessive emissions of greenhouse gases and other harmful pollutants. According to International Energy Agency [2] in 2017, the transport sector accounted for 24% of global CO_2 emissions, where the road transport sector alone was responsible for about 75% of overall transport emissions. Over the last decades, global strategies have taken active efforts to reduce CO_2 emissions. European Union and Council have approved legislation that targets at the reduction in tailpipe CO_2 emission to an average of 95 g/km of newly registered cars by 2021, which will have been reduced by about 45% since 2000 [3]. The ever-increasing stringent emission legislation and fuel economy demands highlight the necessity of developing highly efficient engines.

Fig. 1.1 shows a technology road map published by the UK automotive council that predicts the advances in powertrain technologies over the 20 years. One of the most important trends reflected in this roadmap is to downsize the internal combustion engine, namely replacing large displacement engines with small displacement engines. However, since the reduction in cylinder volume in a naturally aspirated engine results in a reduction in torque and power, downsizing is always accompanied by boosting. There are two main reasons that downsizing

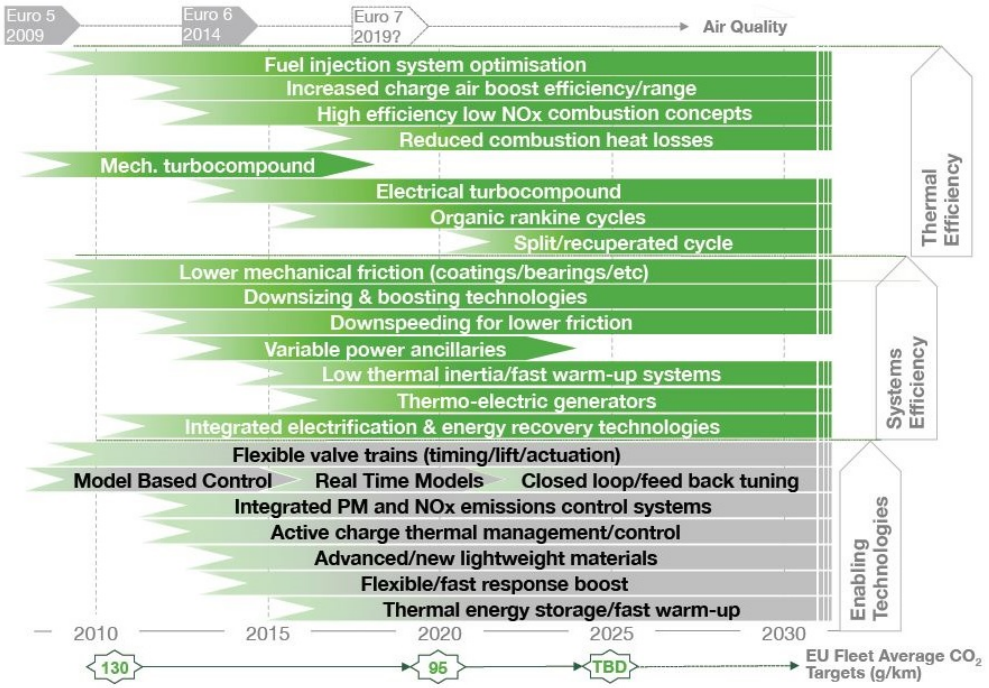

Figure. 1.1 UK automotive Council - IC Engine Technology Road Map [4]

and boosting can improve fuel economy. First is the reduced throttling loss. For petrol engines, the engine power is regulated by adjusting the air entering the engine via a throttle plate. At part load, a small opening throttle plate will have the engine to do additional work to move air in and out of the cylinder. The additional "pumping work" can be significant at low-loading conditions, resulting in poor fuel economy. However, if the engine is downsized, it needs a larger throttle opening to enable the engine operating at a higher specific load to propel the same vehicle, meaning the throttle losses are reduced. The second aspect is the reduced friction loss. A downsized engine normally has less number of cylinders compared with its counterpart natural aspired (NA) engine. Thus the less moving parts directly improve the fuel economy due to the less frictional surface area. Moreover, the downsizing and boosting can also permit engine "down-speeding" as well. Fig. 1.2 shows boosted engine can reach the peak torque at 2000rpm with supercharger fitted, compared to 3500-4000rpm on the base NA engine. As suggested by [5], down-speeding reduces friction losses and moves the operating points of an engine to a higher-efficiency region.

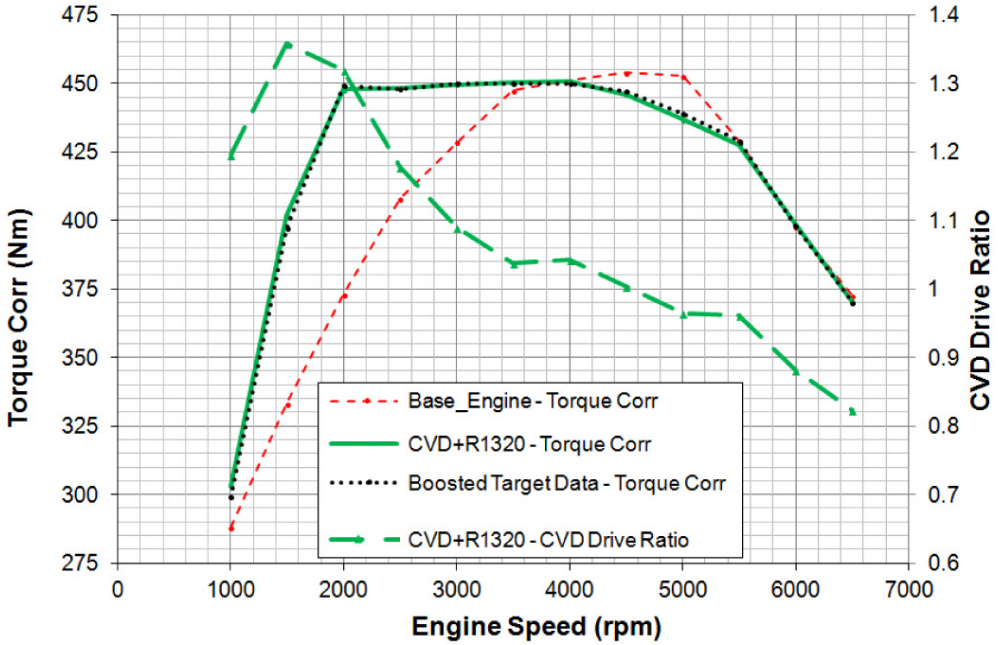

Figure. 1.2 Improvement in low-end torque from a boosted, downsized engine [6]

Due to the numerous advantages, the emission and fuel consumption demands in the near future can be addressed with downsizing technologies. Fig. 1.3 shows the potential improvement for engine downsizing, indicating the benefits in CO_2 reductions with higher downsizing factors. Petitjean et al. [7] compared a 30% downsized engine with its counterpart NA engine. They found the fuel consumption was reduced by 8-10% of the downsized engine for the same engine brake power output. Shahed and Bauer [8] found that 40% downsizing yields a 23% reduction in fuel consumption largely due to a reduction in throttling losses.

1.2 Turbocharger-Engine Matching

The success of engine downsizing technologies essentially attributed to the air charging systems. Simply reducing the engine capacity is not necessarily an effective solution. Without the boosting systems, the engine performance could be deteriorated due to less oxygen existing in the smaller combustion chamber, thereby limiting the amount of fuel to burn. The concept of boosting is by using a compressor to pressurize the intake air to

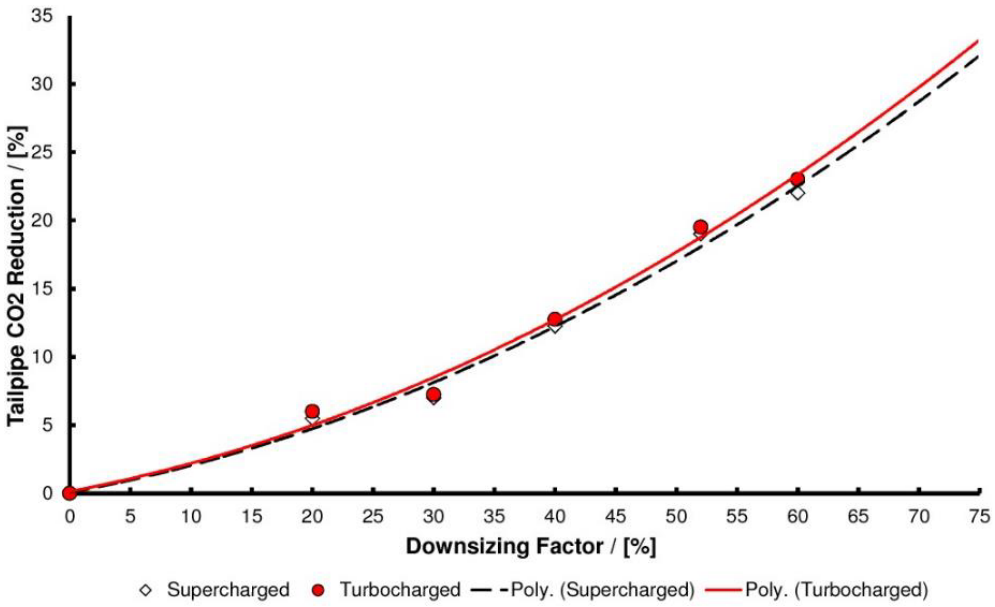

Figure. 1.3 The potential for downsizing based on validation data [9]

approximately 1.2 to 3 times atmospheric pressure depending on the application and degree of downsizing.

Mechanical supercharging is an air pressurizing process where a compressor is coupled to the engine crankshaft by means of a belt, gear or chain [5]. To deliver sufficient pressure, the compressor must rotate at very high speeds, requiring a gear/belt ratio approximately 50 times the speed of the crankshaft. A variable-speed transmission can be employed in supercharging system that adjusts the drive ratio according to the engine speed and boost demand. However, the energy required to drive the supercharger still comes from the power-plant. Consequently, the use of a supercharger will not necessarily lead to an efficiency advantage.

Turbocharging, on the other hand, is a specific form of supercharging. Unlike a supercharger, the turbocharger does not need to be a parasitic load on the engine, since the all energy supplied to a turbocharger comes from the exhaust gases, which is normally wasted. The turbocharger, as shown in the schematic view of Fig. 1.4, consists of a compressor and a turbine coupled on a common shaft. In most turbochargers, the blades of both turbine and compressor are formed using radial turbomachinery since it has a higher flow capacity and it

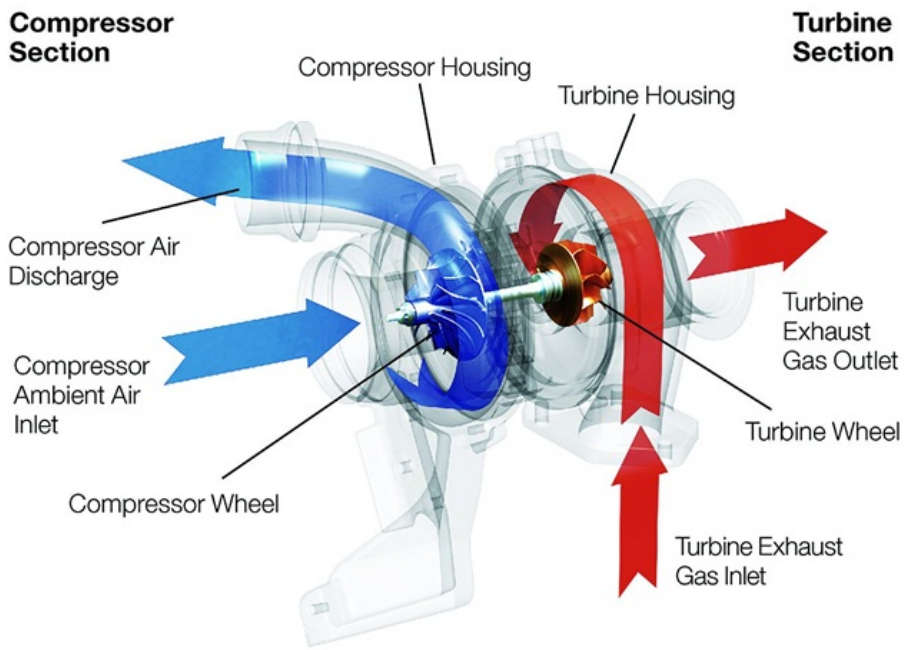

Figure. 1.4 Turbocharger schematic view

can achieve a larger expansion/compression ratio in a single stage compared with the axial turbomachinery [10]. The impellers are enclosed by volutes used to form flow paths between the engine and turbocharger.

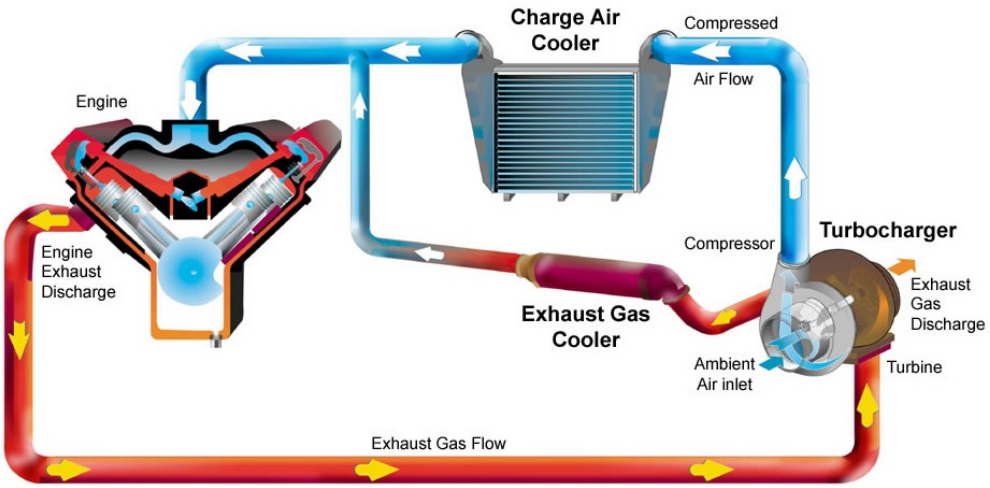

Figure. 1.5 Turbocharger applied to a piston engine

Fig. 1.5 shows the airflow path of a turbocharged engine. The entry of a turbine volute receives hot pressurized exhaust flow from the engine. Within the volute stage, the hot gas is forced to turn and follow the volute shape, forming vortexes around the axis thereby distributing the gases around the circumference of the turbine impeller. As the gases moving radially inward, the flow area gradually reduces thereby accelerating the gas prior to enter the blade passages. The volute casing can be either vaneless or fitted with nozzled guide vanes near the volute exit as shown in Fig. 1.6 (b). The nozzle vanes have a function of further increasing the kinetic energy of the fluid, therefore the nozzle fitted turbines have a better performance at the design point compared with a vaneless. Within the rotor stage, the thermal and pressure energy within the fluid is extracted by the turbine blades and converted into mechanical energy namely the rotation of the shaft. The spinning compressor wheel compresses the air at the engine intake manifold so as to supply the engine cylinders with air density above the atmosphere level. Since all real compression processes raise both pressure and temperature, the temperature rise will offset the benefit of increasing the pressure due to ideal gas law. Therefore, a charge air cooler is normally added to the compressor exit to increase the air density but at the expense of a small pressure drop.

(a) **(b)**

Figure. 1.6 Types of volute (a) vaneless volute and (b) vaned volute [11]

Bypass valves are commonly used for both compressor side and turbine side in order to reach a desired torque demand or maintain the limitations of an engine. The bypass valves,

controlled by a vacuum actuator, can avoid too much flow entering the impeller by passing some of the flow abound. With the opening of the turbine bypass valves, it can effectively reduce the amount of exhaust gases flowing through the turbine, resulting in the drop of turbine inlet pressure, which is also known as engine back-pressure. During the exhaust stroke, the piston is moving against this pressure and consequently consumed some energy of the crankshaft. Meanwhile, the turbocharger shaft power will be also reduced due to less flow energy available to the turbine as opening the bypass valve, resulting in the change of compressor performance. Similarly, the compressor bypass valve will have a direct effect on the boost pressure. During the intake stroke, the boost pressure acts on the piston crown that exceeds the crankcase pressure (ambient pressure) on the underside of the piston, resulting in positive work on the crankshaft. If the boost pressure in the intake manifold is higher than the back-pressure in the exhaust manifold, the intake and exhaust processes produce net positive work. If the opposite is true, this process will act as a negative drain on engine work output.

For a target engine performance characteristic, various combinations of bypass valve positions could achieve the same goal. It is essential to find an optimal combination of compressor and turbine that maximizes the output. However, there are many variables to consider, such as the smoke limit, cylinder pressure limit, exhaust gas temperature limit, turbo speed limit, and etc. A good matching between the turbocharger and the engine should address these technical limitations in order to ensure a durable mechanical endurance, but also maximize system efficiency and reduce the cost.

Turbocharger allows a great energy saving compared with supercharger due to its ability to recover the waster heat energy, but it also arises the need for a good turbocharger-engine matching. It is fundamental to assess the heat recovery process of a turbocharger thereby seeking a method for improving both the turbocharger performance and the matching to an engine.

1.3 Pulsed Flow Turbocharging

There are two approaches to recovering the energy available in the exhaust system using a turbine. The first approach, as shown in Fig. 1.7 (a), is referred to *constant pressure turbocharging*, where exhaust ports from all cylinders are connected to a single exhaust manifold, whose volume is sufficiently large. As the valve opens, the suddenly increased exhaust flow will be damped across the manifold, resulting in a stabilized flow condition prior to the turbine. The second approach, Fig. 1.7 (b), is to produce a more direct connection between the exhaust port and the turbocharger turbine. This is named as *pulsed flow turbocharging* since the turbine is subjected to pulsating flows due to the opening and closing of exhaust valves, as shown in Fig. 1.8. Compared with the first approach, the second approach effectively preserved the peak pressure and kinetic energy in the exhaust gases. Although the turbine is normally designed to be more efficient under steady flow conditions, the benefit from increasing the available energy usually overweights the loss in turbine efficiency due to the increased flow energy at the peak of pulse [10]. Besides, with a constant pressure system, the voluminous exhaust manifold will create packaging issues, since space is usually limited in automotive applications, especially for downsized vehicles. Also, the dynamic response of the turbocharger will be limited in a constant pressure system. Once the load change is demanded, there will be an extra time involved due to pressurizing or decompressing the air inside the chamber, causing the deterioration in the drivability.

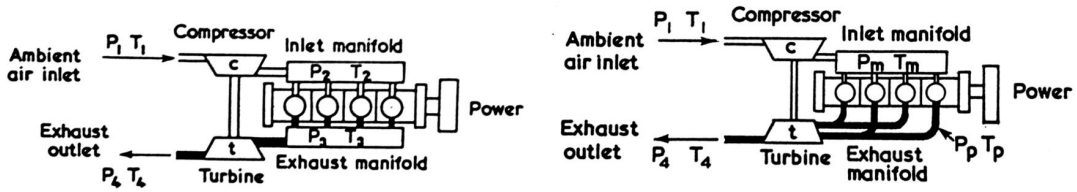

Figure. 1.7 (a) Constant pressure turbocharging (b) pulse turbocharging [10]

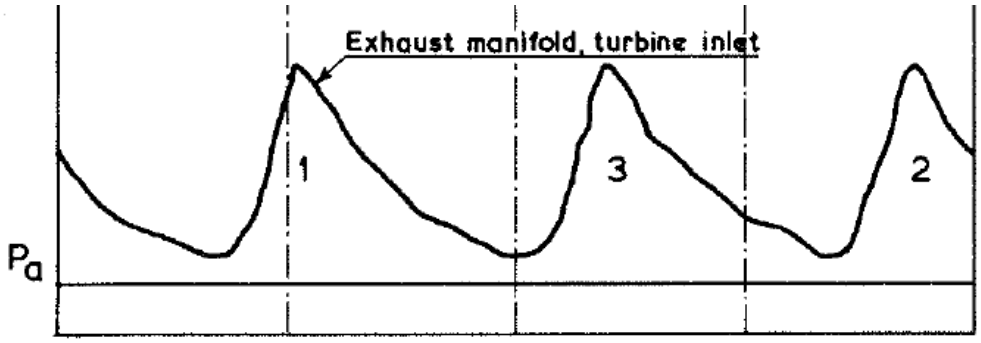

Figure. 1.8 Pressure pulse at turbine inlet [10]

Due to various advantages, pulsed flow turbocharging has become the most widespread approach in most applications of the technology. However, much of the turbine theory has considered optimizing the turbine under steady-state conditions, whereas turbines are inherently subjected to pulsating flow conditions when mounted to engine exhaust. As a result, it remains a contradictory between the turbine design conditions and the real operating conditions. Actually, the turbine operates under off-design conditions for the most of time, and it can even reach some extreme off-design points since the pressure of exhaust gases varies in a wide range from 1 bar to 3 bar, resulting in poor performance. It also rises a question that if the turbine behaves in a similar way as steady-state conditions when it operates under pulsating flow conditions. This is significant since it will have an inevitable impact on the engine development process. In most software of analysing engine performance, the solution of turbocharger performance parameters is usually based on the turbocharger performance maps which is a look-up table gathered from a steady-state gas stand test. If the turbine's behaviour under an engine environment is different from that under steady-state condition, the predefined matching between turbocharger and engine developed based on simulations will be no longer valid.

1.4 Mixed-Flow Turbines

Together with engine downsizing, modern vehicles may also employ technologies such as lean burning, Exhaust Gas Recirculation (EGR), and cylinder deactivations for reducing the fuel consumption and emissions. On the other hand, these technologies reduce the amount of available energy within the exhaust stream, due to a lower exhaust gas temperature or reduced exhaust flow rate [12]. The exhaust flow energy is especially limited under low engine speeds, causing the ineffectiveness of the turbocharger thereby arising the difficulty in meeting the low-end-torque demand. Therefore, to address the problem, it is essential to design high efficiency turbines that are capable of extracting sufficient power from the low-energy exhaust to drive the compressor at high boost pressure. Since most available energy is contained in the region near the peak of exhaust pulses, it seems to be more advantageous to improve the turbine efficiency at the peak pulse region rather than other regions.

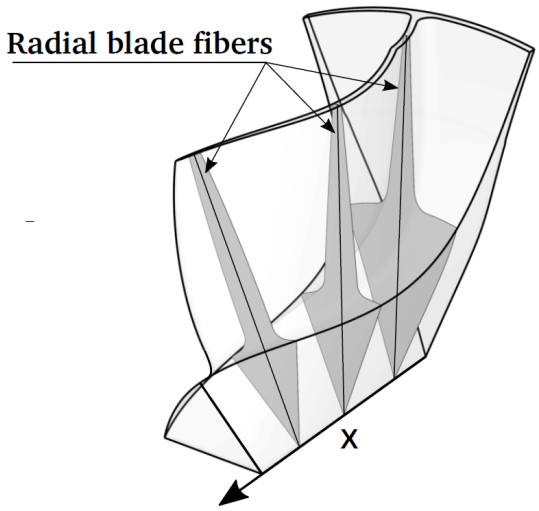

Figure. 1.9 The radial fibre requirement of turbine blade

However, in a conventional radial flow turbine, the inlet blade angle inherently maintains zero in order to meet the radial fibre requirement. As shown in Fig. 1.9, in a radial fibred blade, the section at any cut normal to the axis will be symmetric according to the center line, and

the center line has to be intersected with the axis of rotation. This is an essential requirement in the design process in order to prevent mechanical failure due to the development of the blade stresses as the rotational speed increased. The zero inlet blade angle restricts the radial flow turbine operating at an optimal velocity ratio[1] of approximately 0.7 [10]. The velocity ratio describes the turbine loading conditions, and a higher value implies a lower turbine loading. Improve the turbine performance at the peak pulse region means shifting the optimal velocity ratio to a lower value.

Fig. 1.10 the typical variation in exhaust pressure at the turbine inlet that occurs between exhaust valve opening (EVO) and exhaust valve closing (EVC) from the study of [13]. Point B is the peak pulse point that is supposed to contain maximal available flow energy of the pulse, but it does not correspond to the maximum efficiency point. To demonstrate more clearly, Fig. 1.11 shows the instantaneous variation of turbine efficiency and turbine isentropic power that occur during a pulse. It is clear that in the peak pulse region, the turbine efficiency is approximately 15% lower than its peak efficiency. As a result, the purely radial design of a turbine blade restricts the amount of energy recovered under pulsating flow conditions.

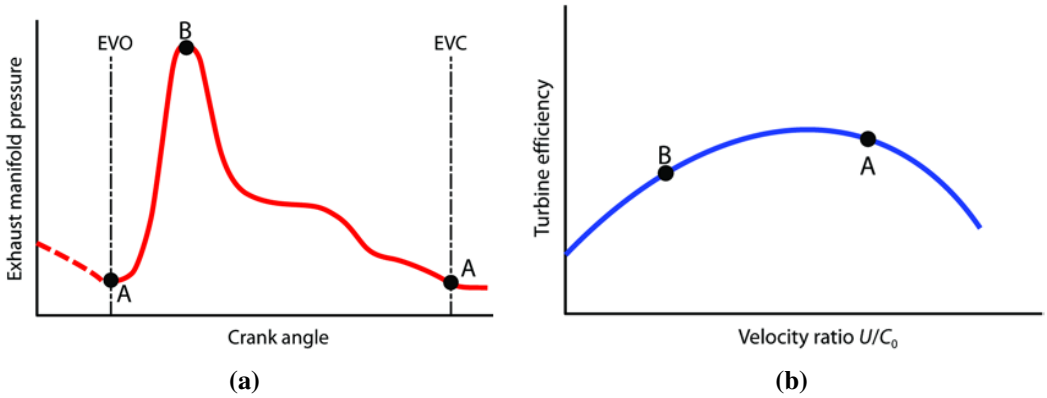

Figure. 1.10 (a) Exhaust manifold pressure and (b) its effect on turbine efficiency [13]

[1] the velocity ratio that leads to the maximal turbine efficiency

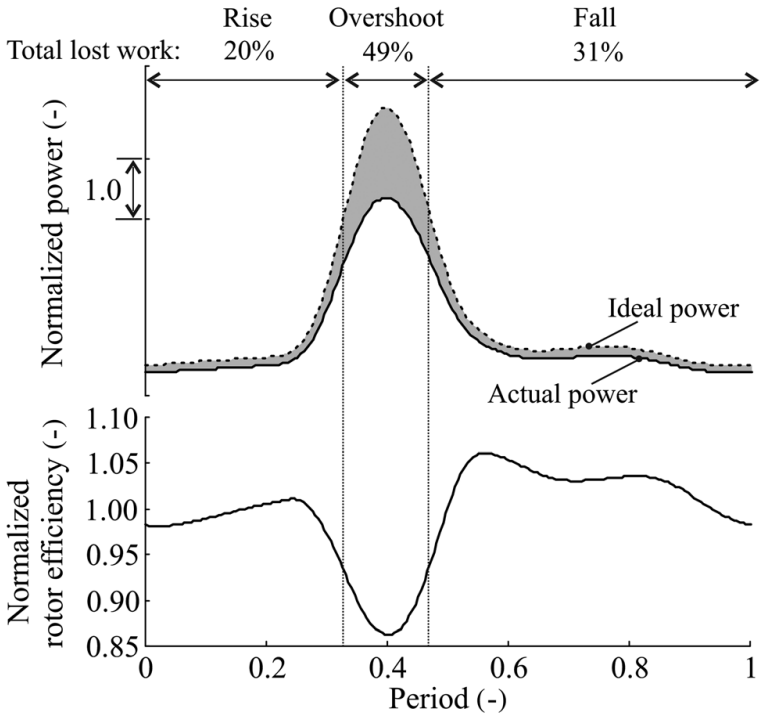

Figure. 1.11 Instantanous efficiency and power over a pulse [14]

Mixed-flow turbines have gained attention since the 1990s due to its various superiorities compared with radial flow turbines, especially its elevated efficiency under higher loading conditions (lower velocity ratios). The mixed-flow turbine can be regarded as an intermediate design between radial and axial turbine, as it possesses features of both. As shown in Fig. 1.12, the blades of a mixed-flow turbine are trimmed at the inlet to allow for a forward sweeping the blade at the leading edge, which can accept flows with both axial and radial components. In this way, the non-zero inlet blade angle is achieved but still remains a radial fibred blade. Mixed-flow turbine offers an additional design variable, the cone angle γ, which can be used to vary the blade angle at the inlet. A positive inlet blade angle will benefit the turbine's performance at higher loading conditions [15]. Fig. 1.13 shows turbine efficiency as a function of the velocity ratio for radial and mixed-flow turbines. It is clear that the peak of the curve has shifted to lower velocity ratios, suggesting much better energy conversion of pulsating flow.

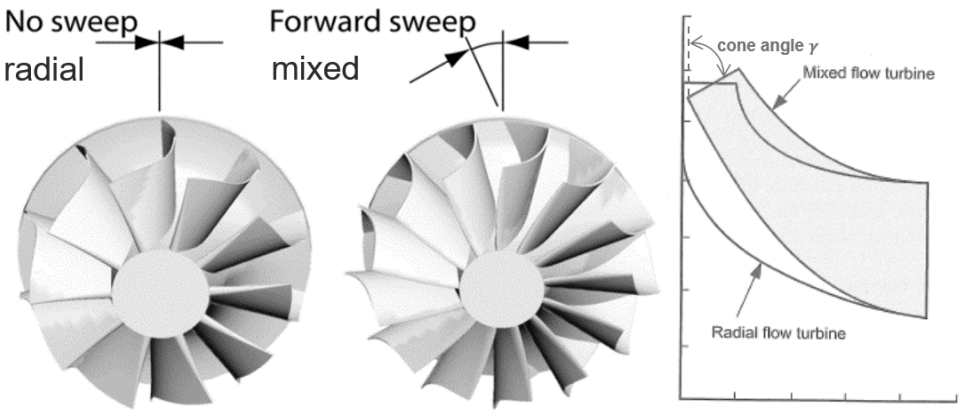

Figure. 1.12 The difference between a radial and a mixed-flow turbine [13, 16]

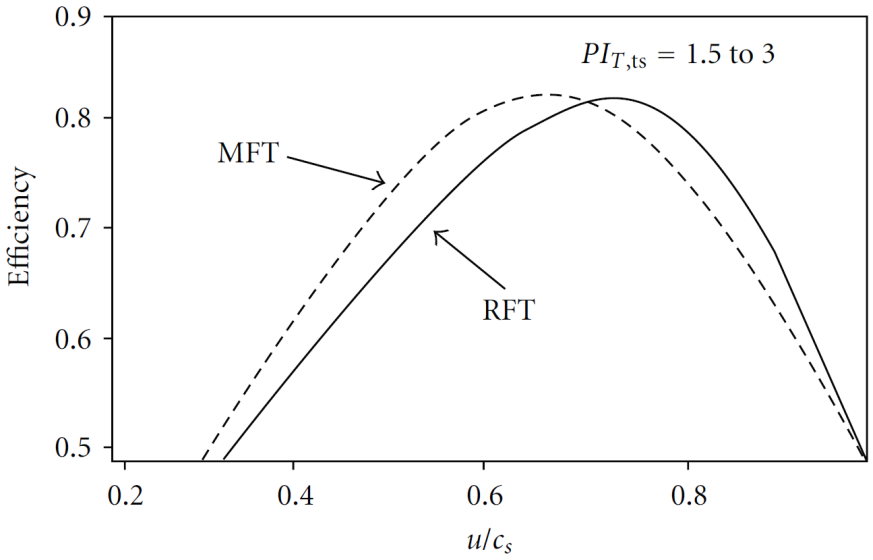

Figure. 1.13 Turbine efficiency as a function of velocity ratio for radial and mixed flow turbines [10]

Mixed-flow turbines also improve flow path curvature [15, 17], which can effectively reduce the formation of secondary flow and increase the flow capacity, as shown in Fig. 1.14. This implies that it is possible to replace a radial flow turbine with a smaller sized mixed flow turbine but remains the same matching to an engine. As a result, using a mixed flow turbine in a turbocharger will benefit an engine from a faster transient response due to the reduced inertia.

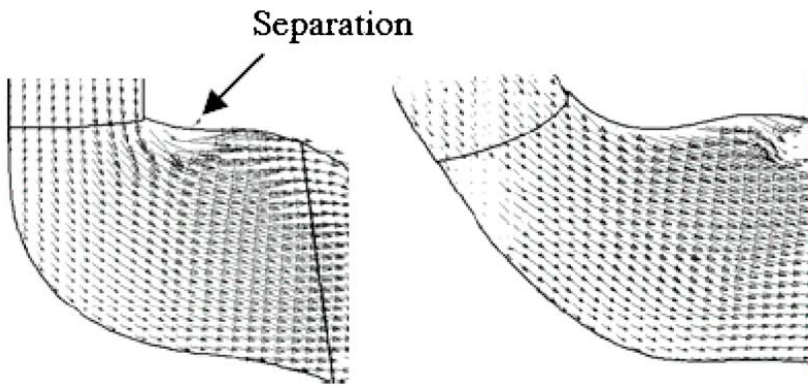

Figure. 1.14 Comparison of meridional flow separation between radial and mixed flow turbine [17]

1.5 Thesis Objectives

The objectives of the present research work are focused on mapping and optimizing a mixed-flow turbocharger turbine under pulsating flow conditions. This can be arranged into three parts:

1. The first objective is to propose a new method of measuring turbine performance under unsteady flow conditions. The turbine unsteady characteristic map obtained from the experiment should be post-processed in a way that is able to be integrated into the one-dimensional gas dynamic code. The difference between the conventional steady-state mapping and the unsteady mapping approach has to be studied based on their influence on the turbocharger performance.
2. The second objective is to optimize the design of a turbine blade for a better overall performance during a pulse period. Unlike the steady-state optimization, which is focused on a single operating point, the turbine blade design should be optimized whilst explicitly taking into account a full range of flow conditions during an exhaust pulse. The unsteady optimization method has to be compared with the steady-state optimization method to demonstrate its benefits. It should ensure that the newly designed turbine blade satisfying the radial fibre requirement and maintaining the same matching to the engine as the baseline turbine.

3. The third objective of this thesis is to investigate the suitable optimization algorithm on the turbine applications in order to achieve the global optimal design. The design parameters of the whole stage turbine has been considered during the optimization process. The novel optimization algorithm will be compared with the commonly used generic algorithm for demonstrating its superiorities. The peak point of the exhaust pulse is chosen as the desired design point since it contains the maximum flow energy during one pulse period.

1.6 Thesis Outline

This thesis consists of eight chapters as summarized below,

Chapter 1: Introduction

This chapter introduces the background of turbocharging technology. The objectives and structure of the thesis are explained.

Chapter 2: Literature Review

This chapter reviews the previous research work related to the present study. The first part reviews the methodologies used to quantify the turbine unsteadiness, where the quasi-steady hypothesis is compared with the truly unsteady performance. Next, the numerical turbine models from simple to complex are introduced. Then, the commonly used turbine design parameters and the related optimization method have been discussed. The final section of this chapter points out the potential methods to address unsolved difficulties.

Chapter 3: Experiment methodology

This chapter introduces the technical specifications of the experimental instrumentations. The turbine steady-state and unsteady performance parameters are defined. The data pre-processing and post-processing techniques are elaborated, especially the phase-shift method

for instantaneous efficiency calculation. A brief description of the effects of the cylinder deactivation on the generation of pulsating flow is included.

Chapter 4: Numerical Methodology

This chapter presents the numerical method that is used for the performance evaluation of turbocharger turbines. It firstly describes the Computational Fluid Dynamic (CFD) approach for solving the three-dimensional Reynolds-averaged Navier-Stokes equations. Next, the CFD solver set-up for both steady-state and unsteady cases is discussed. This is followed by the mesh sensitivity study and the time-step sensitivity study for evaluating the numerical accuracy and stability. Then, a novel turbine model, consisting of a nozzle model and a mean-line model, is proposed. Lastly, a transient turbocharger model is developed with special consideration for implementing the negative turbine efficiency.

Chapter 5: Optimization of Mixed-flow Turbine

This chapter mainly consists of two topics. The turbine optimization parameters, together with the linear and non-linear constraints are first introduced. Then, two algorithms, containing both the genetic algorithm and a novel global optimization algorithm based on the Kriging surrogate model is discussed. The steady-state and unsteady optimization methods are then defined.

Chapter 6: Dynamic Mapping - Experiment Results and Analysis

This chapter firstly presents the steady-state experimental results. This is followed by a validation process, showing the proposed turbine model that is able to predict and extrapolate the swallowing capacity characteristic and the turbine efficiency. The agreement between the CFD model and the experimental data is also demonstrated. Next, the equivalent unsteady turbine map is produced based on the aforementioned turbine model and the unsteadiness criterion. Finally, the transient turbocharger model shows the performance improvement

by using the equivalent unsteady turbine map compared with the conventional steady-state turbine map.

Chapter 7: Results of Turbine Optimization Study

This chapter shows the optimization results from both steady-state and unsteady optimization process. The flow filed analysis demonstrates the essential reason that leads to the performance improvement of turbine. Finally, the elementary effectiveness study reveals the most influential design parameters that contribute most to the turbine performance.

Chapter 8: Conclusion

This chapter is the closure of the thesis, proving the overall conclusion of the work. It summaries the advantages of mapping and optimizing the turbocharger turbine under pulsating flow conditions.

CHAPTER 2

LITERATURE REVIEW

2.1 Performance of Turbocharger Turbines Exposed to Pulsating Flows

The pulsating flow nature of exhaust flow and its effect on the turbine performance has been invested over five decades since the first publication presented by Wallace and Blair [18] in the year of 1965. One of the main motivations of early researches was to assess the validity of the quasi-steady assumption. The quasi-steady hypothesis presumes that, during a pulse cycle, the turbine will behave in the same manner at any instance of time as if the turbine works under steady-state conditions.

Wallace and Blair [18] systematically evaluated the effect of pulse frequency, pulse form, pulse amplitude, pipe length pipe diameter, and turbine speed on the performance of a turbine. They concluded that the quasi-steady hypothesis becomes progressively inaccurate with the increase of pulse frequency and turbine speed. Benson and Scrimshaw [19] found the averaged turbine efficiency under unsteady flow conditions is higher than that under steady conditions based on an experimental study of a nozzled double-entry turbine. Benson and Scrimshaw [19] suggested the using of the quasi-steady method would underestimate both the turbine mass flow and power output, and this finding was later supported by Kosuge et al. [20]. Kosuge et al. [20] found the decreased deviation of averaged mass flow between quasi-steady assumption and unsteady measurement as the pulse frequency increased, but

the measured power yielded the opposite trend. They attributed the phenomenon to the smaller pulse amplitude as increasing the pulse frequency. Benson [21] and Kosuge et al. [20] reported the differences between the quasi-steady and unsteady mean value were not only depending on the pulse frequency, but also influenced by the amplitude and pulse shape. Benson [21] estimated the flow fluctuations will increase the internal losses within the turbine stage as they observed less power generated under unsteady flow conditions compared with the quasi-steady hypothesis.

These early researches generally agreed that the quasi-steady hypothesis could not reflect the real turbine performance when it under unsteady flow conditions. However, these studies were restricted by the low-resolution measurement device at that time, where only pressure can be measured on the time-resolved basis, whilst other parameters such as temperature, turbine speed, mass flow rate and power can only be measured on a time-averaged basis. As Baines [22] remarked, these technical limitations are the major reason that incongruous results were presented by many researchers.

It was until 1986, Dale and Watson [23] were the first to present turbine unsteady performance for a radial turbine with all instantaneous parameters measured, except for the temperature. The pulse was generated by a specifically designed pulse generator located on the upstream of the turbine, which consists of two contour-rotating chopper plates with specially made cutouts to produce the pulse profile. The instantaneous mass flow rate was measured using a constant temperature hot-wire anemometer. The turbine was loaded by a 12 kW eddy current dynamometer instead of a compressor, enabling a broad range of turbine performance data to be collected during the steady-state test, since the operation of the turbine would be otherwise limited by the surge or choke characteristic of the compressor.

Fig. 2.1 and Fig. 2.2 compare the turbine swallowing capacity characteristic (non-dimensional mass flow rate versus total to static pressure ratio) and turbine efficiency between the steady-

state and unsteady operation. A clear sign is observed that the instantaneous mass flow and efficiency deviate from the steady-state profile (dashed line), forming hysteresis loops that encapsulate a portion of the quasi-steady assumption in the map. They commented that the mean mass flow was very close to the steady flow line, but mean efficiency was lower compared to the steady flow efficiency. The hysteresis loop implies the imbalance of turbine performance parameters during the unsteady operation, indicating that the quasi-steady assumption was not appropriate to describe the turbine performance on an instantaneous basis.

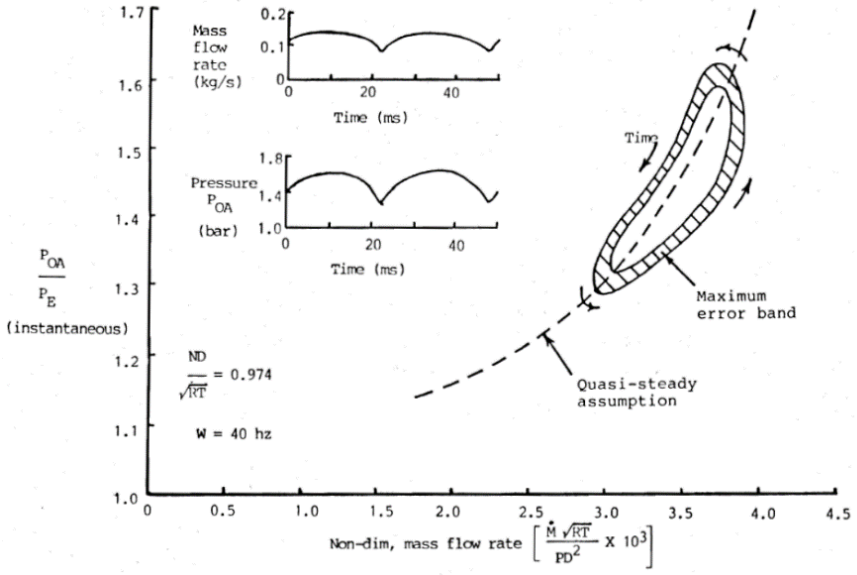

Figure. 2.1 Instantaneous turbine swallowing capacity characteristic for a turbine under pulsating flow [23]

Dale and Watson [23] identified the need for phase-shift in turbine instantaneous efficiency calculation. The turbine efficiency is defined as the ratio of the actual shaft power output to the overall flow energy available to the turbine Since directly measuring the instantaneous torque is a difficult task. Instead, the torque was split into two parts, where the first part is the mean torque acquired from the dynamometer, and the second part is the dynamic variation of the torque calculated based on the instantaneous shaft speed. The parameters used to calculate the isentropic power were gathered from the sensors located in the volute

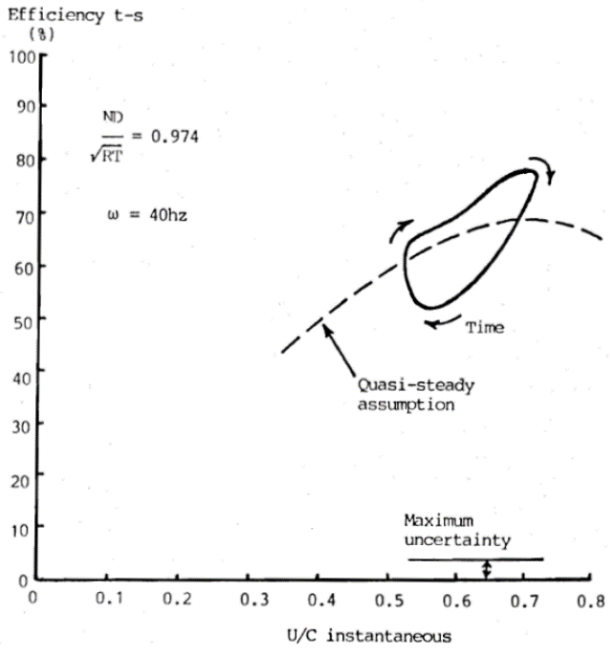

Figure. 2.2 Instantaneous turbine efficiency characteristic for a turbine under pulsating flow [23]

inlet, whereas the torque was measured further downstream at the rotor shaft. Therefore, the measured inlet flow quantities are not the actual flow quantities that really rotate the impeller, due to the spatial difference between the measurement section and the rotor inlet section. As a consequence, it is required to assess the finite amount of time to align these components in a common time frame. However, Shi et al. [24] highlighted the difficulty in defining the exact nominal rotor inlet location where the flow can be assumed to reach the rotor inlet since the flow can enter the rotor from anywhere of the circumference of the volute. Many researchers [25–34] adopted that the nominal rotor entry is located at a 180°azimuth angle downstream of the volute tongue, although there is no theoretical or experimental evidence to support this hypothesis.

Dale and Watson [23] suggested the time duration used for phase shift can be assessed based on the sonic velocity. Karamanis [35] also adopted this method. Researchers of Baines et al. [36] and Winterbone and Pearson [37] proposed that the bulk flow velocity can also be used as an indicator for phase shifting. Other researchers like Rajoo and Martinez-Botas [38],

Szymko et al. [31], Padzillah et al. [14] and Marelli and Capobianco [39] recommended using the sum of bulk flow velocity and sonic velocity. From the CFD study of Hellstrom and Fuchs [40] and Hellström and Fuchs [41], they found a none constant phase-shift between the mass flow, temperature and pressure at the inlet to the turbine and the shaft power. The amount of phase-shift varied during a pulse and is affected by the pulse frequency.

In the 1990s, Dale [42] proposed that one of the most significant reasons causing the deviation between steady and unsteady performance was the large volume of the volute that results in the "filling and emptying" effects. As the opening of the turbine feeding valve, the rapid increase of the fluid properties causes some flows to accumulate within the volume. Thus it takes extra time to empty the mass as closing the turbine feeding valve. Dale [42] estimated that the filling and emptying effect is less significant in the rotor stage than the volute stage due to the smaller volume of the rotor passage. Yeo and Baines [43] used the same test facility as [23, 42] but move a step further by investigating the internal fluid dynamic processes under unsteady flow conditions within a twin-entry type volute. Laser two focus velocimetry was used to take point measurement of 3 velocity components in various positions at the inlet and outlet of the rotor wheel. They demonstrated the rotor inlet velocity profile under unsteady flow condition is similar to that under steady-state condition. Therefore, Yeo and Baines [43] used this evidence to support that rotor is more likely to operate in a quasi-steady manner when exposed to pulsating flows, whereas volute accounts for the most unsteadiness of the turbine stage. The quasi-steady rotor hypothesis is extensively used in 1D modelling today.

However, none of these researchers provided a criterion which is capable of quantifying how much of a turbine deviates from the quasi-steady assumption under pulsating flow conditions. This vacancy was filled until the simulation work by Chen and Winterbone [33], who employed a dimensionless parameter, namely the Strouhal number, to characterize the intensity of unsteadiness of pulsating flows. he Strouhal number St , as defined in Eq.

2.1 where f is the frequency of pulsation; L is the character length of the fluid domain; u is the bulk flow velocity. St relates the time (t_{fluid}) for fluid particles travels through the domain to the time-scale (t_{pulse}) of unsteadiness of pulsating flow. Costall et al. [26] suggested if $St < 0.1$, the turbine is working in quasi-steady manner; $St > 0.16$, unsteady effects dominate; $St \approx 0.16$ is the transition region between quasi-steady and unsteady.

$$St = \frac{fL}{\bar{u}} = \frac{t_{fluid}}{t_{pulse}} \tag{2.1}$$

Szymko et al. [31] modified the St by taking into account that the fact that the waveform of the pulses experienced by a turbocharger turbine is not sinusoidal, where the main pressure pulse only existing over a fraction of the pulse time period, as shown in Fig. 2.3. The modified Strouhal number employed a pulse correction factor $1/2\phi$, where ϕ is the length of the pulse divided by the over-all wavelength, and the multiplier of 2 was used to normalise the pulse frequency that the pulse width constitutes half the wavelength. This leads to the first version namely the *modified Strouhal number* (*MSt*), as defined in Eq. 2.2. The second modification takes into account of the fact that the pressure pulse propagates at a sonic speed, where the gas velocity u was modified by adding the sonic velocity a, as per Eq. 2.3, namely the *pressure modified Strouhal number* (*PMSt*). Szymko et al. [31] recommended the typical threshold value of *MSt* and *PMSt* that used to whether the unsteady or quasi-steady dominates the turbine's behaviour are approximately 0.25 and 0.1 respectively. Rajoo and Martinez-Botas [38] calculated the unsteadiness of a variable geometry turbine (VGT) using *PMSt* as an indicator. They found vane angle has less impact on the turbine unsteadiness, where the *PMSt* in all vane settings is about 0.1 under 40 Hz pulses, whilst *PMSt* increases to 0.15 as the pulse frequency became 60 Hz, implying the nozzle broadly operates in a quasi-steady manner.

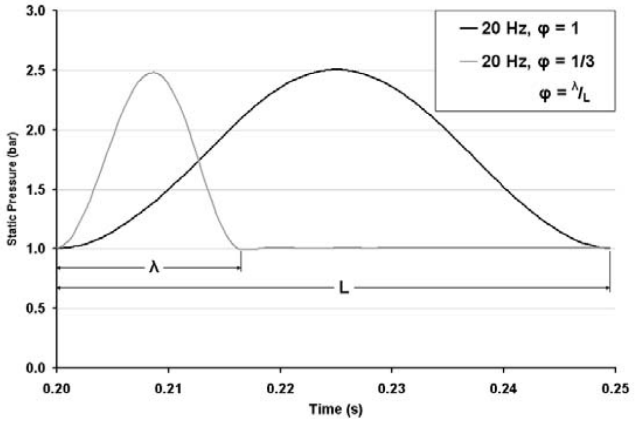

Figure. 2.3 Correction of the non-sinusoidal waveform by taking account the effective length during a pulse [26]

$$MSt = \frac{fL}{\bar{u}} \cdot \frac{1}{2\phi} \tag{2.2}$$

$$PMSt = \frac{fL}{\bar{u}+\bar{a}} \cdot \frac{1}{2\phi} \tag{2.3}$$

Costall and Martinez-Botas [27] pointed out the drawbacks of using the "filling and emptying" hypothesis to model the volute, since the prediction of turbine swallowing capacity is very sensitive to the secondary flow (even with minor features), causing the flow to be undamped as it propagates. Costall and Martinez-Botas [27] analysed the effects of secondary pulses on the turbine unsteadiness by decomposing the overall pulse into many components using Fourier analysis. The Strouhal number was then calculated individually for each component, and the mean Strouhal number of a pulse can be achieved by integrating the *St* of each component k and normalized by the Fourier coefficient (a_k). Eq. 2.4 gives the definition of *Fourier series modified Strouhal number*. Similar to *PMSt* , the pressure wave propagation effects were

taken into account by adding acoustic velocity of flow in the calculation, which was identified as *Fourier series acoustic Strouhal number*, as per Eq. 2.5. Costall and Martinez-Botas [27] suggested that it is suitable to model the turbine using filling and emptying assumption when $FSt \leq 0.15$ and $FaSt \leq 0.02$.

$$FSt = \sum_{k=1}^{\infty} \left(\frac{|a_k|}{\sum_{k=1}^{k} |a_k|} St_k \right) \tag{2.4}$$

$$\begin{aligned} FaSt &= \sum_{k=1}^{\infty} \left(\frac{|a_k|}{\sum_{k=1}^{k} |a_k|} aSt_k \right) \\ aSt_k &= \frac{f_k L}{u+a} \end{aligned} \tag{2.5}$$

The Strouhal number based unsteady criteria, such as St, MSt, $PMSt$, FSt and $FaSt$, imply the higher frequency of flow pulsation, the larger unsteadiness of the turbine will be exhibited. However, many studies [44–49] reported the averaged turbine efficiency and mass flow will move close to the steady-state data when increasing the pulse frequency, especially under an engine exhaust environment. The experimental work by Iwasaki et al. [48] studied the performance of a twin-entry turbine on a 6-cylinder engine. They found the deviation of mass flow between steady-state and unsteady measurement was depended on engine speeds and turbine pressure ratios. That deviation is smaller at higher engine speeds, and for the same engine speed, the deviation is large in low expansion ratio region but reduced as increasing the turbine expansion ratios. As also suggested by Copeland et al. [49], in an engine exhaust environment, the increased pulse frequency (higher engine RPM) will result in a rise of averaged pressure and the decrease in amplitude, which may not necessarily lead to the increase of turbine unsteadiness.

Experimental work by Capobianco et al. [50] and Capobianco and Gambarotta [51] showed the amplitude of the unsteady pulse has a greater impact on the deviation from quasi-steady behaviour than the frequency. Copeland et al. [44] introduced the *Lambda criterion* that included the effect of pulse amplitude for the assessment of turbine unsteadiness. The Λ criterion , as defined as Eq. 2.6, was derived from the mass conservation equation for compressible flows, providing a theoretical evidence that both amplitude and frequency would be important to the turbine unsteadiness. Λ normalizes the conventional Strouhal number by the pulse amplitude factor Π. They evaluated the lambda number for the volute and rotor passage individually, and found the value of Λ for the rotor wheel is an order of magnitude lower than that for the volute. So, they concluded that treating the rotor as quasi-steady will only lead to a small error.

$$\Lambda = \frac{2A}{\gamma \bar{P}} \frac{fL}{\bar{u}} = \Pi St \tag{2.6}$$

Ding et al. [52] systematically studied the effects of various parameters such as amplitude, frequency, pulse load [1], and rotational speed on the unsteady performance. Ding et al. [52] concluded that despite the pulse load, increasing either pulse frequency, pulse amplitude or rotational speed while keeping other parameters unchanged will result in a larger turbine unsteadiness, which is consistent with the finding by Copeland et al. [49]. Fig. 2.4 shows that the turbine unsteady parameters[2], calculated based on the mass flow and torque, have a positive correlation with the Lambda number, confirming the Λ criterion is effective in assessing the unsteadiness.

[1] The time averaged turbine inlet pressure

[2] The relative deviation between the unsteady performance and the quasi-steady performance

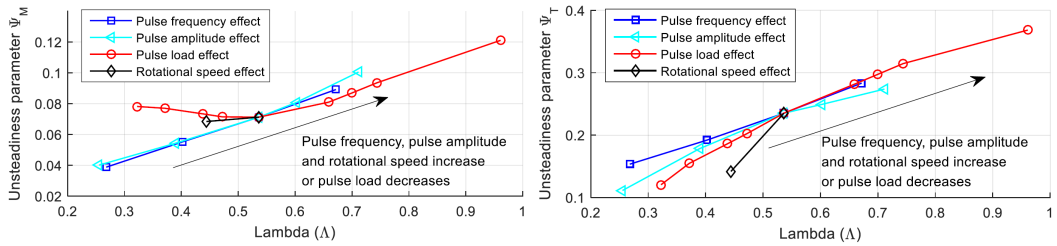

Figure. 2.4 The difference between turbine unsteady performance and quasi-steady assumption as a function of Lambda number (a) Mass flow characteristics (b) torque [52]

Based on a theoretical analysis, Cao et al. [53] introduced temporal local reduced frequency method, defined in Eq. 2.7, which is capable of assessing the time-resolved turbine unsteadiness. $|\varepsilon(t)|$ represents the temporal local gradient of the pressure wave, and $\beta_{local}(t)$ was described as temporal local reduced frequency. t_f reflects the amount of time required for the fluid particle travelling across the domain of interest. The resolution of the unsteadiness was depended on the selection of time-step size Δt. As Cao et al. [53] suggested, the temporal local criterion $|\varepsilon(t)|\beta_{local}(t)$can be reduced to Λ criterion on the cycle-averaged basis. Cao et al. [53] graphically demonstrated this hypothesis, as shown in Fig. 2.5, where the magnitude of instantaneous turbine unsteadiness has a positive correlation with the gradient of pressure pulses. Cao et al. [53] suggested the if this parameter is smaller than 0.07, the turbine is deemed to operate in a quasi-steady manner. When the value is greater than 0.07, the unsteady flow effects will play a dominant role in the turbine performance. They concluded that the turbine rotor can be treated as a quasi-steady device only in terms of cycle averaged performance, and the unsteady effects cannot be neglected if the transient performance is taken into consideration.

$$|\varepsilon(t)|\beta_{local}(t) = \frac{|\Delta P(t)|}{\overline{P}}\frac{t_f}{\Delta t} \tag{2.7}$$

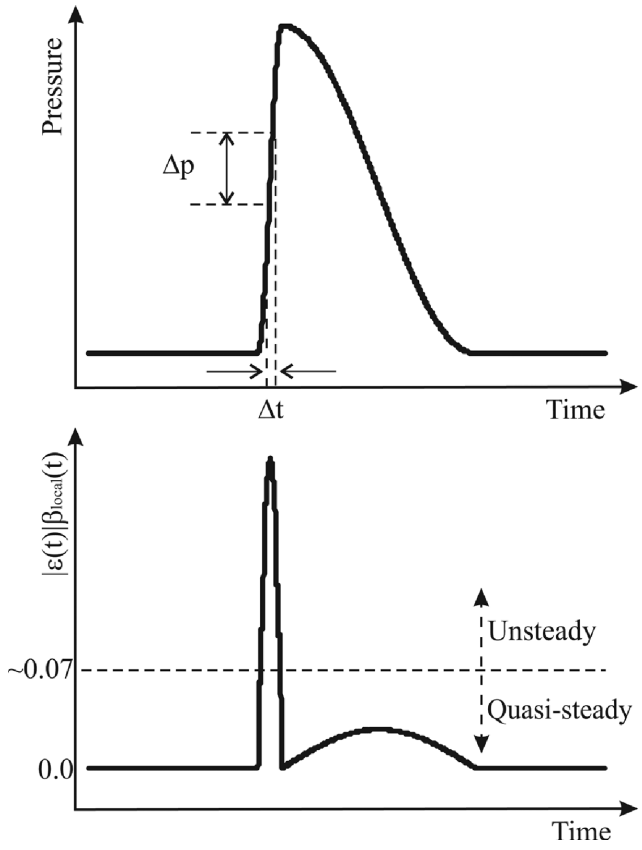

Figure. 2.5 Demonstration of temporal local concept Cao et al. [53]

Marelli and Capobianco [39] compared the efficiency of a waste-gated radial flow turbine between steady and unsteady conditions. Their experiment results show the averaged unsteady efficiency was generally lower than the equivalent steady-state condition regardless of the pulse frequency and the angle of wastegate opening, indicating the overestimation of turbine performance by using quasi-steady assumption. They found the instantaneous efficiency was greater than 100% under 70 Hz pulses when the pressure reached the lowest level, and this phenomenon was not observed in either higher (100 Hz) or lower (40 Hz) frequency. They suspected that the phenomenon was attributed to a resonance effect where the natural frequency of the pulsating flow was close to that of the circuit interposed between the pulse generator and the turbine.

Karamanis et al. [12] and Karamanis and Martinez-Botas [54] investigated the unsteady performance of a mixed-flow turbine with the measurement of instantaneous velocity components at the rotor inlet and rotor exit using Laser Doppler Velocimetry. Their study shows the cycle-averaged unsteady efficiency was lower than the equivalent quasi-steady results for all test cases, and the maximum deviation occurs when the turbo-speed and pulse frequency are minimal, as listed in Table. 2.1. Karamanis et al. [12] found there is a portion of instantaneous efficiency reaching negative, as shown in Fig. 2.6. This is the first time where negative efficiency was experimentally recorded. The case with lowest turbine speed and lowest pulse frequency, as shown in Fig. 2.6 (a), produced the largest portion of negative efficiency. However, With the increase of the pulse frequency and turbine speed, the portion of negative efficiency was reduced and eventually disappeared. The largest portion of negative efficiency in the lower pulse frequency cases could be the reason that the larger deviation between unsteady and quasi-steady on the cycle averaged basis. Karamanis et al. [12] indicated that during the stage of negative efficiency, the momentum energy was transferred from the rotor to the fluid. Watson and Janota [10] also predicted from an early study that when the turbine operates under extreme low loading conditions, where the velocity ratio is greater than 1.1, the turbine will be acting like a compressor. Therefore, the negative efficiency is a physical phenomenon that only occurs in the pulsating flow conditions and cannot be easily captured by standard Gas stand measurements, which is an obvious deviation from the quasi-steady assumption.

Table 2.1 Comparison of unsteady cycle averaged efficiency with quasi-steady assumption [12]

Shaft Speed	**Pulse Frequency**	**Steady**	**Unsteady**
50%	40 Hz	0.69	0.44
50%	60 Hz	0.69	0.57
70%	40 Hz	0.74	0.66
70%	60 Hz	0.74	0.70

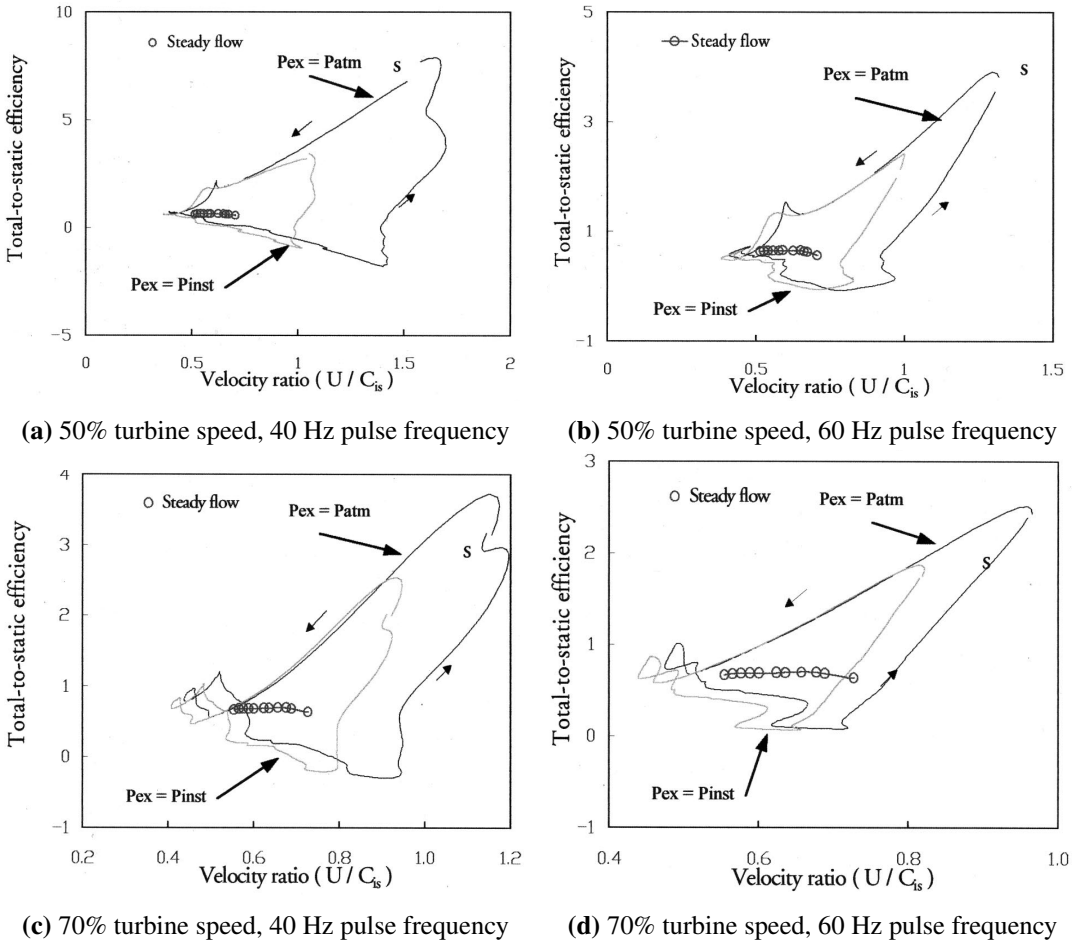

(a) 50% turbine speed, 40 Hz pulse frequency

(b) 50% turbine speed, 60 Hz pulse frequency

(c) 70% turbine speed, 40 Hz pulse frequency

(d) 70% turbine speed, 60 Hz pulse frequency

Figure. 2.6 Instantaneous total-to-static efficiency vs velocity ratio [12]

The negative efficiency phenomenon was also observed from the experimental study [31, 55] and the numerical study [56, 57]. Szymko et al. [31] found 50% of a pulse cycle contains negative efficiency at 20 Hz. Szymko et al. [31] commented that the negative efficiency will have a minimal impact on turbine performance since the negative energy only accounted for 4% of the available energy. Rajoo et al. [55] compared the instantaneous efficiency between nozzle (Fig. 2.7 (a)) and nozzless turbine (Fig. 2.7 (b-c)) in a pulse cycle. They found both nozzled and noozless turbine exhibit more negative efficiency under low pulse frequencies, and the nozzless turbine exhibit more negative efficiency compared with the nozzled counterparts. In the nozzled turbine, they found the turbine no longer produced negative efficiency at close nozzle positions such as 65°and 70°. They concluded the reduced

portion of negative efficiency was due to the nozzle effects, which enhanced the flow kinetic energy available to the rotor during the pulse.

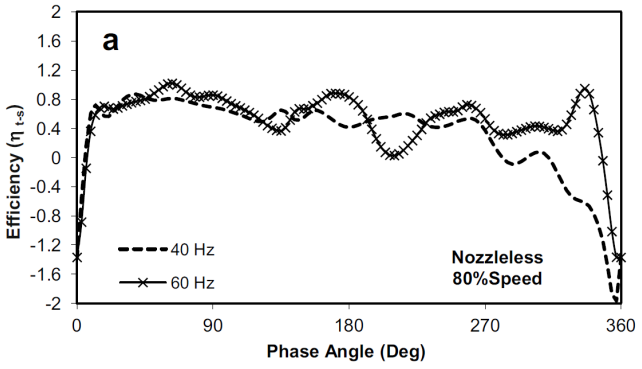

(a)

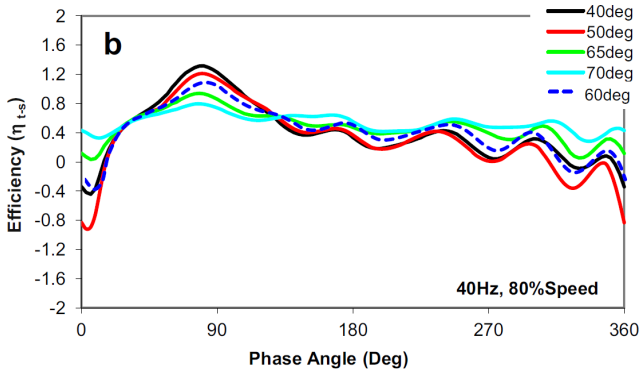

(b)

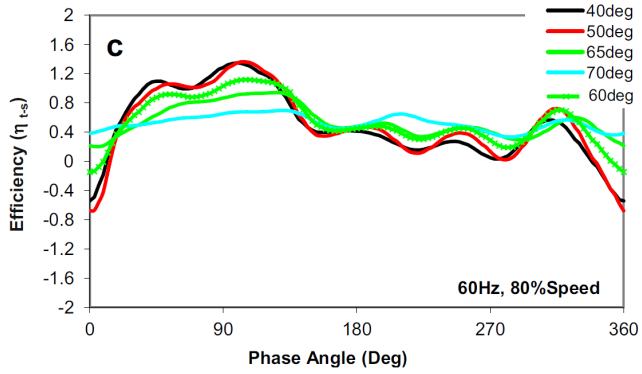

(c)

Figure. 2.7 Comparison of the efficiency curves between the nozzled single-entry and nozzleless turbine for different nozzle vane angles, different flow frequencies conditions at 80% equivalent speed [55]

2.2 Numerical Turbine Models

Over the last few decades, Several turbine models have been proposed to simulate the aerodynamic performance. These turbine models, from simple to complex, can be classified into empirical model, partly empirical model, one-dimensional model, quasi three-dimensional CFD model, and full three-dimensional CFD models.

2.2.1 Empirical and Partly Empirical Models

Empirical models are those using polynomial [58–62], exponential [63], or parabolic [64] expressions fitted with experimental data, to describe turbine swallowing capacity or efficiency characteristics, where the turbine performance parameters were expressed as a function of the turbine expansion ratio, blade speed ratio or speed parameters. Empirical models are normally used for turbine map extrapolations purposes where only limited test data are available.

Partly empirical employed nozzle flow physics where turbine was modelled as adiabatic nozzles of effective area fitted with experimental data. Watson and Janota [10] developed a simple model, defined as per Eq. 2.8, based on the replacement of the turbine by a plain nozzle, whose area could produce the same pressure drop when imposing the same valve of mass flow rate across it. However, a simple nozzle model would easily reach choked flow condition when the expansion ratio is over 1.89, and this is not the case where a radial flow turbine is possible of reaching a total expansion ratio of 3.0 [29]. Jensen et al. [62] improved the model in dealing with the choking flow conditions, where the prediction of mass flow was improved by Eq. 2.9 when the turbine expansion ratio exceeds a critical number (defined in Eq. 2.10), whilst if the expansion ratio was below the critical number, Eq. 2.8 is still applicable for this calculation.

$$\frac{\dot{m}\sqrt{T_{01}}}{P_{01}} = A_{eff} \cdot \sqrt{\frac{2\gamma}{R(\gamma-1)}\left[\left(\frac{1}{PR_t}\right)^{\frac{2}{\gamma}} - \left(\frac{1}{PR_t}\right)^{\frac{\gamma+1}{\gamma}}\right]} \tag{2.8}$$

$$\frac{\dot{m}\sqrt{T_{01}}}{P_{01}} = A_{eff} \cdot \sqrt{\frac{2\gamma}{R(\gamma-1)}\left[\left(\frac{1}{PR_t^{cirt}}\right)^{\frac{2}{\gamma}} - \left(\frac{1}{PR_t^{cirt}}\right)^{\frac{\gamma+1}{\gamma}}\right]} \tag{2.9}$$

$$PR_t^{cirt} = \left(\frac{2}{\gamma+1}\right)^{\frac{\gamma}{\gamma-1}} \tag{2.10}$$

A_{eff} is the effective turbine area as a linear function of pressure ratio and is given as, where k_1 and k_2 are fitting factors:

$$A_{eff} = k_1 \cdot PR_t + k_2 \tag{2.11}$$

Payri et al. [65] proposed an alternative method based on the study of Watson and Janota [10], the turbine was modelled as two nozzles in series, separated by an intermediate chamber to represent the internal volume of the turbine, as shown in Fig. 2.8 (a). The first nozzle represents for the turbine stator and the second nozzle represents for the rotor passages. They assumed the degree of reaction of a radial turbine is about 50%, in which half of the expansion took place in the stator and the other half in the rotor. The effective area of both nozzles was obtained from turbine measurements under steady flow conditions Payri et al. [65] extended this method for twin-entry turbine by setting two nozzles, representing for double entry casing, to discharge into a common intermediate chamber. Serrano et al. [29]

improved the method of using a serial twin-nozzle model for VGT applications, where the stator effective area was expressed as a function of stator vane angles. Their model was tested under pulsating flow conditions and performed a good prediction with respect to the pressure at turbine inlet and outlet. Payri et al. [66] later improved the partly empirical model by employing more flow physics in the model calculation, such as the velocity triangles and fluid fundamental equations, showing the capability in turbine efficiency prediction.

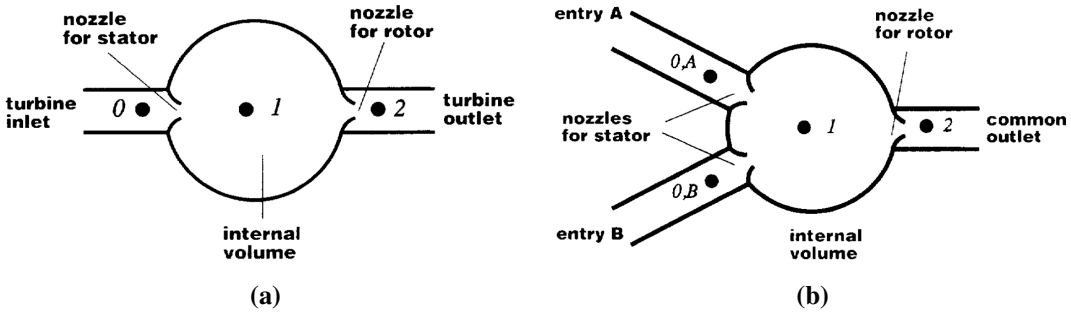

Figure. 2.8 schematic view of turbine models based on adiabatic nozzle assumption (a) single entry turbine (b) twin-entry turbine [65]

2.2.2 One-dimensional code Integrated with Turbine Sub-models

One-dimensional models simplify and solve Navier–Stokes equations, namely the conservation of mass, momentum and energy equations in the dimension of flow direction. The fluid path is contained within ducts in 1D models, which can be straight, curved, and tapered. Since any curvatures will involve in an extrusion in a section dimension, additional friction losses are normally added to account for the curvature effects [67, 68]. The propagating and damping effects of pressure waves can be effectively predicted in 1D models, thereby capturing the pulsating nature of exhaust gases. The flow in one duct can be mixed with another duct through *flow junctions*, where the heat transfer and friction effects due to the flow mixing can be accounted via heat transfer and friction multipliers. Turbines are served as a sub-model in the 1D codes. The volute and rotor were normally modelled separately, where the former can be treated duct, whose volume and length are specified to account for most of unsteadiness of a turbine, namely the filling and emptying effect. The rotor can

be treated by either zero-dimensional maps or mean-line model to account for the energy transfers.

Map-based Turbine Model

Map-based turbine model simulates the performance of a turbine based on a turbine characteristic map, which is normally gathered from the steady-state test. The turbine map contains turbine performance data, such as pressure ratio, mass flow, and efficiency at specific turbocharger speed. However, the turbine performance data is normally limited in the operating range when using the compressor as a loading device during the standard gas-stand test. Empirical extrapolation techniques were used to estimate the turbine performance at off-design conditions since any physical extrapolation technique normally required the geometric data of the turbine which is not easily available. Map-based turbine model is commonly employed in commercial 1D codes, such as GT-Power software [64] and Ricardo-Wave software [69] due to its simplicity in implement, where only experimental data is required. If a steady-sate map was used in 1D for unsteady simulation, at any instantaneous of simulation time, the turbine will follow exactly same as the steady-state performance data, which is also known as the quasi-steady method.

Pesiridis et al. [46] managed to use the *unsteady map* for 1D simulation. The map was constructed based on cycle averaging the experimental data from the unsteady test. By comparing the turbine performance of using conventional steady-state map against the equivalent unsteady map, Pesiridis et al. [46] found the quasi-steady method underestimate the turbine efficiency and mass flow parameter upto 12% and 6% respectively. The deviation between quasi-steady and unsteady was reduced as increasing the pulse frequency. Nevertheless, Pesiridis et al. [46] suggested that it is feasible to apply quasi-steady assumption for 1D engine simulations since a minor difference of less than 1% was found when compared with the case of using unsteady maps. However, this may not be a practical way since it requires a very large library of unsteady testing data to build the map.

Mean-line Turbine Model

Mean-line model calculates the turbine performance as if there is a mean streamline of gas flowing through a turbine. The turbine efficiency is estimated by calculating the energy losses as air flowing through different sections of the turbine. These losses, which are normally described as a function of velocity triangles and loss coefficient, can be classified as passage loss, incidence loss, disc friction loss, exit loss. Naturally, these loss coefficients are empirical, however, accurate predictions required the validation against to validate experimental data. Mean-line models require less computational resources than the higher-order model. Besides, they also provide more physical inside of turbine performance at off-design conditions compared with the with empirical model.

Most early studies towards mean-line models were proposed by NASA researchers [70–76]. Futral and Wasserbauer [70], Todd and Futral [71], Wasserbauer and Glassman [72] developed the mean-line codes for radial flow turbines fitted with nozzle casing. Kastner and Bhinder [77] predicted nozzleless radial flow turbine, with the assumption of adiabatic flow, constant angular momentum in the casing, and the perfect gas relation. Whitfield and Wallace [78] improved the incidence loss calculations for mixed flow turbines, noting the inlet blade angle is not zero. Whitfield and Wallace [78] indicated the optimal efficiency of a mixed flow turbine occurs at a negative incidence angle in the range between -20 to -40 degrees. Meitner and Glassman [74] improved the model developed by Wasserbauer and Glassman [72] by taking into account the variation of stator area and vane end-clearance effects, thus the mean-line model for VGTs have been developed. Meitner and Glassman [73] further modified the mean-line model by taking the rotor back-sweep effects into account. The loss calculations proposed in these early mean-line codes are still valid today and referenced by later researchers.

Romagnoli and Martinez-Botas [79] proposed a model for both nozzled and nozzless mixed flow turbine under the steady-state conditions. Loss terms regarding the enthalpy transfer at

different stations were calibrated for peak efficiency point only and revealed good agreement with experiment. In their model, the Mach number was used to define choking flow conditions, and also employed as a looping factor. A breakdown of loss analysis was performed showing the distribution of each loss element towards the turbine efficiency under various shaft speeds. Fig. 2.9 shows the passage loss accounts for large portions of overall turbine loss and it is less sensitive to velocity ratio across the whole operating range. This indicates that the passage loss could be considered as an ideal calibration parameter due to its uniform influence towards the entire steady-state efficiency curve.

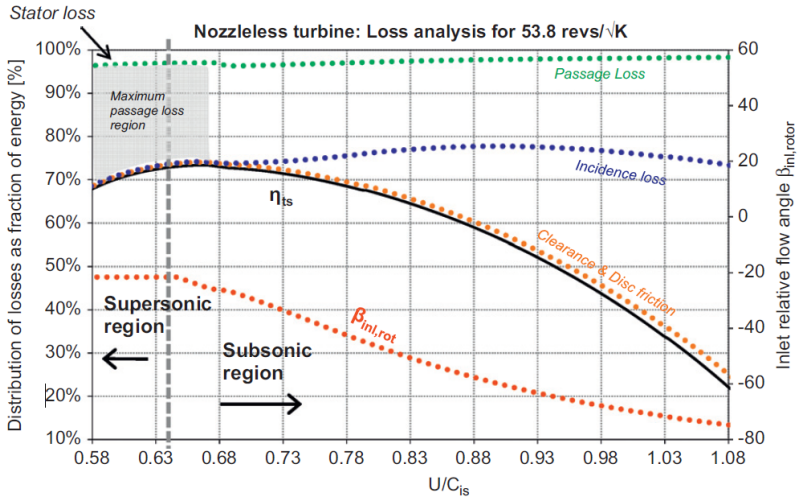

Figure. 2.9 Losses analysis Of mean-line turbine model under steady-state condtion at 53.8 $revs/\sqrt{K}$ [79]

Early attempts that coupling the 1D gas dynamic codes with mean-line models for the prediction of turbine unsteady performances were presented by Chen and Winterbone [33], who used the loss models of Wasserbauer and Glassman [72]. They calculated the incidence of a radial rotor by using free vortex equation based on the flow condition at volute inlet. Chen et al. [34] improved the numerous loss term calculations, where the effects of flow separation were taken into account by using slip factors for the velocity triangle calculation at the incidence. Despite the swallowing capacity was underestimated, the prediction of instantaneous turbine power was in good agreement with experimental data. Abidat et al. [80] used the

same method of [34] for the performance prediction of mixed flow turbine under pulsating flow conditions. By investigating the pulse frequency and amplitude effects on, they found the departure of both mass flow and power was not far from the quasi-steady assumption in terms of cycle averaged value.

Costall et al. [26], Costall and Martinez-Botas [27] simulated the pulsating flow for both single and twin-entry turbines with a further improvement regarding both the boundary condition and solver algorithm. Transmissive boundary condition was used at the volute inlet, enabling the model to reproduce the same pressure profile as recorded in the experiment while allowing the waves leave the domain without reflecting the upon of the boundary, while would otherwise distort the results. Two-step Lax-Wendroff scheme combined with the total variation diminishing flux limiter resulting in a second-order, conservative, shock-capturing finite difference solver. Similar to the study of [33, 34, 80], an azimuthal location 180 deg downstream of the volute tongue was treated as nominal rotor inlet. In order to simulate the pressure drop, the turbine was modelled as a pressure loss boundary condition, where the pressure losses were calibrated against steady flow. Their 1D code demonstrated a good agreement with experimental data when modelling the hysteresis behaviour of turbine swallowing capacity characteristics at 20 Hz, but declined for frequencies greater than 40 Hz. They suspected that the turbine will be exerted different pressure losses under unsteady flow conditions compared with steady flow, especially when the frequency is high.

Chiong et al. [81] utilized the 1D code developed by Costall et al. [26] and mean-line model to simulate both mass flow and efficiency characteristics of a nozzleless turbine on the time-resolved basis. Constant absolute flow angle was assumed and calculated based on the A/r ratio and density change across the volute. In the efficiency calculation, phase-shift method based on the sum of bulk flow velocity and sonic velocity was applied. Their model showed better prediction at low-velocity ratio than at high-velocity ratio, where the negative efficiency phenomenon, as observed in experimental data, has failed to be predicted. Chiong

et al. [67] improved the model of [26] with the consideration that the absolute flow angle will be varied along the volute. Flow entering the rotor was assumed at three nominal locations, corresponding to 90°, 180°, and 270°of the volute azimuth, and left the rotor at a common exit, as shown in Fig. 2.10. The multiple rotor entry method improved the turbine performance prediction especially the instantaneous mass flow rate. For the loss calculations, they utilized a multiplier to correct the loss measured from the steady-state data for unsteady simulations, showing a small improvement in power prediction. In addition, they used non-constant rotor speed, took from experiment, as one boundary condition, leading to an improvement of cycle-average power prediction by 3.7% compared constant speed boundary.

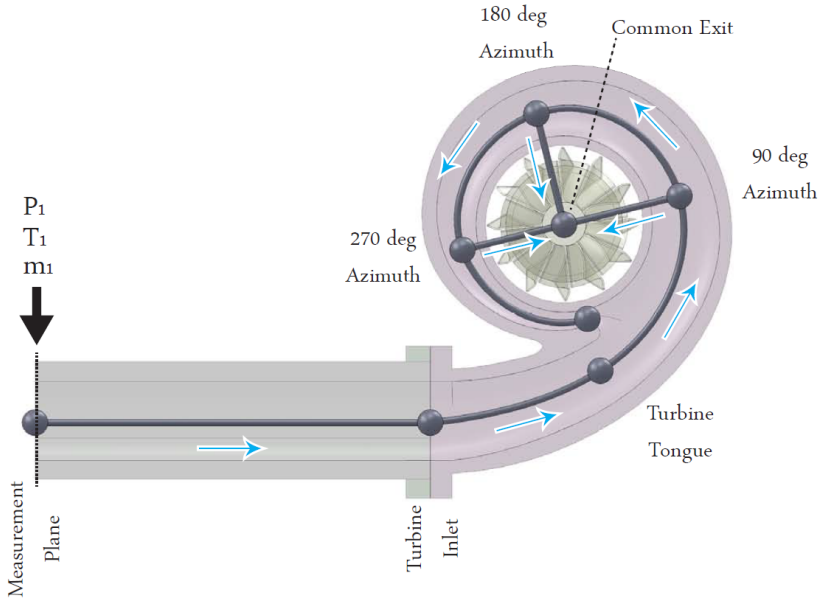

Figure. 2.10 Schematic diagram of 1D turbine model with three inlets to the mean-line model [67]

Chiong et al. [82] extended the model for the performance prediction of twin-entry turbines, found that the tapered ducts in 1D have an effect of magnifying the fluctuation of secondary flows. Chiong et al. [68] constructed an equivalent cycle-averaged unsteady turbine performance map by integrating the 1D model with a steady-state calibrated mean-line model. Turbine performance was then evaluated based on the unsteady map, and compared with

quasi-steady assumption. After the comparison of a series of data on the cycle-averaged basis, they found both the unsteady model prediction and experimental data are quite close to quasi-steady assumption especially the turbine output power. However, there have noticeable deviations in terms of instantaneous performance. This suggests the turbine instantaneous performance could not be effectively reproduced using cycle-averaged maps, and the turbine should be treated as time-resolved manner instead of cycle-averaged manner. Their research confirmed the results by Pesiridis et al. [46], in which the engine performance was found to be quite similar when replacing the steady-state map with cycle-average map. Chiong et al. [83] further studied the number of nominal rotor entries on the prediction of mean-line model based on the work of Chiong et al. [67]. The model performance with single, four, and six entries was compared. The six rotor entries model under-predicted the output power especially at the peak, and the model with four rotor entries seems to have the most satisfactory mass flow rate and actual power predictions. The effects of discretion length were also evaluated, and the maximum L/D (discretion-length/pipe-diameter) ratio of 0.55 served a good compromise between simulation time and accuracy. More recently, Chiong et al. [84] modelled the turbine as a non-adiabatic loss boundary with the inclusion of loss terms in stagnation enthalpy calculation. This method significantly reduced the rotor geometry inputs compared to mean-line integrated model, where only volute inlet/outlet area and rotor inducer/exducer area was required as geometry input variables. Their model showed a highly comparable prediction with mean-line model, but reduced the computational time by 38.6%.

Although the turbine mean-line models offer physical ways of predicting and extrapolating of turbine characteristic maps, it still requires experimental data for calibrating various losses coefficient in order to minimize the errors. Sakellaridis and Hountalas [85] demonstrated that the prediction of turbine performance will be much improved if the mean-line model was calibrated against experimental data rather than directly using the empirical corrections

based on NASA's suggestions, even though only one testing point was selected per speed line was used for calibrations.

2.2.3 Three-dimensional CFD Models

Although 0D or 1D model is able to capture the unsteady behaviour of the turbine, they mainly rely on the hypothesis that modelling rotor in quasi-steady manner. The only experimental evidence of supporting the quasi-steady assumption was come up with Yeo and Baines [43], who found similar rotor inlet velocity profile under steady and pulsating flows. However, it still remains a certain degree of uncertainties until the whole picture of the internal fluid was analysed. The three-dimensional (3D) CFD codes calculate the device performance using physically equations, thus normally without the needs for empirical corrections. It also provides an opportunity of looking insight of the fluid field within a turbine system. However, the CFD method requires much more computational expensive than the lower order models. Therefore, it is normally used for the flow performance analysis of a specific device (turbine, engine's cylinder and etc.), rather than the whole system, such as the power train. Additionally, the CFD method is applicable when there is geometrical model available, so that it is normally unused in the early design stages.

The early pulsating flow CFD work was published by Lam et al. [86], who modelled a single entry turbocharger turbine connected to a four-cylinder, four-stroke engine. They use a frozen rotor approach to model the rotor stage such that the relative position between the volute and rotor is fixed during the simulation. The Coriolis and centrifugal effects were modelled as additional source terms in the governing equations within the rotor domain to account for the change in relative velocity due to rotation. The frozen rotor method is normally used for steady-state conditions when the flow at the interface between stationary and rotating domain is assumed to be relatively uniform. Lam et al. [86] justified this method by noting that the pulse frequency is much lower than the rotor passing frequency. An advantage of the frozen

rotor method is that it allows to using a relatively large time-step to reduce the simulation time since the time-scale of the rotor domain does not to be resolved.

Palfreyman and Martinez-Botas [56] employed the sliding mesh (SM) method to model the interface between the rotor and stator. In SM, the rotor mesh was explicitly rotated during the calculation, and the stationary and rotating meshes being coupled at each instant in time at the stator-rotor interface thus required more computational time. Hellström [57] studied the combined effects of pulsating flow and different secondary perturbations at the turbine inlet on the turbine performance using Large Eddy Simulation. They noticed the shaft power is lower during the acceleration phase of the mass flow compared to the deceleration phase, which forms a hysteresis loop of mass flow versus the shaft power. Hellström [57] mentioned that the SM technique is better than the frozen rotor technique because it could account for the viscous losses at the rotor-stator interface.

Galindo et al. [87] studied a variable geometry turbine under the effects of pulsating flows, and compared the turbine steady-state flow results between the frozen rotor and SM method. They found the difference is low when the turbine is working close to the design conditions, but is large at off–design regions. The swallowing capacity characteristic was analysed in each domain (volute, nozzle, and rotor) at different pulse frequencies. It is observed that the volute is the main reason causing the phase-shift and hysteresis behaviour. The nozzle section presents a limited hysteresis behaviour, and impeller is less affected by wave action and mass accumulation effects than the stator, due to its smaller size.

Padzillah et al. [88] investigated circumferential flow angle distributions between steady and pulsating flow conditions. They found the rotor inlet flow angles under pulsating flow conditions is significantly different from the corresponding steady-state conditions. Besides, a higher pulse frequency would increase the variation of rotor incidence angle across the rotor circumference due to higher wave interactions. The vaneless volute produced larger

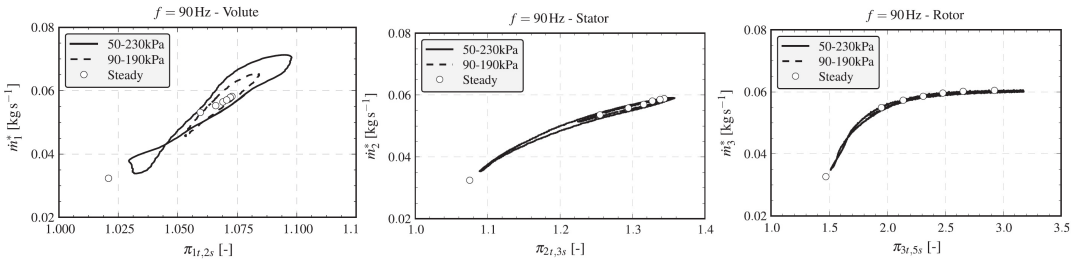

(a) **(b)** **(c)**

Figure. 2.11 Turbine swallowing capacity characteristic of each domain [87]

variations of the circumferential flow angles at both of the rotor inlet and exit than the vaned volute, the variation is more significant near the tongue. Padzillah et al. [88] also compared the frozen rotor with the SM under the unsteady flow condition, and found they have achieved good agreement.

The loss mechanisms of turbomachinery were summarised by Denton [89]. They considered the main loss is entropy generation caused by three factors, namely the profile losses, tip leakage losses, and wall and secondary flow losses. Each of these three types of losses contributes to roughly one-third of the total turbomachinery losses. Under the off-design conditions, turbomachinery suffers from additional loss due to non-optimal incidence angles, which is also known as incidence loss. Based on the detailed flow filed analysis, Palenschat et al. [90] confirmed the loss mechanisms proposed by Denton [89] is also valid for twin-entry radial flow turbines. They found the losses are more dominate in the suction side of the blade. This is contributed by the tip leakage flow, since they can mix with the passage flow and form vortexes, when they leak over the blade tip gap from the pressure side to the suction side. Newton et al. [91] found the tip leakage losses contribute to about half of entropy generation within the rotor stage of a mixed flow turbine. They highlighted the $k-\omega$ *SST* turbulence model is more accurate to account the loss generations than the $k-\varepsilon$ model. Xue et al. [92] compared the loss generations of nozzled twin-entry mixed flow turbine between steady and unsteady flow conditions. They found the cycle-averaged losses of turbine components, including the volute, the nozzle, and the rotor, are lower than the quasi-steady condition.

Moreover, as the turbine unsteadiness increases, indicated by a higher Strouhal number, the loss in all the three components decreases gradually.

2.3 Mechanical Loss Under Pulsating Flow Conditions

Mechanical losses are refereed to the energy losses in transmitting the shaft energy from the turbine to the compressor. These energy losses mainly refereed to the bearing friction losses, including both radial bearing losses and the drag from thrust bearing [93]. As suggested by Baines [16], the mechanical losses were depended on the size of turbocharger, where the smaller turbocharger size, the higher percentage of mechanical losses would be expected. Diango et al. [94] mentioned the heat and friction losses of the turbocharger can be significant when the engine operates under low-loading conditions, which can even be higher than the compressor mechanical power.

In a standard turbocharger gas-stand test, the turbine power was normally calculated on the basis of the power absorbed by the compressor [30]. An advantage of using the compressor as the turbine loading device in the gas-stand test is that the turbine efficiency already lumps various loss mechanisms together, containing bearing losses, aerodynamic losses, and heat transfer losses [95]. It is not necessary to apply mechanical efficiency in simulations when using a "lumped" turbine map since loss terms are already involved, where the compressor power can be correctly predicted providing turbine operating conditions. Many studies have analysed the mechanical loss during the steady-state operation of the turbocharger. Shaaban [96] and Serrano et al. [97] evaluated the turbocharger mechanical losses in quasi-adiabatic cold test platform, where the temperature at turbine inlet, compressor outlet, and oil has to be maintained as close as possible. In this methodology, the heat transfer effects can be neglected, and the mechanical loss can be determined by means of oil temperature drop. Payri et al. [93] proposed an empirical model, where the mechanical efficiency was related to dimensionless numbers such as Reynolds, Prandtl, and a dimensionless net axial load.

The effects of oil temperature and oil pressure were also studied in [93]. Deligant et al. [98] employed CFD methods to study the mechanical losses within turbocharger journal bearings.

The only literature regarding the instantaneous turbocharger mechanical loss under both steady and pulsating flow conditions was published by Serrano et al. [99], who utilized the same quasi-adiabatic test platform as Payri et al. [93]. In the steady-state simulation, the error with respect to the shaft speed was evaluated under different turbine loading conditions. The model performance was compared with experimental data of using mechanical loss model, as shown in Fig. 2.12. They found if the mechanical losses model was not applied, high turbocharger speed errors will be produced in all operating conditions. Using a constant mechanical efficiency of 90% gives satisfactory results at high turbine powers, but fails at low powers. The best results were obtained by using the mechanical loss model, which takes into account the variation of power transmission losses at different turbocharger operating conditions.

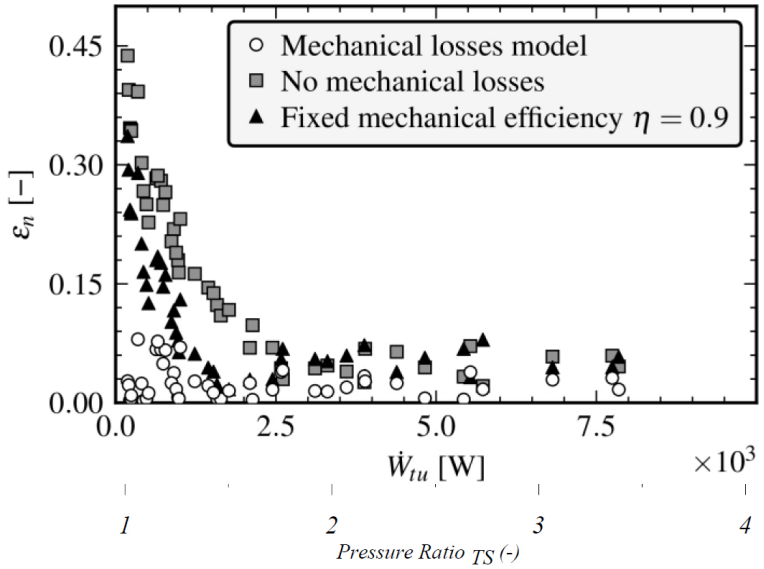

Figure. 2.12 Turbocharger speed error with different mechanical loss applied [99]

In the assessment mechanical loss under pulsating flow conditions, Serrano et al. [99] found the instantaneous mechanical efficiency changed significantly at different turbine

loading conditions, ranging from the highest value of about 0.85 at high loading (velocity ratio of 0.42) to the lowest value of about 0.1 at low loading (velocity ratio of 0.78), as shown in Fig. 2.13 (a). As observed in Fig. 2.13 (b), the mechanical efficiency times the isentropic efficiency can change notably compared to the isentropic efficiency due to the large variations of mechanical efficiency during an engine cycle. Serrano et al. [99] suggested using instantaneous mechanical efficiency rather than a constant value, especially when considering the instantaneous variation of engine performance. However, their model simplified the calculation of instantaneous turbine isentropic efficiency by applying the quasi-steady assumption, as the hysteresis loop of η_t was not found in Fig. 2.13 (a). This implies the mechanical loss will be even difficult to predict when considering the unsteady flow effects. Besides, their model does not take into account windage losses, caused by viscous drag generated in the gap between the rotating wheel back-plate and the fixed turbine inner case Macek and Vítek [100], which should be applied as a part of mechanical efficiency calculation as suggested by Delgado and Proctor [101]. This indicates more uncertainty will be involved if considering pulsating flow effects in mechanical efficiency calculations.

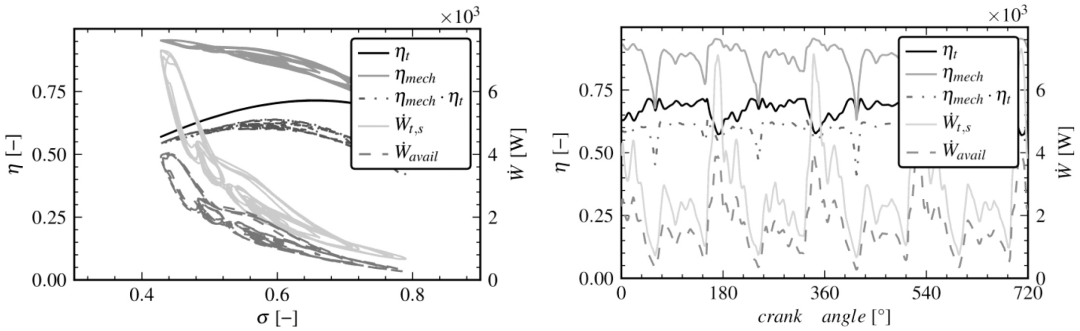

Figure. 2.13 (a) Mechanical efficiency versus crank angle, and (b) mechanical efficiency versus turbine velocity ratio at 2000 rpm engine speed [99]

2.4 Optimization of Turbocharger Turbines

Improving the efficiency of a turbocharger turbine can benefit the engine's performance in many aspects. Firstly, an efficient turbine can convert more thermal energy to mechanical

energy that drives the compressor to a higher boost level, leading to a higher engine power density and faster transient responses. Secondly, for a given steady-state boost requirement, increasing the turbine efficiency enables a larger waste-gate opening, implying a lower back-pressure could be achieved and consequently less pumping losses.

Turbocharger turbines consist of two most important parts, namely the volute and the rotor, as shown in Fig. 1.4. The volute can be vaneless or fitted with a nozzle guided vanes, as shown in Fig. 1.6. It is commonly to optimize either or both of them in order to improve turbine performance. The volute has the function of increasing the kinetic energy of exhaust gas and directing the flow towards the rotor inlet at a favourable flow angle. [102–105] investigated the influence of volute cross-sectional shape on the turbine performances. Martinez-Botas et al. [102] in their numerical study found the sharper corner of the volute cross-sectional shape produced more secondary flow near the corner, which reduced the effective flow area and increase the total pressure losses. This was also confirmed by subsequent unsteady flow simulations of [104]. Many researchers reported that the volute tongue has a large influence on the turbine performance due to the undesirable flow non-uniformity caused by the tongue region. Suhrmann et al. [106] suggested a higher turbine efficiency could be achieved by reducing the tongue radius in combination with tongue angles. Based on the structural analysis, Heuer et al. [107] reported the higher blade excitation forces will be developed as reducing the tongue to wheel distance. Gu et al. [108] found the significant pressure gradient around the tongue is the major reason that causes the volute exit flow deviating from the free vortex assumption. The variation in the area–radius ratio (A/r) with respect to azimuth angle has been studied by Meghnine et al. [103]. They found the non-linear A/r distribution can achieve better uniformity along the circumferential direction.

As has explained in Section. 1.2, the rotor can effectively convert flow energy into mechanical energy. Compared with a radial flow turbine, the mixed-flow turbine offers two additional design variables, namely the non-zero blade inlet angle (β_B) and cone angle (γ) [109]. Their

relation together with the camber angle (ϕ_β) can be described in the analytical equation Eq. 2.12 from Ref. [109], where the subscript β implies the camber angle was defined in β criteria. This equation says that an optimal inlet blade angle can be achieved by optimizing the cone angle and camber angle at the rotor leading edge. It will not produce any blade angle as the cone angle will be 90°.

$$tan\beta_B = cos\gamma\, tan\phi_\beta \tag{2.12}$$

A number of mean-line models [110–112] successfully predicted turbine performances based on empirical loss corrections. Those losses occurred within the rotor stage can be classified into incidence loss, passage loss, tip clearance loss, and disc friction loss. One of the major contributors to loss is the passage loss that depends on the kinetic energy difference between the rotor inlet and exit. In a rotor passage, its shape and volume are mainly affected by the hub and tip diameters, chord length, number of blades, and distribution of camber angles. Therefore, to achieve a better design, it is necessary to consider these design parameters during the optimization process.

Zhang et al. [113] outlined that varying the cone angle can shift the peak efficiency to a lower velocity ratio, but not necessarily increase the level of efficiency. The influence of leading edge was discussed in [114, 115]. Leonard et al. [116] studied the influence of varying the cone angle and the associated inlet blade angle on the mixed-flow turbine performance. They found the inlet blade angle has more influence on the optimal velocity ratio than the cone angle, and the optimal velocity ratio can shift to a lower value as increasing the inlet blade angle.

A number of researchers reported the method of optimizing the turbine blade. Chen and Baines [117] proposed an analytical optimization method for mixed-flow turbines, aiming at reducing the energy losses at both rotor inlet and outlet by modifying the turbine loading factors. Rahbar et al. [111] integrated turbine mean-line loss model with genetic algorithm (GA) to optimize a radial flow turbine for Organic Rankine Cycle (ORC) usage. However, the main problem of using mean-line models is that it requires experimentally validated correction factors in order to make reliable predictions of turbine performance whilst designs are significantly changed. Therefore, by using empirical correlations or, even worse, maintaining the same correction factors throughout the optimization, this may lead to erroneous predictions since radically different blade designs may be created during the optimization process.

Based on three-dimensional CFD optimization, Khairuddin et al. [118] separately optimized different features of a mixed-flow turbine rotor, such as the hub, shroud, camber-line distribution, leading and trailing edge profiles. They found the hub and shroud profiles have the largest impact on turbine performance. Rahbar et al. [119] optimized a radial flow turbine for ORC usage, targeting on maximizing the turbine efficiency. Nineteen design parameters were involved throughout the optimization process, including the shape of hub and shroud, blade angles and blade thickness. To reduce the simulation time, they used a hybrid approach of a GA and a surrogate model, where a DOE constructed response surface which was subsequently optimized. Therefore, the design variables that achieve an optimal turbine can be estimated by examining the response surface. Al Jubori et al. [120] performed the multi-objective optimization of a small-scale radial flow turbine using a similar method as [119], but with both turbine efficiency and power optimized during their study.

Mueller et al. [121] optimized a turbine impeller for a higher isentropic efficiency and a lower moment of inertia using a total number of twenty-four different parameters. Differential Evolution (DE) algorithm with a constant population size of 40 individuals was used to

generate impeller geometries. To accelerate the optimization process, a self-learning Artificial Neural Network (ANN) was employed as a surrogate model. During the optimization process, the accurate turbine performance result will be firstly obtained by CFD and then added to the ANN training database. In their study, the ANN showed a better prediction after 40 DE iterations with an error of less than 1% due to the enriched database. However, at the end of the optimization, they found most designs violate the design constraints (only 10 designs are satisfied with all design constraints) in particular the maximum allowable von Mises stress. [122] compared the ANN with a Kriging surrogate model, and found the later performs better due to the faster convergence rate, higher stability, and lower chance to be trapped in a local optimum. Tüchler et al. [123] conducted multi-point optimization of a radial compressor wheel using a combined CFD - GA approach. A penalty function was added to the objective function that assessed the blade loading of both main impeller and splitter in order to avoid the reduction in surge margin.

2.5 Summary

This chapter has reviewed the technology of turbomachinery. The unsteady flow performance of a turbocharger turbine has been comprehensively studied both experimentally and numerically with the acknowledge of previous researchers. However, there still remains some spaces for further improvement by using state-of-art technologies.

Firstly, many researchers [12, 31, 39, 55–57] have observed the negative efficiency phenomenon of turbine operating under low pulse frequency conditions, but no literatures derailed studied the effects of the negative efficiency on the performance of turbines. Besides, as suggested by [46, 68], the cycle-averaged turbine map could not reflect the true turbine unsteady performance, even though the data was gathered by means of either unsteady experiment or unsteady simulation. Another drawback of using cycle-averaged approaches is that the valuable turbine performance data at off-design regions will be eliminated due to

average. Additionally, Serrano et al. [99] suggested the unsteady mechanical efficiency can be fluctuating and far from the corresponding steady-state condition, which increases the uncertainties of using the steady-state turbine map in modelling. Therefore, it raises the need of mapping the true unsteady performance in a way that is useful to engine modellers.

Although many researchers have investigated the detailed flow field and the dynamic response of a mixed-flow turbine under pulsating flow conditions, there is no study sought to optimize the design whilst explicitly taking into account the full range conditions during an exhaust pulse. That is, to seek to find the best combination of blade design parameters that results in the highest efficiency over a complete engine cycle. This is a very different proposition to a single-point optimization since the dynamic modelling approach requires significant computational resources and may explain why there is no work on this topic in the public domain. It is worth noting that based on the single-point optimization, the aforementioned 3D optimization studies [119, 121, 124] showed good improvement of turbine efficiencies compared with the baseline geometry operating under the same condition. Where the working boundaries are steady-state such as in an ORC system, single-point optimization is therefore highly recommended. However, as pointed out earlier, a turbocharger turbine operates over a broad range of flow conditions resulting from the rapid opening and closing of the engine exhaust valves. Thus, improving the turbine performance at a single operating point may not result in the best overall energy output throughout a pulse cycle, even if this operating condition is an instance in the pulse.

As recommended in the study of [44, 53, 112], when a turbine is exposed to unsteady flow conditions, the quasi-steady assumption is valid only on the cycle-averaged basis and the unsteady effects cannot be neglected if the transient performance is to be taking into consideration. In general, the turbine unsteadiness is greater when the gradient of inlet pressure is significant. In a real engine environment, there will be a large pressure rise as the opening of exhaust valves. During that period the turbine will violate the quasi-steady

assumption. This phenomenon cannot be reflected in any steady-state simulations. Therefore, unsteady (transient) simulation method has to be used in order to reflect the real turbine performance under pulsating flow conditions. Thus, the unsteady optimized blade is more likely matching better to an engine.

Finally, the computational tools in engineering have become ever more complex and computationally expensive. More input design variables are often considered in the geometric representation. Therefore, a large number of computing iterations are required to achieve the final solution. The relation between the physical solution and design parameters is normally non-linear and non-monotonic, implying that the design space may contain many local minimal points. The turbine optimization problem is a typical example that involves these difficulties. This study presents a novel hybrid surrogate model based on the Kriging method and global search method. The surrogate model will be compared with the conventional genetic algorithm in order to analyse its effectiveness in the application of turbine optimization.

CHAPTER 3

EXPERIMENT METHODOLOGY

3.1 Overview of Experimental Facilities

The experimental data in this thesis was gathered in the turbocharger test facility at the University of Bath. This is a hot flow test facility which has been designed with the capability of testing the turbocharger performance under both steady-state and pulsating flow conditions. Fig. 3.1 and Fig. 3.2 show the schematic diagrams of the gas-stand steady-state and pulsating flow test set-up. The instruments shown in the schematic diagrams are specified in Table. 3.1. The pulsating flow test set-up utilized many of the same experimental equipments as the steady-state test set-up, but the former has a pulsation generator placed upstream of the turbine. To capture the instantaneous performance data, fast response pressure and temperature transducers were used during the unsteady test. The pulsation generator utilizes a cylinder head in order to replicate the most realistic pulse-train behaviour such as variable opening actuation. The design parameters of the pulsation generator which will be detailed discussed in Section. 3.5.5.

The experimental facility is particularly suitable for turbocharger testing owing to the availability of two independent air feeding lines. Air supplied to the test cell is compressed externally via two Ingersoll Rand compressors, which is capable of providing a maximum pressure or 8 bar and a maximum mass flow of 0.7 kg/s. In order to have the air arriving at the test facility at ambient temperature and dry conditions, the moisture or humidity is removed via Hankison refrigerated compressed air drier. An air tank is used to store the compressed

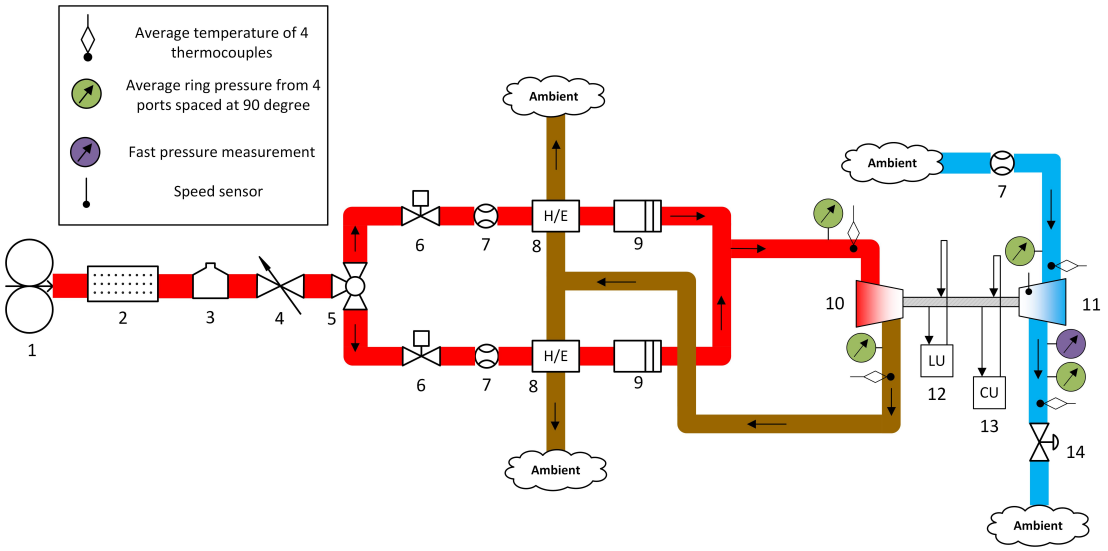

Figure. 3.1 Test set-up for steady-state gas-stand test (equipments refer to Table. 3.1)

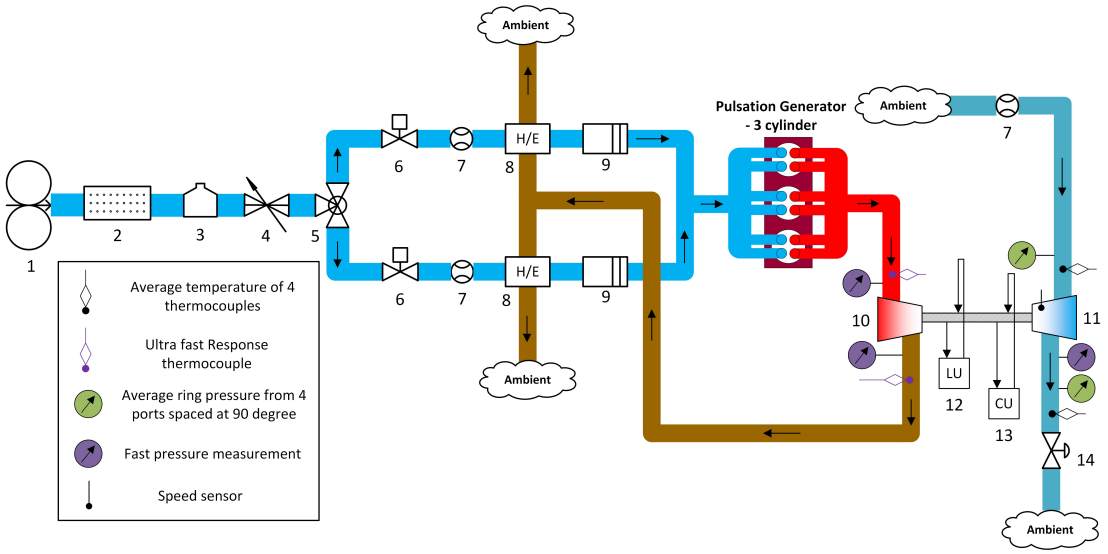

Figure. 3.2 Test set-up for unsteady flow test (equipments refer to Table. 3.1)

air up to a maximum pressure of 8 bar, ensuring that the flow supplied to the test cell is steady and less fluctuating. The control of the mass flow rate of the supply air is achieved via a main ball valve and a pair of motorised gate valves installed on parallel pipework legs. Such a parallel arrangement of the pipework extends the cell's availability for testing twin entry or double entry turbines. Each of the parallel supply air branches includes two sizes of differential pressure V-cone mass flow meters to maintain measurement precision. After the

Table 3.1 List of experimental equipments

Number	Turbocharger gas-stand equipment
1	Two *Ingersoll Rand*® compressors
1	*Hankison*® refrigerated compressed air drier
3	Air tank (about 8 bar)
4	Manual ball type (*Kinetrol*®) shut off valve
5	*Fiesto*® 3-way ball type valve
6	Motorized gate valve with *Schubert & Salzer*® actuator
7	*McCrometer*® V-cone mass flow meter with *Siemens*® DSIII differential pressure transmitter
8	*Bowman*® gas-to-gas heat exchanger
9	*Axes Design*® variable power electric heater
10	Mixed-flow turbocharger turbine
11	Turbocharger compressor
12	Turbocharger lubrication unit
13	Turbocharger bearing housing cooling unit
14	Motorized backpressure valve

mass flow measurement point, the supply air will pass through the recuperator/heat exchanger such that it is heated up by the returning exhaust flow, thereby reducing the power demand of the electric heater. Two electrical heaters which are rated at 44 kW individually and are able to heat the air to 750 °C at prior to the turbine inlet. Before the actual mapping process, a warm-up stage takes place, where the power of the electric heater is continuously regulated by a PID controller until the desired turbine inlet temperature has been reached.

The turbocharger bearing housing is fed by the engine oil conditioned by Regloplas 300s unit, which is equipped with variable-speed magnetic drive pump, allowing for control of the oil flow rate and oil pressure. The turbocharger is equipped with liquid-cooled bearing housing, and cooling water is provided by the cooling module, which is fitted with temperature control unit. Oil and coolant temperatures are fixed at 90 °C throughout the study.

In the compressor side of the test facility, air is drawn from ambient upstream of the compressor and discharged against a back-pressure valve after the compression process has taken place. The back-pressure valve is a motorized gate valve located downstream from

the compressor, which is used to control the mass flow rate of the compressor within its operational range (from choke to surge).

The test facility consists of both slow and fast measurement unit. The Sierra data acquisition system is used to perform the slow measurement at 40 Hz, and the Dewetron Sirius is utilized for the fast measurements up to 100 kHz. To synchronize the data that is recorded between the two platforms at the same time frame, the control terminal sends a trigger signal to both units simultaneously.

3.2 Turbine Geometrical Parameters

As shown in Fig. 3.3, the turbine to be studied was a vaneless mixed-flow turbine, designed for the application of a three-cylinder one-litre spark-ignition engine. The schematic view of the turbine rotor is shown in Fig. 3.4 (a) and its associated geometry parameters have been listed in Table. 3.2, demonstrating that the size of the rotor is small, with a tip diameter of 29.1 mm but with a fairly aggressive cone angle of 60°. On this latter point, according to the accepted empirical evidence that the optimal incidence angle, normally ranges between -20° and -30°[11], the baseline turbine has already taken advantage of the pulsating flow effects, as indicated by the non-zero blade angle at the leading edge resulting from its mixed-flow design. This turbine was also chosen as the baseline for blade optimizations. More detailed blade information will be discussed in Section. 5.2.1;

3.3 Definition of Turbine Performance Parameters

When studying the performance of turbomachinery, it is useful to compare their performances regardless of the machine size and flow conditions. To achieve this, physical turbine performance parameters, such as mass flow rate, turbine speed, pressure and temperature, are necessarily be reduced to either non-dimensional or semi-dimensional parameters. According to [10], the mass flow and turbine speed can be reduced to pseudo non-dimensional

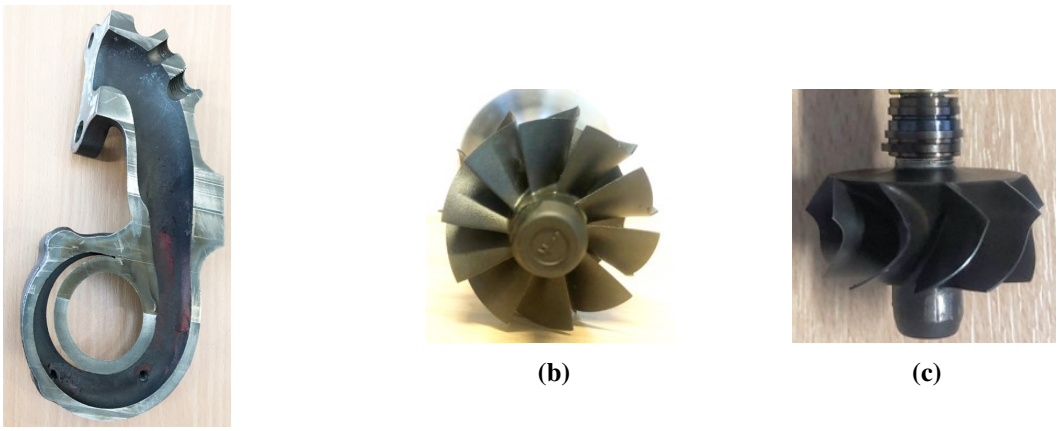

(a) (b) (c)

Figure. 3.3 Studied mixed flow turbine (a) vaneless volute (b) rotor front view (c) rotor top view

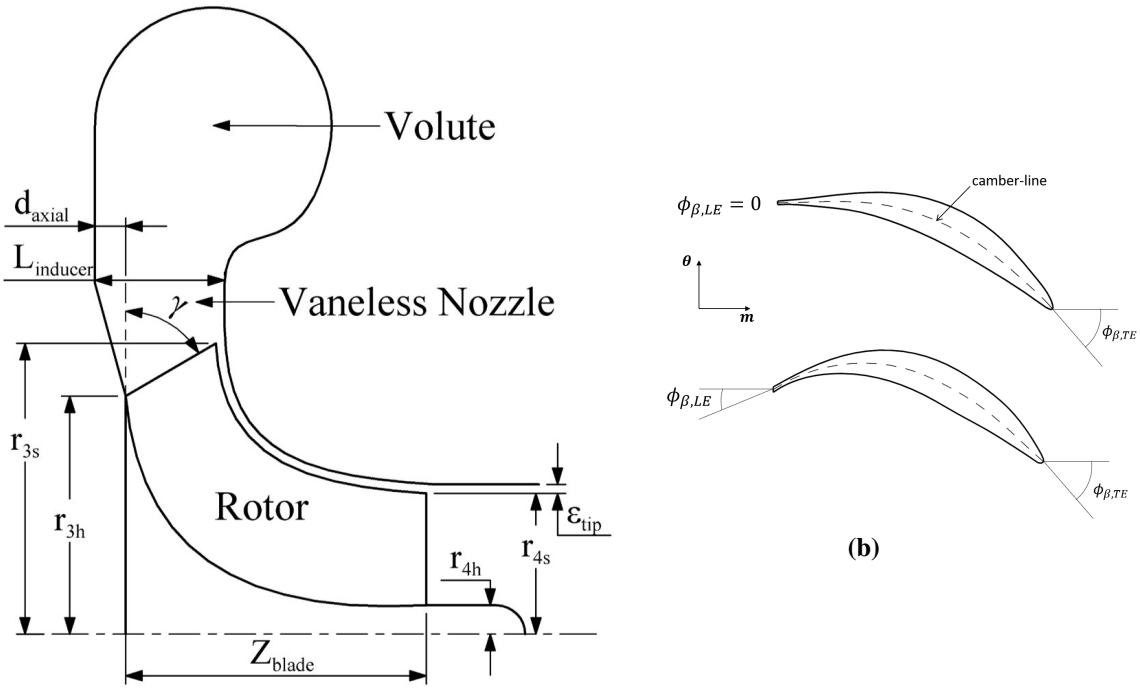

(a) (b)

Figure. 3.4 (a) Schematic of the turbine meridional view labelled with geometric parameters, (b) blade camber angle at the leading edge

parameters, namely the mass flow parameter (MFP) and speed parameter (SP), by providing the incoming stagnation flow conditions such as pressure and temperature.

Table 3.2 Details of the baseline mixed flow turbine rotor geometry

Parameters	**Unit**	**Value**
N_{blade}	-	10
Z_{blade}	mm	14.82
$r_{3.5s}$	mm	17.77
$r_{3.5h}$	mm	15.44
r_{4s}	mm	14.55
r_{4h}	mm	5.63
ε_{tip}	mm	0.2
$\phi_{\beta,3h}$	°	-30.45*
$\phi_{\beta,3m}$	°	-24.05
$\phi_{\beta,3s}$	°	-15.70
γ	°	60
$L_{inducer}$	mm	4.15
d_{axial}	mm	0

*: the negative blade camber angle indicates the clockwise rotation of the impeller

$$MFP = \frac{\dot{m}\sqrt{T_{01}}}{P_{01}} \tag{3.1}$$

$$SP = \frac{N}{\sqrt{T_{01}}} \tag{3.2}$$

The mass flow parameter is commonly plotted against turbine pressure ratio (PR) at different speed parameters. This can describe the flow (swallowing) capacity characteristic of a turbine. The pressure ratio is defined as a ratio between the total pressure at the inlet to the volute and the exit static pressure, given in Eq. 3.3.

$$PR = \frac{P_{01}}{P_4} \tag{3.3}$$

The pressure and temperature sensors normally the parameters at their static conditions. The conversions between the static condition and stagnation (total) condition are calculated as by Eq. 3.4 and Eq. 3.5, where γ is defined as a function of the universal gas constant (R), M is the Mach number of the fluid, and the specific heat capacity at constant pressure (c_p). This study calculates the c_p of the air as a function of static temperature according to Zucrow and Hoffman [125], as given in Eq. 3.7.

$$T_0 = T\left(1 + \frac{\gamma - 1}{2} M^2\right) \tag{3.4}$$

$$P_0 = P\left(\frac{T_0}{T}\right)^{\gamma/\gamma - 1} \tag{3.5}$$

$$\gamma = \frac{c_p}{c_p - R} \tag{3.6}$$

$$c_p = \begin{bmatrix} T & T^2 & T^3 & T^4 & T^5 \end{bmatrix} \times \begin{bmatrix} -0.68388122 \\ 1.7875137 \cdot 10^{-3} \\ -1.1323656 \cdot 10^{-6} \\ -8.2943324 \cdot 10^{-10} \\ 1.1100191 \cdot 10^{-12} \end{bmatrix} + 1083.1165 \tag{3.7}$$

3.3.1 Steady-state Turbine Efficiency

Turbine efficiency is the key parameter that describes the percentage of flow energy, which is available to a turbine, converts to the mechanical energy of the shaft, as defined in Eq. 3.8. It is common to express the efficiency as ratio between the actual and the isentropic enthalpy change across the stage, namely the isentropic efficiency, as per Eq. 3.9. However, the accurate turbine isentropic efficiency cannot be obtained using this method if using the standard way to record turbocharger characteristic maps (SAE J922 and J1826). As discussed by Zimmermann et al. [126], there will be significant heat losses between the turbine outlet and measurement planes, causing the measured T_4 dropping low and increasing the isentropic efficiency to unrealistic values.

An alternative way to calculate the turbine efficiency is based on the energy conservation between the turbine and the compressor. However, there will be some energy losses when the shaft power is transferred from the turbine to the compressor due to the mechanical loss of the shaft. To account for the mechanical losses, the mechanical efficiency is included in Eq. 3.10. In this way, the turbine actual power can be calculated based on the compressor power (Eq. 3.11) and mechanical efficiency. This study treated the mechanical efficiency as unity, such that the turbine map is so-called the lumped turbine map since the mechanical loss is included in the efficiency. The isentropic enthalpy change of turbine can be calculated

by Eq. 3.12, and the lumped turbine efficiency (Eq. 3.13) is derived by combining Eq. 3.11 and Eq. 3.12. Note that the specific heat c_p in Eq. 3.11 and Eq. 3.12 is the mean value across the compressor or the turbine in order to account for temperature variations during the compression or expansion process.

It is common to plot the turbine efficiency against velocity ratio, as defined in Eq. 3.14, which is a dimensionless parameter defined as the ratio between the blade tip speed U_{tip} and the isentropic velocity C_{isen}, which refers to the velocity that the working fluid would be achieved during the isentropic process.

$$\eta_t = \frac{\dot{W}_{t,act}}{\dot{W}_{t,isen}} \tag{3.8}$$

$$\eta_t = \frac{h_{01} - h_{04}}{h_{01} - h_{4,isen}} = \frac{T_{01} - T_{04}}{T_{01} - T_{4,isen}} \tag{3.9}$$

$$\dot{W}_{c,act} = \dot{W}_{t,act}\,\eta_{mech} \tag{3.10}$$

$$\dot{W}_{c,act} = \dot{m} c_p T_{c,0,in} \frac{1}{\eta_c} \left[\left(\frac{P_{c,0,out}}{P_{c,0,in}} \right)^{\gamma - 1/\gamma} - 1 \right] \tag{3.11}$$

$$\dot{W}_{t,isen} = \dot{m} c_p T_{01} \left[1 - \left(\frac{P_4}{P_{01}} \right)^{\gamma - 1/\gamma} \right] \tag{3.12}$$

$$\eta_{t,lumped} = \frac{\dot{W}_{c,act}}{\dot{W}_{t,isen}} \tag{3.13}$$

$$VR = \frac{U_{tip}}{C_{isen}} = \frac{\pi N D_{tip}/60}{\sqrt{2 c_p T_{01} [1 - (P_4/P_{01})^{\gamma - 1/\gamma}]}} \tag{3.14}$$

3.3.2 Unsteady Turbine Efficiency

The unsteady turbine efficiency, as defined in Eq. 3.15, refers to the time-resolved efficiency during the unsteady operation of the turbocharger turbine, requiring both the instantaneous isentropic power (Eq. 3.16) and instantaneous actual power (Eq. 3.17) for the calculations.

$$\eta_t(t) = \frac{\dot{W}_t(t)_{actual}}{\dot{W}_t(t)_{isen}} \tag{3.15}$$

$$\dot{W}_t(t)_{isen} = \dot{m}_1(t) c_p T_{01}(t) \left[1 - \left(\frac{P_4(t)}{P_{01}(t)} \right)^{\gamma - 1/\gamma} \right] \tag{3.16}$$

$$\dot{W}_t(t)_{actual} = \frac{\dot{W}_c}{\eta(t)_{mech}} + \left(\frac{2\pi}{60}\right)^2 I_{tc} N_{tc} \frac{dN_{tc}}{dt} \tag{3.17}$$

where:

$$\eta(t)_{mech} = \frac{\dot{W}_c(t)}{\dot{W}_t(t)}$$

The instantaneous turbine actual power contains both the steady and the fluctuating terms. The steady term refers to the average shaft power, which is obtained by compressor power, whilst the fluctuating term is attributed to the fluctuation of turbine speeds. By adding these two together, an instantaneous turbine power can be calculated by Eq. 3.17, where I_{tc} is the momentum of inertia of the turbocharger. This technique was also adopted by other researchers [22, 39, 127, 128], assuming the mean compressor power does not vary through the pulse cycle. This is a feasible assumption since the maximum fluctuations of shaft speed is less than 1.1% of the mean shaft speed from the experimental study of Capobianco and Marelli [30], who investigated the effects of pulse frequencies (40 Hz - 100 Hz) on the turbine unsteady performance. Therefore, it is feasible to assume the compressor that is operating in a steady-state manner.

Similar to most gas stands, as compressor was used as the loading device of the turbine, this set-up has particular advantages in creating turbine maps that include mechanical friction. That is, the turbine actual power was calculated using the compressor power plus the dynamic power deduced from the torque of the shaft, as shown in Eq. 3.17. Note that this approach includes the mechanical efficiency as shown in Eq. 3.17, as it is a standard practice in gas-stand mapping. This approach is very helpful in 1D simulation codes since no explicit map of mechanical loss is needed since it is already contained in the turbine efficiency map.

What differs from the standard approach is that it includes the unsteady mechanical loss and therefore take into account changes in thrust force over a pulse, where the steady-state mapping approach cannot. As suggested by Serrano et al. [97] and González et al. [129], instantaneous turbocharger mechanical loss is critical in engine simulation work. When the turbine is subjected to high amplitude pulsating flows, the mechanical loss is far from constant even at steady engine simulation. Therefore, the proposed mapping method reduces the mechanical loss correction process, and offers an elevated chance to produce a turbine map that matching better to an ICE.

The fluctuating term of Eq. 3.17 is derived by the multiplication of shaft speed and its differentiation. This means that it requires a sufficiently high accuracy when measuring the shaft speed, and any noise from the measured speed signal will amplify the errors of power calculation. It is common to use low pass filters to minimize the errors from the measurement of shaft speed. However, it is easily for the filter to remove some necessary parts of the signal, such as speed fluctuations due to secondary pulses, since signal filtering is a purely mathematical process without involving any flow physics. To preserve useful information of the data as well as reducing the noises of signal, the data was first smoothed by ensemble averaging and followed by Savitzky-Golay (S-G) finite impulse response (FIR) filtering [130]. The major advantage of S-G FIR filter is that it has zero phase shift so that features of the signal are not shifted [131]. As shown in Fig. 3.5, the noise has been much reduced after ensemble averaging for 40 continuous pulses, and the S-G filter then produces a cleaner signal afterwards.

In order to calculate the turbine instantaneous isentropic power, it is convenient to measure turbine inlet quantities (mass flow, pressure, and temperature) prior to the volute entrance. However, the turbine actual power is calculated by the shaft torque derived by the shaft speed. Therefore, the measured inlet flow quantities are not the actual flow quantities that really rotate the impeller, due to the spatial difference between the measurement section and

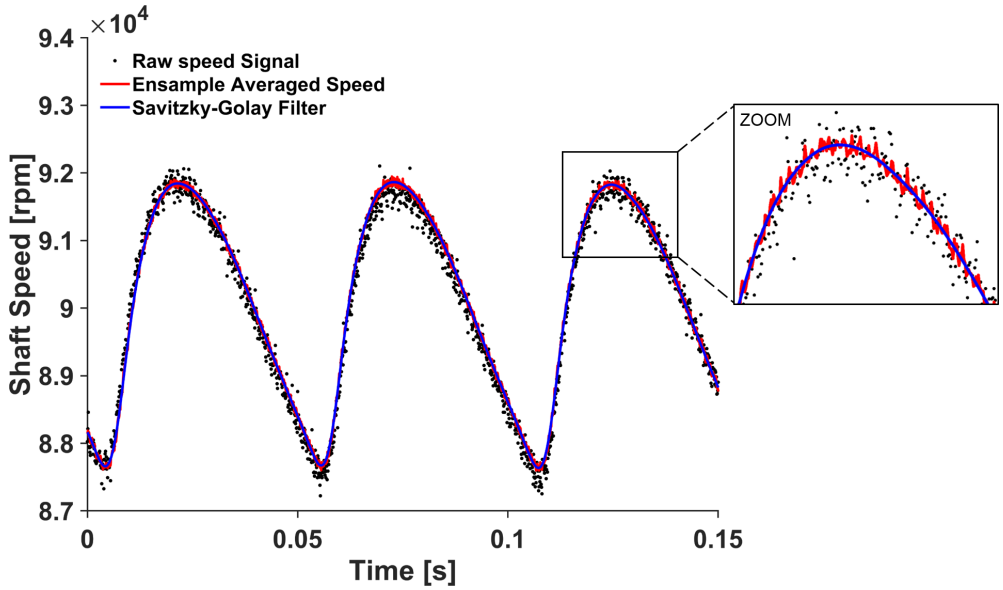

Figure. 3.5 Power phasing at different sections

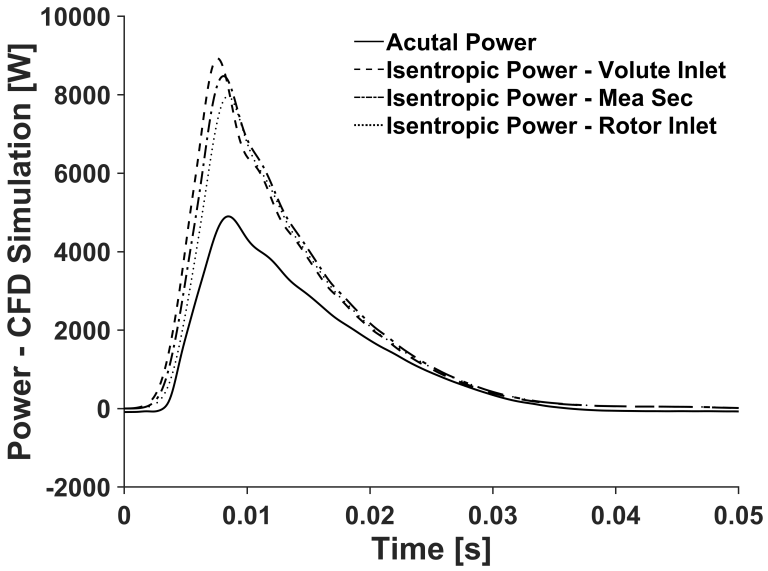

Figure. 3.6 Power phasing at different sections

the turbine blade. As a consequence, it is required to assess the finite amount of time to align these components in a common time frame. As mentioned in Section. 2.1, researchers may adopt different phase-shift techniques, such as bulk flow velocity criteria [36, 37], sonic velocity criteria and the sum of sonic velocity and bulk flow velocity [31, 38]. To figure out which method is more applicable to the current situation, the actual power and

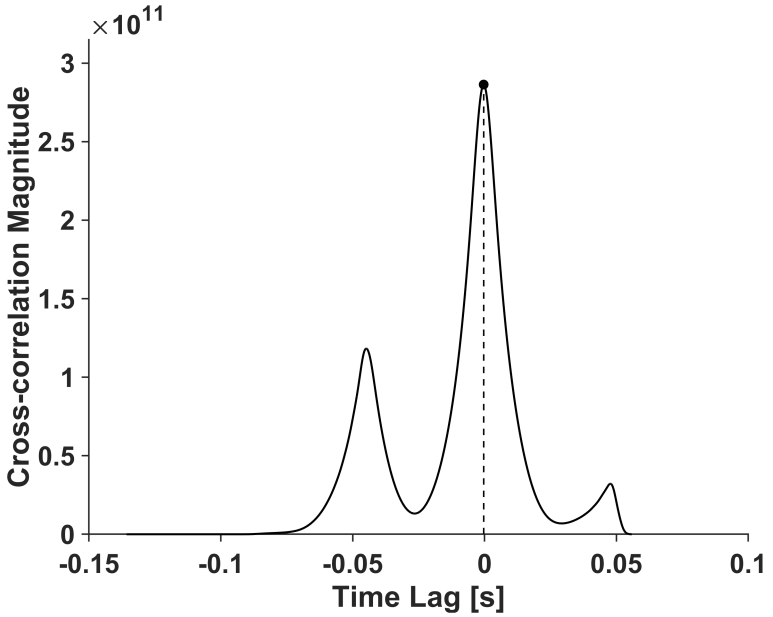

Figure. 3.7 Cross-correlation method to find the time for phase-shifting

isentropic power at different sections, namely the volute inlet section, the measurement section (where pressure sensor is located), and the rotor inlet section, have been obtained by CFD simulations, as shown in Fig. 3.6. Since the sensors were set in a position close to the tongue (as discussed in Section. 3.5), the isentropic power obtained at the measurement section is quite close to that obtained at the rotor inlet section with respect to both magnitude and time frame. Fig. 3.6 also shows that the peak isentropic power has been dropped when the pulse travels from the volute inlet to the measurement section, indicating the amount of energy loss due to convective heat transfer loss and pressure friction loss of the volute. Cross-correlation method [132] was used in order to calculate the finite time difference of the isentropic power between measurement section and rotor inlet section. As shown in Fig. 3.7, the time-lag is found to be 0.26 ms. The flow path length between measurement section and equivalent rotor inlet section (here use 180° volute circumstance) is approximately 95 mm. As a consequence, the targeting velocity for phase-shifting is approximately 365.4 m/s, whilst the sonic velocity is 401.46 m/s in this case. Although there has a difference between

the targeting velocity and the sonic velocity, the sonic velocity is the closest to the targeting velocity, and was therefore used as the phase-shift criteria in the efficiency computations.

3.4 Steady-state Turbomachinery Performance Measurement

Fig. 3.8 shows the Steady-state gas stand experimental facilities, where the sensor positioning used during the test can be referred to Fig. 3.1. Standard measuring sections, as specified in the SAE J1723 and ASME PTC 10 gas stand code, were applied at the compressor and turbine inlet and outlet. The turbine integrated waste-gate valve was kept completely shut throughout the tests. In order to minimize any convective heat transfer between the turbocharger hardware and the temperature measurement section, the turbine and compressor inlet and outlet pipe works are insulated using thermal insulation material.

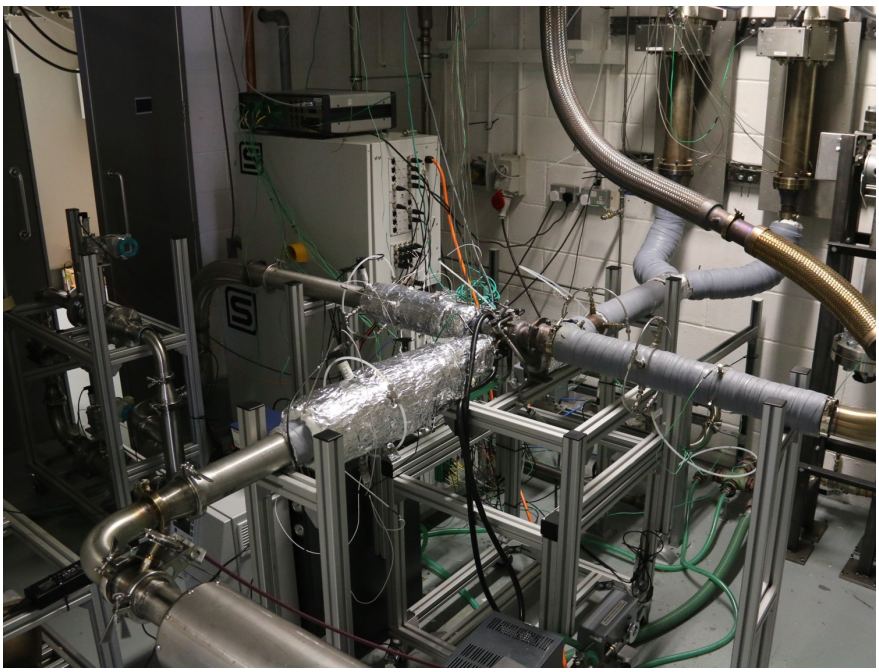

Figure. 3.8 Steady-state gas stand experimental facilities

3.4.1 Steady Pressure Measurement

There are four static pressure sensors that are used to measure the pneumatically averaged pressure at the compressor and turbine inlet and out. The location, type, make, accuracy, and measurement frequency of the pressure transducer are listed in Table. 3.3. Averaged pressure is achieved mechanically by installing a ring connected with four tappings, as shown in Fig. 3.9. Each tapping is perpendicular to the pipe wall whereas the angle between each tapping is fixed at 90°.

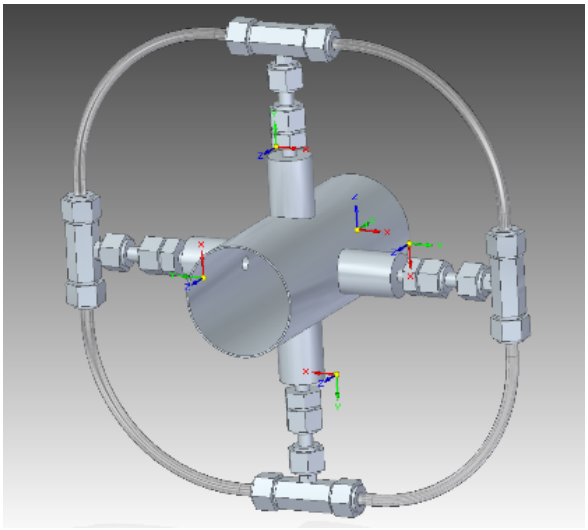

Figure. 3.9 A stainless steel ring for averaging the static pressure measurements [133]

Table 3.3 Pressure transducer - location, type, make, accuracy, and measurement frequency

Sensor location	Quantity	Sensor model	Manufacturer	Accuracy	Measurement frequency
Compressor inlet	Static pressure	PXM419-3.5BAV	Omega	±0.08%	40 Hz
Compressor outlet	Static pressure	PXM419-002BGV	Omega	±0.08%	40 Hz
Turbine inlet	Static pressure	PXM419-007BGV	Omega	±0.08%	40 Hz
Turbine outlet	Static pressure	PXM419-007BGV	Omega	±0.08%	40 Hz

3.4.2 Steady Temperature Measurement

The measurement of the static temperature is based on an arithmetical average of four static temperatures measured by temperature sensors located downstream the pressure transducers. As indicated in the schematic view of Fig. 3.10, the temperature sensors were inserted perpendicularly to the pipe wall with an angle of 90° between each other. At 0 and 180 degrees of the tube section, the sensor inserted at 1/3 the diameter of the tube. The thermocouple at 90 degrees inserted 1/2 the diameter of the tube, and the thermocouple at 270 degrees inserted 1/4 the diameter of the tube. Table. 3.4 listed the specifications of temperature sensors.

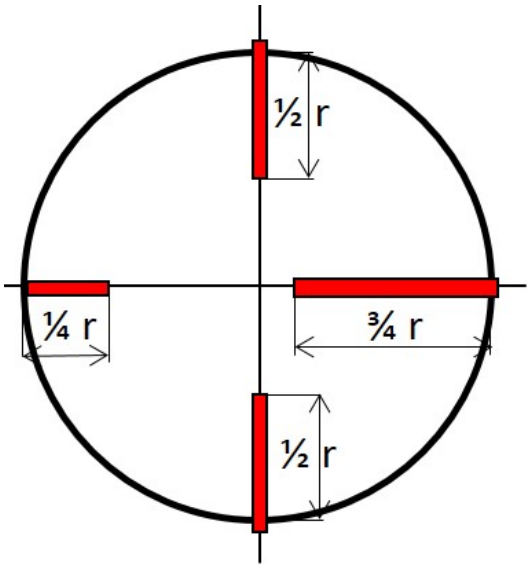

Figure. 3.10 Thermocould location for the averaged temperature measurement

Table 3.4 Temperature sensor - location, type, make, accuracy, and measurement frequency

Sensor location	Quantity	Sensor model	Manufacturer	Accuracy	Measurement frequency
Compressor inlet	Static temperature	Pt100	TC Direct	$\pm(0.03+0.0005\cdot t)$	40 Hz
Compressor outlet	Static temperature	Pt100	TC Direct	$\pm(0.03+0.0005\cdot t)$	40 Hz
Turbine inlet	Static temperature	1.5mm K-type	TC Direct	$\pm 2.5°C$ *or* $\pm$ 0.75%	40 Hz
Turbine outlet	Static temperature	1.5mm K-type	TC Direct	$\pm 2.5°C$ *or* $\pm$ 0.75%	40 Hz

3.4.3 Steady Mass Flow Measurement

The volume flow rate, measured on both compressor and turbine side, was captured by differential pressure type *McCrometer*® V-cone meters. The principal theory among these is Bernoulli's theorem for the conservation of energy in a closed pipe [134]. This states that for a constant flow, the pressure in a pipe is inversely proportional to the square of the velocity in the pipe. The differential pressure created by the v-cone prime element (Fig. 3.11) is measured by a previously calibrated Siemens Sitrans DS III transmitter. The flow meter instrumentation is completed with a thermocouple install prior to V-cone entry and a pressure transducer located at the high-pressure side of the V-cone. The temperature and pressure measurements allow for the calculation of flow density so as to calculate the mass flow rate. Specifications of sensors used in the mass flow measurement instrumentation is listed in Table. 3.5.

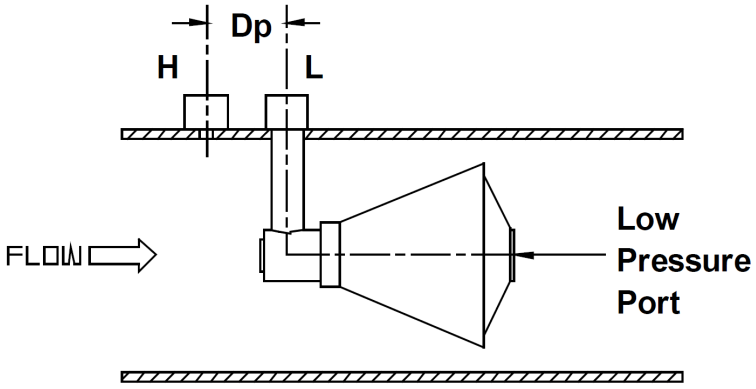

Figure. 3.11 V-cone flow meter geometry [134]

Table 3.5 Sensors used for mass flow measurements - location, type, make, accuracy, and measurement frequency

Sensor location	Quantity	Sensor model	Manufacturer	Accuracy	Measurement frequency
V-cone pipework	Differential pressure	Sitrans P DSIII transmitter	Siemens	0.51%	40 Hz
V-cone pipework	Static pressure	PX312	Omega	0.25%	40 Hz
V-cone pipework	Static temperature	Pt100	TC Direct	$\pm(0.03 + 0.0005 \cdot t)$	40 Hz

3.4.4 Shaft Speed Measurement

As shown in Fig. 3.12, an eddy current – micro epsilon DZ 135 speed sensor, with a full-scale output (FSO) resolution of $\pm 0.22\%$, was mounted close to the compressor wheel in order to measure the turbocharger speed. A coil is placed inside the tip of the speed sensor, and is supplied by a high frequency alternating current, thereby generating an electromagnetic field. Whenever the rotor tip passing by the sensor tip, eddy currents will be energized, and be detected by the sensor. Considering the number of blades, the instantaneous turbocharger speed can be estimated by measuring the time interval between two subsequent eddy pulses.

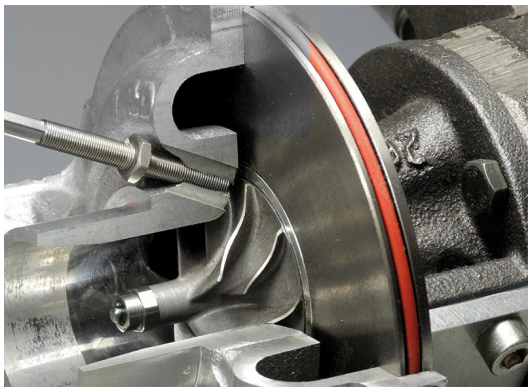

Figure. 3.12 sectional view of speed sensor mounting

3.5 Unsteady Turbomachinery Performance Measurement

Fig. 3.13 shows the unsteady experimental facility. A pulsation generator was used to produce the engine-like exhaust pulses. The upstream of the pulsation generator is similar to the steady-state experimental facilities, and the sensor positioning used during the unsteady test can be referred to Fig. 3.2.

From the literature study, one can conclude that the major contribution of turbine unsteadiness is resulted from the "filling and emptying" effects of the volute, whereas rotor itself is deemed to operate in a broadly quasi-steady manner [33, 44, 53, 87, 135, 136]. This section will present a novel way of mapping the turbine performance exposed to pulsating flows. To

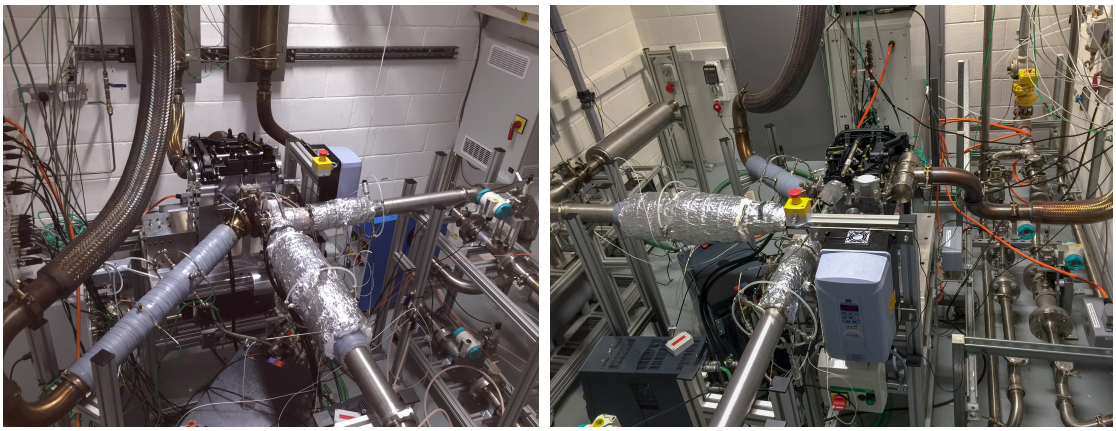

(a) (b)

Figure. 3.13 Unsteady experimental facility

prevent the filling and emptying effects, this study put the pressure and temperature sensors close to the volute tongue. Therefore, this method can effectively reduce the unsteadiness captured during the test due to a smaller character length between the measurement section to the nominal rotor inlet section according to the theoretical analysis of [44, 53], and Eq. 2.6 and Eq. 2.7. In this way, it can reduce the hysteresis loop noticed from the turbine characteristic maps, as observed in Fig. 2.1, thereby creating quasi-steady rotor performance maps based on unsteady test, named as *equivalent unsteady maps* in this thesis. The major advantage of equivalent unsteady maps is that it can create a very broad range of data that is normally achievable in steady-state using a turbine dynamometer. Also, it reduces errors involved in the extrapolation process since the flow physics can be captured in the off-design performance regions. Besides, the unsteady mechanical efficiency will be lumped in the equivalent unsteady map, which is beneficial in the 1D engine modelling process if use the map-based turbine model as a sub-model as discussed in Section. 2.2.2.

However, since the sensor was set after the volute entry, the energy losses between the volute inlet and the measurement section cannot be captured using this method. Nevertheless, this problem can be addressed by creating a one-dimensional pipe model to correct the losses that would be encountered across the volute. To reproduce the mass accumulation effect

that would happen in a turbine under pulsating flow conditions, the one-dimensional pipe should have the same character length and as the volute from its entry to the measurement section. The energy loss within the volute can be estimated by assigning a proper heat transfer coefficient and friction coefficient [26, 27, 67, 83].

3.5.1 Instantaneous Pressure Measurement

Water-cooled Piezo-Resistive Kistler sensor 4049B10DS1 and 4049A5S, with the FSO resolution of $\pm 0.08\%$, were used to measure the turbine instantaneous inlet and outlet static pressure respectively. Note that the location of turbine outlet pressure sensor is opposite to the thermocouple in the middle of the cone connected with the turbine outlet. In order to reduce the filling and emptying effects due to the volume of the volute, the turbine inlet pressure sensor was set to close to the tongue, as shown in Fig. 3.14.

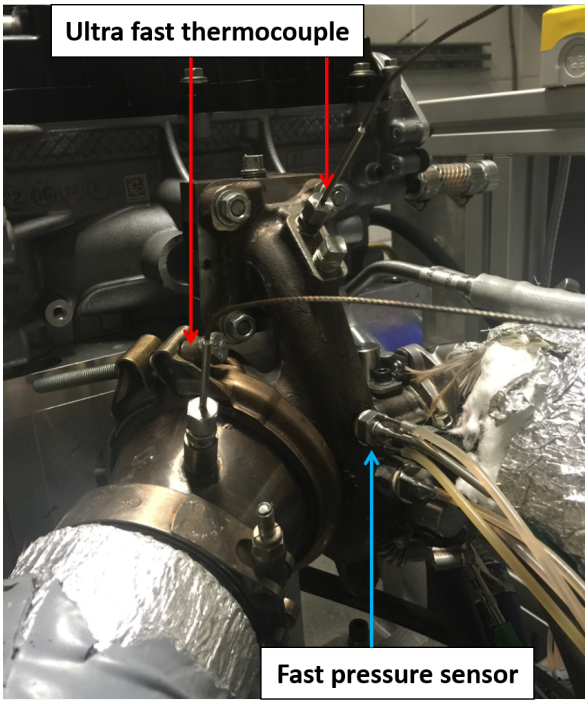

Figure. 3.14 Locations of fast-response sensors

3.5.2 Instantaneous Temperature Measurement

The use of very fine-wire thermocouples permitted the study of the dynamic temperature change at the turbine inlet resulting from the pulses induced by the facility. These thermocouples are bespoke units made for this specific measurement as shown in Fig. 3.15. Stainless steel (SUS) pipe with ceramic adhesive fixes the thermocouple in place and supports it physically. This thermocouple is designed with a small contact area of the thin tip (small heat capacity) to minimize the heat loss and response time.

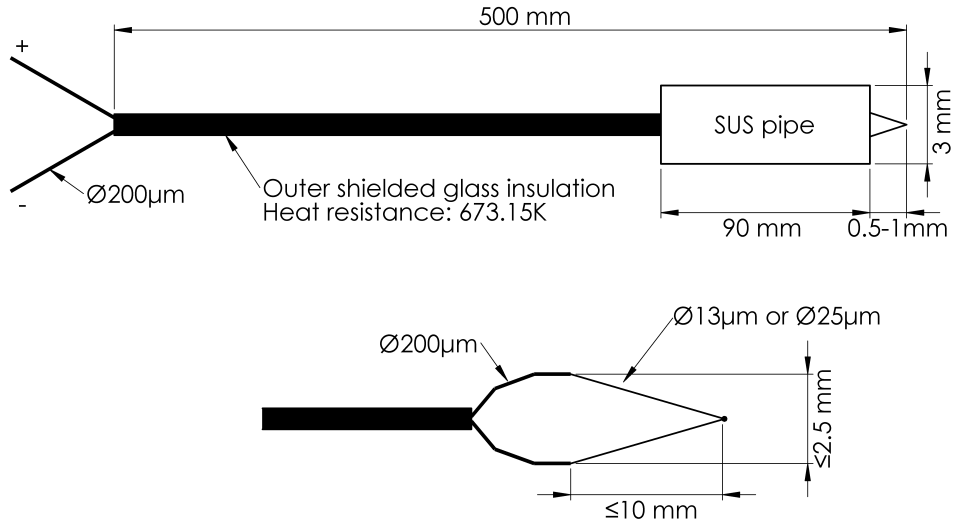

Figure. 3.15 Ultra-fast response thermocouple

Two sizes of thermocouples were tested, namely 13 μm and 25 μm, to check the response time to pulsatile fluctuations at the turbine inlet. A smaller thermocouple can be expected to exhibit a faster response to temperature changes, and this is borne out by the experimental results. The thermocouples were tested under pulsating flow conditions at an average temperature of 400 K. As shown in Fig. 3.16, the smaller 13 μm demonstrated a steeper (quicker) rise and larger amplitude that is indicative of the smaller time constant. To gain some confidence, this measurement was compared to the temperature profile that would result from an isentropic expansion and contraction of air. Eq. 3.18 is provided for completeness that describes this relationship. Eq. 3.18 has been adopted by other researchers in the study

of [30] and was demonstrated to be a valid assumption for a rotating valve pulse facility. In particular, Szymko et al. [31] showed good agreement between the experimental results obtained by a pair of 10 μm hotwires sensors and the assumption of isentropic expansion and compression. In this study, Fig. 3.16 shows that the assumption of isentropic expansion also matches very well to the 13 μm fast-response thermocouple. Therefore, thermocouples of 13 μm were used in this study.

$$T_{s,inst} = T_{mean}\left[\frac{P_{s,inst}}{P_{mean}}\right]^{\frac{(\gamma-1)}{\gamma}} \tag{3.18}$$

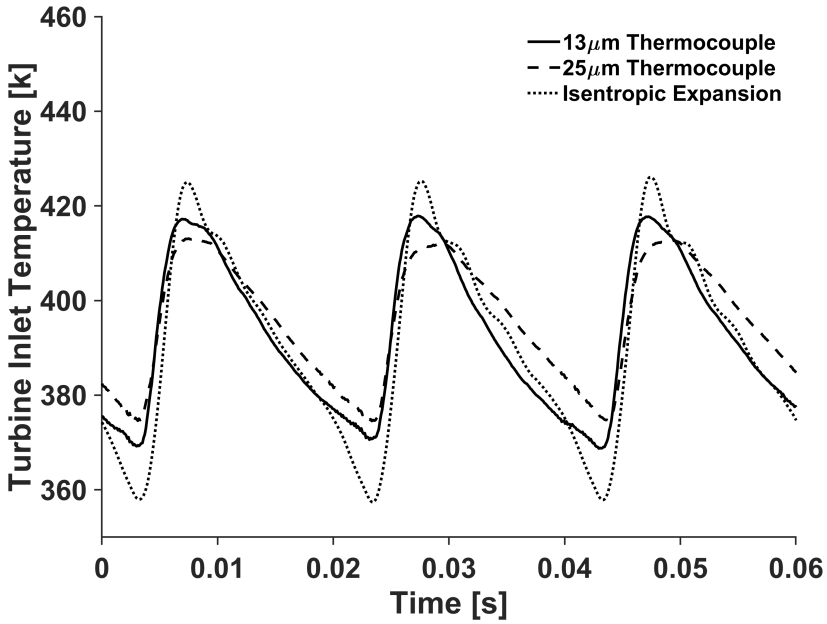

Figure. 3.16 Comparison of the instantaneous temperature at turbine inlet

3.5.3 Instantaneous Mass Flow Prediction

Due to the lack of fast mass flow measurement devices in the pulsating flow study, the instantaneous mass flow was obtained using a quasi-steady approach based on a validated 1D model. The 1D model was developed by using a commercial 1D code, GT-Suite [64], which solves the conservation equations (mass, momentum and energy) using the finite volume

method, where the flow domains are spatially divided into many small domains connected by boundaries. Fifth order explicit Runge-Kutta scheme was used to solve the governing equations due to its effectiveness in capturing wave advections.

The 1D model was developed according to the unsteady test step-up shown in Fig. 3.2, but it is simplified by removing the components 1-9. Instead, a boundary condition was set at the upstream the pulsation generator to provide the desired inlet pressure and temperature as if the airflow has already been compressed by the scroll compressor (component No.1) and heated by the electric heater (component No.9). Special attention was paid to model the 1D turbine volute to capture the "filling and emptying" behaviour. The schematic view of the 1D turbine model is shown in Fig. 3.17, which consists of two parts, with both modelled as tapered pipes. The first pipe is equivalent to the portion from volute inlet to the pressure measurement section (refer to the experimental set-up in Fig. 3.14). The second pipe is equivalent to the portion from the measurement section to the nominal rotor inlet section, here chosen as 180° volute azimuth to be consistent with the literature [26, 83]. The sectional area of nominal rotor inlet is equal to the area of the volute exit. A PID controller was used to achieve a desired turbine speed by adjusting the position of compressor back-pressure valves thereby changing the turbine loading conditions. Therefore, the instantaneous mass flow rate can be derived by the solver.

It is required to validate the heat losses and pressure losses produced by the pipe works and the pulsation generator, in order to achieve a satisfactory prediction of turbine inlet flow conditions i.e. temperature, pressure, and mass flow rate. The validation process of the 1D model consists of two stages. The first stage is to match the cycle-averaged mass flow that is closer to the experimental value. The mass flow was measured by the V-cone meter shown as component No.7 in Fig. 3.2, considering the fact that the mass flow far upstream from the pulse generator will not be varied on the cycle-averaged basis. Fig. 3.18 shows that the difference regarding the averaged mass flow rate between the experiment and 1D model lies

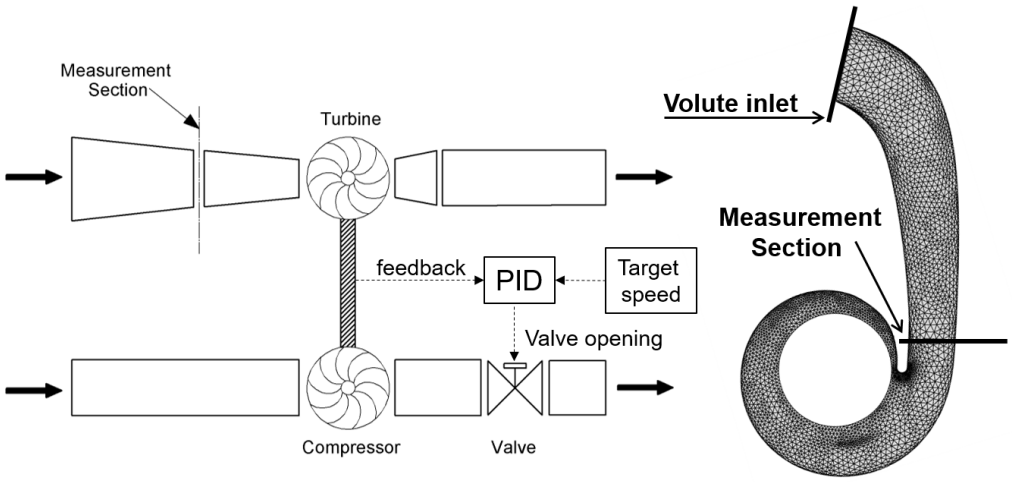

Figure. 3.17 Schematic view of the 1D model for the instantaneous mass flow prediction

within 5% limits. The close match between the two shows that the calibration of the 1D model represents the hardware behaviour well on an average basis.

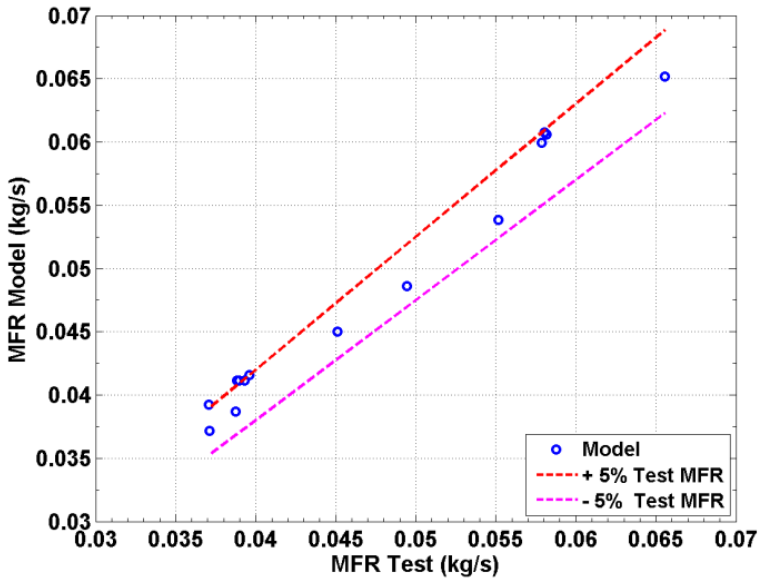

Figure. 3.18 Mass flow comparison between test and 1D model at the pulsation generator inlet with ±5% margin

The second stage is to calibrate the 1D model against the CFD model to obtain a satisfactory prediction of unsteady "filling and emptying" characteristic. The volume, flow area, and character length of the 1D volute were modified during the validation process. The set-up of

CFD model will be discussed in Section. 4.3. Fig. 3.19 shows the mass flow comparisons between the CFD and 1D at the volute inlet section and the measurement section. The 1D model shows good agreement in terms of phase and amplitude, where the mean mass flow difference between CFD and 1D during one pulse at the volute inlet and measurement section are 1.63% and 1.67% respectively. Fig. 3.20 shows the Comparison of swallowing capacities at the measurement section. The size of the hysteresis loop is similar, indicating a similar mass accumulation effect in both models. Besides, during the emptying stage when pressure is decreasing, the turbine swallowing capacity characteristics are especially close to the steady-state results, implying the quasi-steady effects dominate the turbine performance. Although the CFD model shows a lower peak pressure, possibly due to the curvature of the volute that would produce a larger pressure loss, its effect on the mass flow is minimal.

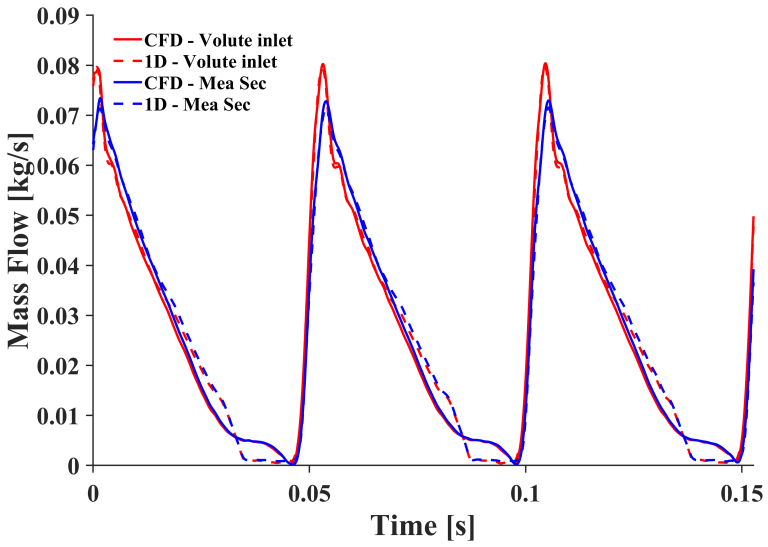

Figure. 3.19 Comparison of the instantaneous mass flow rate between CFD and 1D

3.5.4 Raw Signal Processing

In order to acquire a clean signal for the calculation of turbine performance, the noise of the raw signal was preprocessed by physical low pass filters, designed with specific resistors and capacitors. These filters were connected to the pressure and temperature measurement channels to filter the high-frequency noise. Except for the speed signal, which was filtered

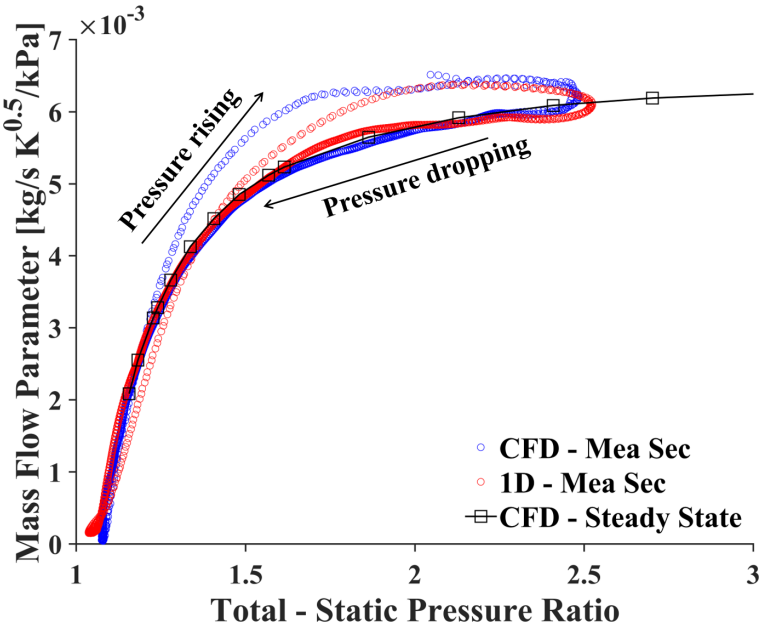

Figure. 3.20 Comparison of swallowing capacities between CFD and 1D at the measurement section

using the ensemble averaging method as discussed in Section. 3.3.2, the rest signals were not processed by any digital filters.

3.5.5 Pulsation Generator

The development and use of a bespoke piece of experimental hardware that aims to generate flows in a gas-stand that have similar characteristics to that would be produced by an internal combustion engine. This is achieved using a specially modified cylinder head placed between the gas-stand hot supply and the turbocharger. Fig. 3.21 (a)-(c) show the key components of the pulsation generator, the isometric and cutaway views of the pulsation generator respectively with the constituting parts. Table. 3.6 shows the components of the pulsation generator, specification, rating and the materials used.

The usage of each component is described as follows,

Deck plate: The top plate of the cylinder enclosure contains the head oil feed/drains and coolant feed. Standard head gaskets are used and an external lubrication system pumps oil to cams and the phasers.

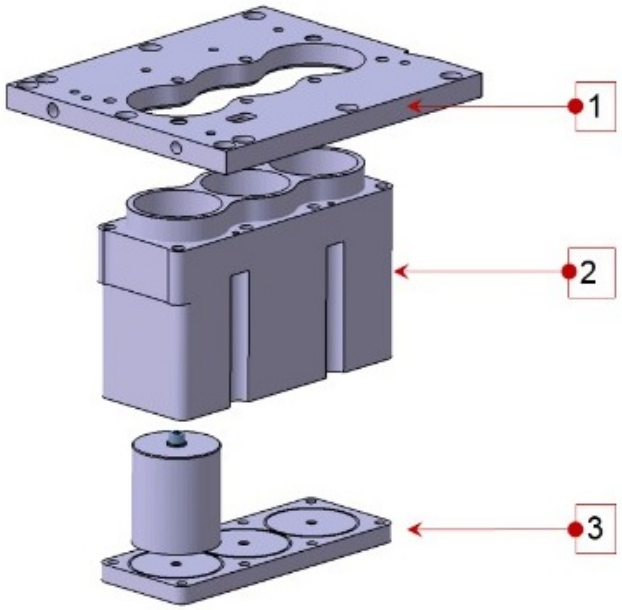

(a) Key components of the pulsation flow generator

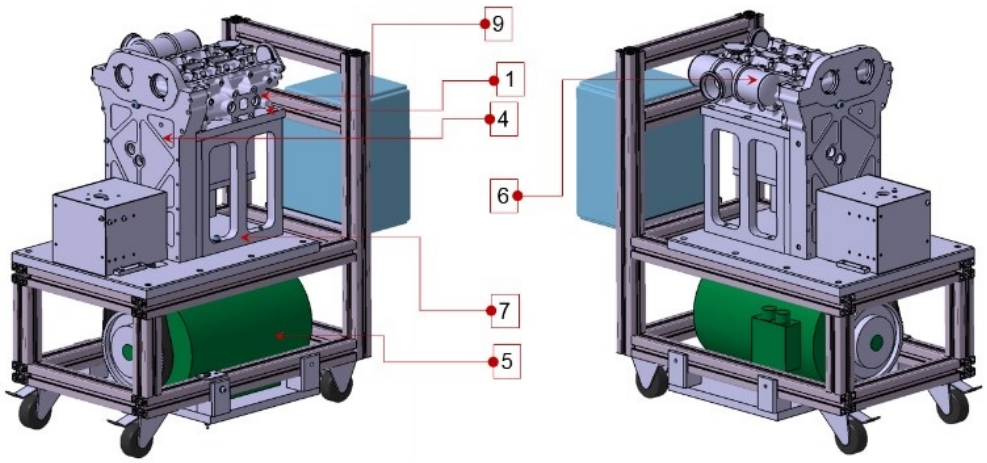

(b) Isometric view of the pulsation flow generator

Cylinder: The stainless steel cylinders maintain the thermal energy. These cylinders can also be insulated for better thermal energy retention.

Cylinder sealing plate: A plate at the bottom part of the cylinder enclosure houses a swappable fixed cylinder that adjusts the cylinder swept volume uses Wills rings to seal the cylinders.

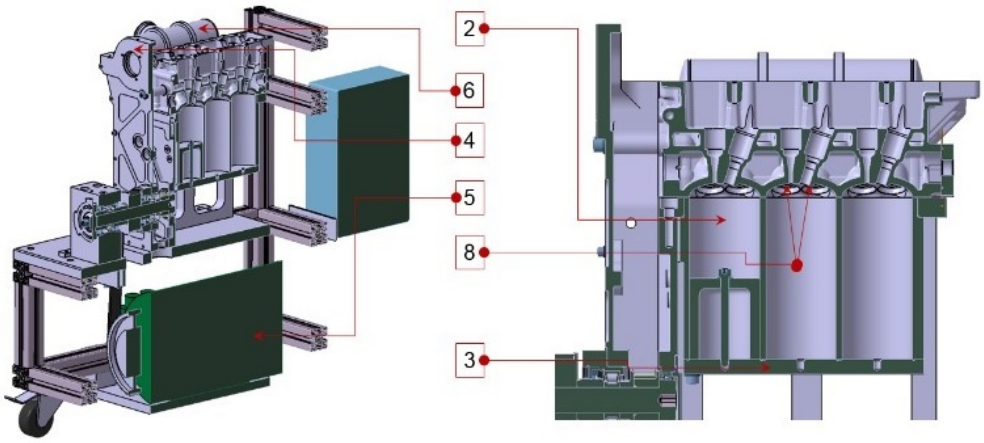

(c) Cutaway view of the pulsation flow generator

Figure. 3.21 Layout of the pulsation flow generator

Table 3.6 List of pulsation generator components

Number	Component	Specification	Material
1	Deck plate	-	Aluminium
1	Cylinder	-	Stainless Steel
3	Cylinder sealing plate	-	Stainless Steel
4	Front cover	-	Aluminium
5	Drive arrangement	22 kW AC motor	-
6	Inlet manifold	750 °C and 8 bar	Stainless Steel
7	Side plate	-	Aluminium
8	Intake and exhaust valves	450 N/m	Engine exhaust grade
9	Integrated Exhaust Manifold	750 °C and 8 bar	Stainless Steel

Front cover: This Aluminium metal cover is an enclosure for the intake and exhaust camshafts, phasers, timing gear, timing belt, O-ring seal and the drive gear (connected to the motor).

Drive arrangement: An under slung drive system powered by a 22 kW AC motor runs a synchronous cam belt drive which opens and closes the intake and exhaust valves linked by a timing belt. The drive ratio of the motor driving the cam to engine is 2.23. The functionality of the original intake and exhaust cam phasers are retained from the production part.

Inlet manifold: A bespoke stainless steel manifold shown in can withstand hot air at 750°C and 8 bar feeds into the inlet valves.

Intake and Exhaust Valves: To withstand high temperature operation, the same exhaust valve grade material was chosen for the intake valves. Also, 450 N/m uprated inlet valve springs are used to ensure the intake valves do not float under the high inlet pressures and temperatures.

Integrated Exhaust Manifold and Turbocharger: The original integrated exhaust manifold style is retained to maintain flow similarity on the exhaust subsystem level and the turbocharger is mounted directly to it as is on the engine.

The pulsation generator was designed based on a cylinder head of three cylinders. Different from an engine, the pulse rig reduces its complexity by removing the crankshaft and pistons, since the air has already been compressed via the external compressor. The engine-like pulses are generated by the opening and closing the intake and exhaust valves, driven by a 22 kW variable speed electric motor. Due to the absence of compression and expansion stroke of the pulse rig, three pulses are generated by only one revolution of the motor shaft. Therefore, the corresponding engine speed can be easily obtained by multiplying the electric motor speed by two. The cam timing of the pulse rig can be adjusted through the cam phasers if needed, providing the flexibility of varying the pulse amplitude. Stainless steel cylinders maintain the thermal energy and enclose the plug which can be positioned to vary the swept volume. To enable the testing at high turbine speed and prevent the air condensing at the turbine outlet, the cooling system was employed on the deck plate to allow the hotter gases to be used. Those design characters enable the pulsation generator to reproduce engine like environment and offer the possibilities to study the effects of pulse frequency, pulse amplitude, and cylinder deactivation effects on turbine performance. In this study, the plugs in the cylinder were set to a position where the total volume of 1.73 litre was used.

A standalone oil pump supplies oil to the turbocharger bearings. A temperature controlled water system (Regloplas 90 smart) was used to regulate the cylinder block temperature levels and to cool the turbocharger. Both Regloplas units were set to a fixed temperature of 80 °C. A gate valve regulates backpressure at the compressor outlet and controls the compressor operating point. This varies the load on the turbine concurrently. Thus, to maintain the same turbocharger speed, the mass flow rate and pressure ratio across the turbine is varied (a different operating point) and also gives a control over the turbocharger speed.

3.6 Deactivation of Cylinder's Air Flow

The bespoke pulsation generator has the availability of blocking flow through one of the cylinders using a blank plate at inlet manifold, as shown in Fig. 3.22. This option will produce the pulses that have similar characteristics as if it comes from an engine that adopts cylinder deactivation technology, providing the chance for studying the influence of cylinder deactivations on the turbine unsteady performance. In this thesis, depending on how many cylinders that the effective flow only passes through, it will be referred to either *two cylinder mode* or *three cylinder mode*.

Cylinder deactivation is seen as one of the means to improve the part-load fuel savings of both diesel and gasoline engines [137]. Cylinder deactivation changes the operating point of the turbocharger and affects the engine turbocharger matching. Hence, there comes a necessity to consider the turbocharger performance during deactivation and a facility to test the TC under such pulsating conditions is extremely useful. When a cylinder is deactivated on a running engine, the energy delivered to the turbine is reduced if nothing else is changed. This will result in a change in the turbocharger operating condition including a drop in its speed and boost level. However, owing to two different air flow paths in this unsteady gas-stand facility, it is able to maintain the same averaged turbine loading by varying the

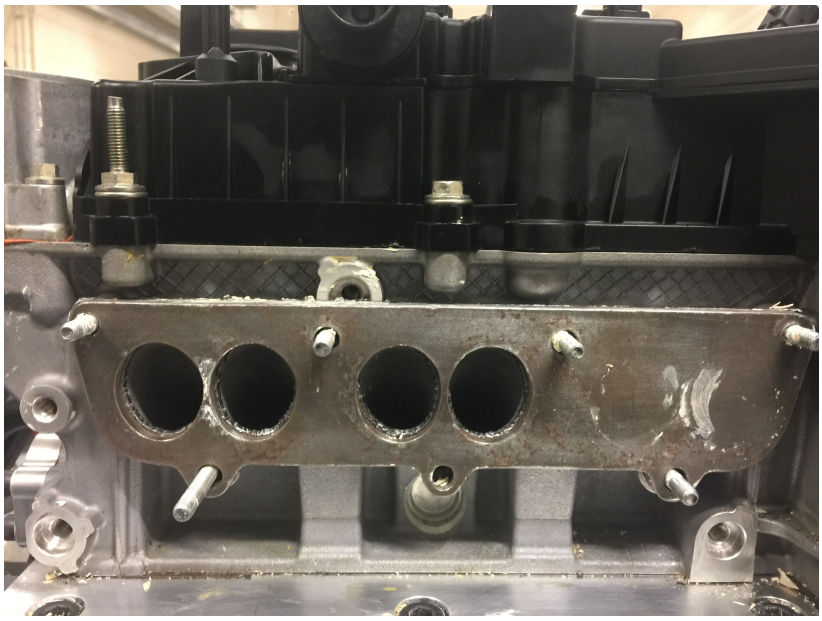

Figure. 3.22 Blank plate used in cylinder deactivation

compressor back-pressure valve so as to achieve the same averaged compressor operating point between the two and three cylinder modes.

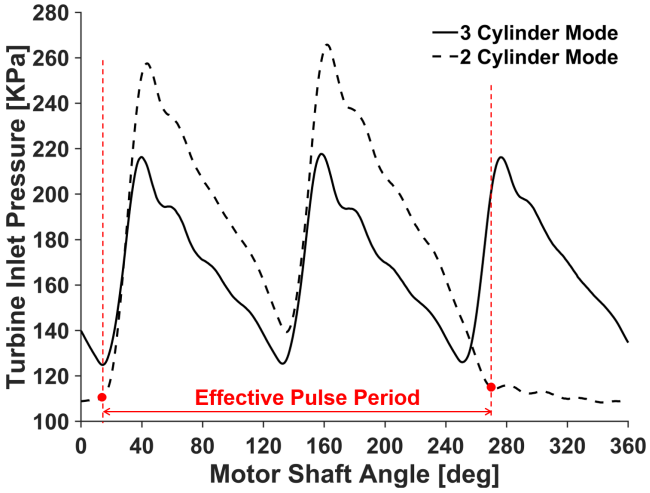

(a) Comparison of instantaneous pressure

Fig. 3.23 shows the pulse performance comparison between two and three cylinder mode, where they have a similar electric motor speed of 1150 rpm and a similar velocity ratio of 0.55. It is clear from Fig. 3.23 (a) that in order to compensate for the missing pulse, the pressure amplitude in the two-cylinder mode increases substantially, thereby resulting in a

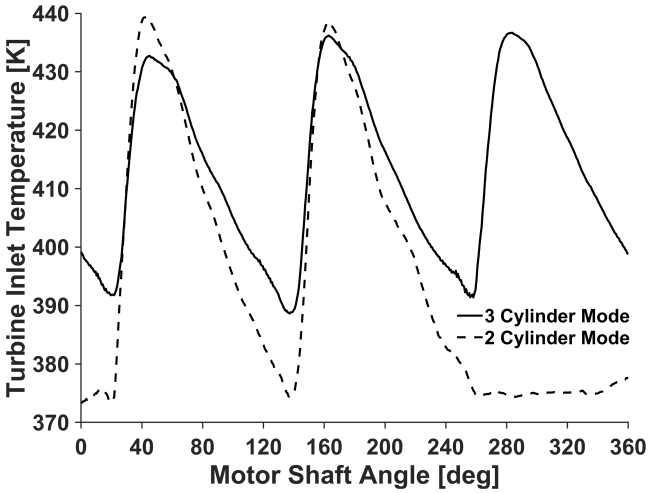

(b) Comparison of instantaneous temperature

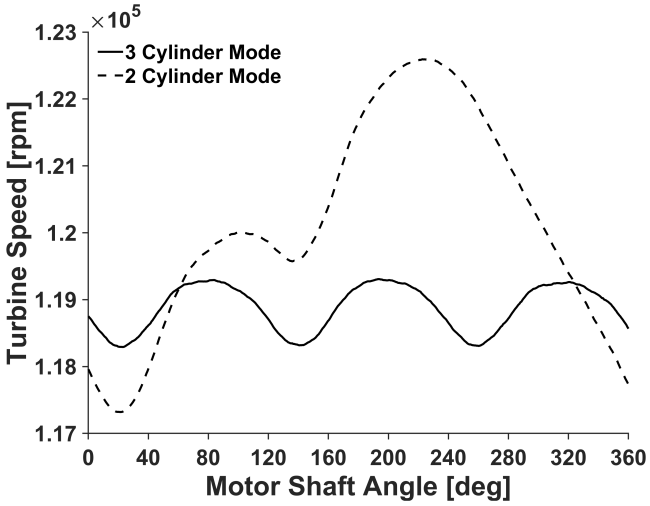

(c) Comparison of instantaneous rotational speed

Figure. 3.23 Instantaneous turbine performance comparison between two and three cylinder modes

much higher amplitude of the rotational speed under two-cylinder mode (5.2 times higher in this case). Besides, the speed profile is very different between two and three cylinder mode. There is a large drop in the turbine speed during the period of blank pulse in the two-cylinder mode, starting from 240 motor shaft angle. To compensate this speed drop, the flows from the rest cylinders have to continuously increase the turbine speed in order to maintain the same mean speed during a complete cycle. The two-cylinder mode also results in a higher amplitude temperature pulse, albeit without a substantial change in temperature.

In this aspect, there is a clear difference to a running engine which would likely result in a temperature and pressure change due to differences in fuelling.

As introduced in the literature review of Section. 2.1, the turbine will produce negative efficiency when the pressure ratio is close to unity. Under this circumstance, the turbine impeller operates in a free-wheeling manner so that momentum energy of the spinning wheel and shaft is transferred (dissipated) to the gas thereby resulting in an actual power that is below zero. The effects of negative efficiency on the turbine performance is expected to be more significant under two-cylinder mode. Considering a three-cylinder engine of deactivating one cylinder, free-spinning behaviour of a turbine will last for one-third period of one engine cycle. Therefore, this study will also investigate how much of the turbine performance would be influenced if the negative efficiency is considered, especially taking into account the cylinder deactivations and various pulse frequencies.

CHAPTER 4

NUMERICAL METHODOLOGY

4.1 Introduction

This chapter will present the simulation methods that will be used in this study. Firstly, the numerical algorithm of the CFD model will be introduced. This is followed by the proposal of a novel turbine map extrapolation techniques. The extrapolation process is achieved by including a nozzle-based model for the prediction of turbine swallowing capacity characteristics, and a mean-line model for the prediction of turbine efficiency. Compared with the conventional mean-line code, the proposed model is capable of predicting the negative turbine efficiency, representing the energy loss during the free-wheeling process. Lastly, a transient turbocharger model is developed for analysing the influence of negative turbine efficiency on the turbocharger performance.

4.2 Basics of Computational Fluid Dynamics

Computational Fluid Dynamics (CFD) method was extensively used in this study for the performance prediction and the internal flow field analysis of the radial turbine. The conservation laws of fluid flow and related transport phenomena are governed by the Navier-Stokes equations, namely the conservation equations of mass, momentum, and energy. These governing equations, fundamentally the partial differential equations (PDEs), unless substantially simplified, have no known analytical solutions. The basis of CFD is to discretize these PDEs

in the three-dimensional space such that they can be solved numerically to obtain a prediction of the fluid field.

In CFD applications, Finite Volume Method (FVM) is more preferred discretization method for solving the PDEs than Finite Element Method or Finite Difference Method due to various advantages. In FVM, the fluid domain is discretized into non-overlapping finite volumes and the final solution of the entire fluid field is therefore achieved by integrating over each discretized small cell. Many terms of governing PDEs are turned into face fluxes and evaluated at the finite volume faces. Since the flux leaving a face of a finite volume is identical to that entering an adjacent volume face such that the FVM is conservative in nature. Besides, the FVM discretization can be formulated in the physical space on unstructured polygonal meshes with no need for any transformation between the physical and the computational coordinate system, making it capable of dealing with all kinds of complex physics and geometries.

4.2.1 Governing Equations

The conservation of mass equation, also known as the continuity equation, is the most fundamental equations of the governing equations. The continuity equation says that the rate of change of mass within a fluid system is equal to the net mass flux, coming in or out of that system. The conservative form of the continuity equation is defined in Eq. 4.1. Note that each component of the velocity vector in a three-dimensional cartesian coordinate system will be denoted by **u**, **v**, and **w** in the corresponding x, y and z direction, written as Eq. 4.2. where **i**, **j**, and **k** correspond to the unit vectors in the x, y, and z direction, and the bold font implies that it is a vectorial variable.

$$\frac{\partial \rho}{\partial t} + \nabla \cdot (\rho \mathbf{v}) = 0 \tag{4.1}$$

$$\mathbf{v} = u\mathbf{i} + v\mathbf{j} + w\mathbf{k} \tag{4.2}$$

The conservation of momentum equation is the consequence of Newton's Second Law of motion, stating that the rate of change of momentum is equal to the sum of all forces acting on a fluid particle. The conservative form of the momentum equation is obtained as Eq. 4.3. where $\rho\mathbf{vv}$ is the dyadic product, which is a special case of tensor product with its divergence being a vector. $\mathbf{f}$ is the external force per unit volume, and it can be split into two parts (Eq. 4.4) with one denoted by $\mathbf{f_s}$ representing the surface forces acting on the fluid particle. The second part, $\mathbf{f_b}$, corresponds to the body forces of the fluid particle.

$$\frac{\partial}{\partial t}(\rho\mathbf{v}) + \nabla\cdot(\rho\mathbf{vv}) = \mathbf{f} \tag{4.3}$$

$$\mathbf{f} = \mathbf{f_s} + \mathbf{f_b} \tag{4.4}$$

The forces acting at the surface of a fluid particle consist of both pressure forces and the viscous forces. The surface force expressed in the PDE form is given in Eq. 4.5. τ is the viscous stress tensor and its divergence is expanded in Eq. 4.6. This is achieved with the assumption of Newtonian fluid that the stress tensor is a linear function of the dynamic viscosity of fluid μ. λ is the bulk viscosity coefficient. For gases, a good working approximation can be obtained by taking the value $\lambda = -\frac{2}{3}\mu$ [138].

$$\mathbf{f_s} = -\nabla P + \nabla \cdot \tau \tag{4.5}$$

$$\nabla \cdot \tau = \nabla \cdot (\mu \nabla \mathbf{v}) + \nabla \cdot \left[\mu (\nabla \mathbf{v})^T\right] + \nabla(\lambda \nabla \cdot \mathbf{v}) \tag{4.6}$$

In general the body forces $\mathbf{f_b}$ can involve the gravitational, electrical, centrifugal and Coriolis forces. For turbomachinery applications, when solving the fluid flow problems in a rotating frame of reference (such as rotor), the body forces mainly involve the centrifugal force and Coriolis force, which is a result of the rigid body rotation of the reference frame. This is expressed as per Eq. 4.7, where $\mathbf{r}$ is the vector of the rotational axis, defined according to the right-hand screw rule.

$$\mathbf{f_b} = \underbrace{-2\rho(\omega \times \mathbf{v})}_{\text{Coriolis forces}} \underbrace{-\rho[\omega \times (\omega \times \mathbf{r})]}_{\text{Centrifugal forces}} \tag{4.7}$$

The governing equation for the conservation of energy is derived from the first law of thermodynamics, which states that the rate of change of energy of a fluid particle is equal to the rate of heat addition to the fluid particle plus the rate of work done on the particle. The conservation of energy is written in terms of specific internal energy ($\hat{u}$) in the conservative form as per Eq. 4.8. k is the thermal conductivity of the medium; $\dot{q}_V$ represents the rate of heat source or sink within the material volume per unit volume (e.g. due to a chemical reaction). Φ is the viscous dissipation term due to viscous stresses as shown in Eq. 4.9. Since all terms in Eq. 4.9 are squared, it will always be positive, so that acting as a source term

for the internal energy. This represents the dissipation of mechanical energy into heat as the fluid is deformed due to viscous effects.

$$\frac{\partial}{\partial t}(\rho\hat{u}) + \nabla\cdot(\rho\mathbf{v}\hat{u}) = -P\nabla\cdot\mathbf{v} + \nabla\cdot(k\nabla T) + \Phi + \dot{q}_V \tag{4.8}$$

$$\Phi = \lambda\left(\nabla\cdot\mathbf{v}\right)^2 + \mu\left\{\begin{array}{l} 2\left[\left(\frac{\partial u}{\partial x}\right)^2 + \left(\frac{\partial v}{\partial y}\right)^2 + \left(\frac{\partial w}{\partial z}\right)^2\right] + \\ \left(\frac{\partial u}{\partial y} + \frac{\partial v}{\partial x}\right)^2 + \left(\frac{\partial u}{\partial z} + \frac{\partial w}{\partial x}\right)^2 + \left(\frac{\partial v}{\partial z} + \frac{\partial w}{\partial y}\right)^2 \end{array}\right\} \tag{4.9}$$

In these system of equations Eq. 4.1 - 4.9, there are six unknown fluid properties i.e. P, $\mathbf{v}$, T, ρ, $\hat{u}$, μ. In this study, the perfect gas assumption was applied to describe the equation of state as Eq. 4.10-4.11. Where R is the universal gas constant of air ($287\frac{J}{kg\ K}$). The viscosity of air can also be described as function of pressure and temperature shown in Eq. 4.12. Therefore, the three conservation equations (Eq. 4.1, Eq. 4.3 and Eq. 4.8) together with Eq. 4.10-4.12 makes a series of six equations with a total of six unknown parameters forming a closed mathematical problem.

$$P = \rho RT \tag{4.10}$$

$$\hat{u} = c_v T \tag{4.11}$$

$$\mu = f(P,T) \tag{4.12}$$

It is possible to formulate the overall governing equations for mass, momentum, and energy to a general transport equation for any intensive property ϕ. The general conservation equation

is expressed as per Eq. 4.13. The first term on the left-hand-side represents the accumulation of ϕ within the control volume, the second term corresponds to the transport of ϕ due to convection. The first term on the right-hand-side account for the transport of ϕ by diffusion, where Γ is the diffusion coefficient, the last term stands for the sources. By assigning ϕ equal to 1, $\mathbf{v}$ and $\hat{u}$ and selecting the proper values for the diffusion coefficient and source term, Eq. 4.13 can be formulated to a general form of the PDEs for mass, momentum, and energy equation.

$$\underbrace{\frac{\partial}{\partial t}(\rho\phi)}_{\text{unsteady term}} + \underbrace{\nabla\cdot(\rho\mathbf{v}\phi)}_{\text{convection term}} = \underbrace{\nabla\cdot(\Gamma\nabla\phi)}_{\text{diffusion term}} + \underbrace{Q}_{\text{source term}} \tag{4.13}$$

4.2.2 Turbulence Models

Whether the flow is laminar or turbulent can be characterized by the Reynolds number (*Re*). The flow inside a turbocharger turbine will be entirely turbulent even though under steady-state conditions due to the high flow velocity within the rotor passages. Turbulent flows are time-dependent, irregular, diffusive, and involve three-dimensional vorticity fluctuations with a broad range of time and length scales [139]. In theory, the motion of the turbulent eddies could be directly resolved with the use of the Navier-Stokes equation. However, to resolve the smallest eddies requires a very small time step and a large number of grid points (order of Re^3). In most industrial applications, the resolution and motion of the turbulent scales are not of particular interest and in any case would impose an unrealistic computational burden. Therefore, it is common to model the turbulence effects on the macroscopic flow characteristics rather than direct numerical simulations (DNS).

The solution of industrial turbulent problems is based on solving the Reynold Averaged Navier-Stokes (RANS) equations, where the turbulent eddies are statistical averaged based

on a proper time-scale Moukalled et al. [140]. The major advantage of the RANS model is that the solution can be achieved in a steady-state solver thus reducing the restrict time-step requirement such as a transient solver. This will significantly reduce the simulation duration of reaching a convergent solution. As shown in Fig. 4.1, the Reynolds decomposition says the flow variable ϕ (P, $\mathbf{v}(u,v,w)$, T, $\hat{u}$, etc.) can be split into a mean value component $\bar{\phi}$ and a fluctuating component ϕ' as per Eq. 4.14.

$$\phi = \bar{\phi} + \phi' \tag{4.14}$$

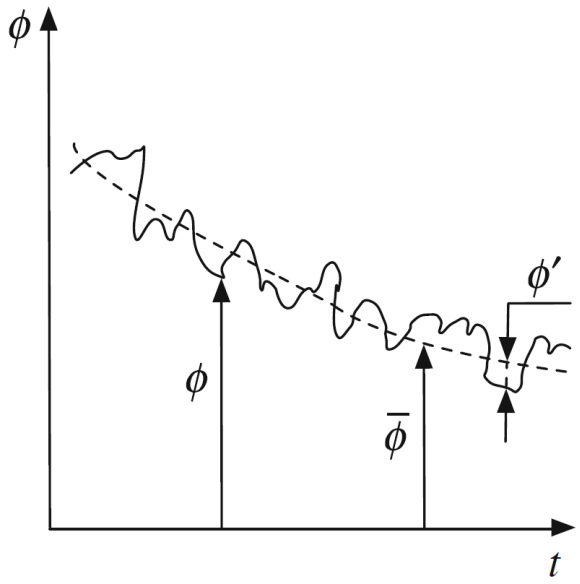

Figure. 4.1 Fluctuating and mean variable components [140]

When substituting ϕ term of Eq. 4.13 by Eq. 4.14, it will introduce a Reynolds stress tensor term τ^R to the momentum equation and turbulent fluxes $\dot{q}^R$ to the energy equation, as per Eq. 4.15 and Eq. 4.16 respectively. This introduces additional unknowns, making the system of equations unclosed unless additional assumption provided.

$$\tau^R = -\rho \mathbf{v}'\mathbf{v}' = -\rho \begin{bmatrix} \overline{u'u'} & \overline{u'v'} & \overline{u'w'} \\ \overline{v'u'} & \overline{v'v'} & \overline{v'w'} \\ \overline{w'u'} & \overline{w'v'} & \overline{w'w'} \end{bmatrix} \tag{4.15}$$

$$\dot{q}^R = -\rho c_p \begin{bmatrix} \overline{u'T'} \\ \overline{v'T'} \\ \overline{w'T'} \end{bmatrix} \tag{4.16}$$

A common approach to model the Reynolds stress tenor is based on the Boussinesq hypothesis [138, 141, 142], which assumes the Reynolds stress to be a linear function of the mean velocity gradients such that Eq. 4.17. Where I is the identity tensor defined as Eq. 4.18, k is the turbulent kinetic energy defined as Eq. 4.19. This reduces the unknowns of the Reynolds stress tensor to the the turbulent eddy viscosity (μ_t) itself, which is evaluated using a variety of turbulence models.

$$\tau^R = -\rho \mathbf{v}'\mathbf{v}' = -\rho \mu_t \left[\nabla \mathbf{v} + (\nabla \mathbf{v})^T\right] - \frac{2}{3}\left[\rho k + \mu_t (\nabla \cdot \mathbf{v})\right]\mathbf{I} \tag{4.17}$$

$$\mathbf{I} = \begin{bmatrix} 1 & 0 & 0 \\ 0 & 1 & 0 \\ 0 & 0 & 1 \end{bmatrix} \tag{4.18}$$

$$k = \frac{1}{2}\overline{\mathbf{v}' \cdot \mathbf{v}'} \tag{4.19}$$

Similarly, turbulent thermal fluxes are derived as per Eq. 4.20, where k_t is the turbulent thermal diffusivity also depended on the turbulent models.

$$\dot{q}^R = -\rho c_p \overline{\mathbf{v}' \cdot T'} = k_t \nabla T \tag{4.20}$$

$k-\varepsilon$ turbulence model

Over the years, many different correlations have been proposed to model turbulence terms based on Boussinesq hypothesis with varying degrees of simplicity. $k-\varepsilon$ turbulence model [143] was the most popular two equation models in solving industrial CFD problems. As its name implies, the basis of this model is that the turbulent eddy viscosity can be related to the turbulence kinetic energy and k and turbulence kinetic energy dissipation rate ε as shown in Eq. 4.21, and the turbulent thermal diffusivity is formulated as as Eq. 4.22. C_μ is the dimensionless constant, Pr_t is the turbulent Prandtl number (recommended value is 0.9).

$$\mu_t = C_\mu \rho \frac{k^2}{\varepsilon} \tag{4.21}$$

$$k_t = \frac{c_p \mu_t}{Pr_t} \tag{4.22}$$

As [139, 140] suggested $k-\varepsilon$ model predicts well for free-shear flows that far from walls while are likely to fail in predicting flows with adverse pressure gradient (near-wall flows) since this model assumes the flow to be fully turbulent and the effects of molecular viscosity to be negligible.

$k-\omega$ turbulence model

Another family of two equation turbulence model is the $k-\omega$ model, which involves many alternative definitions proposed by different researchers [144, 145]. The basis of $k-\omega$ is to utilize turbulence frequency ω to replace the turbulence kinetic energy dissipation rate ε. This method is better capable of predicting separated flows such as boundary layer flows but requires fine mesh near the wall with the dimensionless wall distance $y^+ < 2$ in order to resolve velocity profile near the wall. The importance of y^+ will be introduced in Section. 4.2.3.

SST turbulence model

Shear Stress Transport (SST) model can be deemed to be the mixing of both, which employs blending functions to switch from $k-\omega$ in the near-wall region to $k-\varepsilon$ in free stream regions and generally gives reasonably good results for separated flows under adverse pressure gradients.

4.2.3 Wall Functions

Both experimental and DNS data reveal that the turbulent boundary layer consists of multiple layers. According to their positions from the wall, each layer has different flow physics. As shown in Fig. 4.2, the layer nearest to the wall is the extremely thin viscous sub-layer. In this region, the molecular viscous effects dominate the effect of the Reynolds stresses where approximately 70% of the velocity gradient is found in this region [146]. The next layer after sub-layer region is the logarithmic region (also known as inertial sub-layer), where viscosity effects are small and turbulent shear effects dominate. The intermediary between viscous sub-layer and the logarithmic layer is so-called the buffer layer, where the effects of molecular viscosity and turbulence are equally important. Outside the inner layer is called the wake turbulent region, which behaves differently depending on the Reynolds number. The

region of each turbulent boundary layer can be classified according to their non-dimensional wall distance shown below.

$$0 < y^+ \leq 5 : \ viscous\ sublayer$$
$$5 < y^+ \leq 30 : \ buffer\ layer$$
$$30 < y^+ \leq 300 : \ inertial\ sublayer$$

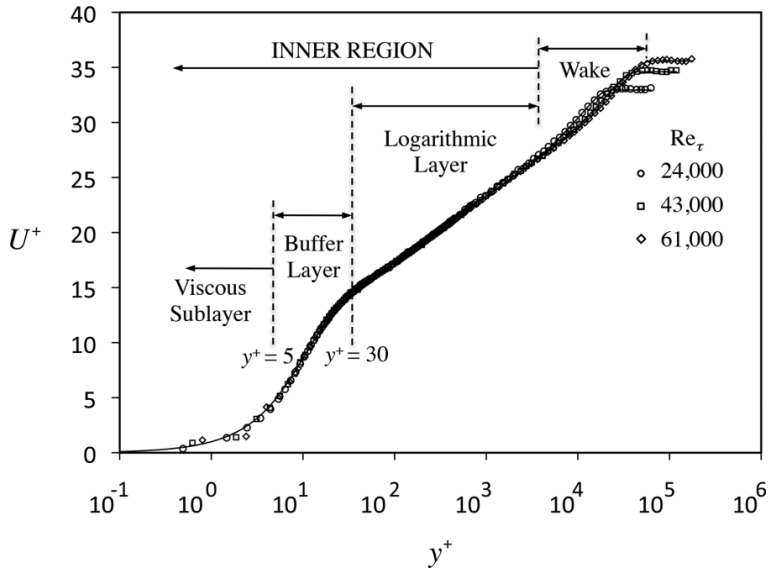

Figure. 4.2 Law of the wall plot for a turbulent boundary layer [147]

The dimensionless wall distance is calculated as Eq. 4.23, where $d_\perp$ is the normal distance to the wall, ν is the kinematic viscosity (Eq. 4.24), u_τ is the friction velocity expressed in terms of the wall shear stress τ_w as Eq. 4.25. It is common to define the wall as non-slip, where the fluid velocity adjacent to the wall is zero, leading to zero Reynolds stresses so that the wall shear stress is entirely due to the contribution of molecular viscous effects defined as Eq. 4.26.

$$y^+ = \frac{d_\perp u_\tau}{\nu} \tag{4.23}$$

$$\nu = \frac{\mu}{\rho} \tag{4.24}$$

$$u_\tau = \sqrt{\frac{|\tau_w|}{\rho}} \tag{4.25}$$

$$\tau_w = \mu \left.\frac{du}{dy}\right|_{y=0} \tag{4.26}$$

Due to the small thickness and high strain in the viscous sub-layer, directly resolve the velocity profile within this region requires a fine near-wall mesh ($y^+ < 1$) and at least 10 inflation layers within the inner layer [148]. Under this circumference, the velocity profile near the wall was resolved, which is computationally expensive. Instead, in most industrial applications, the flow nearest to the wall is modelled by wall functions. In this method, theoretical profiles between the boundary surface and the first near-wall node are modelled and superimposed, which significantly reduces the computational cost. The wall function relates the dimensionless near-wall flow velocity as a function of dimensionless wall distance, as defined in Eq. 4.27 where $|\mathbf{v} - \mathbf{v_w}|_\parallel$ is the magnitude of the velocity parallel to the wall. This takes into account the general case of a moving wall with a velocity $\mathbf{v_w}$. The wall function modelled the near-wall velocity differently according to the region where the first grid point is placed as shown in Eq. 4.28, where κ is von Karman's constant (0.4187) and C is constant depending on the roughness of the wall [139]. However, near-wall flow in the buffer layer is also depended on the Reynolds number making it difficult to model. Thus, it is necessary to avoid placing the first internal grid point in the buffer layer.

$$u^+ = \frac{|\mathbf{v} - \mathbf{v_w}|_\parallel}{u_\tau} \tag{4.27}$$

$$u^+ = \begin{cases} y^+ \ (viscous\ sublayer) \\ \frac{1}{\kappa} ln(y^+) + C \ (inertial\ sublayer) \end{cases} \tag{4.28}$$

4.3 Development of CFD Model

The performance evaluation of the mixed flow turbine was carried out using the commercial CFD solver Ansys-CFX. Both steady-state and unsteady CFD solver will be used in this study for different purposes described as blow,

The steady-state CFD model was used for

1. In comparison with steady-state experimental data (Section. 6.3)
2. Validation of the one-dimensional model (Section. 6.2.2)
3. Steady-state optimization of the mixed-flow turbine (Section. 5.3.4)

The unsteady CFD model was used for the unsteady optimization of the radial turbine blade, as will be discussed in Section. 7.1.

As shown in Fig. 4.3, the CFD domains contain four different components, namely the volute domain, the rotor passage domain, a vaneless nozzle domain, and an exit duct. The vaneless nozzle domain is used for the connection between volute and rotor passage. The exit duct was modelled with an extra length in order to dump the unsteady flow for better numerical stability during the unsteady simulation.

Each of these domains was meshed individually and then assembled in the CFX-Pre using fluid interfaces. The general grid interface was applied for the connection between volute and vaneless nozzle. The rotor-stator interface was treated as frozen rotor, where the rotor and stator kept the same relative position during the simulation. This approach uses moving

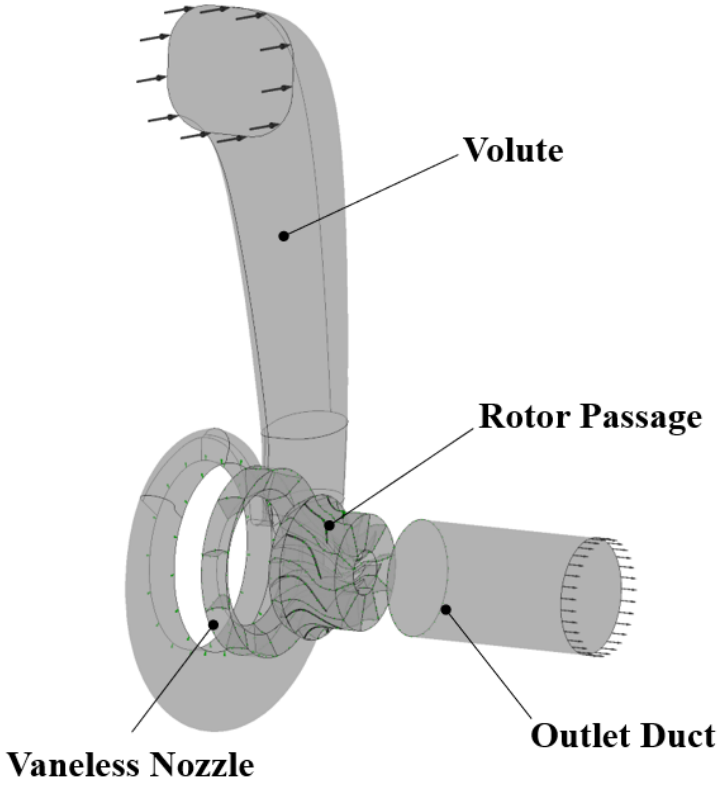

Figure. 4.3 CFD domains - full stage model

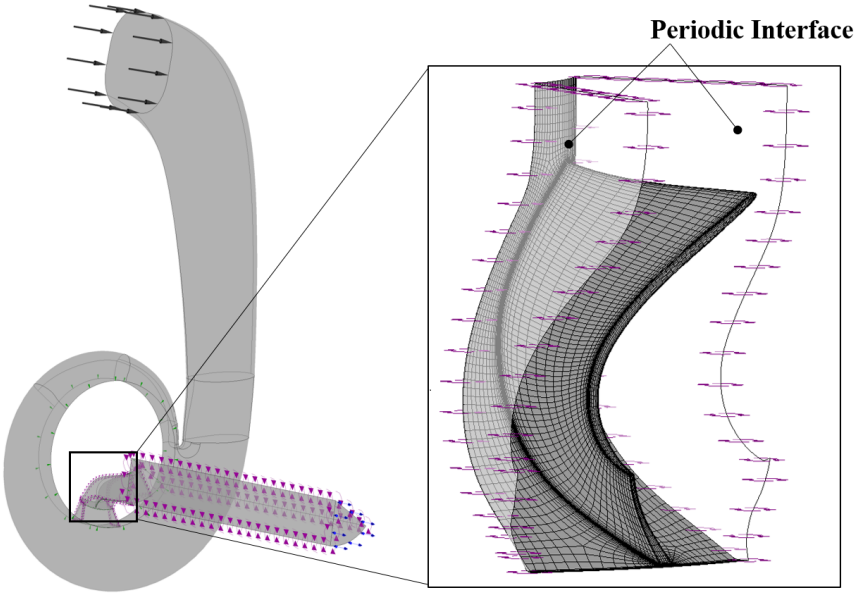

Figure. 4.4 CFD domains - single passage model

reference frame equations to model the Coriolis effects and centrifugal forces caused by rotation in the turbine rotor (Eq. 4.7). The frozen rotor approach is less computational expensive than the sliding mesh (SM) technique since it avoids the merging the mesh files prior to starting the calculation. Galindo et al. [87] showed the SM is better in capturing the turbine performance under off-design conditions but Hellström [57] mentioned frozen rotor approach is still applicable to unsteady simulations when the pulse frequencies are much lower than the blade passage frequencies. With the advantage of being less computationally expensive, this study utilizes the frozen rotor interface model since the objective of the CFD model is for either validation or comparison purposes rather than the detailed flow field analysis which has been extensively studied by many researchers. It is also useful to note that a 3D viscous turbulent solver used in this study still represents a big step up in accuracy compared to a 1D mean-line or 2D through flow solver.

Both single passage rotor and the full stage model were used in this study for different applications. The single passage model (shown in Fig. 4.4) utilizes only one blade to simulate the whole turbine performance by assuming that the flow would behave identically for every blade. Since this turbine wheel has 10 blades, single passage model reduces this to just 1 passage thus hugely reducing the computational workload. However, this method is expected to be more accurate when the flow angles produced at the exit of the volute circumference are similar. In order to account for the missing blade effects on the conservation equations (mass, momentum, and energy), the pitch angle was specified to scale the flow between the rotor and stator. The interaction between rotor passages was simulated by using periodic boundary conditions, where the pressure side of the rotor passage domain was virtually connected to the suction side using a periodic interface. On the other hand, in the full stage model, all rotor passages are explicitly modelled to take into account the maldistribution of rotor in-flow that will occur due to the volute – especially known to exist around the tongue area, and therefore more accurate in the prediction of turbine performance

parameters. The results that show the difference between the single-passage model and full-stage model are present in Section. 7.1.1. Note that in the single passage model, only $1/6$ portion of the exit duct was modelled for further reduce the computational cost.

Table. 4.1 lists and compares the CFD set-ups and boundary conditions between steady-state solver and unsteady solver. Ideal gas assumption was chosen for both set-ups. The solution of turbulent Reynolds tensors was achieved by using $k-\omega$ *SST* turbulent model due to its superiority in modelling both free stream flows and separated flows. Automatic wall function was used to obtain a smooth transition from the viscous sublayer to the log-law region in the turbulent boundary layer, allowing a range of y^+ number up to 300 [149].

High-resolution scheme and second-order backward Euler option were applied for the advection scheme and transient scheme respectively. To account for the compressibility effects, resulting from high speed flows within the rotor passages, the transport of enthalpy was modelled using the total-energy scheme. All the walls including the impellers were assumed to be non-slip and adiabatic.

Table 4.1 CFD setup and boundary conditions

Analysis Type	Steady	Unsteady
Time Steps	Conservative Auto	1.38×10^{-5} $[s]$
Inlet Type	Mass Flow	Inst Total Pressure
Inlet Temp	600 °C Static	Inst Total
Outlet	Static Pressure	Opening Static Pressure
Rotational Speed	90 krpm - 212 krpm	120.75 krpm
Converge Criteria	*RMS* 5×10^{-6} or *Std*.τ 5×10^{-5}	*RMS* 1×10^{-5}
Max Coeff Loops	-	12
Medium	Air, Ideal Gas	
Walls	Non-slip, Adiabatic	
Turbulence Model	$k-\omega$ *SST*	
Wall Function	Automatic	
Heat Transfer	Total Energy	
Advection Scheme	High Resolution	
Transient Scheme	Second Order Backward Euler	

In the steady-state set-up, mass flow inlet boundary was chosen for better convergence rate. 600°C is set for the temperature at the inlet in order to match the experimental conditions.

Turbine performance at various speed lines was assessed from 90 krpm to 212 krpm, where the maximum rotational speed was also treated as 100% in this study. The simulation converged at with the RMS residual smaller than 5×10^{-6} for all governing equations or the moving standard deviation (MSTD) of the torque with the window size of 10 is smaller than 5×10^{-5}. The MSTD has been defined in Eq. 4.29, where y_i is metric value at the i^{th} row, y the average of metric, m the window size and n is the number of rows/metric values. Fig. 4.5 shows an example of the torque and the corresponding MSTD. This can avoid the situation that the solution is actually stabilised but at a higher RMS residual causing an extra cost of computing resource.

$$S = \sqrt{\frac{1}{m-1} \sum_{i=k-m+1}^{k} (y_i - \bar{y})^2} \quad where, \ \forall k = 1, ..., n \tag{4.29}$$

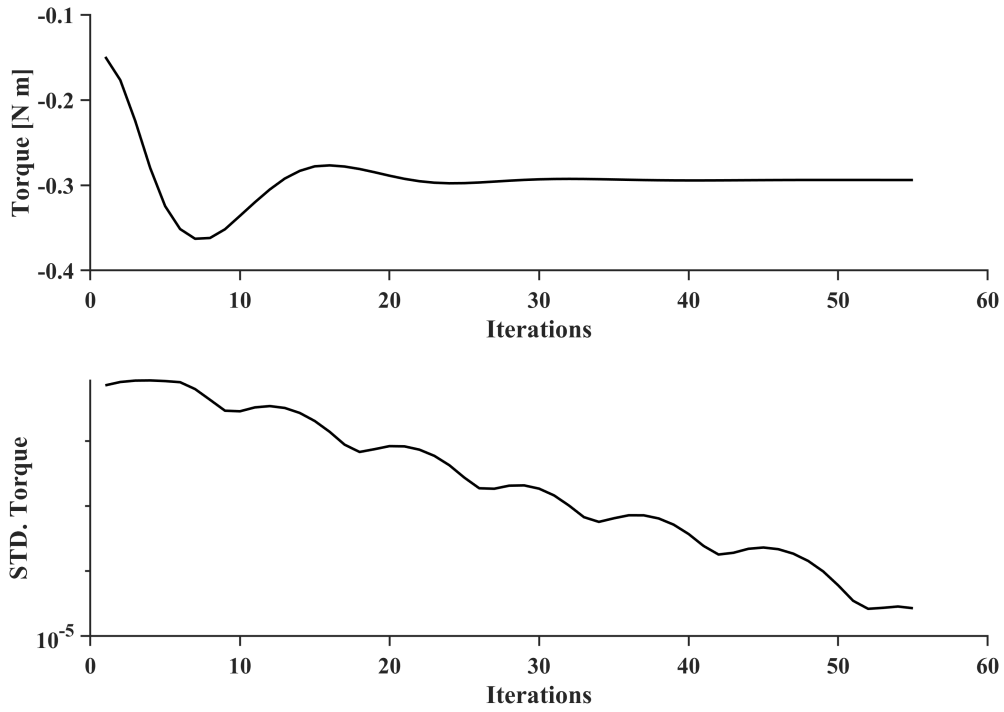

Figure. 4.5 The convergence progress of rotor's torque during steady-state simulation

The unsteady simulation was extensively used for the optimization purposes. In the transient simulation set-up, time-varying stagnation pressure, taken from an experiment measurement, with the magnitude ranging from 1.26 bar to 2.42 bar, was specified at the volute inlet. The instantaneous stagnation temperature was derived from the adiabatic assumption between pressure and temperature, as per Eq. 3.18. This has been shown to be a good representation of fluctuating temperature by [31]. The outlet was set as an opening boundary condition in order to allow for reverse flow resulting from the fluctuation pressure. The rotational speed was assumed constant during the simulation since the fluctuation magnitude at this particular speed is less than 1% of the mean speed according to the experimental data. The pulse frequency is 50 Hz, corresponding to a three-cylinder engine with a rotational speed of 2000 rpm. The choice of this particular pulse frequency is to simulate a condition that represents one of the more common conditions for road vehicles.

4.3.1 Study of Mesh Convergence

Mesh convergence studies were conducted on both rotor and volute domains. The hexahedral grids were generated in the rotor passage and vaneless nozzle using TurboGrid V18.1, whilst the meshes in the volute and outlet duction were formed using ANSYS Meshing V18.1. Table. 4.2 shows the number of mesh elements of the volute and its influence on the turbine MFP and efficiency. The MFP and efficiency were normalized by the results produced from the finest mesh. The rotor mesh was kept as a constant of 145,614 per passage and the number of inflation layer of the volute was set as 8. It shows that both turbine MFP and efficiency are nearly unaffected by the mesh density of the volute when number of mesh elements ranging from 126 K to 1,944 K.

Similarly, the mesh density study of the rotor passage has been conducted with a constant volute mesh density (elements number: 153,528). Table. 4.3 shows the number of mesh elements per rotor passage and its influence on the turbine MFP and efficiency. If finds that when increasing the mesh elements number from 90 K to 174 K, the influence on the turbine

Table 4.2 Mesh convergence study of the volute

No. Elements	Norm. MFP	Norm. Efficiency
126,348	0.9997	1.0012
178,316	1.0003	1.0014
300,728	0.9988	1.0016
634,081	0.9993	1.0008
1,173,170	0.9986	1.0003
1,944,305	1.0000	1.0000

performance is negligible. Based on the mesh convergence study, the mesh settings have been listed in Table. 4.3. This will be used throughout this study for the CFD simulations.

Table 4.3 Mesh convergence study of the rotor passage

No. Elements per Passage	Norm. MFP	Norm. Efficiency
90,365	1.0016	0.9974
113,882	1.0004	0.9983
133,680	1.0016	0.9990
152,168	1.0008	0.9996
173,770	1.0000	1.0000

Table 4.4 Number of mesh elements in each computational domain

Domain	Mesh Type	No. Elements
Vaneless Nozzle*	Hex	71 k
Volute	Tet,Pri,Pyr	153 k
Rotor*	Hex	134 k
Outlet Duct	Hex	38 k

$*$: refers to the mesh of single blade passage

4.3.2 Study of Time-step Sensitivities

As will be apparent in forthcoming sections, it was of vital importance to reduce the computational effort owing to the time-consuming nature of the pulsating optimization strategy. In order to reduce the simulation time whilst maintaining numerical stability, it is important to evaluate the maximum time-step that would still result in a stable and converged solution. CFX utilizes a pressure-based coupled implicit solver to calculate the pressure and velocity field simultaneously at each time-step, achieving fast convergence rates. Compared to an

explicit solver, the implicit solver allows for larger time-steps and offers better stabilities. The coupled implicit solver is not restricted by the Courant Number, a stable solution of transient physics can be achieved by specifying an appropriate time-step with a number of coefficient loops [150]. In a transient simulation, the overall simulation time is discretized with many small time-steps. In each time-step, all unknowns of the equations were solved [149]. However, as simulation time progresses, the boundary condition (such as pressure, mass flow, temperature and etc.) might be changed and this change can be significant under some circumferences. Therefore, the time-step may not be small enough that leads to a converged solution. To compensate, a certain number of inner loop iterations, which is named as coefficient loops in CFX, have to be performed to repeat the process of equation evaluations until a converged solution that is achieved at each time-step or the maximum number of iterations is reached. In this study, the required RMS residuals at each time-step were set as 1×10^{-5} for all criteria (mass, momentum, energy, and turbulence). The upper limit of the coefficient loops was set as 12.

Table. 4.5 listed the simulation time during one pulse and the number of coefficient loops per time-step. A Dual Xeon E52690v3 CPU including 42 processors with the total RAM of 256 GB were used for this computation. This study found that the simulation time can be significantly reduced by using a larger time-step whilst maintaining the same residual requirement. However, the number of coefficient loops also increased which tends to offset the reduced simulation time as can be noted by the decreased time intervals.

However, it is not enough to simply rely on the residuals when considering the maximum time-step. Fig. 4.6 demonstrates the influences of the time-step on the turbine mass flow parameters and efficiencies. The left-hand Y-axis shows the difference (in percentage) compared with the case of 2.5° rotation per time-step (the finest time-step), whilst the right-hand Y-axis shows the base parameter value. It can be found that the largest error occurs during rapid changes in the parameter resulting from the main pulse event. However, both the

Table 4.5 Summary of time-step study

Rotational deg per time-step	**Simulation time per pulse**	**coeff loops per time-step**
2.5°	28 h	6
5°	21.2 h	7
7.5°	15.2 h	8
10°	10.5 h	10

instantaneous and time-averaged change in the parameters between the different time-steps is deemed sufficiently low to prioritize the simulation time. For example, the time-averaged error of MFP during a pulse is 0.11%, 0.21%, and 0.32% for 5°, 7.5°, and 10° of rotation per time-step respectively. Similarly, the time-averaged error of rotor efficiency is 0.04%, 0.07% and 0.11%. Thus, the time-step size corresponding to 10°of rotation was used throughout this study.

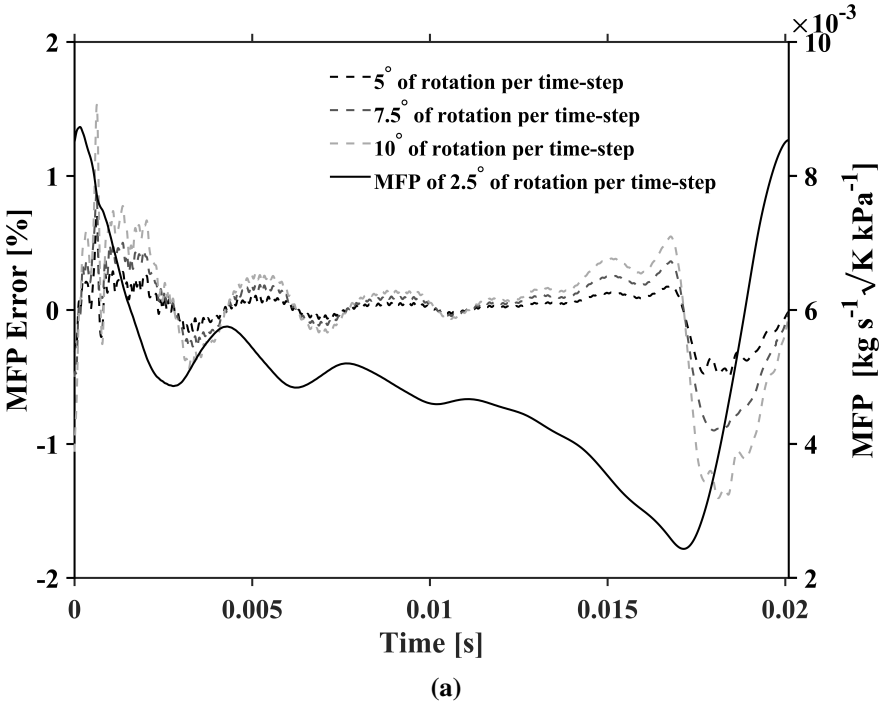

(a)

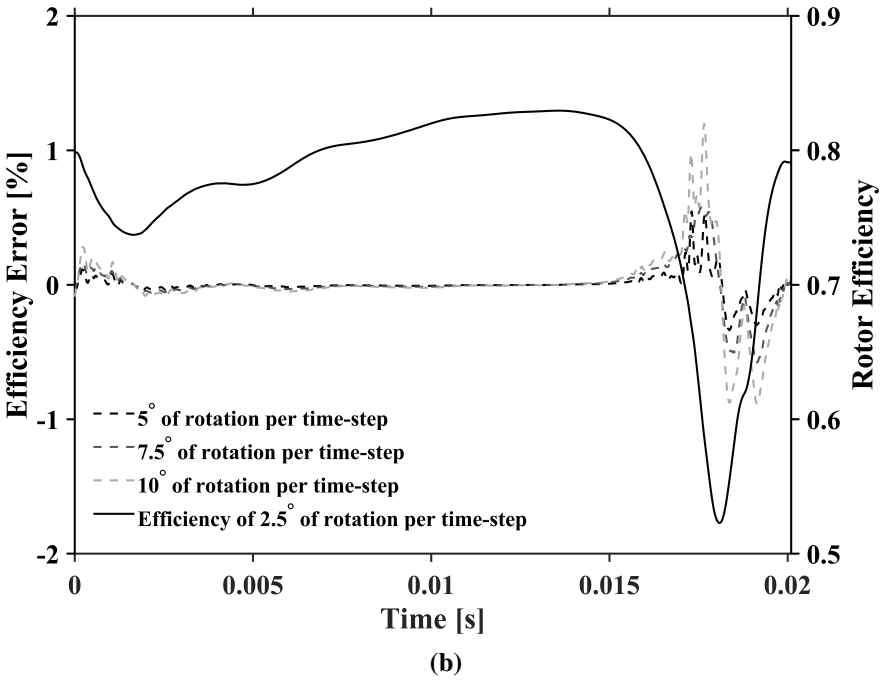

(b)

Figure. 4.6 Influence of time-steps on the performance of (a) mass flow parameter (b) rotor efficiency

4.4 Turbine Map Extrapolations

This section introduces the physical method of extrapolating turbine performance maps. The extrapolation method will be used for both steady-state and unsteady experimental data.

4.4.1 Extrapolation of Turbine Swallowing Capacity Map

Turbine swallowing capacity characteristics determined how quickly the turbine is able to process incoming gases at a certain expansion ratio and turbine speed. The proposed extrapolation model is based on the isentropic nozzle concept, where turbine mass flow was extrapolated by assuming compressible flow across a single orifice. This concept was first proposed by Watson and Janota [10], and many authors have posed different modified versions which fit the experimental results [29, 62, 65]. The problem of the single nozzle approximation is that it leads turbine choking at a low expansion ratio, which did not provide successful results for radial turbines. To overcome this, this study utilises a single nozzle model but introduced a heat capacity ratio multiplier k_3, as defined in Eq. 4.30. Therefore,

the choking conditions can be easily modified since the critical expansion ratio is mainly affected by the heat capacity ratio. The heat capacity ratio in EQ. 4.31-4.33 has to be replaced by the new value accordingly, where k_1 and k_2 are fitting parameters.

$$\gamma^* = k3 \cdot \gamma \tag{4.30}$$

$$\dot{m}_T = k_1 \cdot PR_t \cdot \left\{ \sqrt{\frac{2\gamma'}{\gamma^* - 1} \left[\left(\frac{1}{PR_t} \right)^{\frac{2}{\gamma^*}} - \left(\frac{1}{PR_t} \right)^{\frac{\gamma^*+1}{\gamma^*}} \right]} + k_2 \right\} if PR_t < P_{crit} \tag{4.31}$$

$$\dot{m}_T = k_1 \cdot PR_t \cdot \left\{ \sqrt{\frac{2\gamma^*}{\gamma^* - 1} \left[\left(\frac{1}{P_{crit}} \right)^{\frac{2}{\gamma^*}} - \left(\frac{1}{P_{crit}} \right)^{\frac{\gamma^*+1}{\gamma^*}} \right]} + k_2 \right\} if PR_t < P_{crit} \tag{4.32}$$

$$P_{crit} = \frac{2}{\gamma^* + 1}^{\frac{\gamma^*}{1-\gamma^*}} \tag{4.33}$$

As suggested by [62, 151, 152], turbine effectively is a nozzle that expands gases, but this expansion is also depended on the speed of rotation (by varying the centrifugal head). In this study, fitting parameters k_1, k_2, and k_3 are assumed to have linear variation with turbine speed parameter (SP), as per Eq. 4.34-4.36.

$$k_1 = k_{1,a} + k_{1,b}\left(\frac{SP}{min(SP)} - 1\right) \tag{4.34}$$

$$k_2 = k_{2,a}\left(\frac{SP}{min(SP)} - 1\right) \tag{4.35}$$

$$k_3 = k_{3,a} + k_{3,b}\left(\frac{SP}{min(SP)} - 1\right) \tag{4.36}$$

4.4.2 Extrapolation of Turbine Efficiency Map

A mean-line loss model was used for extrapolating the turbine efficiency data. This model was developed for the nozzleless turbine, where the turbine is divided into three stations: volute inlet station (subscript 1), rotor inlet station (subscript 3), and turbine outlet station (subscript 4). Mean-line model calculates the turbine power based on Euler's turbomachinery equation, which is derived based on the conservation of angular momentum as per Eq. 4.37. Euler turbomachinery equation solves the velocity triangles (as show in Fig. 4.7) at the rotor inlet and exit, where parameters U, C and W represent for the tip velocity, absolute flow velocity and relative flow velocity respectively. Therefore, geometric features of turbine are required to perform such calculations.

The velocity components of flow are calculated at each station with imposing loss equations. Fig. 4.8 shows the model flowchart for mean-line model calculation. This mean-line model requires the turbine operating conditions as input parameters i.e. turbine inlet stagnation

temperature T_{01} and pressure P_{01}, and turbine rotational speed N. Geometry parameters, such as shroud tip radius at leading edge r_{3s} and trailing edge r_{4s}, hub tip radius at leading edge r_{3h} and trailing edge r_{4h}, tip clearance ε_{tip}, cone angle γ, mean blade angle at the leading edge β_{b3}, number of blades Z_{blade}, volute cross-sectional area to radius (A/R) at the inlet $\frac{A_1}{r_1}$, as listed in Fig. 4.8 are required for estimating velocity triangles so as to estimate the enthalpy losses. Turbine exists static pressure is assumed to be a constant of 98 kPa. The turbine inlet mass flow rate is deduced from the nozzle model by proving the turbine inlet pressure, as discussed in Section. 4.4.1.

$$\dot{W}_t = \dot{m}(U_3 C_{\theta 3} - U_4 C_{\theta 4}) \tag{4.37}$$

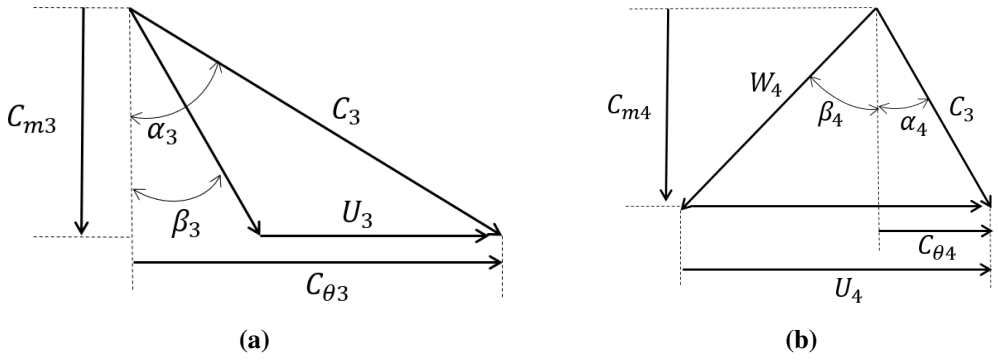

Figure. 4.7 (a) Inlet and (b) exit turbine wheel velocity triangles

Stator

The stator region consists of both volute region and a vaneless region between the volute exit and rotor inlet, as shown in Fig. 3.4. Eq. 4.38-4.39 listed the major equations that are employed for the calculation of flow parameters in the stator region.

The stagnation pressure loss coefficient K_{PL} describes the drop of available stagnation pressure as flow passing through the volute due to wall frictions or bends. This model

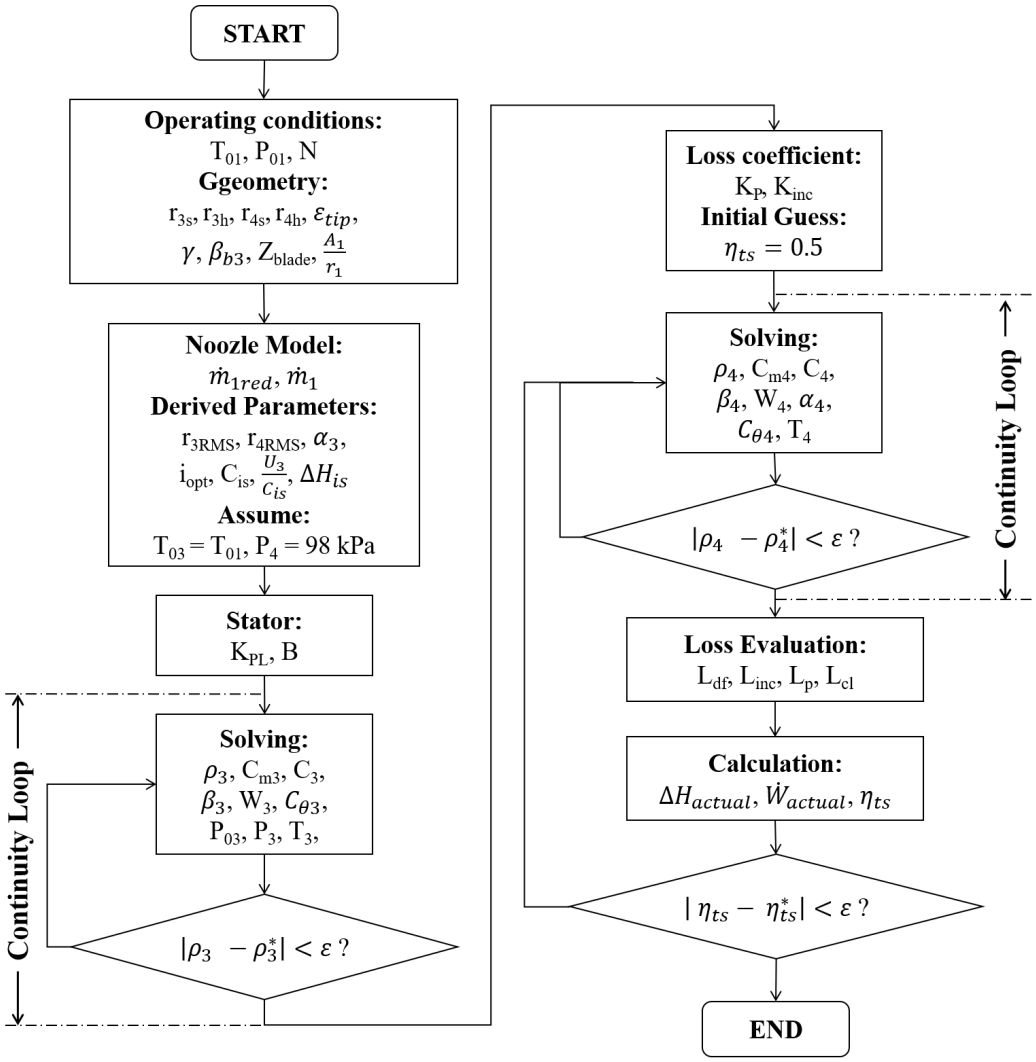

Figure. 4.8 Calculation procedure of mean-line model

employs K_{PL} as a fitting parameter, which is determined by the fitting algorithm. The typical range of K_{PL} can be varied from 0.1 to 0.3 as suggested by Rahbar et al. [153].

The flow angle at the stator exit is important in calculating the incidence losses. Based on CFD studies, Padzillah et al. [11, 88] compared the flow angle between vaned and vaneless turbine at the volute exit and rotor inlet as shown in Fig. 4.9. It shows that the absolute flow angle of a vaneless turbine can be varied more than 40° across the circumference, whereas this variation is less significant for a vaned turbine since the flow mostly follows the shape of vanes. From the analysis of flow fields Padzillah et al. [11], the most non-uniformity of flow

angles came from the tongue region due to the flow recirculation. Besides, when the flow travels from the volute exit to the rotor inlet, the flow angle also changed, making it difficult to estimate the absolute flow angles for a vaneless turbine, which is the case of the study. Instead, the proposed mean-line model treats the rotor inlet flow angle as a fitting parameter, and thereby letting the algorithm to find the mean flow angle that fits better with the data.

The blockage factor B in Eq. 4.39, came from boundary layer growth and secondary flows, having an effect of restricting the air flowing towards the rotor. This typical range of this factor is from 0.05 to 0.15 [110]. For the current mean-line model, the blockage factor of 0.05 was found to fit this turbine. It should be noted that the volute wall is assumed to be adiabatic. Thus, no heat loss is considered along the volute, deriving $T_{01} = T_{03}$.

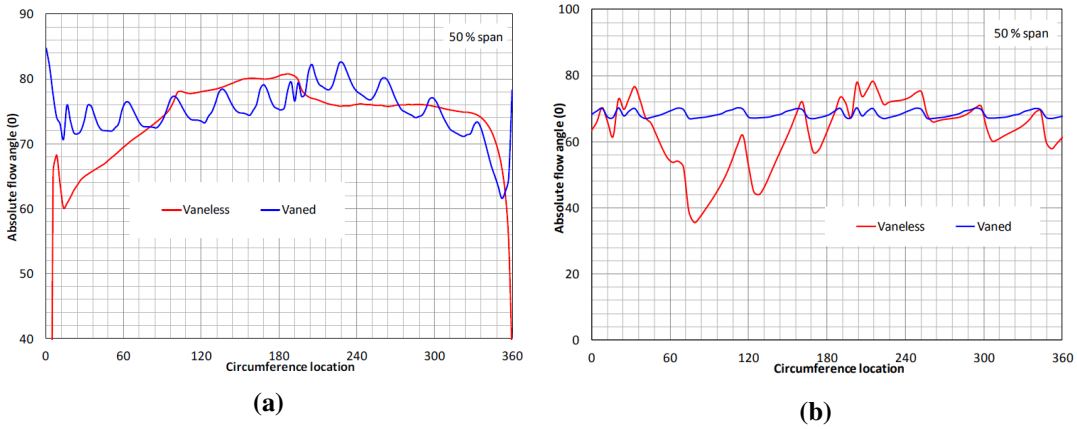

Figure. 4.9 (a) Plot of absolute flow angle at the volute exit during steady state condition, (b) plot of absolute flow angle at the rotor inlet during steady state condition [88]

$$K_{PL} = \frac{P_{01} - P_{03}}{P_{03} - P_3} \tag{4.38}$$

$$\dot{m}_3 = \rho_1 A_1 C_{m1} (1 - B) \tag{4.39}$$

Rotor

In order to calculate the velocity triangles at the mean streamline of the rotor, the root mean square (RMS) averaged radius at the mixed-flow turbine inlet/exit should be first calculated using Eq. 4.40.

$$r_{RMS} = \sqrt{\frac{r_s^2 + r_h^2}{2}} \tag{4.40}$$

The turbine efficiency calculation is based on the actual and isentropic enthalpy change across the stage (as defined in Eq. 4.41). The isentropic enthalpy drop ΔH_{isen} of the stage is calculated by Eq. 4.42 based on the isentropic velocity C_{isen}. As flow passing through the rotor stage, various loss mechanisms will produce entropy generations. Therefore, the actual enthalpy drop ΔH_{actual} of the stage is calculated by subtracting the total losses $\sum L$ from isentropic enthalpy. On the other hand, the actual enthalpy change can also be calculated based on Euler's turbomachinery equation (Eq. 4.37). In this way, the loss mechanisms can be related to the rotor geometry due to velocity triangles, as expressed in Eq. 4.43.

The main difference between the proposed mean-line code and the conventional models [110, 153, 154] is the way that efficiency is calculated. Most researchers used actual enthalpy as a basis to estimate the efficiency, as expressed in Eq. 4.44. However, this would limit the turbine efficiency not bellowing zero since it always results in a positive number. Therefore, the proposed model uses isentropic enthalpy as a basis to calculate the efficiency, and takes into account the fact that losses can exceed the isentropic enthalpy, thereby producing negative efficiency.

$$\eta_t = \frac{\Delta H_{actual}}{\Delta H_{isen}} = \frac{\Delta H_{isen} - \sum L}{\Delta H_{isen}} \tag{4.41}$$

$$\Delta H_{isen} = \frac{C_{isen}^2}{2} \tag{4.42}$$

$$\Delta H_{actual} = \Delta H_{isen} - \sum L = U_3 C_{\theta 3} - U_4 C_{\theta 4} \tag{4.43}$$

$$\eta_t = \frac{\Delta H_{actual}}{\Delta H_{actual} + \sum L} \tag{4.44}$$

Four main losses were assumed to take place in the rotor, namely passage loss, incidence loss, disk friction loss, and clearance loss, which are calculated using empirical equations.

- Passage loss L_P, is a combination of friction and secondary flow effects in the rotor [109, 110, 155]. As expressed in Eq. 4.45, passage loss is expected to be proportional to the meridional kinetic energy at the inlet and exit. K_P is the passage loss coefficient and used for the correlation with experimental data. i_{opt} is the optimum incidence angle that is defined as the angle of approach at which the smallest loss occurs once the flow goes into the rotor. It is calculated based on the Stanitz relation [156] for slip factor, as defined in Eq. 4.46.

$$L_P = K_P \frac{W_3^2 cos\left(|\beta_3 - i_{opt}| + W_4^2\right)}{2} \tag{4.45}$$

$$i_{opt} = tan^{-1}\left(\frac{-1.98 \cdot tan\alpha_3}{Z - 1.98}\right) \tag{4.46}$$

- Incidence loss L_{inc}, refers to any work done in turning the working fluid from its direction of approach to the rotor to the direction determined by the blade passage [157]. Thus, entropy will be generated when the turbine operates at off-design conditions due to the incidence angle away from the optimal condition. This study used a correlation proposed by Futral and Wasserbauer [70], which is based on the kinetic energy loss tangential to the blade, as shown in Eq. 4.47.

$$L_{inc} = K_{inc}\left[W_3 sin(\beta_3 - \beta_{b3} - i_{opt})\right]^2 \tag{4.47}$$

- Disk friction loss L_{df}, is estimated by the frictional loss due to leakage fluid between the rotor and the backplate [73]. It is generally small and also related to the fluid viscosity, as expressed in Eq. 4.48.

$$L_{df} = \frac{0.02125 U_3^2 \rho_3^2 r_3^2}{\dot{m}\left(\frac{\rho_3 U_3 r_{3,h}}{\mu_3}\right)^{0.2}} \tag{4.48}$$

- Clearance loss L_{cl}, is produced clearance gap between the rotor and its shroud. This is primarily associated with the mixing processes taking place between the leakage flow

and mainstream. This study used the empirical correction presented by Japikse et al. [155], which is based on the fraction of leakage flow rate to the mainstream flow rate and multiplied by the fluid kinetic energy. In the leakage flow definition as Eq. 4.49, K_{cl} is the clearance loss coefficient, which is 1.5 as suggested by Japikse et al. [155]. ε_{tip} is the clearance gap, l_r is the length of radial clearance.

$$\dot{m}_{cl} = \frac{1}{2} K_{cl} \rho_3 U_3 \varepsilon_{tip} l_r Z \tag{4.49}$$

$$L_{cl} = \frac{1}{2} \frac{\dot{m}_{cl}}{\dot{m}} U_3^2 \tag{4.50}$$

- Total losses, is the sum of the individual loss within the rotor stage, as per Eq. 4.51.

$$\sum L = L_P + L_{inc} + L_{df} + L_{cl} \tag{4.51}$$

As shown in Fig. 4.8, two continuity loops are employed at rotor inlet and exit to ensure that the mass conservation is satisfied at both stations. The first continuity loop is created due to the fact that the pressure loss will influence the flow density and flow velocity. In return, the flow density and velocity will feedback on the magnitude of pressure losses, causing the fluid properties at the rotor inlet cannot be solved at once. After the estimation of the initial flow density, the iterative flow density can be calculated according to Eq. 4.52-4.57. Here the ideal gas assumption was used in Eq. 4.57. Subscript m refers to the meridional direction, and it is assumed to be radial at the inlet and axial at the outlet for a radial flow turbine. A_3 is the circumferential area at the rotor inlet, as calculated in Eq. 4.58.

$$C_{m3} = \frac{\dot{m}}{\rho_3 A_3} \tag{4.52}$$

$$C_3 = \frac{C_{m3}}{cos\alpha_3} \tag{4.53}$$

$$P_{03} = P_{01} - K_{PL}\frac{\rho_3 C_3^2}{2} \tag{4.54}$$

$$P_3 = P_{03} - \frac{\rho_3 C_3^2}{2} \tag{4.55}$$

$$T_3 = T_{01} - \frac{C_3^2}{2c_p} \tag{4.56}$$

$$\rho_3 = \frac{P_3}{RT_3} \tag{4.57}$$

$$A_3 = 2\pi r_{RMS3} \cdot L_{inducer} \tag{4.58}$$

The second continuity loop is created in a similar reason to the first one, where the density has to be used for velocity calculations at the first place but it is also influenced by the results of flow velocities. The calculation procedure is shown in Eq. 4.59-4.64, and the rotor exit area is estimated by Eq. 4.65. Subscript θ is the tangential component of velocity triangle, referring to Fig. 4.7. In this model, the mass conservation is deemed to be achieved if the density change (the difference between current iteration and previous iteration) is smaller than 1×10^{-6}.

$$C_{m4} = \frac{\dot{m}}{\rho_4 A_4} \tag{4.59}$$

$$\alpha_4 = tan^{-1}\left(\frac{C_{\theta 4}}{C_{m4}}\right) \tag{4.60}$$

$$C_4 = \frac{C_{m4}}{cos\alpha_4} \tag{4.61}$$

$$T_{04} = T_{03}\left\{1 - \eta_t\left[1 - \left(\frac{1}{PR}\right)^{\frac{\gamma-1}{\gamma}}\right]\right\} \tag{4.62}$$

$$T_4 = T_{04} - \frac{C_4^2}{2c_p} \tag{4.63}$$

$$\rho_4 = \frac{P_4}{RT_4} \tag{4.64}$$

$$A_4 = \pi\left(r_{s4}^2 - r_{h4}^2\right) \tag{4.65}$$

Since the enthalpy losses are influenced by the velocity triangles, and the velocity triangles are also as a function of enthalpy losses, which means this process can be solved iteratively. An initial guess of efficiency is first used to estimate the exit velocity triangles, followed by the losses calculation based on velocity triangles. The turbine efficiency for the next iteration is then calculated as per Eq. 4.41. This procedure is repeated until defined convergence criteria are satisfied, where the efficiency residual is less than 1×10^{-7}. However, it is found that the model is difficult to converge, as observed by the large fluctuations of residuals. Therefore, an under-relaxation factor of 0.1 is used as per Eq. 4.66 to stabilize the iteration process, where the subscript * stands for the value of the previous iteration.

$$\eta_t^{iter} = \frac{\Delta H_{isen} - \left[\sum L^* + K_{relax}\left(\sum L - \sum L^*\right)\right]}{\Delta H_{isen}} \tag{4.66}$$

In summary, there are four fitting parameters, namely the rotor inlet absolute flow angle α_3, stator loss coefficient K_{PL}, passage loss coefficient K_P and incidence loss coefficient K_{inc}. These parameters were calibrated against the experimental data. Non-linear least square algorithm was used to minimize the differences between experiment data and model predictions of *each speed-line*.

4.5 Transient Turbocharger Model

Most 0-dimensional turbine models in the commercial 1D gas dynamic code do not allow the user to enter negative efficiency in the map. Therefore, to study the negative efficiency effects on the turbocharger speed prediction, a transient turbocharger model was developed using Simulink. The purpose of this exercise is to quantitatively demonstrate the improvement in predictive capability of unsteady mapping, especially where there are periods of negative efficiency. The results will be demonstrated in Section. 6.5.

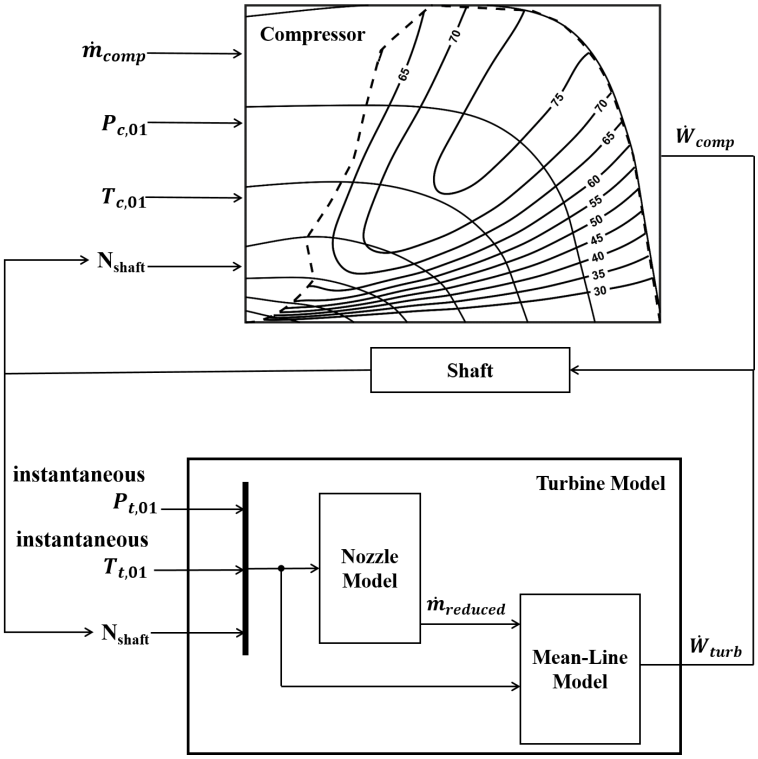

Figure. 4.10 Diagram of Simulink turbocharger model

Fig. 4.10 shows the diagram of the proposed turbocharger model, consisting of a map-based compressor model, a nozzle model, a mean-line model and a shaft model. For the compressor side, inlet boundary conditions include inlet stagnation pressure, inlet stagnation temperature, mass flow and shaft speed, where the first three components are taken from experiment. Compressor performance map, gathered from gas stand test, were used in the model to predict the compressor power, working as look-up tables. To enable the prediction of negative turbine power, the turbine model was developed by integrating the nozzle model to the mean-line model, as discussed in above sections. The instantaneous turbine power can be predicted by imposing instantaneous pressure and temperature measured from experiment at the inlet boundary of turbine. Moreover, both compressor and turbine require shaft speed as an input variable for the power prediction, whilst the turbine/compressor power is also a function of shaft speed. Therefore, the shaft speed is solved iteratively after setting an initial speed, as per Eq. 4.67, similar to the turbo shaft model used in most 1D commercial code.

$$\dot{W}_{shaft} = \dot{W}_t - \dot{W}_c = I \cdot \omega_{shaft} \cdot \frac{d\omega_{shaft}}{dt} \tag{4.67}$$

CHAPTER 5

OPTIMIZATION OF MIXED-FLOW TURBINE

5.1 Introduction

In general, the aim of any optimizations is to minimize an objective function (OF), defined in Eq. 5.1, which is a function containing n design variables X_i and the performance parameters $P(X_i)$. It is common to set constraints to allow these design variables varying between lower and upper bounds. In many applications, it is useful to set linear or non-linear constraints in order to describe the relationship between design variables thereby decreasing the possibility of the creation of faulty designs. The objective function can be any linear combination of differently weighted penalties.

$$\begin{gathered} Min.\ OF = OF(P(X_i),\ X_i) \\ X_i^{lb} \leq X_i \leq X_i^{ub},\ i = 1,2,3,...,n \end{gathered} \tag{5.1}$$

The first part of this chapter will introduce the optimization parameters of a mixed-flow turbine. Thirteen design parameters in total are considered during the optimization process. Six volute design parameters were used to control the aspect ratio, intake area, exit area, and the circumferential distribution of the cross-sectional area. Seven rotor parameters were utilized to modify the cone angle, blade axial location, and the camber-line angle

distribution. The optimization process consists of both unsteady optimization and steady-state optimization. Two different optimization algorithms were used to optimize the turbine, namely the *Genetic Algorithm* and a novel *Kriging Surrogate* based optimization algorithm.

5.2 Optimization Variables of the Mixed Flow Turbine

5.2.1 Rotor Optimization Variables

The turbine to be optimized was a small automotive vaneless mixed-flow turbine designed for a three-cylinder, one-litre spark-ignition engine. The geometric features of the baseline turbine have been discussed in Section. 3.2. Three features were considered for the rotor optimization, namely the blade cone angle γ, blade axial location d_{axial} and blade angle distributions $\phi(m)$ from the leading edge to the trailing edge. The blade thickness was kept unchanged throughout the study since it has a minor influence on secondary flows [118] and it is already thin enough. To avoid the thrust force produced by the new design is significantly different from the baseline, which deviates the existed shaft's thrust balancing between the turbine and compressor, features such as the number of blades, tip diameter, and chord length are kept same as the baseline design.

The rotor geometry was generated using ANSYS-BladeGen. BladeGen is a specialized tool for the rapid 3D design of rotating machinery components, allowing the user to define the blade parameters in either graphical user interface (GUI) mode or batch mode. In order to access the information of the baseline rotor, the first step is to convert the blade CAD file, provided by the manufacture, to the BladeGen readable format. This was achieved by using a built-in function "CAD Import" provided in the ANSYS DesignModeller software. Since the blade parameters need regular updates during the optimization, it is not feasible to use the GUI mode due to the requirement of human intervention. To make it easier to modify the blade parameters and thus implementing optimizations, a code interface has been developed between Matlab and BladeGen. The code interface is able to read the BladeGen batch file,

which contains all the information that can fully define a blade. In the BladeGen batch file, the blade meridional shape, camber angle distributions, and blade thickness distributions are constructed by a series of B-spline points. The Matlab code interface can then read and redefine those B-Spline points in order to modify the shapes of curves. After the update of blade parameters in Matlab, the code interface will first export this data to BladeGen batch format (bgi format), and then convert it into BladeGen data format (bgd format), which is a required format in order to generate the CAD for meshing. To achieve the format conversion from bgi to bgd, an executable tool named "BladeBatch" has been used, which is located in the BladeGen installation directory.

Blade Cone Angle

The cone angle, as shown in Fig. 5.1, is defined in the meridional plane and its magnitude is dependent on the relative position between the hub and shroud at the leading edge. As mentioned earlier, the blade tip radius r_{4s} maintained the same value throughout the optimization. The cone angle is then only dependent on the hub construction point at the leading edge (Point A and B in Fig. 5.1 (a)). In order to have a smooth transition of the hub curve, but not significantly affect the meridional shape at the trailing edge, a fifth-order bezier spline curve was fitted to the hub curve, as shown in Fig. 5.1 (a). By radially moving the point at the leading edge upwards or downwards, the cone angle could be varied whilst keeping the remaining four spline construction points fixed.

Blade Axial Location

The blade axial location d_{axial} is the result of the relative axial movement between the main blade and the inlet block. Unlike a radial flow turbine where the relative blade angle is zero across the leading edge from the hub to the shroud, the inlet blade angle of a mixed-flow turbine is not constant as listed in the Table. 3.2. It follows that the variation of the inlet blade angles of a mixed-flow turbin also causes a variation in the incidence angle from hub to shroud. This, therefore, will influence the work generated according to the Euler

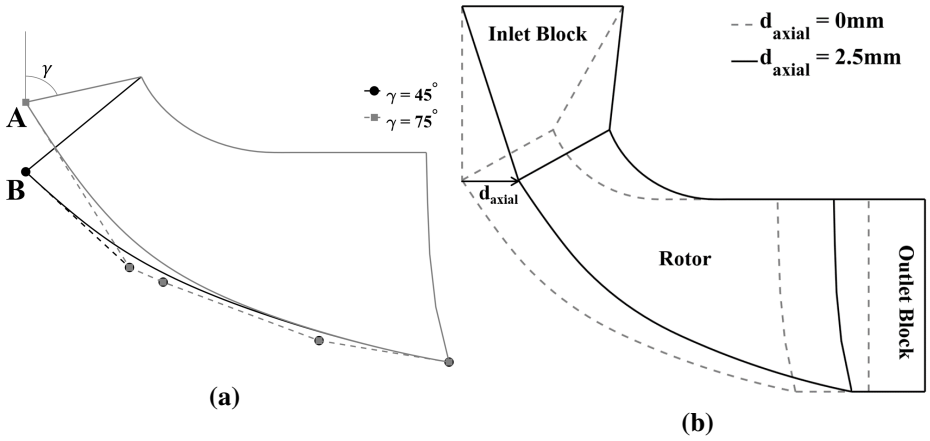

Figure. 5.1 Modification of (a) blade cone angle (b) blade axial location

turbomachinery equation Eq. 4.37. As shown in Fig. 5.1 (b), varying the axial distance d_{axial} has the effect of changing the shape of the *inlet block* - the nozzleless volume linking the volute outlet to the rotor inducer. This volume region plays a key role in guiding the flow at the rotor leading edge thus making it an important parameter to vary when optimizing the geometry. Therefore, it is necessary to include the blade axial location as an optimization parameter since it will influence the leading edge incidence distribution.

Blade Camber-line Angle Distribution

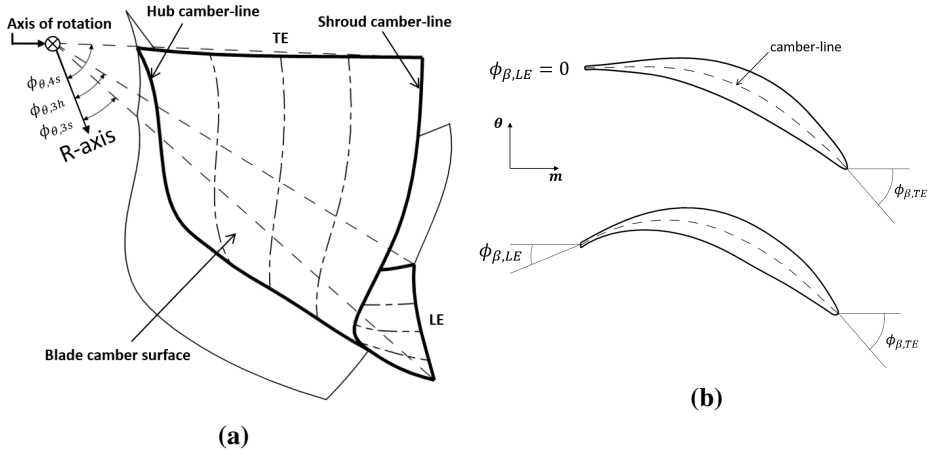

Figure. 5.2 Blade camber angle definition (a) in θ criteria (b) in β criteria

The parametrization of blade angles along the camber-lines from the leading edge (LE) to the trailing edge (TE) has a crucial impact on the blade shape and turbine efficiencies. It

is necessary to create an extensive range of blade shapes with a minimum group of design points. As shown in Fig. 5.3, the blade angle distributions from the LE to TE along the axial direction were defined using the Bezier spline curve with four control points. Blade camber angles ϕ were defined in the θ-distribution rather than β-distribution, since the former one can generate the same blade shape with fewer control points. The θ and β camber-line definition are illustrated in Fig. 5.2 (a) and (b), in which the former, donated as ϕ_θ, defines the camber angle in the radial plane which is perpendicular to the axis of rotation. The magnitude of ϕ_θ is depended on the relative location between the point on the camber-line and a predefined radial-axis, i.e. the inlet blade camber angle on the shroud is shown as $\phi_{\theta,3s}$. On the other hand, the camber angle in β, donated as ϕ_β, defines the relative angle between the tangential vector of the camber-line and the meridional axis. The conversion of camber-line angles from θ to β criteria is obtained according to Eq. 5.2, where r is the radial distance of the point on the blade camber surface to the axis of rotation.

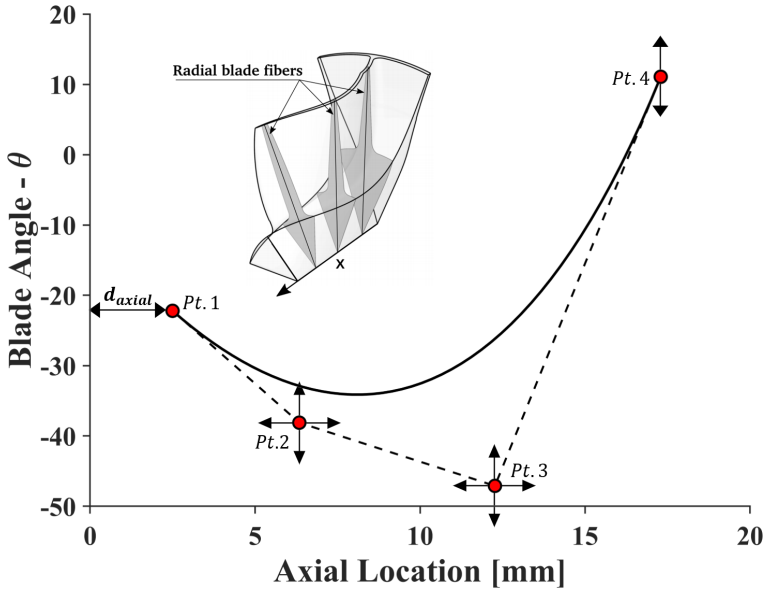

Figure. 5.3 Blade camber angle distribution controlled by four Bezier points

$$\phi_\beta = tan^{-1}\left(r\frac{d\phi_\theta}{dm}\right) \tag{5.2}$$

To avoid the mechanical failure caused by the large centrifugal force induced from the high rotational speed, the turbine rotor blades must have a strict radial fibre requirement. This ensures that the internal stresses along the blade are tensile in nature. Fig. 5.3 shows the radial fibre requirement where whichever way the blade is cut in the radial direction, the pressure side and suction side of the blade is symmetrical with respect to the center line and the center line must intersect with the axis of rotation. In other words, the blade should have a uniform camber angle from the hub to the shroud at a given axial location.

It is also necessary to add blade camber layers (hub to the shroud profiles as shown in Fig. 5.4) to preserve the internal blade curvatures from hub to shroud. Otherwise, if only two layers defined from the hub to the shroud, the blade surface will be formed from a "ruled" profile from the hub to the shroud, resulting in the deterioration of aerodynamic performance. In this study, five blade layers have been used to create the camber-line distribution. As shown in Fig. 5.4, the camber-line angles (in θ criteria) in the five blade layers collapse into a single curve with respect to the axial location, which is not the case as it is defined in the β criteria. Therefore, camber-line angles defined in the θ criteria have the advantage of ensuring the radial fibre requirement, and it also simplifies the blade parametrization process, since all blade layers can be defined in a single curve.

Four Bezier points Pt.1 - Pt.4 was used to define the camber-line distribution. The axial distance between Pt.1 and Pt.4 is set according to blade axial length Z_{blade}, which is fixed throughout the optimization. Due to the parameter d_{axial} included, the first point Pt.1 may not start at 0 mm in the axial direction. The parameter d_{axial} can move these four control points axially without changing the shape of camber-line. The shape of the camber-line curve is

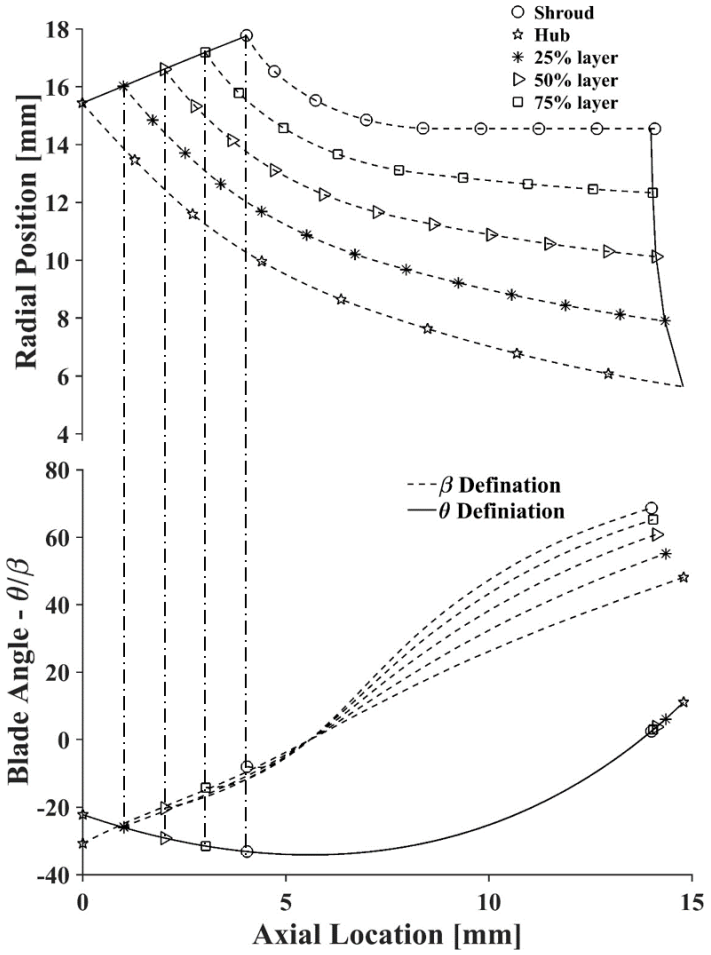

Figure. 5.4 Blade angle definition in θ and β distribution at different layers

depended on the relative movement of Pt.2, Pt.3 and Pt.4. Note that Pt.2 and Pt.3 have two degrees of freedom, whereas Pt.4 only has one in the θ direction. Pt.1 is fixed in its position to prevent the curve moving in the θ direction without changing its distributions, resulting in the same blade but rotated $\Delta\theta$ degree with respect to the axis.

5.2.2 Volute Optimization Variables

The schematic and sectional view of the baseline volute is shown in Fig. 5.5 (a). The shape of cross-sections is based on a circular profile and has the exit on one side. However, the near tongue region was designed differently since the complex fillet features which are difficult to

reproduce faithfully. For the simplification, the volute intake duct was designed as a circular profile. All the volute geometric parameters were calculated in MATLAB, and the CAD was produced in the Ansys Design Modeller. A JavaScript application programme interface was used to enable data communication between the two software.

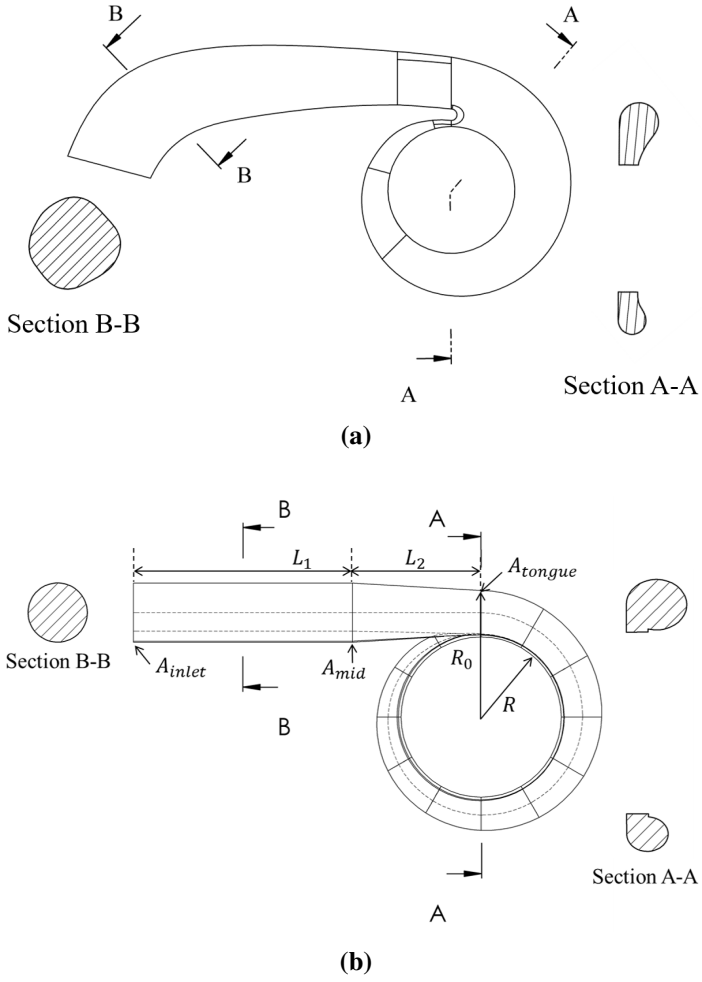

Figure. 5.5 Schematic and sectional view of (a) baseline volute (b) re-designed volute

There are six independent design parameters considered in the volute optimization,

- The tongue to wheel distance of volute, labelled as R in Fig. 5.5 (b). Since the volute exit is connected with the entry of the inlet block, as shown in Fig. 5.1 (b), the radial location of the entry to the inlet block has to be changed according to this parameter.

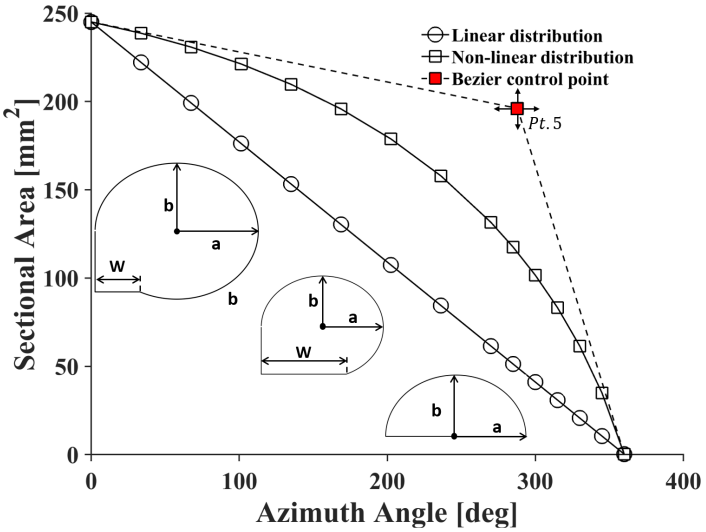

Figure. 5.6 Volute area as a function of azimuth angle

- Elliptical factor K_{ellip} , defined as a/b shown in Fig. 5.6. This parameter enables the cross-sectional profiles to be either elliptical or circle.
- Volute exit width, which is w shown in Fig. 5.6. This parameter together with the volute exit radius defines the volute exit flow area.
- Tongue area factor K_{tongue}. This parameter calculates the tongue area of the volute by multiplying the tongue area of baseline, which is 256 mm^2. In this study, the tongue area refers to the cross-sectional area at zero azimuth as shown in Fig. 5.6.
- The last two independent parameters define the distribution of the volute cross-sectional area with respect to the azimuth angle. As shown in Fig. 5.6, a Bezier spline control point Pt.5 has two degrees of freedom, which can form both linearised and non-linearised distributions.
- Other parameters, such as A_{inlet}, A_{mid}, L_1, and L_2, are treated as depended parameters or constants.

Since the cross-sectional area of the volute can be varied significantly from 0° to 360° azimuth, three different designs of cross-sectional shapes have been considered, shown in Fig. 5.6, but maintained the same elliptical factor and exit width.

5.2.3 Constraints of Optimization Variables

The constraints of turbine optimization variables have to be defined to restrict the turbine size in a reasonable range. The upper and lower bounds of the design variables are listed in Table. 5.1. Note that the relative positions with respect to the baseline's data were used to define Bezier points of Pt.2, Pt.3 and Pt.4. For example, if the $\Delta X_{Pt.2}$ is zero, the axial location of Pt.2 will be the same as baseline. The x and y coordinates of the volute Bezier point Pt.5 was normalised against the axis limits.

Table 5.1 Constraint of optimization parameters

Domain	Parameters	Unit	Lower bounds	Upper bounds
Rotor	γ	$^\circ$	40	90
	d_{axial}	mm	0	3
	$\Delta X_{Pt.2}$	mm	-3	10
	$\Delta\theta_{Pt.2}$	$^\circ$	-25	25
	$\Delta X_{Pt.3}$	mm	-8	5
	$\Delta\theta_{Pt.3}$	$^\circ$	-25	25
	$\Delta\theta_{Pt.4}$	$^\circ$	-25	25
Volute	K_{ellip}	-	0.6	1.8
	K_{tongue}	-	0.5	2.5
	w	mm	5	8
	R	mm	22.5	55
	$Pt.5X$	normalised	0	1
	$Pt.5Y$	normalised	0	1

In addition, linear constraints are applied to rotor design variables to ensure the Bezier points of camber-line are allocated in an appropriate sequence. For instance, the Pt.1 is located at the left-hand side of Pt.2 and its axial distance is greater than 2 mm. The Pt.2 is constrained to the left-hand side of Pt.3 and its axial distance is greater than 3 mm. Lastly, the Pt.3 is sited on the left-hand side of Pt.4. These constraints can be written in a matrix format, as defined in Eq. 5.3, where the superscript $*$ represents the value of the baseline. The reason for doing this is to, first, reduce incidences of an invalid camber-line and secondly, to avoid the axial distance between Pt.2 and Pt.3 being too close to each other such that the diversity of the camber-line distributions is reduced according to the Bezier spline definition.

In order to make sure a smooth transition of the blade angle from the leading edge to the trailing edge and thereby reducing the generation of failure blade, the non-linear constraint was also applied to the rotor design variables. This was achieved by evaluating if the first-order derivative of the camber-line curve is monotonously increasing.

$$\begin{bmatrix} -1 & 0 \\ 1 & -1 \\ 0 & 1 \end{bmatrix} \times \begin{bmatrix} \Delta X_{Pt.2} \\ \Delta X_{Pt.3} \end{bmatrix} < \begin{bmatrix} -X^*_{Pt.1} + X^*_{Pt.2} - 2 \\ -X^*_{Pt.2} + X^*_{Pt.3} - 3 \\ -X^*_{Pt.3} + X^*_{Pt.4} \end{bmatrix} \tag{5.3}$$

5.3 Optimization Methodology

The optimization algorithm and the flow conditions are summarized in Table. 5.2. The optimization study consists of two different optimization algorithm, namely the genetic algorithm (GA) and a kriging surrogate (KS) based optimization algorithm, and are conducted under both steady flow and unsteady flow conditions. The rotor was optimized under both steady and unsteady conditions using GA. The whole turbine, including both volute and rotor, was optimized by both GA and surrogate model. There are two reasons for using two different algorithms for the same objective function. First is to test if the global optimal was achieved and the second is to investigate which method is more effective in the application of turbine optimizations.

Table 5.2 Summary of optimization algorithm and flow conditions

Condition / Algorithm	Unsteady	Steady
GA	Rotor	Rotor Rotor+Volute
Surrogate Model	-	Rotor+Volute

5.3.1 Optimization by Genetic Algorithm

GA refers to an adaptive heuristic search algorithm that is well suited to solving non-linear optimization problems, and in most cases, they can find the global optimum solution with a higher probability. This algorithm reflects the process of natural selection where the fittest individuals are selected for reproduction in order to produce better offspring of the next generation.

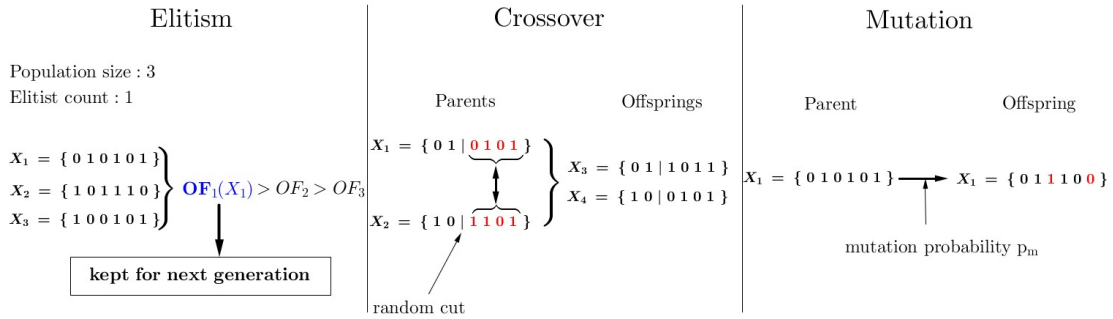

Figure. 5.7 Principles behind (a) Elitist Selection, (b) Crossover and (c) Mutation

There are five phases considered in a GA:

1. Initial Population, GA begins with creating a set of individuals which is called a Population. Each individual is an array that includes all design parameters. One can either define each individual of the initial population manually, or let the GA create stochastic individuals automatically which covers the design space as much as possible in order to reduce the possibility to get trapped in a local minimum. In each individual, the design parameters of that are encoded in a binary string format, where each binary bit is known as a gene, and the entire binary string is known as a chromosome. For this specific optimization, the population size was set as twice of the design variables, similar to compressor blade carried optimization carried out by Tüchler et al. [123]. It means 14 individuals were evaluated by a fitness function (Ansys CFX solver in this case) in one generation during the rotor optimization. This number is 26 in the case of whole turbine optimization.

2. Fitness Scaling. GA first evaluates the raw fitness values of individuals in one generation, and then scales to values in a range that is suitable for the selection function.
3. Selection. two pairs of individuals (parents) are selected by a selection function for producing offspring. Individuals with high scaled fitness have more chance to be selected for reproduction. The default stochastic uniform technique was used for the selection of parents.
4. Reproduction. reproduction options specify how the genetic algorithm creates children for the next generation. This phase employs three methods, demonstrated in Fig. 5.7 and described as follows:
    - Elitism Concept. The individuals, who have the best fitness values, are guaranteed to survive to the next generation without any change. This will ensure that the offspring fitness value will not become worse. This optimization set elitist count as 1, means that the best individual is survived.
    - Crossover. Two parents, who are selected in the previous step, exchange their genes by a crossover function to generate individuals of next generation. Crossover fraction specifies the fraction of the next generation, other than elite children, that are produced by crossover. This optimization utilized 0.7 as the crossover fraction so the remaining children are produced via mutation.
    - Mutation. Some of the parents' genes can be subjected to a mutation with a low random probability, implying some of the bits in the binary string switched from 0 to 1. To avoid that the mutation created children are too far away from its parents, adaptive feasible mutation method was used, where a reasonable step and length size are defined that comply with parameter constraints.
5. Termination. GA is subject to termination if one of the stopping criteria is met,
    - Reached the maximum generations.

- Average relative change in the best fitness function value over stall generations is less than or equal to function tolerance.

5.3.2 Optimization by Surrogate Model

Model Definition

Surrogate modelling approaches refer to a group of techniques that utilize the previously obtained data in order to build surrogate models, which is able to predict the performance of untried points in the design space. The Kriging method was originally proposed by Krige [158] in the aspect of geostatistics. The computational expensive function $P(\mathbf{x})$, which is the CFD solver for this case, is replaced by the sum of two other computational efficient functions, as per Eq. 5.4. The first component $\mu(\mathbf{x})$ is a deterministic function (usually polynomial) that approximates the mean trend of the output. The second component $Z(\mathbf{x})$ is a function that describes the approximation error.

$$P(\mathbf{x}) = \mu(\mathbf{x}) + Z(\mathbf{x}) \tag{5.4}$$

The deterministic function is defined by a linear combination of p basis functions $f(\mathbf{x}) = [f_1(\mathbf{x}), f_2(\mathbf{x}), ..., f_p(\mathbf{x})]$ and p regression coefficient $\beta = [\beta_1, \beta_2, ..., \beta_p]$. The regression model of Eq. 5.5 can approximate any arbitrary mention with high accuracy.

$$\mu(\mathbf{x}) = \sum_{j=1}^{p} \beta_j f_j(\mathbf{x}) \tag{5.5}$$

The simplest regression model is given by the first-order polynomial of Eq. 5.6, where the total number of regression coefficient is $p = n + 1$.

$$\mu(\mathbf{x}) = \beta_0 + \sum_{i=1}^{n} \beta_i x_i \tag{5.6}$$

The regression model in the second-order polynomial form is given by Eq. 5.7, and the total number of regression coefficients is $p = (n+1)(n+2)/2$.

$$\mu(\mathbf{x}) = \beta_0 + \sum_{i=1}^{n} \beta_i x_i + \sum_{i=1}^{n} \sum_{j=1}^{n} \beta_{ij} x_i x_j \tag{5.7}$$

These regression coefficients can be determined by minimizing the sum of squared error between the regression model and the true function value $y = P(\mathbf{x})$, using least-square methods. The deviation function $Z(\mathbf{x})$ interpolates the errors between the regression model and the true function, which is a stationary Gaussian process that has mean zero, constant variance σ^2, and non-zero covariance [159, 160].

$$Var\left[Z(\mathbf{x})\right] = \sigma^2 \tag{5.8}$$

$$Cov\left[Z(\mathbf{x}), Z(\mathbf{x}')\right] = \sigma^2 R(\mathbf{x}, \mathbf{x}') \tag{5.9}$$

$$d_i = |\mathbf{x_i} - \mathbf{x_i}'| \tag{5.10}$$

where x and x' are two arbitrary locations in the design space. $R(x,x')$ is referred to a correlation function, where its value is inversely correlated to the spatial distance of corresponding points. $R(x,x') = 1$ when the distance d_i is zero, whilst $R(x,x') = 0$ when the distance is infinity [161]. The most widely used correlation function is the anisotropic Gaussian correlation function [160],

$$R(\theta, \mathbf{x}, \mathbf{x}') = \prod_{i=1}^{n} exp(-\theta_i d_i^2) \tag{5.11}$$

where $\theta = [\theta_1, \theta_2, ...\theta_n]$ is a vector of parameters that define the inverse of the correlation length in each direction. Thus, the Kriging surrogate model can estimate the complex function by finding the appropriate regression coefficients and correlation parameters. This study utilized a MATLAB Kriging toolbox DACE [162] to define the surrogate model with the second-order regression and Gaussian correlation method used.

Global Search Method

To avoid the optimization that is trapped in the local minimal point, this study utilized a global search method with special search pattern. Prior to the optimization process, an initial surrogate model should be fitted with a series of independent variables $\mathbf{X}$, and the corresponding dependent variables $\mathbf{Y}$, as defined in Eq. 5.12 that includes k design candidates. In this study, the independent variables are the optimization parameters, and the dependent variable is the turbine efficiency. The initial design candidates $\mathbf{X}$ can be created by Latin Hypercube Sampling or other sampling techniques. Then, each design parameter is normalized to the same range between 0 to 1 in order to reduce the chances of getting stuck in local optima.

$$
\begin{aligned}
\mathbf{Y} &= F(\mathbf{X}) \\
\begin{bmatrix} y_1 \\ y_2 \\ \vdots \\ y_k \end{bmatrix} &= F\left(\begin{bmatrix} \mathbf{x_1} \\ \mathbf{x_2} \\ \vdots \\ \mathbf{x_k} \end{bmatrix}\right) \\
\begin{bmatrix} y_1 \\ y_2 \\ \vdots \\ y_k \end{bmatrix} &= F\left(\begin{bmatrix} x_{11}, x_{12}, \cdots, x_{1n} \\ x_{21}, x_{22}, \cdots, x_{2n} \\ \vdots \\ x_{k1}, x_{k2}, \cdots, x_{kn} \end{bmatrix}\right)
\end{aligned}
\tag{5.12}
$$

This is followed by calculating the minimal distance d_i between a specific design candidate $\mathbf{x_i}$ to the rest candidates $\mathbf{x_j}$. This process is repeated for evaluation of the minimal distance of all candidate $\mathbf{x_i}, i = 1,2,...k$, where a vector of distance $\mathbf{d}$ is produced. Here, the global search radius r_g is defined as the maximum value in the distance vector, $r_g = Max\ \mathbf{d}$. The local search radius is defined as $r_l = \psi r_g$, where ψ can scale the global search radius in order to vary the search region.

$$
\begin{aligned}
d_i &= Min.|\mathbf{x_i} - \mathbf{x_j}| \\
for j &= [1,2,...n],\ j \neq i
\end{aligned}
\tag{5.13}
$$

Fig. 5.8 shows an example of a two-dimensional design space, demonstrating the effects of the local search radius. It is observed that a circular region with a radius of r_l is created and encloses each previous obtained design candidate, which corresponds to the center of each

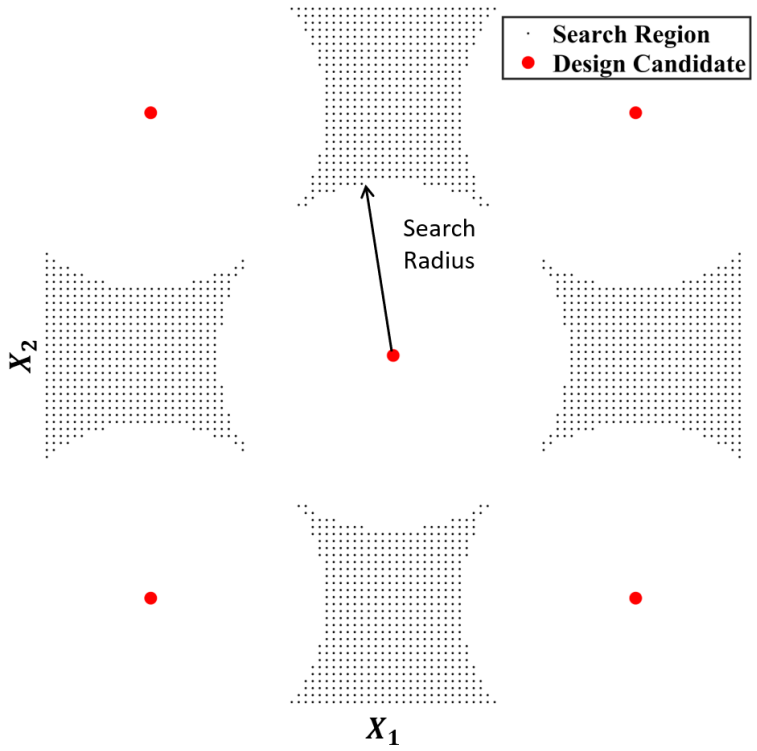

Figure. 5.8 An example shows search region and search radius in 2D

circle. The hatched area is the region that excludes the circular area, namely the search region (Ω). This can be regarded as a non-linear constraint, which limits the new design candidate $\mathbf{x_{new}}$ to be only varied within Ω, as per Eq. 5.14. The new design candidate is produced by searching the optimal point in the Ω, and this is achieved by using the *GlobalSeach* method in the MATLAB global optimization toolbox. For consecutive iterations, the scaling factor ψ is varied accordingly in a specific pattern, in order to ensure all the possible optimal locations to be evaluated. In this study, the pattern is set as $\psi = [0.5, 0.25, 0.1, 0.05, 0.02, 0]$. Note that $\psi = 0$ implies the *GlobalSeach* is conducted in the entire design space.

$$
\begin{aligned}
d &= Min|\mathbf{x_{new}} - \mathbf{x_i}|, \ for\ i = 1, 2..., k \\
d &\geq \psi r_g
\end{aligned}
\tag{5.14}
$$

The new design candidate found by the surrogate model is then examined by the CFD model. Therefore, the size of the design matrix **X** is incremented by one, and followed by re-fitting the Kriging surrogate model and so on. This process is repeated iteratively until met the stop criteria, i.e. the max number of iteration and function residual. Fig. 5.9 shows the diagram of the optimization procedure based on the Kriging surrogate model.

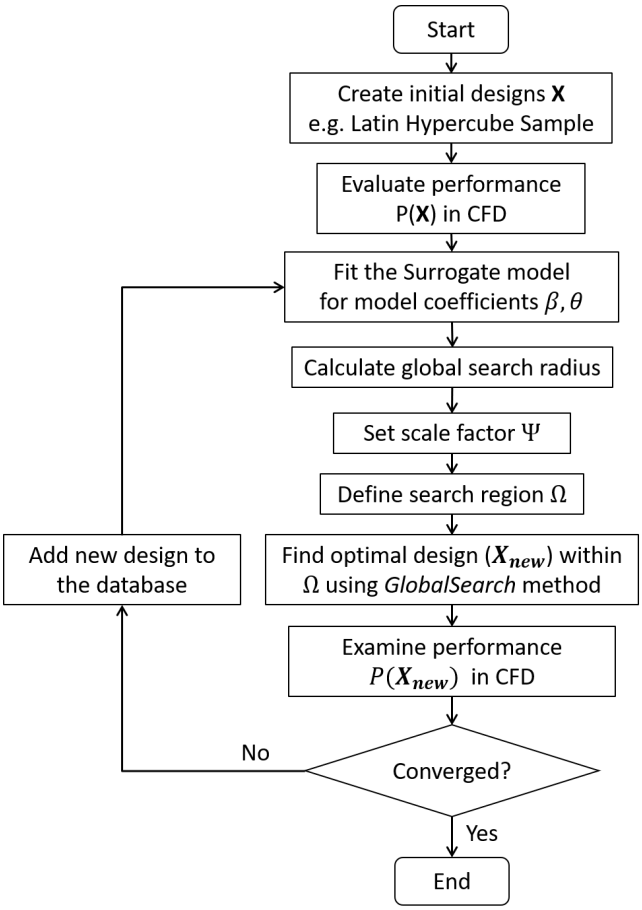

Figure. 5.9 Optimization procedure based on Kriging surrogate model

Model Validation

To gain confidence that the Kriging model together with the proposed searching method is capable of optimizing a complex objective function. The Rasterigin function Eq. 5.15, was used to test the effectiveness of the model, where d is the number of dimensions and $x_i \in [-5\ 5]$. Fig. 5.10 shows the Rasterigin function in its 2-dimensional form, which contains

a large number of local minima, but the locations of the minima are regularly distributed. This function has one global minimum, which is zero at the origin. As suggested by Mühlenbein et al. [163], finding the global minimum of Rasterigin function is a fairly difficult process since it is easily for the optimization model to be trapped in the local minima.

$$f(x) = 10d + \sum_{i=1}^{d} \left[x_i^2 - 10cos(2\pi x_i) \right] \tag{5.15}$$

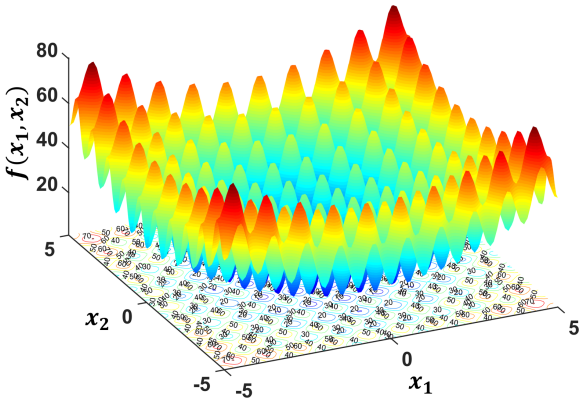

Figure. 5.10 Rasterigin function in the 2-dimensional form

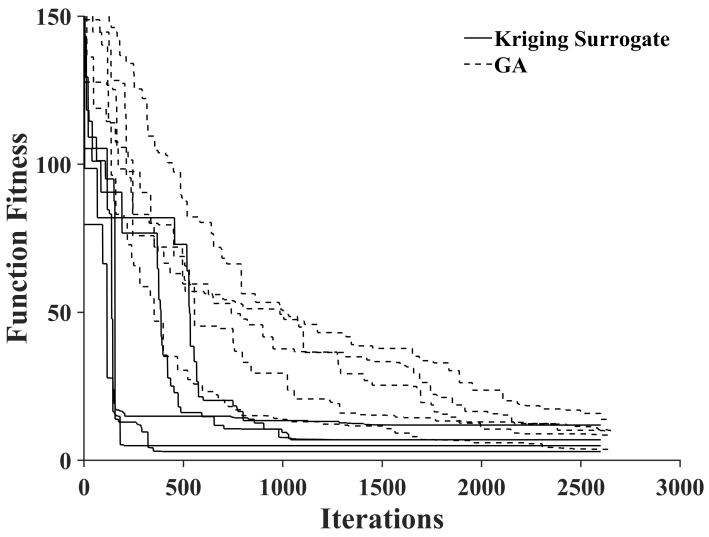

Figure. 5.11 Comparison between the Kriging based optimization algorithm and GA, tested by the 13-dimensional Rasterigin function

The proposed optimization algorithm was compared with the conventional GA, and each algorithm was evaluated five times. Since the number of turbine optimization parameters is 13, a 13-dimensional Rasterigin function was used to test the performance of the model. The number of function evaluations (iterations) is limited by 200 times of the function dimensions ($MaxIter = 200d$). Fig. 5.11 shows the comparisons in which the best function fitness was plotted against the number of function evaluations. The model's performance evaluated by Rasterigin function from 2-dimension to 12-dimension is presented in the Fig. 5.12. It is shown the proposed optimization algorithm can approach the global minima at a much higher rate than GA. Based on all the results regarding the model's performances, it can be summarised that a generally good result can be achieved when the number of iteration reaches approximately 60 times the problem dimensions $Iter \approx 60d$.

5.3.3 Unsteady Flow Optimization

The unsteady optimization study attempts to fill the gap that no literature sought to optimize the turbine blade design whilst explicitly taking into account full range conditions during an exhaust pulse. Particular attention has been paid to ensure that the swallowing capacity characteristic of optimized turbine is maintained to be the same as the baseline. If the turbine swallowing capacity characteristic is changed, this may affect the match between turbocharger and engine. For instance, for a specific 4-stroke engine, the averaged exhaust flow rate during an engine cycle is fixed at certain engine speed. Thus, if the turbine swallowing capacity has been changed significantly as a result of the optimization, the back-pressure on the engine will change, likely leading to a different boost requirement. Therefore, ideally an optimized turbine design should be more efficient than the baseline, but still maintain the same engine match by ensuring the swallowing capability is maintained.

The pulse frequency of 50 Hz was selected for the unsteady optimization, corresponding to a three-cylinder engine with a rotational speed of 2000 rpm. The choice of this particular pulse frequency is to simulate a condition that represents one of the more common conditions

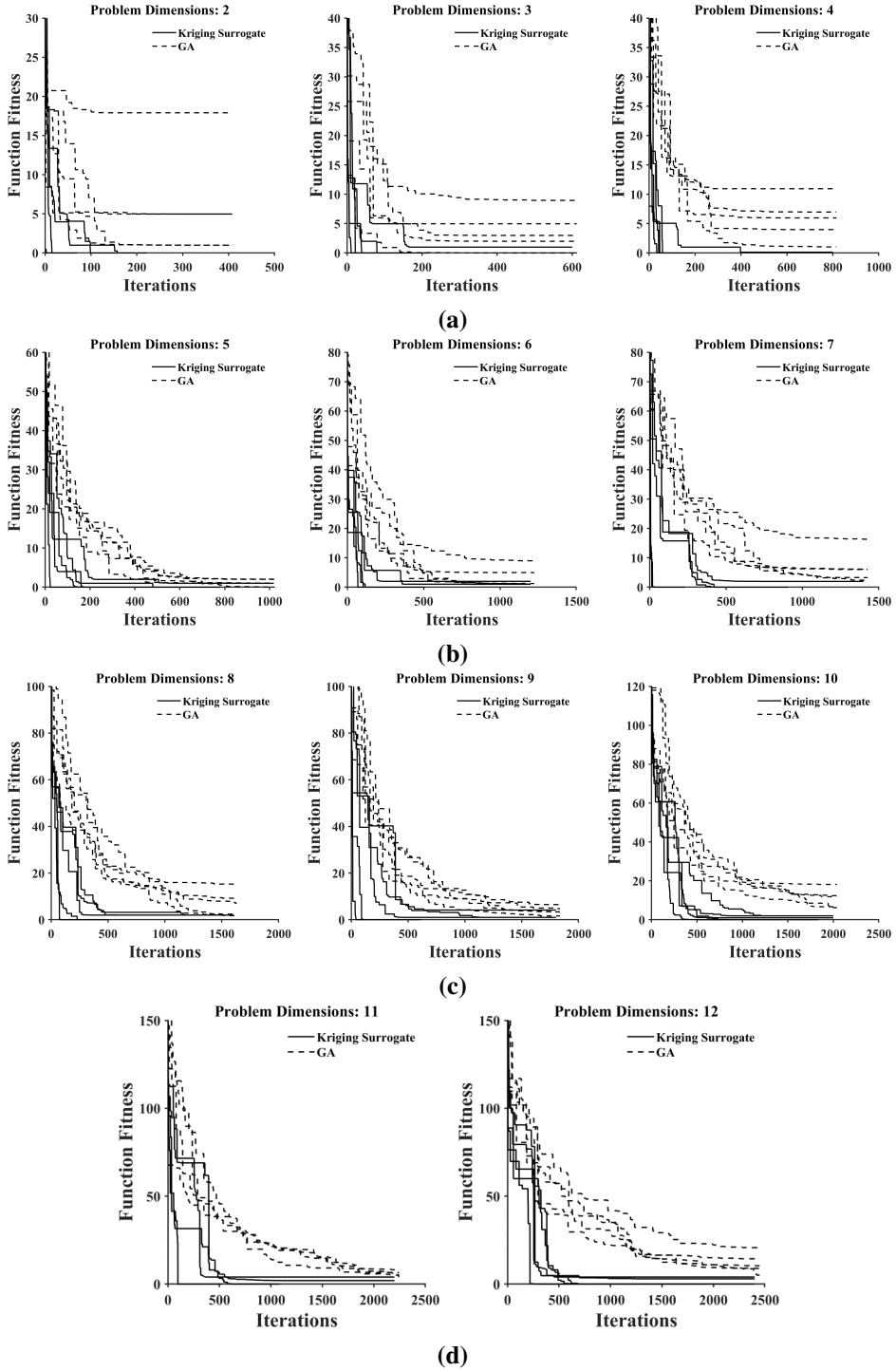

Figure. 5.12 The comparison between KS and GA for different function dimensions

for road vehicles. The objective of the unsteady optimization is to improve both the *rotor efficiency* (Eq. 5.17) and *energy output* (Eq. 7.10) during a pulse. Since the volute geometry

is not been modified during the unsteady optimization process, the unsteady performance parameters were only evaluated for the rotor stage only. The instantaneous shaft power was calculated by multiplying the blade torque with respect to the axis by the rotational speed, defined in Eq. 5.18. The instantaneous turbine isentropic power was modified for the rotor stage, as per Eq. 5.19. To represent the mean efficiency during a pulse, the instantaneous efficiency was energy weighted by including the isentropic power, as per Eq. 5.17. As suggested by [31, 46, 164], compared with arithmetic averaged efficiency, the energy-weighted efficiency affords better comparison to the steady-state results and correctly measures the energy conservation of the turbine, which will otherwise underestimate the isentropic power available in the pulse. Thus, due to the influence of this weighting the efficiency near the peak power region will dominate the final result. During the trough of the pulse, the influence of the instantaneous efficiency on the energy-weighted efficiency is not significant to the design of the turbine wheel due to its low flow energy. Therefore, in order to reduce the simulation time further, but without losing important performance data during a pulse, this study focuses on the region that covers 80% of the power of a pulse and thus, the turbine performance data was only analyzed for that period, as shown in Fig. 5.13. This period occupies approximately 55.6% of one pulse period.

Note that the efficiency was only calculated for the rotor stage, where the flow parameters were taken from the rotor inlet instead of turbine inlet. That is because there is a time delay for the flow to translate from the volute inlet to the rotor [1, 31]. Normally, it is required to apply the phase-shift method to align the flow parameters that have the same time frame of the torque so as to calculate the turbine instantaneous efficiency. However, the phase-shift method is debatable and will introduce additional uncertainties. Since all the designs have the same volute design and same boundary conditions, the loss generated across volute was assumed to be similar. Therefore, for the simplification, the flow parameters were taken from the rotor inlet, which has the minimum time delays and reduces the need for phase-shift.

$$W_r = \int_0^{TT} \dot{W}_r(t)_{actual} dt \tag{5.16}$$

$$\overline{\eta}_{r\,energy\ weighted} = \frac{\int_0^{TT} \left[\eta_r(t) \times \dot{W}_r(t)_{isen}\right] dt}{\int_0^{TT} \dot{W}_r(t)_{isen} dt} \tag{5.17}$$

$$\dot{W}_r(t)_{actual} = \tau(t)\frac{2\pi N}{60} \tag{5.18}$$

$$\dot{W}_r(t)_{isen} = \dot{m}_3(t) c_p T_{0,3}(t) \left[1 - \left(\frac{P_4(t)}{P_{0,3}(t)}\right)^{\frac{\gamma-1}{\gamma}}\right] \tag{5.19}$$

$$\eta_r(t) = \frac{\dot{W}_r(t)_{actual}}{\dot{W}_r(t)_{isen}} \tag{5.20}$$

In order to initialize the transient simulation, it is necessary to set the initial flow field using a steady-state solution with the same boundary conditions. However, this will not represent the correct flow field since the solution is non-quasi-steady. Fig. 5.14 compares the pressure at the volute inlet and rotor inlet when using the initial condition from the steady-state run. It shows that a finite amount of time is required for translating the flow field from

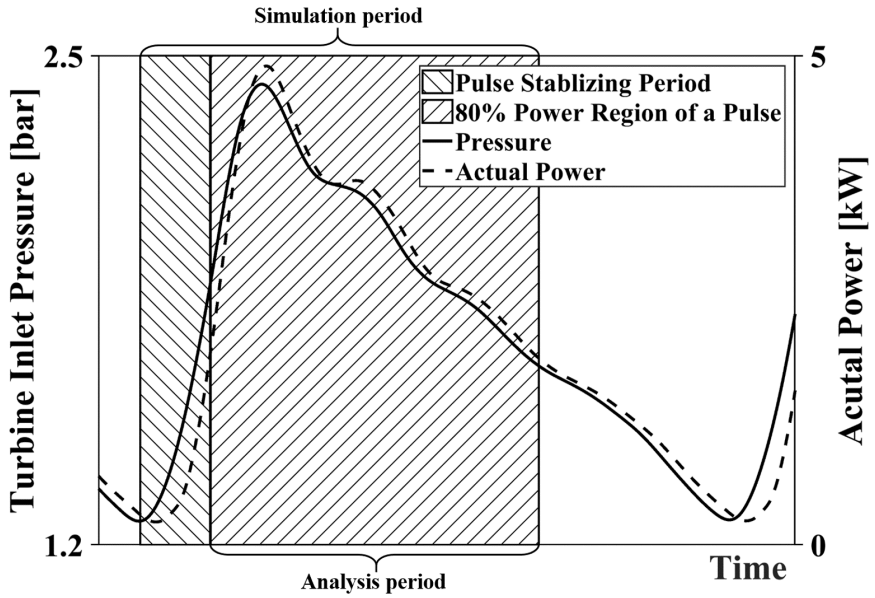

Figure. 5.13 Period of simulation

steady-state to the unsteady solution, where the pressure pulse gradient has developed. At the beginning of the simulation, although the pressure is increasing at the volute inlet, it remains constant at the rotor inlet, causing the rotor isentropic power to remain constant. Therefore, to address this problem, as shown in Fig. 5.13, extra time was given prior to the analysis period, referred to here as the pulse stabilizing period. To reduce the time required to stabilize, the simulation starts at the end of the trough of a pulse where the pressure distribution across the stage is more likely to be closer to steady-state. The overall simulation period including the pulse stabilizing and the analysis period, which is corresponding to 67% of one pulse. Therefore, compared to modelling the entirety of the pulse, approximately 4 hours per unsteady simulation was saved by using this method. This represents a significant savings overall time of the optimization.

The CFD set-up of the unsteady simulation has been discussed in Section. 4.3. The flowchart of the transient optimization of the turbine blade performed in this study is shown in Fig. 5.15. A standard elitist genetic algorithm was implemented in Matlab. The initial population was created in a way that the individuals are randomly and evenly distributed within the

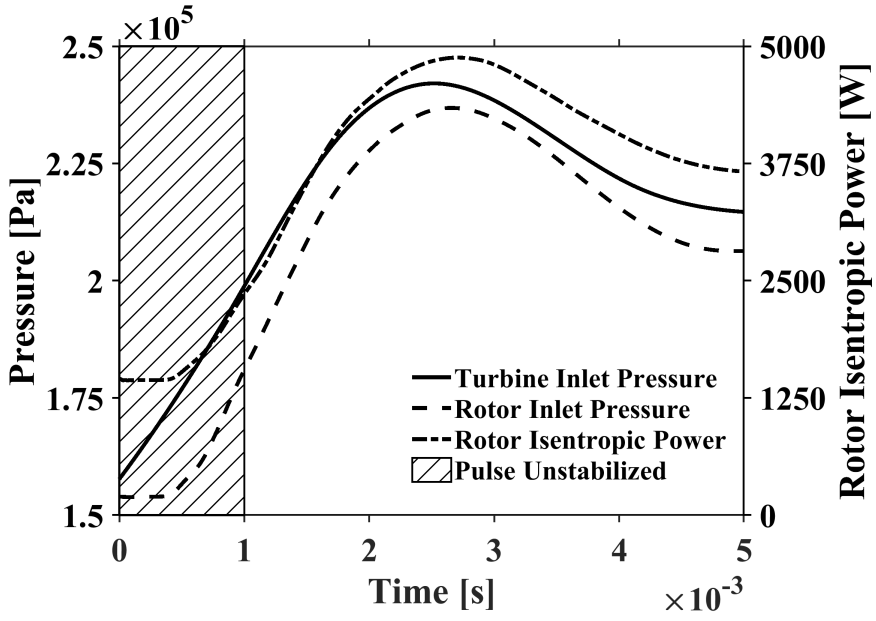

Figure. 5.14 Pulse unstabilized period using initial condition from steady-state run

design space, except for the baseline design point, which is required to be included in the initial population in order to generate comparable results.

Prior to the simulation, a checking algorithm will examine if the design satisfies all the linear or non-linear constraints. If the design requirement is not met, a large penalty will be assigned to this candidate, where the turbine performance parameters $P(X_i)$ are equivalent to 60% of the baseline design - that is $0.6 \cdot P(X_{baseline})$. Since there is at least one candidate having exact same design variables X_i as one in the previous generation, it is unnecessary to rerun the simulation. If the current design point is found to be a repeat one, the algorithm will apply the same results and skip the simulation so as to save time.

A steady-state simulation was then performed to evaluate the swallowing capacity of the current candidate. If the difference of the mass flow parameter between the new design and the baseline design is within $\pm 5\%$, this candidate can be carried over to the unsteady simulation. It should be noted that three operating points were checked during the steady-state run, corresponding to the turbine pressure ratio of 4.1, 3.27, and 2.33. If any of these

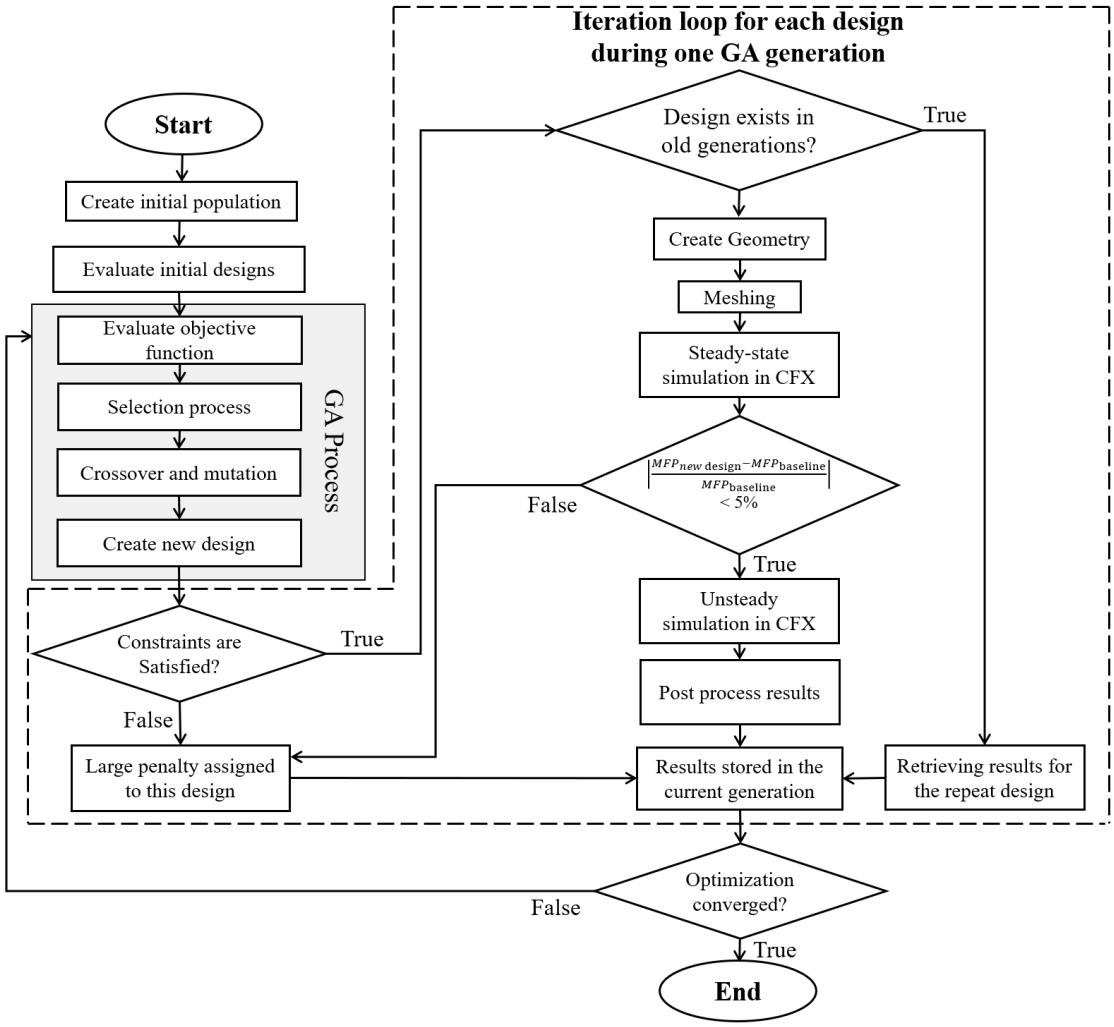

Figure. 5.15 Diagram of optimization by GA

points exceeds the limit, another penalty rule, as per Eq. 5.21, will be executive for this candidate, where $\eta(X_i)$ is the efficiency obtained via CFD simulation for the design candidate X_i. Parameter κ is introduced in Eq. 5.21, indicating that the larger the deviation in turbine swallowing capacity compared to the baseline, the greater penalty will be applied in the algorithm. This will ensure the optimized blade maintains a similar engine match as the baseline.

If the candidate satisfied all design constraints, it will move to the transient optimization subjected to 50 Hz pulsating flows. The unsteady simulations terminate when either the

maximum number of generations (here set at 20) is reached, or the weighted average relative change between two following generations in the spread of the Pareto solutions is less than function tolerance 10^{-2}.

$$P(\mathbf{x}) = \begin{cases} \eta(\mathbf{x}),\ if \kappa <= 5\% \\ (0.6-\kappa)\cdot\eta(\mathbf{x}),\ if \kappa > 5\% \end{cases}$$
$$where\ \kappa = \frac{\mid MFP(\mathbf{x}) - MFP_{baseline} \mid}{MFP_{baseline}}$$
$$\mathbf{x} = [x_1, x_2, \cdots, x_n] \tag{5.21}$$

5.3.4 Steady Flow Optimization

This study has been carried out the steady flow optimizations in three times for different purposes as indicated in Table. 5.2.

- For the comparison between the unsteady optimization method and the single point optimization method. Seeing that the transient optimization over a pulse conducted using vicious, turbulent CFD solver requires enormous computational resources, it is also of interest to compare the performance of a steady-state, single-point optimized turbine with the unsteady optimized turbine. The steady-state optimization was carried only focusing on maximizing the efficiency at the peak of the pulse since this is where the maximum available energy exists for an instance in time. The steady-state optimization algorithm is similar to Fig. 5.15, including the mass flow constraint, except that the unsteady simulation is replaced with a single simulation with boundary conditions representing peak pressure. The population size of the steady-state optimization is also set as twice as the design variables. The stopping criteria is specified as soon

as optimization reaches the 100 generations or the function tolerance is smaller than 10^{-3}.

- For the comparison between the standard GA and Kriging surrogate based optimization algorithm. This was carried out for the optimization of the entire turbine, including both the volute and rotor. The performance of the two algorithms was compared for the same number of function evaluations, which is 750. The total number of optimization parameters is 13, where 7 parameters for defining the geometric features of the blade, and 6 for the volute, aiming at improving the turbine efficiency for a single operating condition corresponding to the peak of the pulse (inlet total pressure of 2.42 bar). The penalty function that was used in the unsteady simulations (Eq. 5.21) was modified in this steady optimization. The steady-sate penalty function ensures that the swallowing capacity characteristic of optimized turbine has the maximum difference of $\pm 2.5\%$ at the design point.

$$P(\mathbf{x}) = \begin{cases} \eta(\mathbf{x}),\ if\, \kappa <= 2.5\% \\ (0.5 - \kappa) \cdot \eta(\mathbf{x}),\ if\, \kappa > 2.5\% \end{cases} \tag{5.22}$$

CHAPTER 6

DYNAMIC MAPPING - EXPERIMENT RESULTS AND ANALYSIS

6.1 Introduction

This chapter will present both steady and unsteady turbine performance results that were gathered from the turbocharger test facility at the University of Bath. It should be noted that all the experimental data are supposed to be encountered with uncertainties due to the accuracy of the instruments, as mentioned in the steady-state measurement instruments of Section. 3.4 and unsteady measurement instruments of Section. 3.5. A detailed discussion regarding the uncertainties during the measurement can be found in the PhD thesis by Tomasz [133], who utilized the same turbocharger test facility and instrumentations.

The first part of this chapter shows the validation process that utilizes the proposed nozzle model and mean-line model to extrapolate the steady-state performance data. Subsequently, the extrapolation method was applied for the unsteady performance data so as to create the equivalent unsteady turbine performance maps. In this way, the negative efficiency, which was captured in the experiment, can be involved in the unsteady turbine maps. The unsteady performance maps were then utilized in the proposed transient turbocharger model, as discussed in Section. 4.5, to investigate the effects of negative turbine efficiency on the turbocharger performance.

6.2 Validation of Turbine Extrapolation Methods

6.2.1 Nozzle Model Performance

In order to ensure the model viability, the proposed nozzle model and mean-line model as discussed in Section. 4.4 is firstly tested against the steady-state experimental data. Fig. 6.1 (a) shows the result of the extrapolated steady-state swallowing capacity map using the nozzle based turbine model, where the scatter data points are the experimental results and the solid lines are the model extrapolations. Despite the data of the lowest speed-line (42%), the proposed model showed a good extrapolation quality, where the extrapolation errors were mostly smaller than $\pm 2\%$, as shown in Fig. 6.1 (b). The fitting coefficients, as specified in Eq. 4.30-4.36, of the nozzle model is listed in Table. 6.1. In order to obtain these fitting coefficients, trust-region least square algorithm was used for minimizing the differences between experimental results and model predictions.

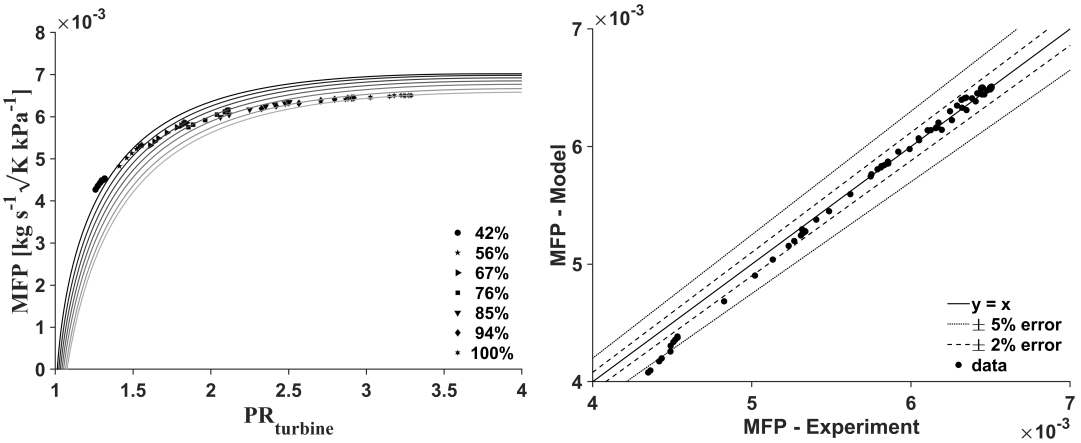

Figure. 6.1 Steady-state swallowing capacity map (a) experiment data and nozzle model extrapolations, (b) error analysis

Table 6.1 List of fitting parameters for steady-state turbine map extrapolations

Parameters	$k_{1,a}$	$k_{1,b}$	$k_{2,a}$	$k_{3,a}$	$k_{3,b}$
Value	4.95×10^{-1}	7.79×10^{-2}	-9.23×10^{-3}	3.54	3.64×10^{-1}

The impacts of the fitting coefficients on the model performance are shown in Fig. 6.2, showing an example at 85% turbine speed. In each plot, the solid curve corresponds to the baseline results and the dashed curve is produced by either increasing or decreasing the value of fitting coefficients of baseline. Fig. 6.2 (a) shows that k_1 can effectively control the magnitude of the extrapolated curve. Fig. 6.2 (b) shows that k_2 has the ability to change both the amplitude and the location of the anchor point, which is the pressure ratio at zero mass flow. Fig. 6.2 (b) shows that k_3 has a large impact on varying the critical pressure ratio when the turbine starts to choke. A large value of k_3 can avoid choking to happen at low pressure ratios. k_3 also has a small effect on changing the magnitude of the curve.

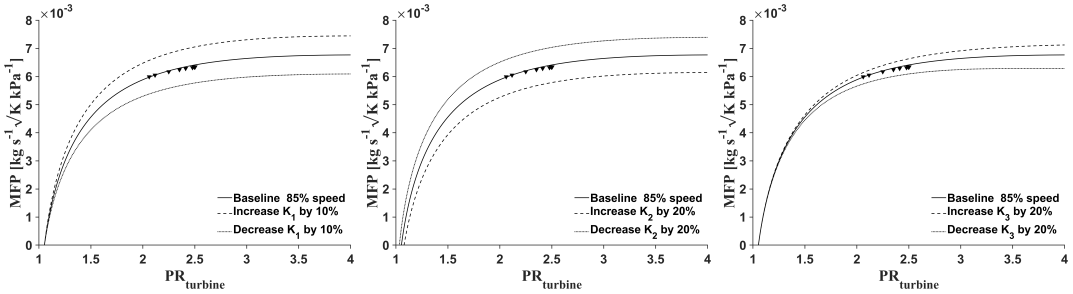

Figure. 6.2 The response of nozzle model by modifying the fitting coefficient of (a)k_1, (b)k_2, (c)k_3

6.2.2 Mean-line Model Performance

The fitting coefficients of the mean-line model, namely the rotor inlet absolute flow angle α_3, stator loss coefficient K_{PL}, passage loss coefficient K_P and incidence loss coefficient K_{inc} as introduced in Section. 4.4.2, have been calibrated against both experimentally measured data and CFD predicted data. Non-linear least-square algorithm was used to find the fitting coefficient that minimizes the errors, and the model performance is shown in Fig. 6.3 and Fig. 6.4 respectively. Both Fig. 6.3 (b) and Fig. 6.4 (b) show that the negative efficiency has been predicted when the turbine operates under extreme low loading conditions. This is a novel feature compared with the conventional mean-line model, implying the actual losses can be greater than the isentropic energy available to the turbine.

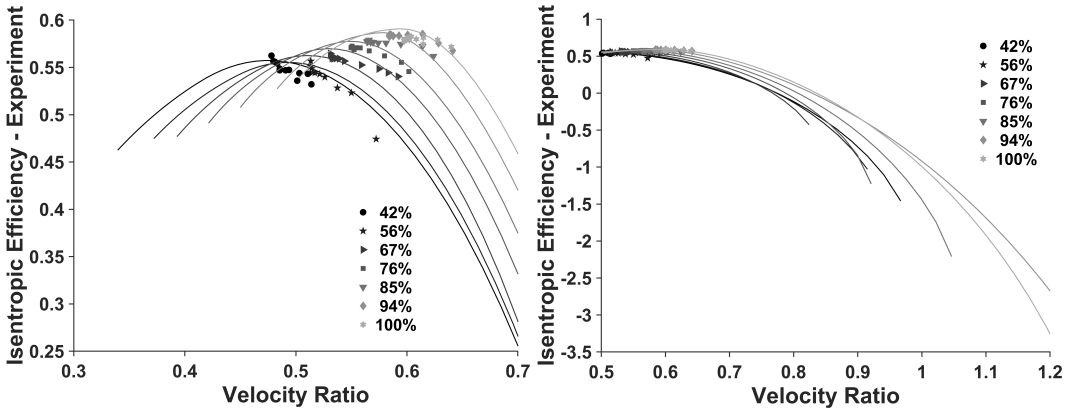

Figure. 6.3 Steady-state (Experiment) efficiency map and mean-line extrapolations (a) normal region (b) region with negative efficiency

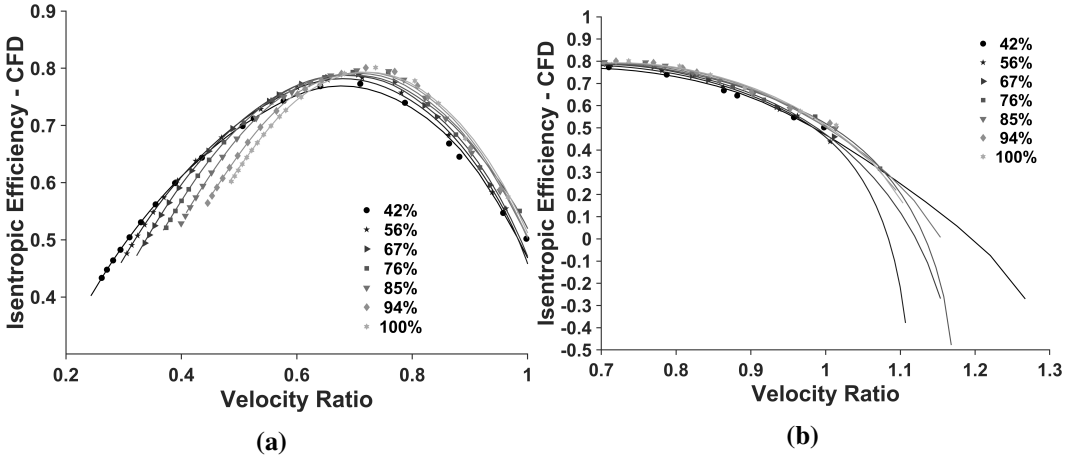

Figure. 6.4 Steady-state (CFD) efficiency map and mean-line extrapolations (a) normal region (b) region with negative efficiency

Fig. 6.5 (a) and Fig. 6.5 (b) show the error analysis. The model predictions have the mean error of 1.68% by using experimental data In the case of using CFD data, the mean error is 0.63%. The proposed mean-line model performs a good prediction for both cases, especially using the data from CFD simulations. This is probably because the larger range of data available to the model will improve the evaluation of loss coefficients, thus producing a better prediction. It is also shown that experimental data is restricted in a smaller range since the compressor was chosen as the loading device of the turbine.

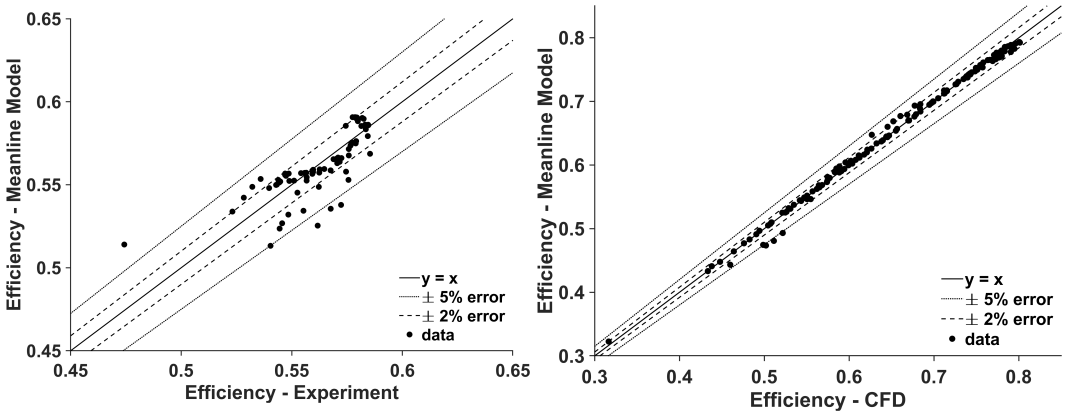

Figure. 6.5 Error analysis of the mean-line model under steady-state conditions (a) Experiment (b) CFD

The influence of the loss coefficients on the efficiency performance has been investigated at 67% turbine speed. The passage loss coefficient (K_P) and incidence loss coefficient (K_{inc}) are varied by $\pm$50% with respect to the value of baseline. The model response to the loss coefficients is consistent with the study carried out by Romagnoli and Martinez-Botas [79]. Fig. 6.6 (a) shows that K_P have an effect on changing the optimal velocity ratio, and it has a large influence on the efficiency performance in the lower velocity ratio regions, but less significant in the high velocity ratio regions. Since passage loss is a function of the relative kinetic energy at the entry and the exit to the rotor, it can affect the overall energy distribution throughout the rotor stage. On the contrary, as shown in Fig. 6.6 (b), K_{inc} mainly affects the efficiency predictions when the velocity ratio is greater than the optimal velocity ratio, but its impacts on the other aspects are negligible. This indicates that, to obtain the appropriate K_{inc}, it is essential to have some data points at high velocity ratio regions during the calibration process, which will be otherwise detrimental to the off-design performance predictions due to the lack of flow physics.

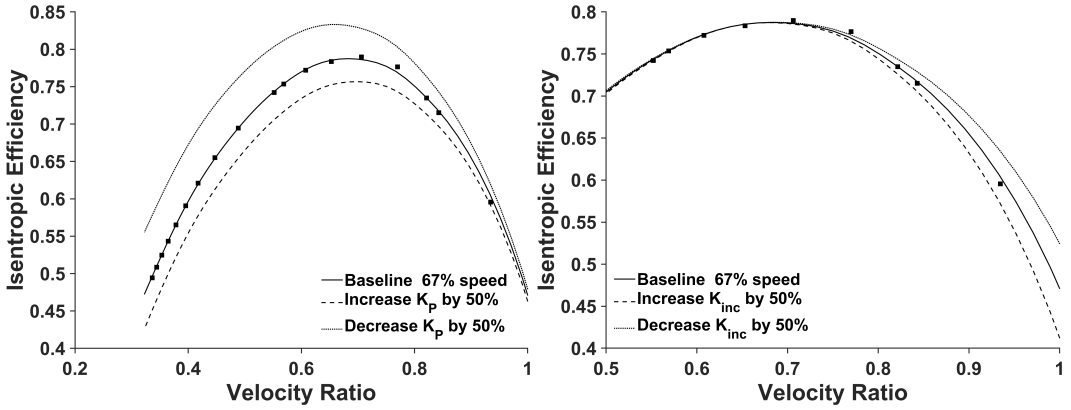

Figure. 6.6 The response of mean-line model by modifying the (a) passage loss coefficient K_P, (b)incidence loss coefficient K_{inc}

6.3 Validation of CFD Model

The comparison regarding the turbine swallowing capacity characteristic between the CFD and experiment is shown in Fig. 6.7 (a). The CFD model shows good a prediction of the turbine swallowing capacity characteristics at the same expansion ratio with the maximum difference of 3.43% and the mean difference of 1.07%. Fig. 6.7 (b) shows differences were bounded within $\pm$2.5 of most cases.

The turbine isentropic efficiency was not provided here. As one would expect, the CFD model would produce a much larger efficiency than that measured during the experiment due to the inherent simplifications. CFD simulations can only account for the aerodynamics losses, whilst the efficiencies gathered from experiment are the lumped turbine efficiencies, including various loss mechanisms. First is the back disc losses, which are not taken into account in the calculation. Besides, the roughed surface caused by rapid-prototyped ducts and outlets is not included in the CFD model. Furthermore, the turbine was tested under the inlet temperature higher than the ambient temperature, and any heat losses the were not accounted in the CFD model as the adiabatic wall was used.

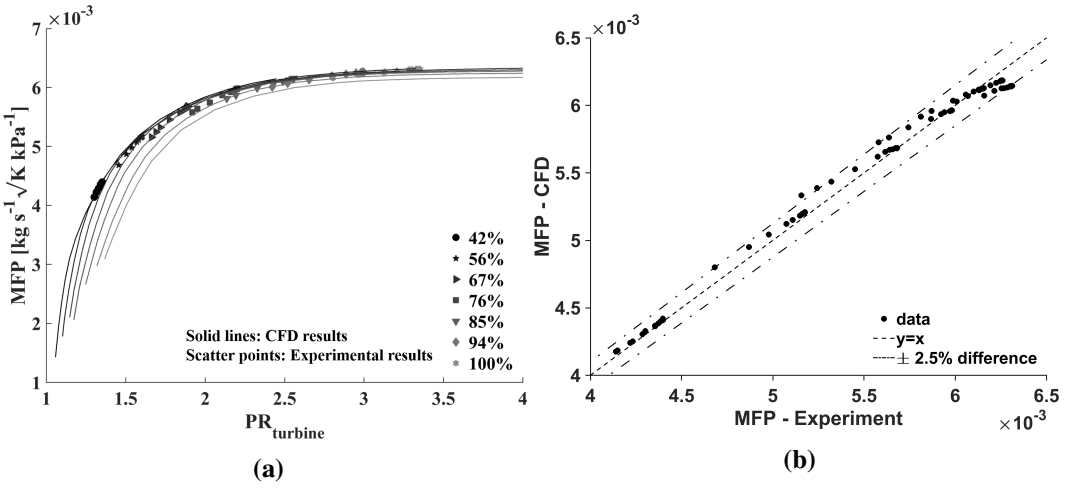

Figure. 6.7 Performance of the single passage CFD model (a) predictions and (b) error analysis

6.4 Turbine Unsteady Performance

This section has assessed both turbine cycle-averaged unsteadiness and turbine instantaneous unsteadiness under two and three cylinder mode. The hypothesis that the quasi-steady data can be obtained during the emptying stage of a pulse has been tested by temporal local criterion [53] and CFD results.

Table 6.2 Cycle-averaged test conditions

Case No.	f [Hz]	N_{motor} $[krpm]$	$N_{t,ave}$ $[krpm]$	$N_{t,reduced}$ $[rpm \cdot K^{0.5}]$	U_{tip}/C_{isen}	Π	St	Λ
3 cylinder mode								
1	19.7	394.15	90.1	4583.84	0.5	1.299	0.063	0.082
2	37.6	752	90.7	4672.99	0.543	0.946	0.103	0.097
3	50	1000	90.7	4594.42	0.546	0.717	0.132	0.095
4	50	1000	141.7	6407.31	0.6	1.035	0.093	0.097
5	57.5	1150	90.7	4549.69	0.552	0.658	0.147	0.097
6	57.5	1150	142	6278.19	0.593	0.953	0.104	0.099
2 cylinder mode								
7	47.6	1000	91.6	4736.97	0.53	0.987	0.113	0.112
8	46.3	1000	121.6	6279.78	0.612	1.26	0.096	0.121
9	54.5	1150	91	4642.51	0.534	0.88	0.129	0.113
10	53.5	1150	90.2	4605.47	0.547	0.839	0.133	0.111
11	53.3	1150	119.7	6008.26	0.6	1.14	0.108	0.123
12	25.8	500	94.8	5116.4	0.534	1.315	0.065	0.085
13	36.5	1230	91.5	4766.88	0.5	1.103	0.11	0.121

Turbine Cycle-averaged Unsteadiness

Table. 6.2 listed the test matrix of the experiment, including the pulse frequency, motor speed, mean turbine speed, velocity ratio, normalized amplitude, strouhal number and lambda number. Lambda criterion proposed by Copeland et al. [44] was used to assess the cycle-averaged turbine unsteadiness. Energy-weighted mean velocity ratio, which is calculated as per Eq. 6.2, is used to assess the turbine loading conditions, where a smaller value is corresponding to a higher turbine loading.

Fig. 6.8 shows the pulse comparison between case 5 and case 10, where they have similar engine speeds and blade speed ratios. As expected, when one cylinder is deactivated, the remaining two cylinders compensate to deliver much more peak power to the turbine in order to maintain the same compressor speed. As the effective flow is only through two cylinders during cylinder deactivation, the pulse frequency has to be modified to account for the missing pulse. This was achieved by dividing the motor frequency by the effective pulse fraction φ, as per Eq. 6.2, and then multiply by 2 because each effective pulse period contains two sub-pulses. The rest parameters in Table. 6.2 are adjusted accordingly, only taking the effective pulses period into account.

$$BSR = \frac{U_{tip}}{C_{isen}} = \frac{\int_0^{TT} \left[\frac{U_{tip}}{C_{isen}} \times \dot{W}_{isen}(t)\right] dt}{\int_0^{TT} \dot{W}_{isen}(t) dt} \tag{6.1}$$

$$f_{modified} = \frac{2 f_{pulse-rig}}{\varphi} \tag{6.2}$$

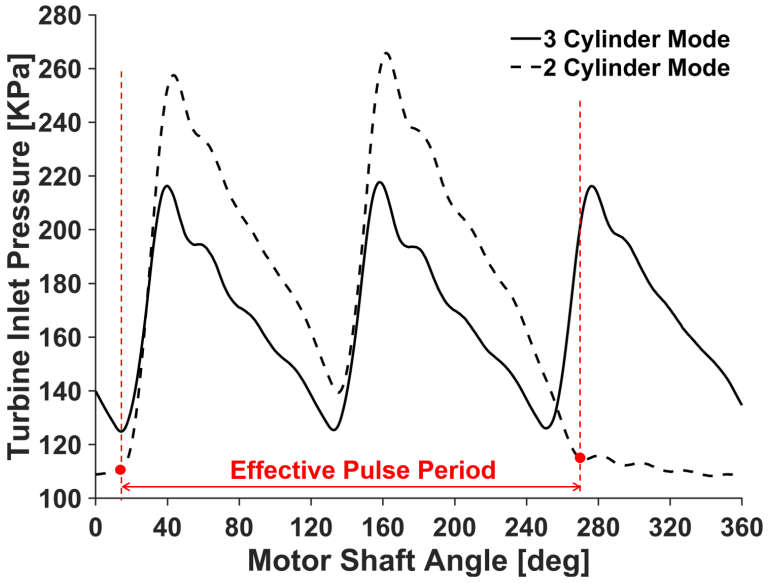

Figure. 6.8 Pulse comparison between three cylinder mode and two cylinder mode

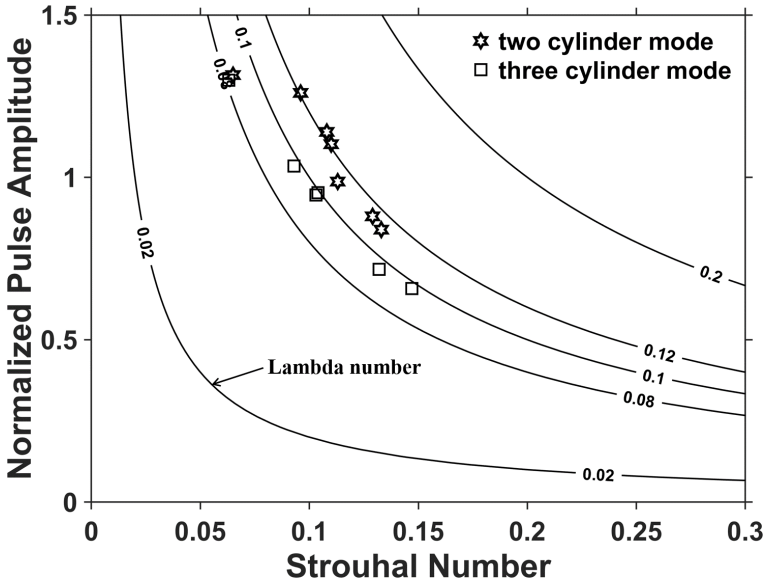

Figure. 6.9 Assessment of turbine averaged cycle-averaged unsteadiness

Fig. 6.9 shows the turbine unsteadiness assessment based on the lambda criterion. Despite two low pulse frequency cases (No. 1 and No. 12), a general trend was found that the turbine unsteadiness of two cylinder mode is higher than three cylinder mode and the averaged unsteadiness of pulsating flow is 0.1. As suggested by Copeland et al. [44], this indicates the turbine is working closely to quasi-steady behaviour when it subjects to the pulsating flow

generated by the bespoke pulsation generator. In addition, the pulse amplitude is inversely proportional to the pulse frequency, and as a consequence, turbine unsteadiness assessed by lambda criterion maintained at the same level in both pulse-rig operating mode. The small lambda number also indicates that putting the measurement section closer to the rotor is an effective way to reduce the turbine unsteadiness.

6.4.1 Analysis of Negative Power

The percentage of turbine negative work (ζ) during a pulse cycle is calculated as per Eq. 6.3 in order to reveal its relation with pulse frequency, where subscript pos and neg stand for the positive and negative fraction of the turbine actual power. As discussed in Section. 2.1, the negative power is generated during the period when the pulse energy is low, so that the turbine is free-wheeling under its own inertia.

$$\zeta = \frac{\int_{t=0}^{TT} \dot{W}_{neg}(t)dt}{\int_{t=0}^{TT} \left[\dot{W}_{neg}(t) + \dot{W}_{pos}(t)\right] dt} \tag{6.3}$$

Fig. 6.10 shows the negative work percentage at different pulse frequencies, labelled as case numbers. It is observed that the negative work percentage is higher in two cylinder cases. That is because the turbine is working in a free-wheeling manner for a longer period when one cylinder is deactivated. Considering a three cylinder engine of deactivating one cylinder, free-spinning behaviour of a turbine will last for one-third period of one engine cycle, thereby producing a larger percentage of negative work as demonstrated in Fig. 6.11. Additionally, the negative power percentage has a negative correlation with pulse frequencies, which can reach up to 15% in the three cylinder mode at 20 Hz, and the value is 18% in the two cylinder model at 25 Hz. That is because that the higher pulse frequency, the higher chance for the

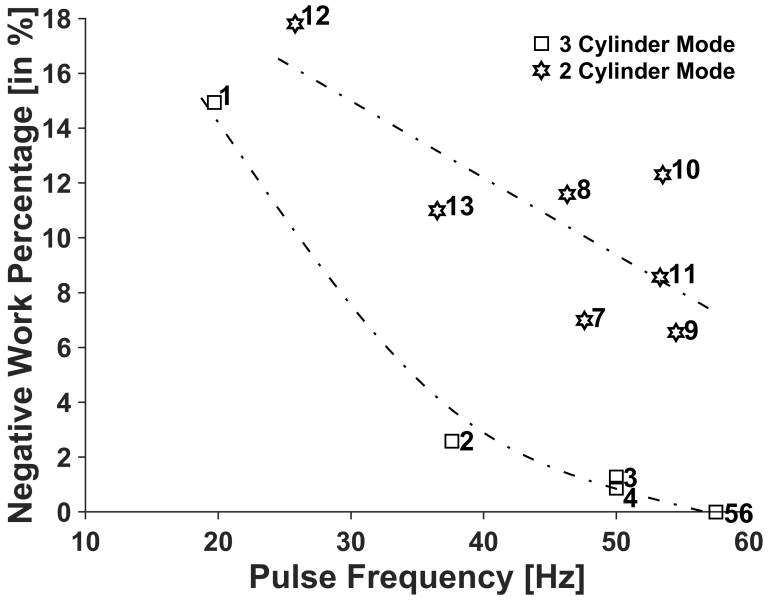

Figure. 6.10 Pulse frequency versus negative work percentage under two and three cylinder mode, labelled as the case numbers referring to Table. 6.4

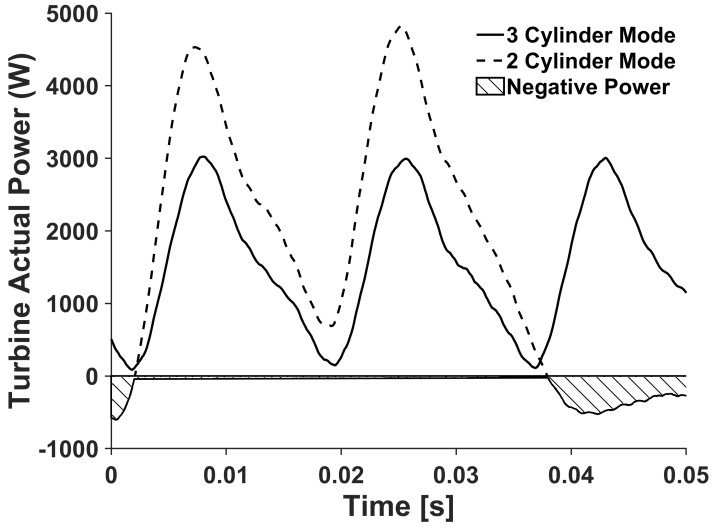

Figure. 6.11 Negative power produced during the cylinder deactivation period

pulse generator to provide continuous energy to the turbine and avoid the free-wheeling behaviour. It is also important to note that this type of data is impossible to gather using a steady-state gas stand since it is a purely transient phenomenon.

6.4.2 Data Filtering Based on the Unsteadiness Criterion

Fig. 6.12 shows the measurement of turbine inlet instantaneous pressure and the assessment of turbine instantaneous unsteadiness over a pulse, estimated according to Eq. 2.7. The data in these plots were taken from case No.1 (50 Hz) and No.2 (20 Hz), where the turbine was working at a similar mean speed but subject to different pulse frequencies. It is clear that during the increasing stage of a pulse, it results in a higher peak of $|\varepsilon(t)|\beta_{local}(t)$number, indicating the unsteady behaviour dominates during that period, whereas at the decreasing stage of a pulse, the magnitude of $|\varepsilon(t)|\beta_{local}(t)$is much lower, meaning the quasi-steady behaviour dominates. To obtain the quasi-steady turbine behaviour over a pulse, experimental data (black scatters in the plots) of $|\varepsilon(t)|\beta_{local}(t) < 0.1$ was selected as a basis for the extrapolation of turbine unsteady maps. This is an important feature in the proposed method for generating true unsteady maps, namely, to select the unsteady data where quasi-steadiness can be assumed.

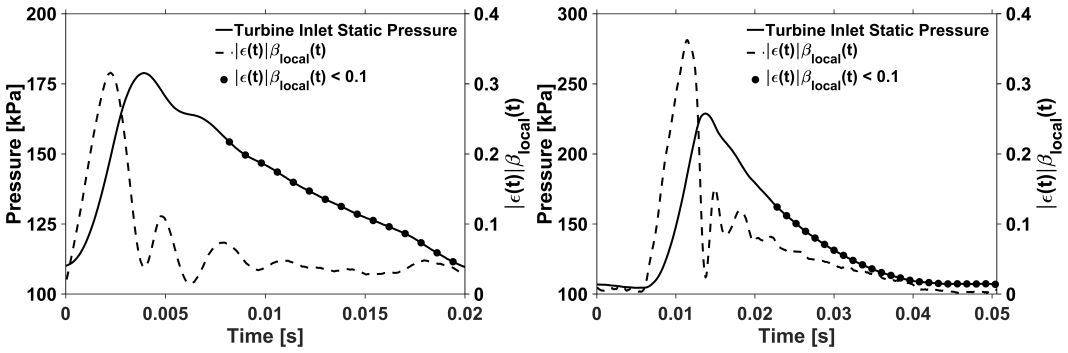

Figure. 6.12 Turbine inlet instantaneous pressure and turbine instantaneous unsteadiness subjected to pulse frequency (a) 50 Hz (b) 20 Hz

To verify the hypothesis that the decreasing pulse part is closer to quasi-steady behaviour, Fig. 6.13 (a) compares the turbine swallowing capacities (based on CFD simulation, corresponding to case No.1), calculated by using the data from different sections. It is clear that the hysteresis loop is about to collapse into the quasi-steady data if the measurement section is selected close to the rotor. Fig. 6.13 (b) illustrates the absolute difference of mass flow parameter

between CFD unsteady-data and CFD steady-state data during the pressure decreasing stage (also known as the emptying stage) of the pulse. It could find that turbine swallowing capacity at "experiment measurement section (shown in Fig. 3.14)" is quite close to the data taken from "rotor inlet section". Thus, from the instantaneous unsteadiness assessment and CFD simulation, it can be confirmed that it is feasible to use the "quasi-steady" data from the decreasing stage of a pulse to obtain the equivalent steady-state turbine swallowing capacity performance.

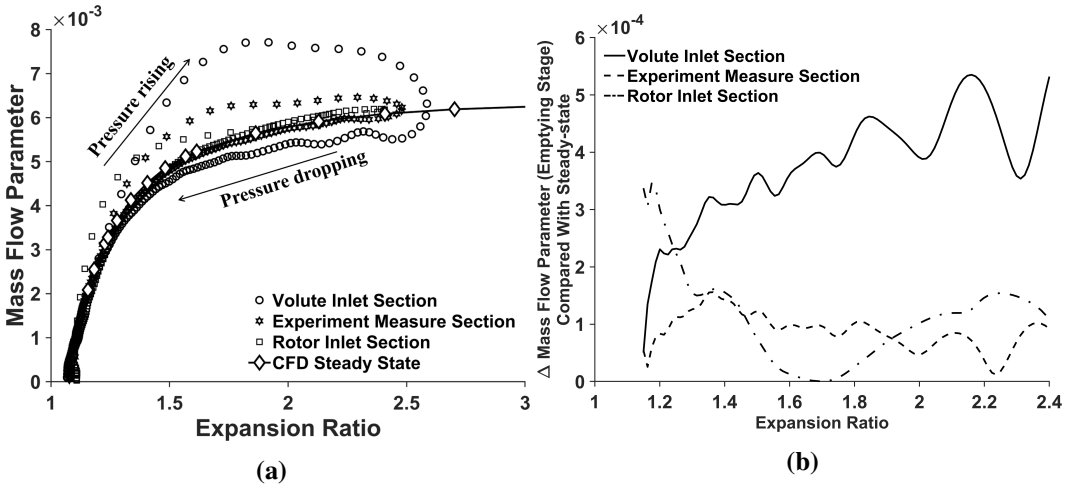

Figure. 6.13 (a)Turbine swallowing capacities at different sections from CFD simulation, (b)Mass flow difference during the emptying stage of the pulse compared with steady-state CFD data

6.4.3 Extrapolation of Turbine Unsteady Swallowing Capacity

The extrapolation method, as discussed in Section. 6.2, was then used for extrapolating the turbine unsteady performance data. Fig. 6.14 (a) shows the unsteady turbine mapping at three different turbine speeds under 50 Hz frequency pulses, and its extrapolated curves. The points in the plot correspond to the data extracted from the quasi-steady region of the pulse, according to the black dots in Fig. 6.12,as calculated by using the temporal local criterion proposed by Cao et al. [53]. It can be found that using the pulsating flow for turbine mapping will generate a much larger range of data than the state-state conditions. However, some unsteady tendencies, such as small mass flow fluctuations, are still noticeable which may

violate the quasi-steady assumption. Therefore, perhaps it is not surprising from that from Fig. 6.14 (b), it is evident that the deviation from the extrapolated curves is generally larger when using the unsteady data. This could also be attributed to the speed variations during the unsteady turbine mapping. The fluctuating turbine speed could reach to a maximum amplitude of approximately 1500rpm, representing approximately 1.5% to 2% of the overall speed magnitude. Thus, the extrapolated curve represents swallowing capacity of the mean speed over a pulse. Nevertheless, despite these drawbacks, what is clear is that the unsteady pulse can be used to generate a much broader range of data available to create more reliable maps.

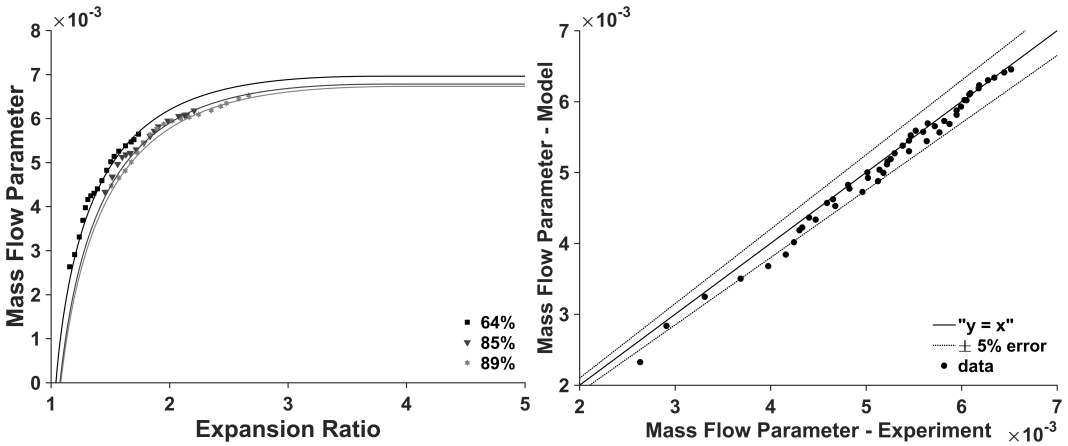

Figure. 6.14 Performance of nozzle model of extrapolating unsteady performance data

6.4.4 Extrapolation of Turbine Unsteady Efficiency

Prior to calculate the unsteady efficiency, the phase-shift methods, based on the sonic velocity criteria, was applied to align the actual power and isentropic power to the same time frame, as discussed in Section. 3.3.2. Also, the shaft speed was filtered using the ensemble-averaging for 40 continuous pulses, followed by Savitzky-Golay filter. Fig. 6.15 shows the turbine instantaneous efficiency measurement under pulse frequencies of 20 Hz and 50 Hz, where both 20 Hz and 50 Hz case exhibit hysteresis loops. Although the turbine instantaneous efficiency at 50 Hz forms a much larger hysteresis loop than the 20 Hz case, they have similar

magnitude data near the quasi-steady region, which is assessed by $|\varepsilon(t)|\,\beta_{local}(t)$criterion as one would expect. It is also clear that the 20 Hz case has a much lower negative efficiency than the 50 Hz case, with even reaching the minimum efficiency of -9.3% recorded.

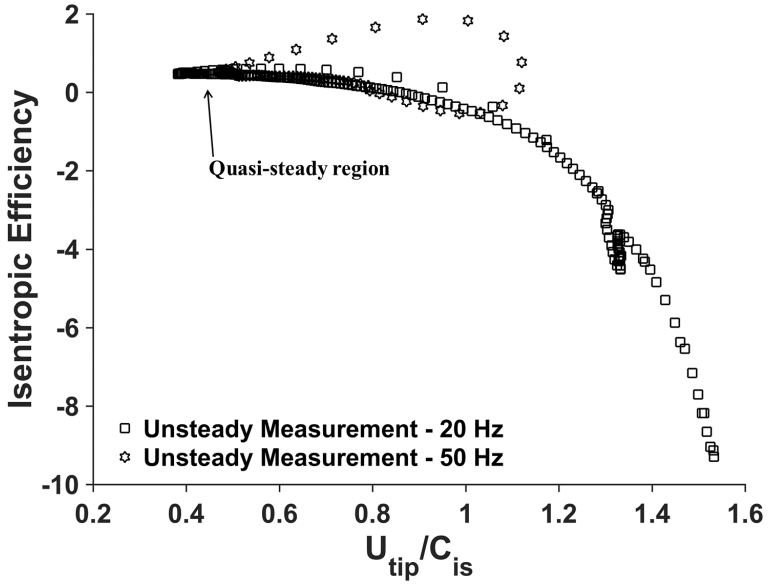

Figure. 6.15 Turbine instantaneous efficiency measurement under 20 and 50 Hz pulses

Fig. 6.16 shows that this "quasi-steady" data from the 20 Hz case can be used to inform the mean-line model and thus create a map of the turbine efficiency from the unsteady pulse. For comparison, this figure also shows the steady-state measurement and the corresponding GT-Power extrapolation. The proposed pulse-calibrated mean-line model is able to predict the turbine efficiency under unsteady flow conditions and also take into account the negative efficiency behaviour. The difference between mean line model prediction and experimental data is small when the velocity ratio is smaller than 1.2, but is large when the velocity ratio exceeds 1.2, where the measured efficiency is quite steep at the end. That is possibly because some additional windage loss arises during that period, where the current loss model is not able to take into account. The mean-line code terminates at the minimum efficiency of approximately -4.8%. That is because the high passage losses at the high velocity ratio regions lead to very large tangential velocities, as per Eq. 4.43, which in return increases the passage losses during iterations, and cause the model to diverge.

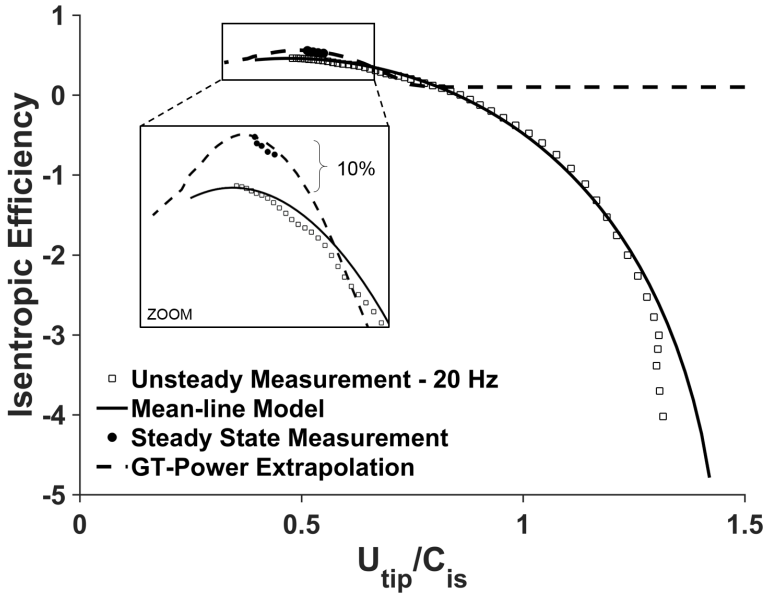

Figure. 6.16 Extrapolations of turbine instantaneous efficiency

Nevertheless, by using the measured instantaneous efficiency, the mean-line model produced physical extrapolations to the high load regions, which is important in engine full-load simulations. The GT-Power based extrapolation results show a large difference with the proposed pulse-calibrated mean line model. This is on the one hand because of the limited range of data collected from steady-state test. On the other hand, GT-Power assumed the minimum turbine efficiency is 10% by default creating this fixed efficiency above a velocity ration of 0.8. In addition, Fig. 6.16 shows a zoom window into the peak efficiency region to show differences in peak efficiency measured during steady-state measurements and unsteady measurements. For this example, the peak unsteady efficiency is approximately 10% points lower than the steady-state data. The result of the differences in these maps will be quantified later in relation to the difference in compressor power that would result from these two data sets. There are two explanations for the differences in peak efficiency. First, the result highlights that the true unsteady efficiency of the turbine may be influenced by the fluid dynamic unsteadiness resulting from the pulse. Secondly, and perhaps more likely, this efficiency definition includes the dynamic frictional loss (see Eq. 3.17) and thus is likely to

result in differences between the friction that occurs during steady-state mapping where the operating point is held for an extended settling period. Therefore, using unsteady data to inform the maps of turbine efficiency should result in a much more accurate means to obtain the true efficiency – especially where it is used in 1D modelling tools.

6.5 Turbine Instantaneous Speed and Power Predictions

The above sections discussed the turbine mapping method under pulsating flow condition, and introduced physical ways to extrapolate turbine unsteady maps. A transient turbocharger model has been developed, as discussed in Section. 4.5, to implement the unsteady maps. It is of interest to investigate how the shaft response to pulsating flows by using turbine map containing negative efficiency.

The testing conditions, as listed inTable. 6.2, show that case No.1 and case No.13 which are the two typical cases in three and two cylinder mode, which is selected here since they have a similar shaft speed and loading conditions. Fig. 6.17 and Fig. 6.18 show the comparison of turbine instantaneous speed between experiment and model prediction under three and two cylinder mode respectively. The simulation results that use negative efficiency have the best agreement to experimental data in terms of the speed magnitude with an error of mean speed prediction less than 0.8%. If the turbine unsteady map does not involve negative efficiency, the cycle-averaged turbine speed of case No.1 and case No.13 will be increased by 3% and 1.35% respectively. It should be noted that the "unsteady map without negative efficiency" utilized 10% as its minimum efficiency in order to have the same basis as the GT-Power extrapolation model. However, if directly using turbine map from steady-state measurement and apply GT-Power extrapolation method, it will result in a larger error in speed prediction, at the maximum of 8.93% in terms of cycle averaged value. That is because of the higher peak efficiency in GT-power extrapolated map, as shown in Fig. 6.16, thus producing a higher turbine actual power.

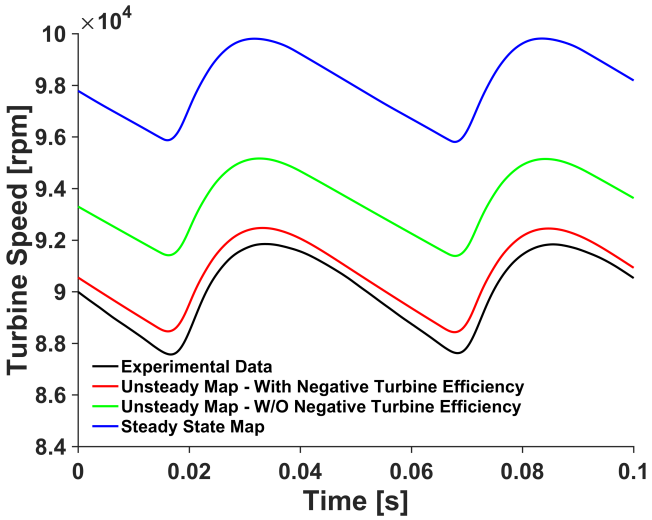

Figure. 6.17 Turbine instantaneous speed – 3 cyl mode (case No.1)

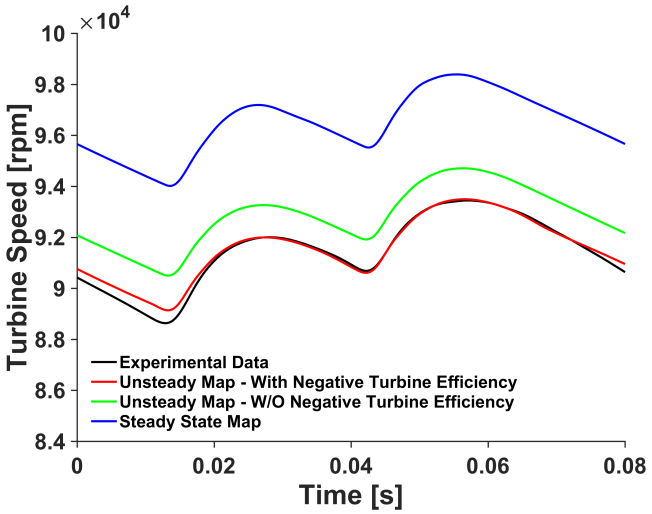

Figure. 6.18 Turbine instantaneous speed – 2 cyl mode (case No.13)

Fig. 6.19 and Fig. 6.20 compared the predicted turbine actual power with experiment measured results under three and two cylinder mode respectively. The proposed transient turbocharger model is able to predict negative turbine power as expected. However, compared with the experimental data, some differences in terms of negative power prediction are still noticeable. For instance, under three cylinder mode, the amount of predicted negative power is less than the experimental results. That is because the mean-line extrapolated efficiency terminates at approximately -4.8%, whilst the minimum measured efficiency is -9.3%, as

shown in Fig. 6.16. For the two cylinder mode, the predicted power is close to zero during the cylinder deactivated period even though the map includes negative efficiency. That is because there available isentropic energy is quite low during that period, whilst the efficiency kept at the fixed minimum point. As a result, the predicted actual power is thereby approaching to zero during the cylinder deactivated period. Nevertheless, the cycle-averaged turbine power prediction was improved by including the negative efficiency in the map, which in return facilitates the compressor power prediction in the model.

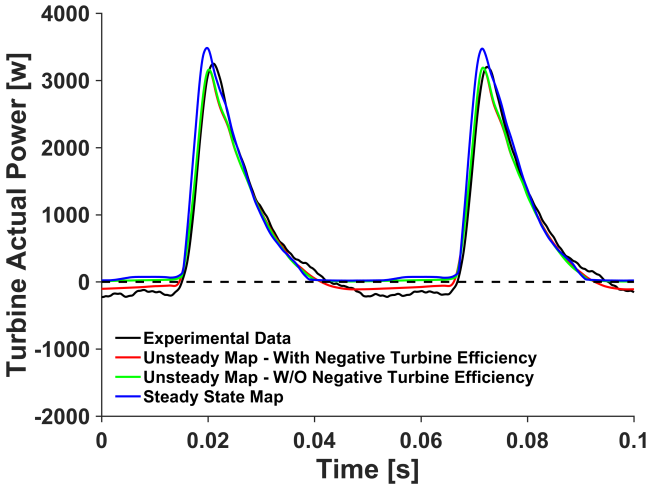

Figure. 6.19 Turbine instantaneous power – 3 cyl mode (case No.1)

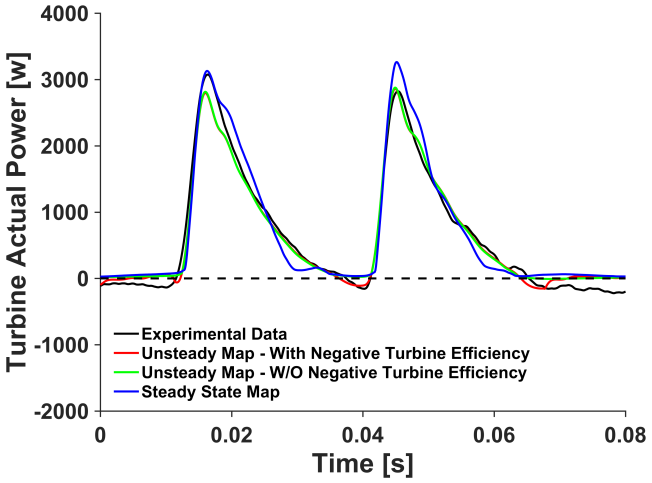

Figure. 6.20 Turbine instantaneous power – 2 cyl mode (case No.13)

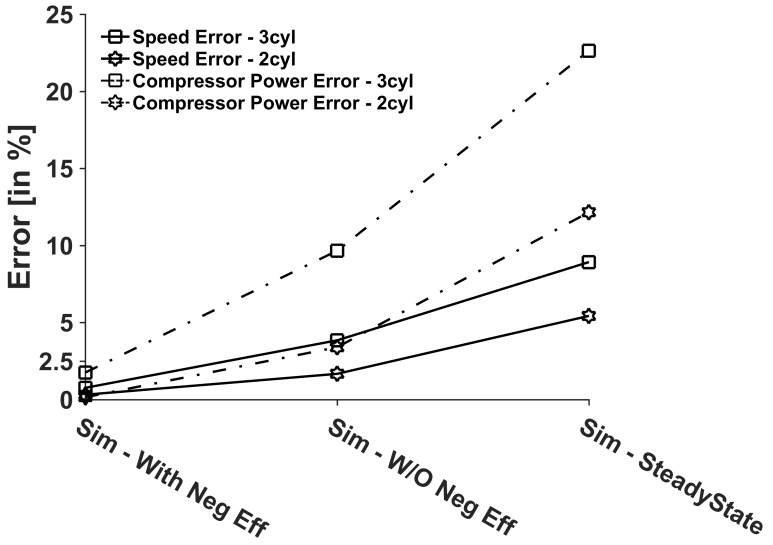

Figure. 6.21 Error analysis of average speed and compressor power prediction of case No.1 and case No.13

Fig. 6.21 shows the error of compressor power prediction comparing the three cases, first, using the extrapolated steady-state data, secondly, an extrapolation of the unsteady data without negative efficiency, and finally, the fully pulse-informed map that includes negative efficiency. As is evident, since the 3-cylinder case is the lowest frequency, it shows the greatest benefit from the approach to unsteady mapping. Comparing to experimental results, the error in compressor power prediction is up to 23% whilst the error in turbocharger speed is up to 8.9%. It is also clear that the error simply attributed to negative efficiency is non-trivial and should be considered, especially in lower pulse frequency scenarios.

6.6 Summary of the Unsteady Mapping Methodology

Fig. 6.22 gives a detailed summary of the proposed mapping approach based on unsteady measurements. To demonstrate this, a bespoke pulsating flow generator was developed at the University of Bath, which was able to expose the turbine to a range of pulses, but still make use of a controlled environment of a gas-stand.

The compressor side data was simply used to measure compressor power, and was then used to derive the mean turbine power which was added to the fluctuating power component

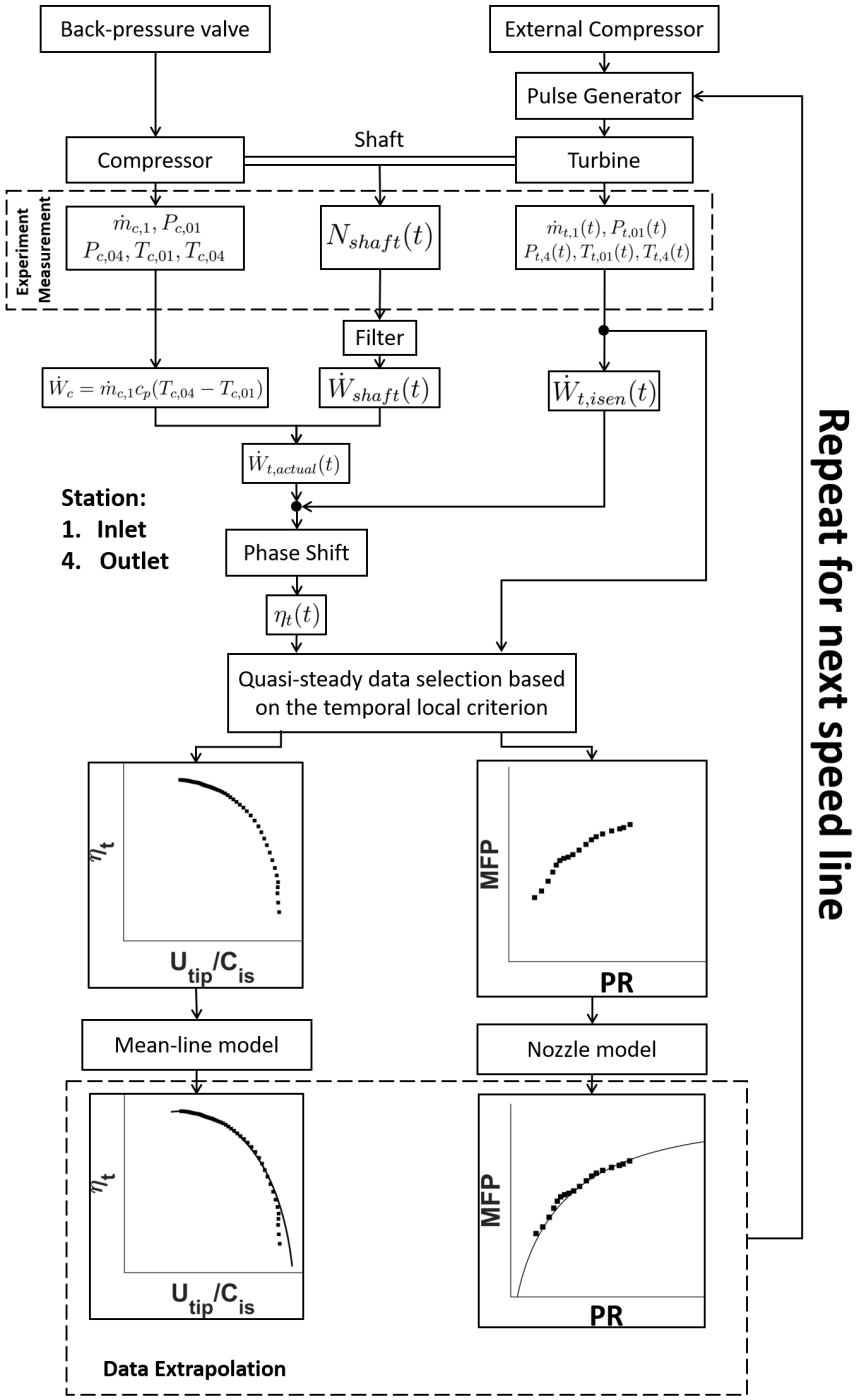

Figure. 6.22 Flow chart of new mapping approach

derived from acceleration. Measurements of turbine pressures and temperatures were placed close to the rotor in order to reduce unsteadiness due to the mass accumulations within the volute. Based on turbine instantaneous unsteadiness assessment and CFD simulation, it

proved that it is feasible to use the data of low pulse frequency gathered from the volute tongue region to measure the turbine quasi-steady performance.

The dynamic data set was then evaluated based on the temporal local criterion proposed by Cao et al. [53]. During the decreasing stage of pulses, this criterion indicated quasi-steady behaviour and hence was selected as a basis the generated unsteady swallowing capacity map and unsteady efficiency map. In order to extrapolate this data effectively, a nozzle model based on a modified version of [10] was used for the turbine swallowing capacity characteristics. The maximum error of the proposed nozzle model was generally within $\pm 5\%$ compared to the unsteady measurement. A mean-line loss model was also developed to extrapolate turbine instantaneous efficiencies. The mean-line model was improved versus literature sources making it possible to account for negative efficiencies. The mean-line model showed generally good agreement in efficiency prediction, but was not always able to capture the efficiency trend at extremely low load regions. This is possibly due to additional windage losses that the current loss model do not take into account. Finally, a Simulink turbocharger model was developed to implement the unsteady maps.

CHAPTER 7

RESULTS OF TURBINE OPTIMIZATION STUDY

7.1 Results of Turbine Unsteady Optimization

The optimization conducted under unsteady conditions was accomplished at 18 generations with 199 different designs considered. Fig. 7.1 shows the Pareto optimal front for energy-weighted efficiency and work output at the end of the optimization. The unsteady optimization produced two different designs with respect to the maximum work output and efficiency, labelled as the $Max.\overline{\eta}_r$ and $Max.W_r$ in the following paper. Also, a single-point steady-state optimization has been conducted for studying the difference between the unsteady optimization approach and the conventional steady-state optimization approach. It is clear that most exhaust flow energy is contained in the region near the peak of pulses where pressure, mass flow and temperature all tend to be maximum. Thus, the objective of the steady-state optimization is to improve the turbine efficiency at the point corresponding to the peak of pulse. The steady-state optimization of the turbine blade spanned over 80 generations with 961 different designs considered. Fig. 7.2 shows the changing of rotor efficiencies during the optimization process. The best candidate design regarding the steady-state performance indicates an efficiency improvement of 1.14 percentage point. The performance of steady-state optimized candidates, referred as $Opt.Steady.$, was then assessed under the same unsteady flow conditions for the comparison purpose.

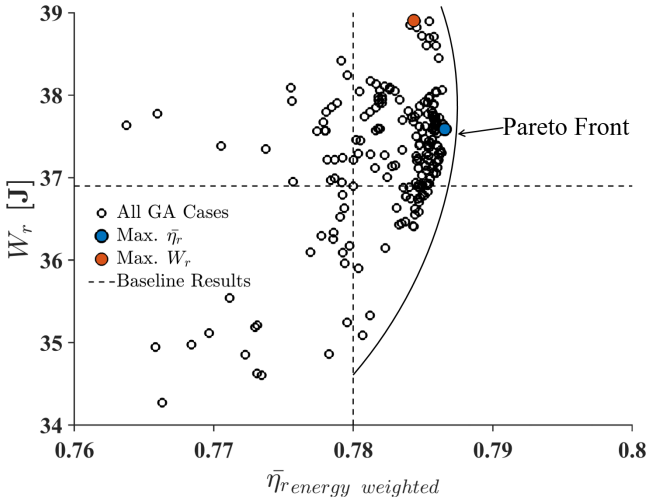

Figure. 7.1 Unsteady optimization results

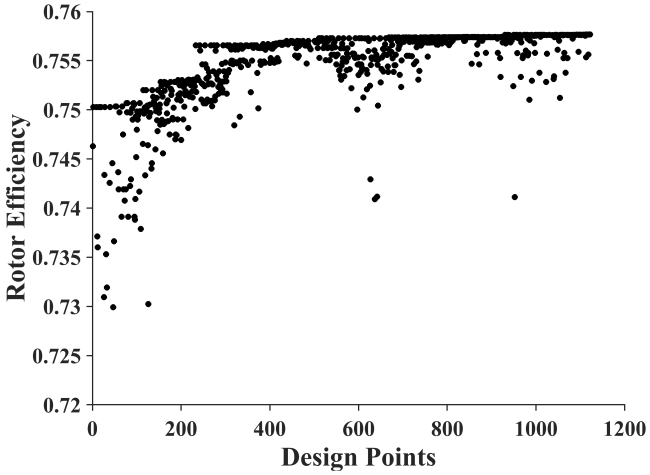

Figure. 7.2 Steady-state optimization results

7.1.1 Design Parameters and the Validation Against the Full-rotor Model

Table. 7.1 lists the design variables and the derived variables (blade camber angles at the LE and TE) of the optimized blades. The optimized designs show similar results regarding the cone angle, which is 73°, but shows different camber-line distributions as demonstrated in Fig. 7.3. To have a more intuitive demonstration of the blade camber angles, Fig. 7.4 shows the blade stream-wise profiles at the midspan. The *Opt.Steady* shows the strongest curvature among all blades. The different locations of the leading edge imply that incidence angles

have been shifted to a better condition that may reduce the associated incidence losses. This will be analysed in Section. 7.1.4.

Table 7.1 Design and derived variables of optimized turbines

		Baseline	Max. $\overline{\eta}_r$	Max. W_r	Opt. Steady
Design Parameter	γ [°]	60	72.9	73.1	73
	d_{axial} [mm]	0	1.1	0.8	1.8
	$\Delta X_{Pt.2}$ [mm]	0	0.3	0.9	0.4
	$\Delta\theta_{Pt.2}$ [°]	0	-4.3	-10.5	-20
	$\Delta X_{Pt.3}$ [mm]	0	2.7	2.7	3.2
	$\Delta\theta_{Pt.3}$ [°]	0	10.8	6	0
	$\Delta\theta_{Pt.4}$ [°]	0	0.7	-10.1	-12
Derived Parameter	$\phi_{\beta,3.5h}$ [°]	-30.45	-33.35	-36.98	-49.10
	$\phi_{\beta,3.5m}$ [°]	-24.05	-17.08	-22.50	-29.08
	$\phi_{\beta,3.5s}$ [°]	-15.70	-5.71	-10.32	-13.31
	$\phi_{\beta,4h}$ [°]	49.69	62.85	60.44	67.50
	$\phi_{\beta,4m}$ [°]	61.98	65.80	63.74	66.43
	$\phi_{\beta,4s}$ [°]	68.51	71.89	70.15	72.18

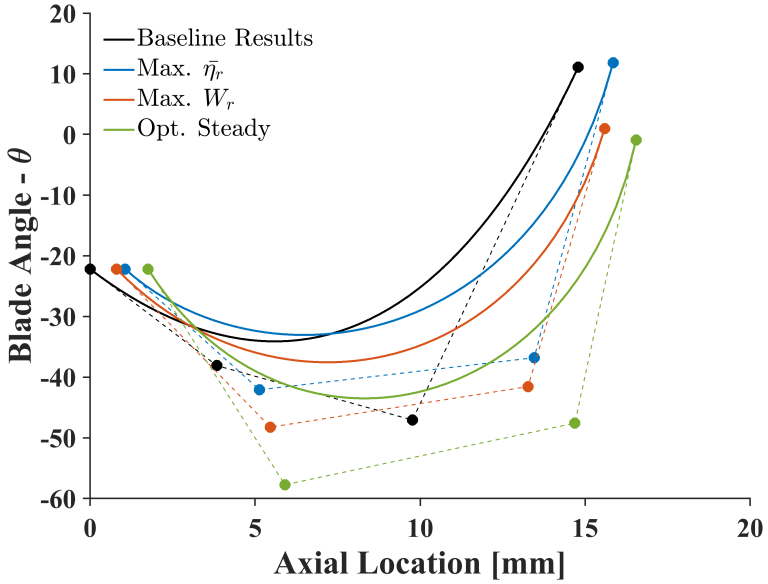

Figure. 7.3 Camber-line distributions of optimized blades

In order to have the confidence that the simplified model assumption, single passage (SP) and frozen rotor approach, can produce a reliable result, the four designs have been validated against the full-rotor (FR), including ten blade passages. Besides, the rotor to stator interface

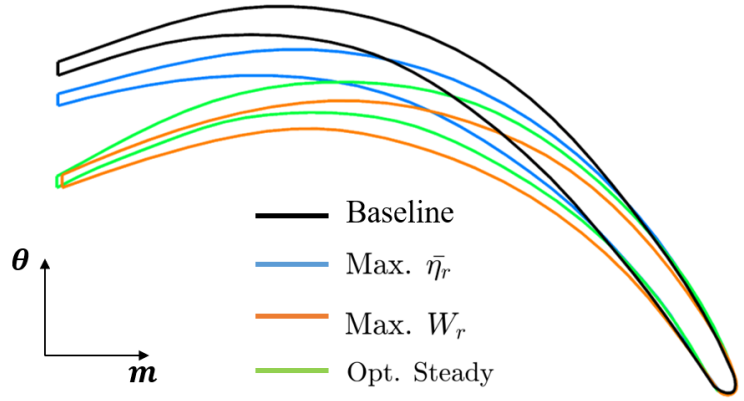

Figure. 7.4 Comparisons of blade stream-wise profile at the midspan

was treated as transient rotor-stator, which is also known as the sliding mesh approach, in which the rotor explicitly rotated at an angle of 2.5° per time-step. The analysis has taken into account the whole pulsating period.

Fig. 7.5 (a) shows the comparisons of the instantaneous turbine mass flow parameters between the SP and the FR model. All the FR models show a higher mass flow than the corresponding SP model. The instantaneous performance of the SP model follows the same trend as the FR model. Table. 7.2 lists the cycle-averaged performance parameters during the same period that corresponds to 80% of the pulse energy region. The $Max.\overline{\eta}_r$ candidate produces the largest deviations of MFP of 1.75%.

Fig. 7.5 (b) shows the comparisons of the instantaneous blade torque. It is observed that the FR models generally produce higher torque than the SP contour-parts. The FS model produces many secondary fluctuations, which is not the case in the SP model. That is a result of moving mesh for every time step. The maximum difference occurs at the peak pulse region. Regarding the cycle-averaged performance, the actual power has been compared, and the $Max.\overline{\eta}_r$ also shows the largest deviations, which is 2.39%. In addition, the cycle averaged

efficiency is also compared, where the baseline design shows the maximum difference of 0.36 percentage points. However, the efficiency at the peak of the pulse shows a relatively large difference, with the maximum value of 0.98 percentage points. That is possibly due to the difference between the SP model and the FR model reaches the maximal value at the peak of the pulse. Nevertheless, it is concluded that the difference between the SP model and FR model is small with respect to the cycle-averaged results. Therefore, using the SP model for the optimization is a feasible approach, since the objective function only focuses on the cycle-averaged performance. Besides, the FR model does not affect the order of the cycle-averaged results, which were achieved by the SP model.

The discussion of the following sections is based on the results produced by the SP model.

Table 7.2 Validation the single passage method against the full rotor method

		$\overline{MFP}$ $[\frac{10^3 \cdot kg\sqrt{K}}{s \cdot kPa}]$	W_r $[J]$	$\overline{\eta_r}$	$\eta_{r,peakPulse}$
Baseline	SP	5.52	36.9	78%	74.04%
	FR	5.45	36.3	78.36%	75.02%
	-	1.45%	1.66%	0.36pp	0.98pp
Max. $\overline{\eta}_r$	SP	5.59	37.59	78.66%	74.97%
	FR	5.49	36.71	78.79%	75.90%
	-	1.75%	2.39%	0.13pp	0.93pp
Max. W_r	SP	5.77	38.9	78.43%	75.16%
	FR	5.68	38.14	78.24%	75.67%
	-	1.56%	2%	-0.19pp	0.51pp
Opt. Steady	SP	5.65	38.06	78.64%	75.37%
	FR	5.57	37.26	78.52%	75.94%
	-	1.47%	2.15%	-0.12pp	0.57pp

7.1.2 Analysis of cycle-averaged performance

Concerning the cycle-averaged performance, compared with baseline, the $Max.\overline{\eta}_r$ candidate shows the maximum improvement of efficiency by 0.66% and $Max.W_r$ shows the largest gain in terms of work output during a pulse (5.42%). The $Opt.Steady$ candidate obtains the largest efficiency at the peak of the pulse with an improvement of 1.34% and a medium

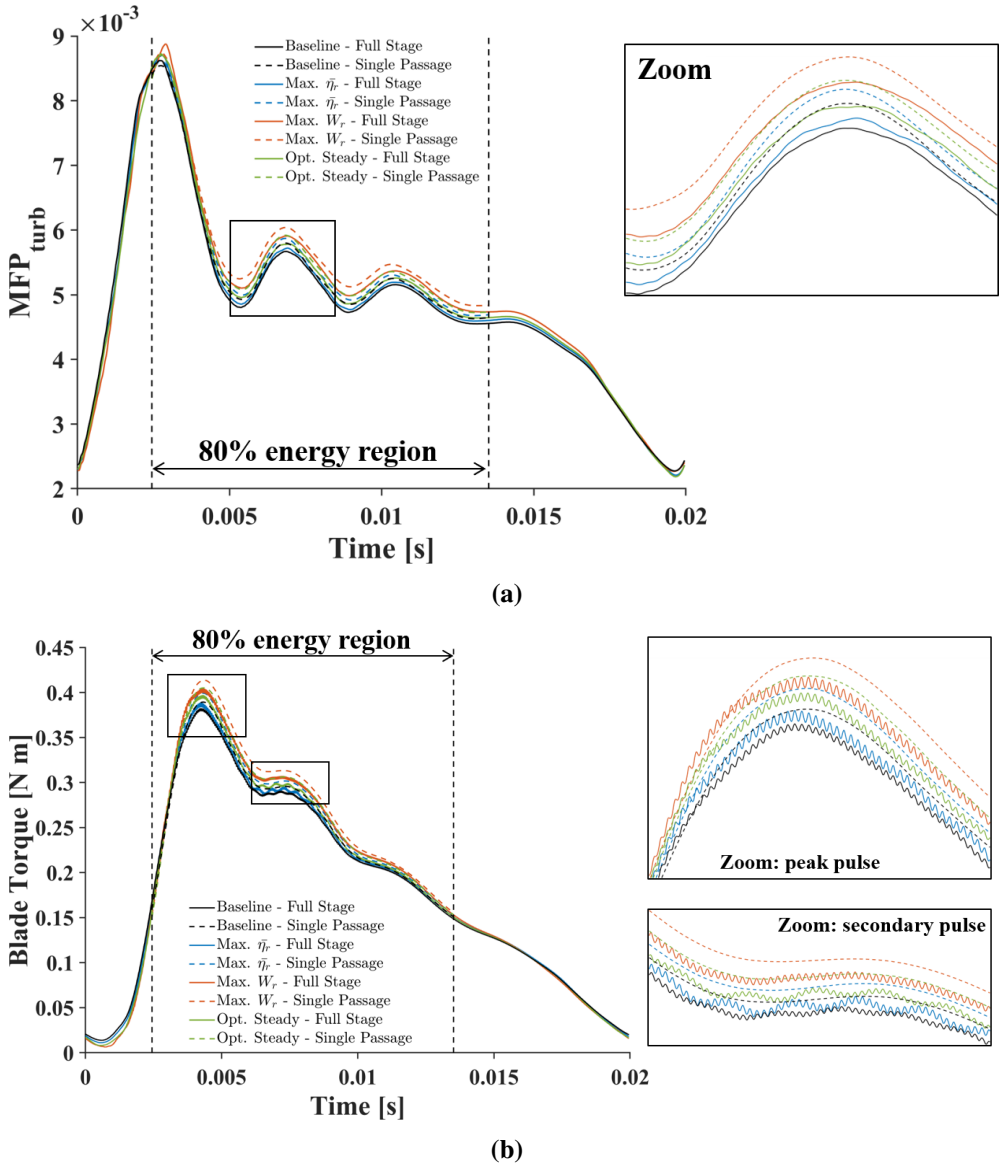

Figure. 7.5 Comparisons of the instantaneous (a) turbine mass flow parameters and (b) blade torque between the single-passage model and the full-rotor model

gain in terms of work output of 3.14%. *Opt.Steady* shows a comparable result with $Max.\overline{\eta}_r$ regarding the cycle-averaged efficiency with the difference of only -0.02%.

7.1.3 Analysis of the Instantaneous Performance

The comparison of instantaneous efficiency and swallowing capacity characteristics is shown in Fig. 7.6 (a)-(b). Although the result was assessed for the rotor stage, a small hysteresis

behaviour is still existed in both maps due to the volume of blade passage, indicating the deviation from the quasi-steady assumption.

As shown in Fig. 7.6 (a), the $Max.\overline{\eta}_r$ candidate shows elevated rotor efficiencies under all design conditions (the velocity ratio ranging between 0.51 to 0.68). This is not the case for both $Max.W_r$ and $Opt.Steady$ candidate, where the deterioration of efficiency is shown when the velocity ratio greater than 0.62 for $Max.W_r$ and 0.66 for $Opt.Steady$. This indicates the deterioration in turbine performance when the turbine is operating under low loading conditions.

The instantaneous swallowing capacity characteristic is shown in Fig. 7.6 (b). All three designs demonstrate an overall increase in swallowing capacity characteristics. At the peak pulse point (pressure ratio of 2.45), the MFP of $Max.\overline{\eta}_r$, $Max.W_r$, and $Opt.Steady$ candidates is higher than the baseline by 1.44%, 5%, and 2.53% respectively.

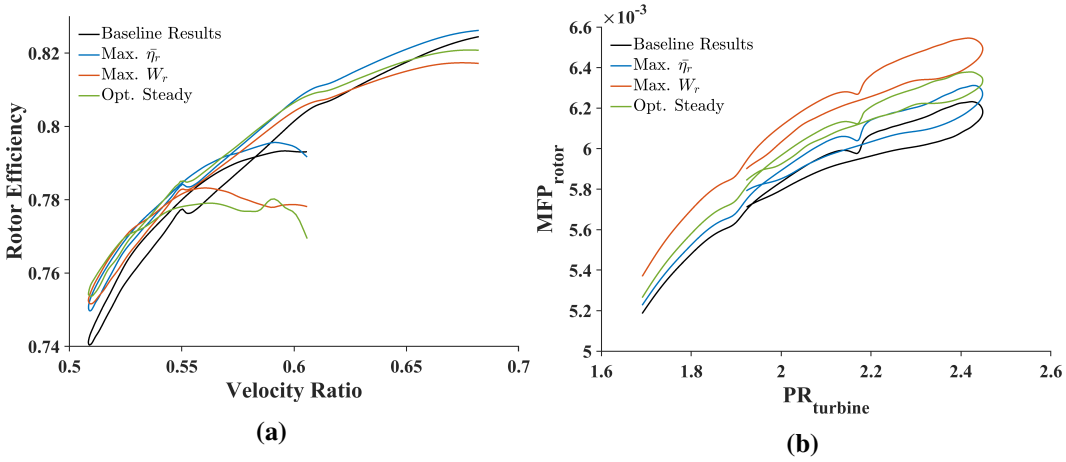

Figure. 7.6 comparison of (a) instantaneous efficiency and (b) instantaneous swallowing capacity characteristic

In order to have a full picture of the turbine performance, the three optimized designs and the baseline were analysed under steady-state conditions, subjected to a constant inlet temperature of 431.2K (mean value of unsteady instantaneous temperature), constant rotational speed of 120749.42 rev min^{-1} (same as the unsteady simulation), and the pressure ratio was varied

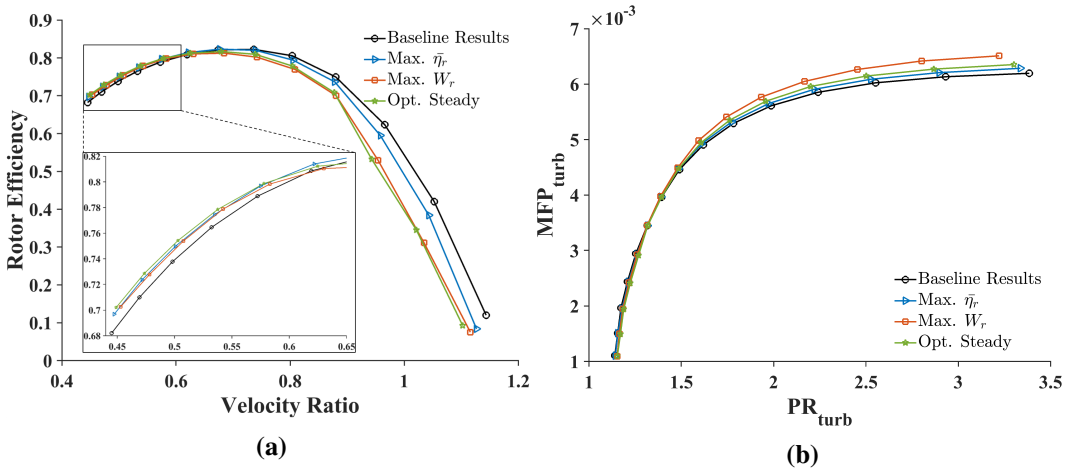

Figure. 7.7 Comparison of steady-state performance at the design speed (a) efficiency and (b) swallowing capacity characteristic

from 1.15 to 3.3. As shown in Fig. 7.7 (a), the largest efficiency gain (approximately 2%) is produced by the *Opt.Steady* candidate at the minimum velocity ratio. As the turbine operating points shift to the lower loading conditions (increase in velocity ratio), the efficiency of the three optimized designs shifts closer to the baseline, which is also observed in the unsteady results. However, with the extrapolated results from steady-state simulation, the $Max.\overline{\eta}_r$ candidate also shows a deterioration in efficiency when the velocity ratio greater than 0.7. Nevertheless, the $Max.\overline{\eta}_r$ is still the best optimized design as it preserves the turbine performance at low loading conditions. The turbine swallowing capacity characteristic under steady-state conditions has been shown in Fig. 7.7 (b), which follows the same trend as the unsteady conditions.

7.1.4 Flow Field Analysis of Two Operating Points During the Unsteady Operation

Flow field analysis was conducted in order to investigate the detailed loss mechanism within the rotor passage. Two specific turbine operating points (OP) are selected for this analysis. As shown in Fig. 7.8, first is corresponding to the peak power point (A) with the velocity ratio of

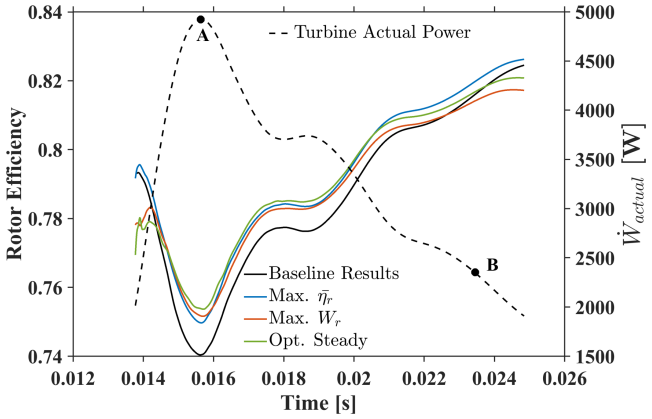

Figure. 7.8 Instantaneous Rotor Efficiency on top of the turbine actual power

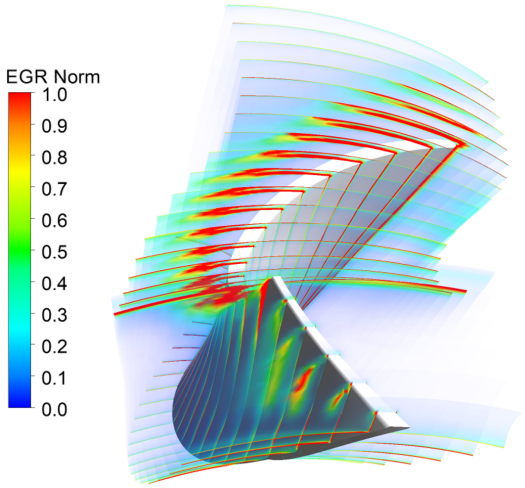

Figure. 7.9 Normalised entropy generation rate of the baseline result on sample of slices in the stream-wise direction

0.509, and the second point is located at the emptying stage during the pulse, corresponding to a medium loading condition with the velocity ratio of 0.644.

Fig. 7.9 shows the contour plot of the normalised entropy generation rate (EGR) per unit volume on sample slices in the stream-wise direction of the baseline blade. The EGR was calculated using the method suggested by [90, 91, 165]. According to their study, the entropy generation in turbulent flow can be broken down into four parts, as given in Eq. 7.1. The first two terms $\overline{\Phi}_d$ and Φ'_d signify the entropy generation due to viscous dissipation and turbulent dissipation respectively, whereas $\overline{\Phi}_c$ and Φ'_c represent the entropy generation due

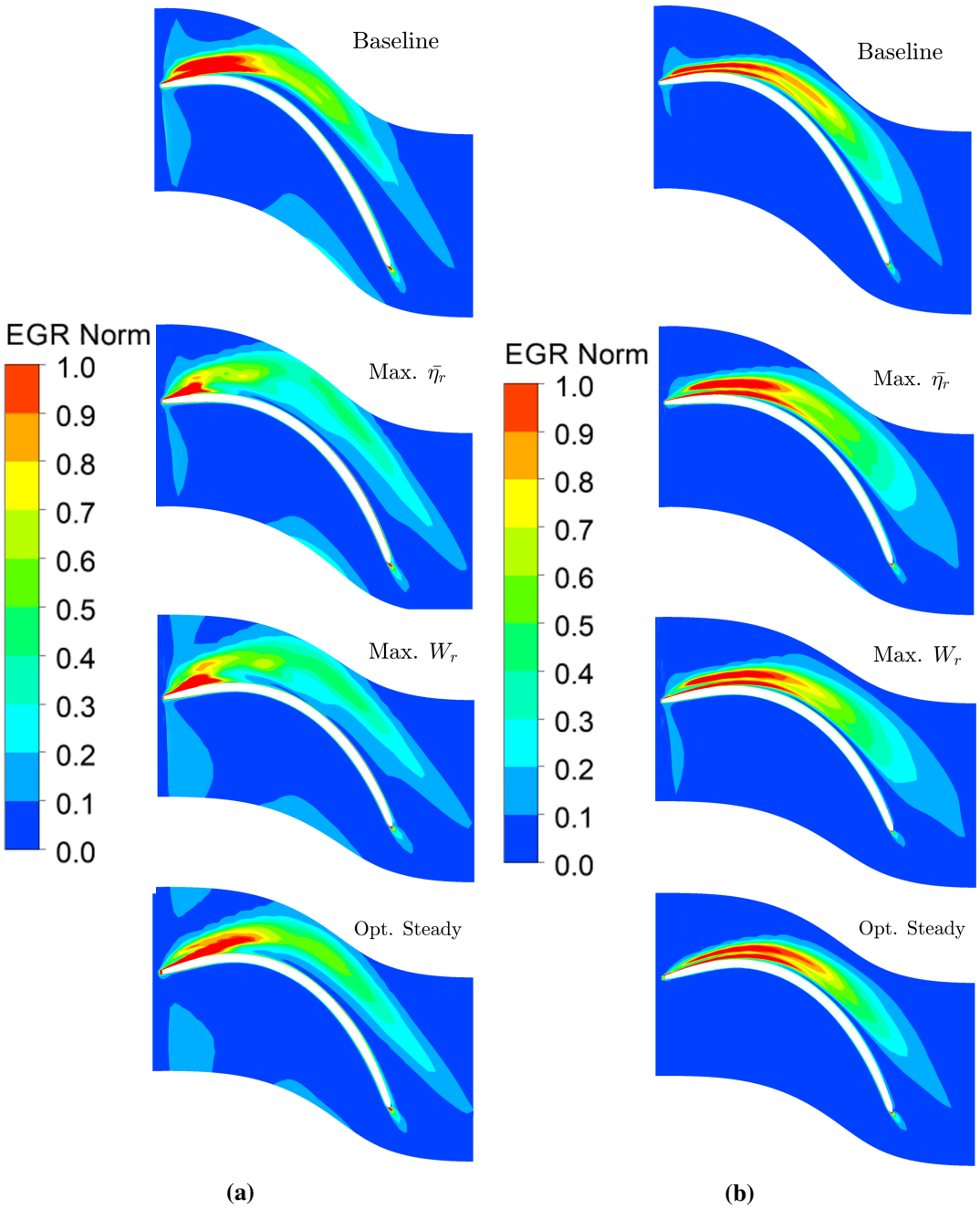

Figure. 7.10 Normalised Entropy Generation Rate at 95% Span between different designs at the operating point of (a) A and (b) B

to the averaged and fluctuation temperature gradients. The calculation of each term is given in the Appendix. As demonstrated in Fig. 7.9, the biggest contributor to the loss generation in the rotor is the tip leakage flows of the blade near the leading edge. In order to have an

intuitive comparison of the loss generations, Fig. 7.10 plots the normalised EGR at 95% span (closer to the shroud). The EGR at point A and B are normalised by the respective value of $1.3 \times 10^6\ Wm^{-3}K^{-1}$ and $9.2 \times 10^5\ Wm^{-3}K^{-1}$.

$$\frac{Ds}{Dt} = \frac{1}{\rho}\left(\overline{\Phi}_d + \Phi'_d + \overline{\Phi}_c + \Phi'_c\right) \tag{7.1}$$

Entropy generation due to viscous dissipation is computed as Eq. 7.2.

$$\begin{aligned}\overline{\Phi}_d = &\frac{\mu}{\overline{T}}\left\{2\left[\left(\frac{\partial \overline{u}}{\partial x}\right)^2 + \left(\frac{\partial \overline{v}}{\partial y}\right)^2 + \left(\frac{\partial \overline{w}}{\partial z}\right)^2\right]\right. \\ &\left. + \left(\frac{\partial \overline{u}}{\partial y} + \frac{\partial \overline{v}}{\partial x}\right)^2 + \left(\frac{\partial \overline{u}}{\partial z} + \frac{\partial \overline{w}}{\partial x}\right)^2 + \left(\frac{\partial \overline{v}}{\partial z} + \frac{\partial \overline{w}}{\partial y}\right)^2\right\}\end{aligned} \tag{7.2}$$

The entropy generation due to turbulence dissipation is calculated based on the turbulence dissipation rate ε, which is a known variable in Reynolds averaged turbulence models such as $k-\varepsilon$, $k-\omega$, SST, and extra.

$$\Phi'_d = \rho\frac{\varepsilon}{\overline{T}} \tag{7.3}$$

The losses due to the mean temperature gradient are computed by Eq. 7.4, where λ is fluid thermal conductivity.

$$\overline{\Phi}_c = \frac{\lambda}{T^2}\left[\left(\frac{\partial \overline{T}}{\partial x}\right)^2 + \left(\frac{\partial \overline{T}}{\partial y}\right)^2 + \left(\frac{\partial \overline{T}}{\partial z}\right)^2\right] \tag{7.4}$$

The last term of the entropy generation rate equation is computed as Eq. 7.5, where the turbulent thermal conductivity λ_t can be obtained by assuming the turbulent Prandtl number to be unity [166].

$$\Phi'_c = \frac{\lambda_t}{T^2}\left[\left(\frac{\partial \overline{T}}{\partial x}\right)^2 + \left(\frac{\partial \overline{T}}{\partial y}\right)^2 + \left(\frac{\partial \overline{T}}{\partial z}\right)^2\right] \tag{7.5}$$

$$Pr_t = \frac{c_p \mu_t}{\lambda_t} \tag{7.6}$$

These contours show that most losses are generated at the suction side of the blade near the leading edge. As shown in Fig. 7.10 (a), at the peak of the pulse (OP. A), the efficiency improvement of the three optimized designs is attribute to fewer loss generations near the leading edge, indicating a better flow incidence. However, at OP.B, the contour plots show a comparable pattern between these designs, revealing a similar EGR at 95% span.

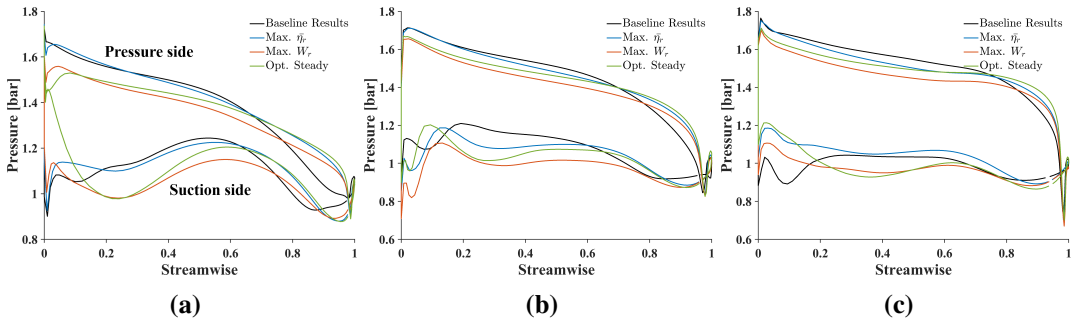

Figure. 7.11 Blade loading distribution (operating point A) at (a) hub (10% span), (a) midspan (50% span) and (c) shroud (90% span)

Fig. 7.11 and Fig. 7.12 demonstrate the blade loading as function stream-wise location (0 stands for the leading edge and 1 refers to the trialling edge) of OP. A and Op. B at three locations, that is the hub (10% span), the midspan, and the shroud (90% span). The size of the enclosed area indicates the amount of net torque generation, where the larger area the higher torque produced. In general, both $Max.W_r$ and $Opt.Steady$ candidates show a lower pressure

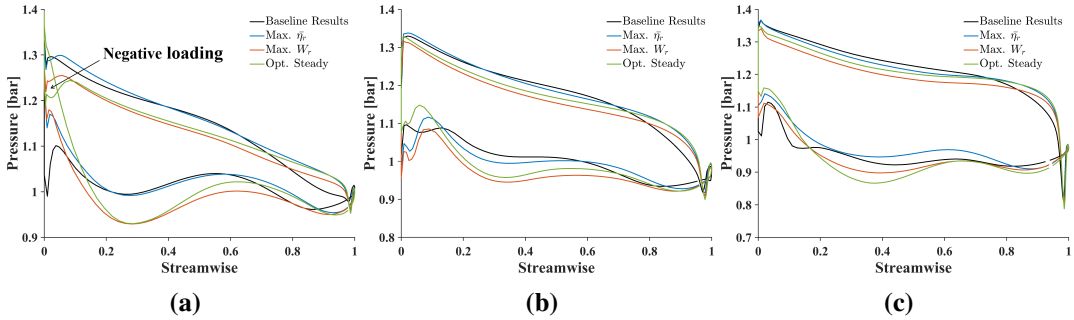

Figure. 7.12 Blade loading distribution (operating point B) at (a) hub (10% span), (b) midspan (50% span) and (c) shroud (90% span)

magnitude on both pressure side and suction side due to the higher swallowing capacities of these two designs. The blade loading improvement is more obvious in the midspan rather than in the hub and shroud. For example, in the midspan at both OP. A and OP. B, these three optimized designs show a pressure drop on the suction side at the stream-wise location between 0.2-0.6, leading to more torque produced in this region.

Although the $Opt.Steady$ candidate has the highest efficiency value at the OP. A, its blade loading performance shows the worst performance at the stream-wise location between 0-0.2, especially near the hub, which starts to produce the negative loading at the peak pulse (OP. A), and the negative loading becomes more obvious when shifts to OP. B. The $Max.W_r$ and $Max.\overline{\eta}_r$ candidates also reveal the performance deterioration in the same region (see Fig. 7.11 (a) and Fig. 7.12 (a)). Nevertheless, the blade loading deterioration in the hub of $Max.\overline{\eta}_r$ candidate is less significant compared with the other two designs. This could explain the reason that $Max.\overline{\eta}_r$ candidate has a better efficiency performance when the velocity ratio is high.

7.2 Results of Steady-State Optimization

This section presents the steady-state optimization results, obtained by two different optimization algorithms, namely a conventional genetic algorithm and a novel optimization algorithm based on the Kriging surrogate model. The objective of both algorithms was to

optimize the design parameters of both rotor and volute, in order to maximize the turbine efficiency at the point corresponding to the peak of a pulse (2.42 bar).

Fig. 7.13 shows the maximum turbine efficiency improvement compared with the baseline at the design point during the optimization process. The performance of the optimization algorithm based on Kriging surrogate (KS) model is compared with the corresponding GA, and the maximum number of function evaluations is set as 750. It is clear that the proposed optimization algorithm produces a better design at the end of the optimization, in which the gain in efficiency reaches 3.65 percentage points (pp). The optimal design produced by GA has an efficiency improvement of 3 pp. Besides, the KS based algorithm tends to achieve the optimal design at a higher rate.

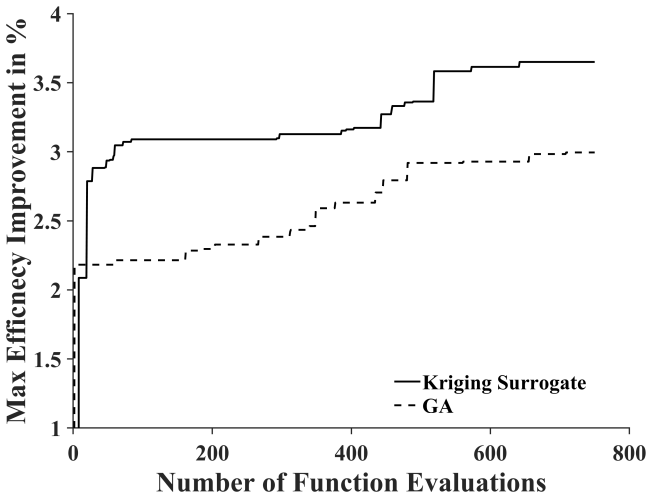

Figure. 7.13 The maximum turbine efficiency improvement during the optimization process, compared between Kriging surrogate based optimization algorithm and GA

The design parameters of the turbines optimized based on KS and GA are listed in Table. 7.3. The derived parameters are listed in Table. 7.4, including the blade camber angle at leading ($\phi_{\beta,3}$) and trailing edge ($\phi_{\beta,4}$), blade angle (β_{B3} calculated according to Eq. 2.12) at the leading edge, optimal velocity ratio (VR_{opt}), volute tongue cross-sectional area ($Area_{tongue}$), degree of reaction (RN), and the mass of the rotor, which is normalised by the baseline value.

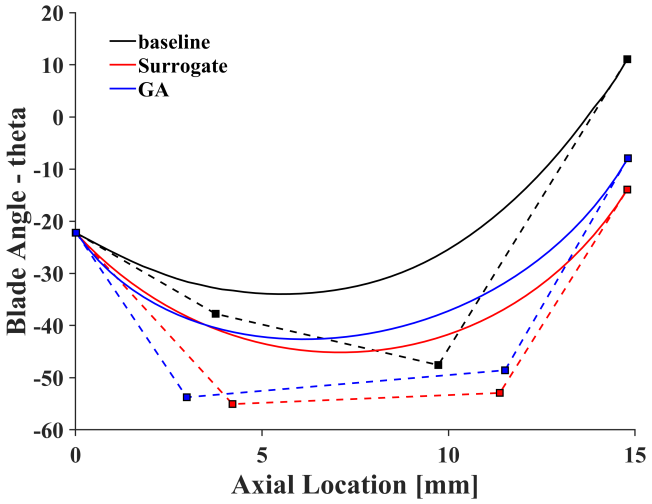

Figure. 7.14 Blade camber-line distribution of optimized cases and baseline

Table 7.3 Design parameters of the optimized turbines

Domain	Parameters	Unit	KS	GA
Rotor	γ	°	89.97	80.00
	d_{axial}	mm	0.00	0.02
	$\Delta X_{Pt.2}$	mm	0.45	-0.79
	$\Delta\theta_{Pt.2}$	°	-17.31	-16.00
	$\Delta X_{Pt.3}$	mm	1.65	1.77
	$\Delta\theta_{Pt.3}$	°	-5.35	-1.00
	$\Delta\theta_{Pt.4}$	°	-25.00	-19.00
Volute	K_{ellip}	-	1.40	1.44
	K_{tongue}	-	0.7	0.78
	w	mm	6.02	6.58
	R	mm	22.91	29.36
	$Pt.5X$	normalised	0.51	0.56
	$Pt.5Y$	normalised	0.77	0.71

Note that the subscript h, m, and s represent the data was taken from blade hub, midspan, and shroud respectively.

The results show that both optimized cases produce similar results regarding the d_{axial} and K_{ellip}. Besides, both cases generate the almost linearised distribution of the volute's cross-sectional across the circumference. But the blade camber-line distributions show a big difference compared with the baseline, as shown in Fig. 7.14. As also indicated in the blade meridional profile in Fig. 7.15, both optimized designs show a larger cone angle than the baseline data (60°), especially the KS case, which has a cone angle of approximately

Table 7.4 Derived parameters of optimized turbines

Parameters	Unit	Baseline	KS	GA
$\phi_{\beta,3h}$	°	-30.45	-44.32	-54.37
$\phi_{\beta,3m}$	°	-24.05	-29.06	-27.04
$\phi_{\beta,3s}$	°	-15.70	-15.74	-10.64
β_{B3h}	°	-16.38	0	-13.62
β_{B3m}	°	-12.58	0	-5.07
β_{B3s}	°	-8	0	-1.87
$\phi_{\beta,4h}$	°	49.69	47.78	49.83
$\phi_{\beta,4m}$	°	61.98	57.40	58.18
$\phi_{\beta,4s}$	°	68.51	65.37	66.09
VR_{opt}	-	0.7	0.61	0.61
$Area_{tongue}$	mm^2	256	179.2	199.7
RN	-	44.2%	35.2%	36.7%
$mass$	normalised	1	1.1	1.06

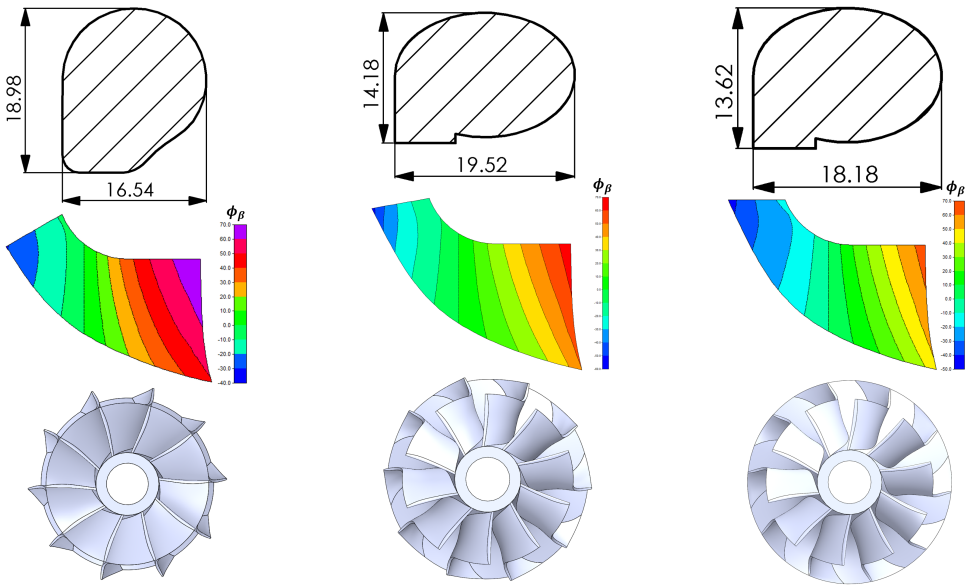

Figure. 7.15 Comparison of turbine geometric features, including volute cross-sectional profile at the tongue, blade meridional profile (with color map showing the blade camber angle in β), and 3D view of rotor, (a) baseline (b) GA optimized (c) KS optimized turbines

90°. This implies that the optimized blade tend to be transformed into a radial flow turbine, since they have a lower inlet blade angle (absolute value) at hub (β_{B3h}), midspan (β_{B3m}), and shroud (β_{B3s}), as listed in Table. 7.4. The larger cone angle also marginally increases the turbine mass. According to the conventional theory, the larger cone angle together with a

smaller inlet blade angle will increase the optimal velocity ratio, thereby deteriorating the turbine performance under the high loading conditions. However, this is not the case in this study since the results show that the efficiency of optimized turbines was improved at high loading conditions.

$$RN = \frac{H_3 - H_4}{H_1 - H_4} \tag{7.7}$$

The distinct difference regarding the volute's design parameters lies in the tongue area factor K_{tongue}, tongue to wheel distance R and volute exit width w. KS based design has a smaller value of K_{tongue} and w, which leads to a smaller flow area at both of the volute inlet and exit, as demonstrated in Fig. 7.15. The small flow area will develop a higher flow velocity at the inlet and exit of the volute under the same boundary condition. This means that more the optimized volutes have the greater ability to accelerate the flow to higher kinetic energy, thereby affecting the degree of the reactions (RN). The degree of reaction, as defined in Eq. 7.7, describe how the static enthalpy drop (ΔH) is divided by the stator and rotor [167]. A lower value corresponds to a larger part of acceleration taking place in the stator than the rotor, and a higher value results in a reverse situation. The degree of reaction is typically 50% for most RFT. Both KS and GA cases produce a RN (the former is 35.2%, the latter is 36.7%) lower than the baseline value of 44.2%, suggesting the optimized turbines contribute to a higher enthalpy drop in the stator stage than the baseline.

7.2.1 Loss Analysis

The loss generation in each domain has been analysed to figure out the reasons for efficiency improvement. Note that the volute and the vaneless nozzle have been altogether denoted as the stator. The overall entropy generation through each domain can be evaluated by Gibb's

equation, as per Eq. 7.8, across the inlet and outlet planes of the domain. Since the all the walls are defined as adiabatic, the heat transfer term $\dot{Q}$ can be eliminated.

$$\dot{S} = \dot{m}(s_{out} - s_{in}) - \frac{\dot{Q}}{T} \tag{7.8}$$

Where,

$$s_{out} - s_{in} = c_p ln(\frac{T_{out}}{T_{in}}) - Rln(\frac{P_{out}}{P_{in}}) \tag{7.9}$$

As shown in Fig. 7.16, it is observed that the performance improvement of optimized turbines mainly due to the less loss generated in the exit duct domain, namely the exit losses. The exit loss normally related to the exit kinetic energy since it is normally unused. The loss generations in the rotor domain are comparable. The GA optimized turbine has the minimum exit loss generation. The KS optimized turbine has the overall best performance due to the smallest loss generation in both stator and rotor domain, though it produces larger exit losses than the GA case.

Fig. 7.17 compares the averaged circumferential velocity in the meridional plane between the baseline and the KS optimized turbine. The circumferential velocity represents for the tangential component of the exit flow, and leads to the exit swirl. A general principle of turbine design is that the exit swirl should be close to zero to minimise the exit dynamic head, thereby minimizing the exit losses [168]. It is clear that the optimized turbine has decreased the tangential component of the exit flow. Therefore, the efficiency improvement of optimized turbines is mainly due to a lower exit kinetic energy produced.

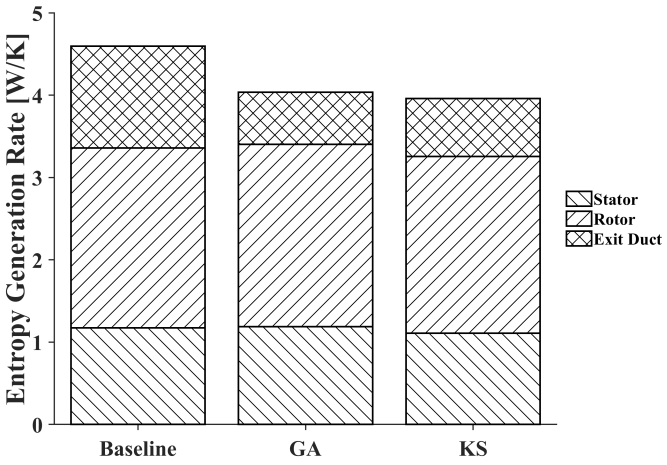

Figure. 7.16 Entropy generation rate in different domains of three turbines at the design point

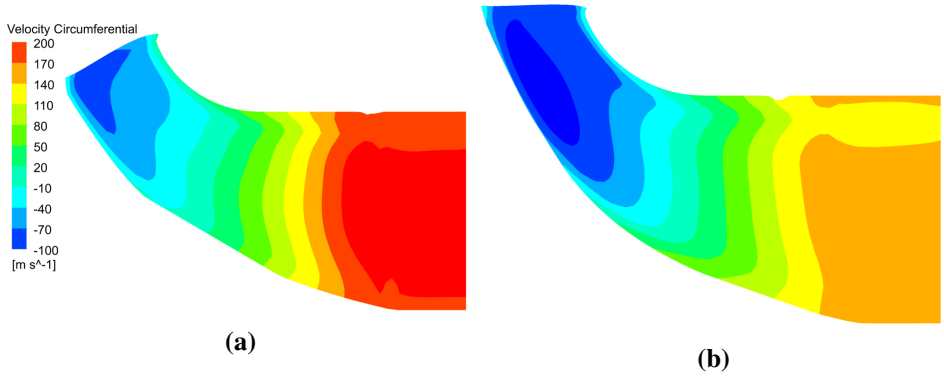

Figure. 7.17 Averaged circumferential velocity in the meridional plane (a) baseline (b) KS optimized turbine

Fig. 7.18 shows the contour plot of the normalised entropy generation rate per unit volume on the meridional plane. As one would expect, the baseline shows that the exit duct has a larger region of high EGR that result in the performance deteriorations. To demonstrate it more clearly, Fig. 7.19 shows the EGR contours and the velocity vector filed on the sample slice of the exit duct as highlighted in Fig. 7.18. The swirls of the baseline turbine are much significant than the KS contour-part, leading to higher loss generations.

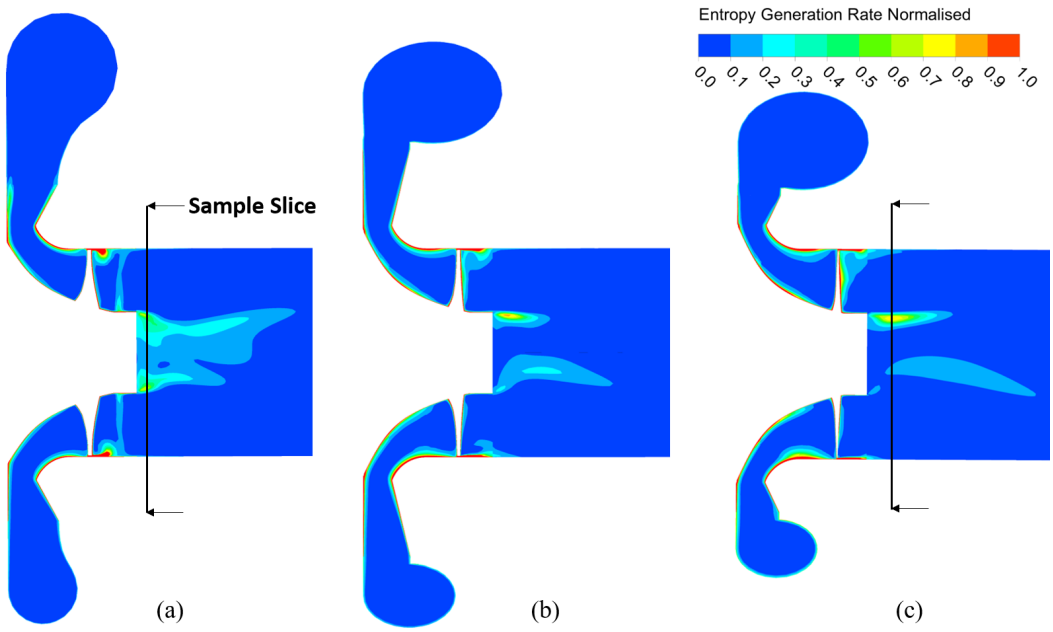

Figure. 7.18 Contour plot of normalised entropy generation rate on the meridional plane of (a) baseline (b) GA and (c) KS optimized turbine

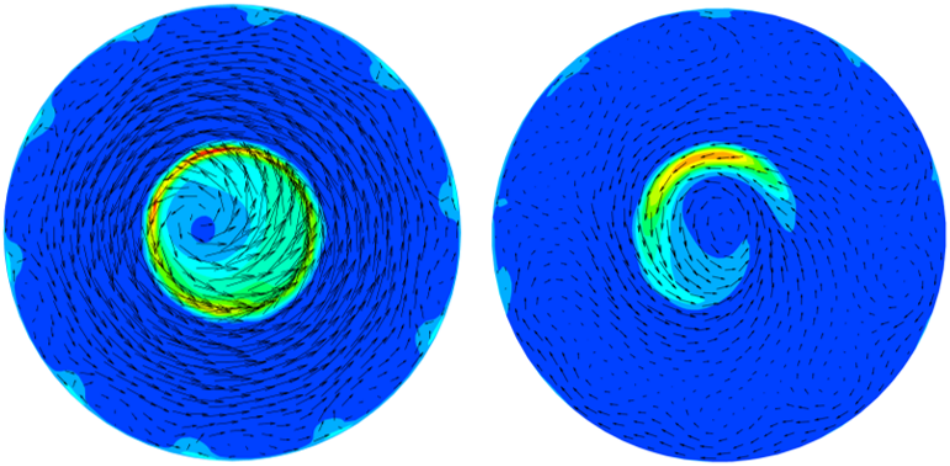

Figure. 7.19 Normalised entropy generation rate and velocity vector field on the sample slice of the exit duct of (a) baseline (b) KS optimized turbine

7.2.2 Flow Field Analysis - Volute

Fig. 7.20 shows the comparisons of the volute exit absolute flow angle as a function azimuth angle at the design point. The flow angle, taken from the middle line of the circumference, is the angle between the flow velocity component in the radial direction and the circumferential

direction. The three cases, namely the baseline, surrogate, and GA optimized turbines, resulting in a similar averaged flow angle, which is 81.6°, 80°, and 83° respectively. The peak to peak difference of flow angles of the three cases is 10.7°, 11.4° and 7.8°. It is clear that the distributions of the flow angle in the circumference of volute exit are not uniformly distributed. A large fluctuation is observed in the near tongue region, implying the strong wake and flow separation effects. The GA optimized turbine has shows the smallest fluctuation of the flows in the near tongue region. All three cases show a drop in flow angle when the azimuth is greater than 250°, implying the drop of the circumferential velocity, and the drop is more significant in the KS case.

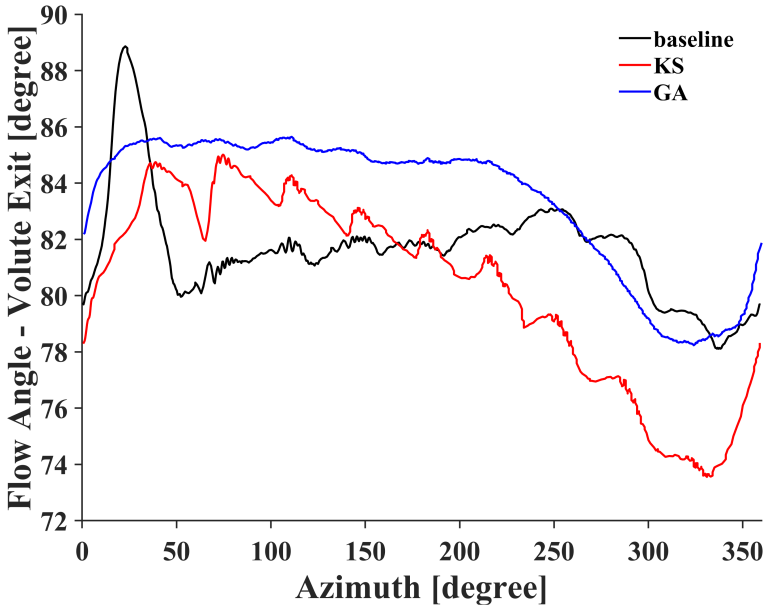

Figure. 7.20 Volute exit flow angle (absolute) at the design point, taken from the middle line of the circumference

Fig. 7.21 demonstrates the pressure filed in the stator region at the design point, in which the black circle represents the circumference of volute exit. It can be observed that the tongue design has a large impact on the flow field. The tongue design of the baseline produces significant disturbance, which can lead the generation of enthalpy losses. Besides, the flow filed is also influenced by the tongue to wheel distance. The KS optimized turbine has the smallest tongue to wheel distance, so that the largest pressure gradient was developed

upstream of the rotor. This can also be confirmed by the secondary fluctuations in the red curve shown in Fig. 7.20. Larger secondary fluctuations will be produced as reducing the tongue to wheel distance. This can be deemed as another factor that deviates the volute from the free-vortex assumption.

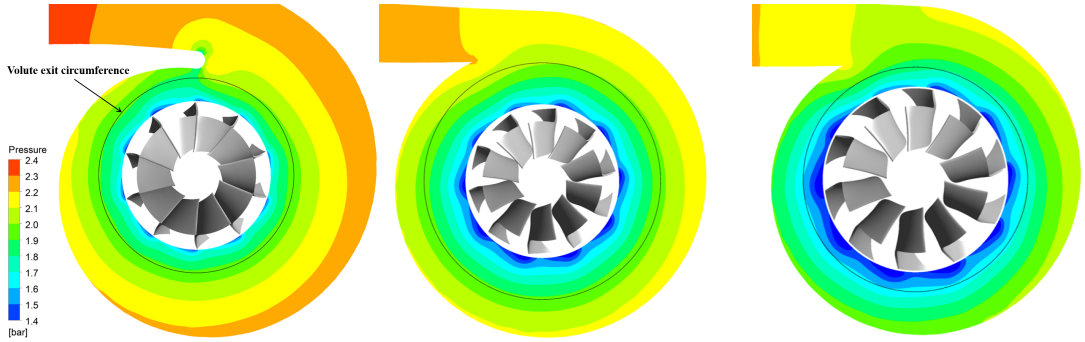

(a) **(b)** **(c)**

Figure. 7.21 Pressure distributions in the midspan of stator at the design point (a) baseline (b) GA optimized turbine (c) KS optimized turbine

7.2.3 Flow Field Analysis - Rotor

Fig. 7.22 shows the blade loading analysis at 10% span (close to the hub), 50% span and 90 % span (close to the shroud). It is observed that optimized designs have a lower averaged pressure force acting on the blade surface even though they have the same inlet total pressure. That is because the optimized designs have smaller flow areas at the inlet and the exit of the volute. As indicated by the tongue area factor K_{tongue} in Table. 7.3, the flow area of the KS and GA optimized turbines are corresponding to 70% and 78% of the baseline. Since the overall available flow energy to the turbine is similar in the three cases, a smaller cross-sectional area will accelerate the flow to higher kinetic energy. Thus, the remaining static energy will be reduced, appeared as lower static pressure. Nevertheless, the torque was produced by the pressure difference between the pressure side and the suction side of the blade, indicated as the enclosed area of the blade loading curves.

It can be observed that the optimized turbines show a better performance in the 0.2-0.4 stream-wise location, i.e. greater pressure difference between the pressure surface and suction surface. Besides, the optimized turbines show an overall improvement in the midspan.

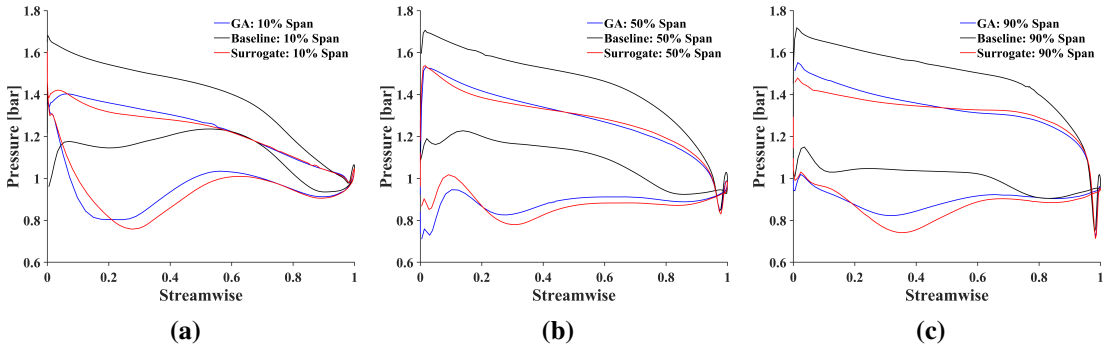

Figure. 7.22 Blade loading analysis at (a) 10% span (b) 50% span (c) 90 % span

Fig. 7.23 shows the blade to blade velocity filed of the three cases. A significant difference between the optimized turbines and the baseline turbine is that the formers have achieved a higher flow velocity at the suction side between the 0.2-0.4 stream-wise location, especially when the azimuth angle is from 0° to 180°. Higher velocity in the suction side indicates the blade converts the flow to higher kinetic energy, thereby decreasing the static pressure on the suction side, which is beneficial to the blade loading characteristic, as observed in Fig. 7.22.

7.2.4 Quasi-steady Analysis

To have a whole picture of the turbine performance at the design speed (120.75 krpm), this study evaluated the steady-state turbine performance based on the optimized designs. Fig. 7.24 shows their performance compared with the baseline data. Both cases show a general smaller swallowing capacity compared with the baseline. The difference is small as it moves to the design point and subsequent choking point. The efficiency characteristic shows big differences compared with the baseline. Both KS and GA cases shift the optimal velocity ratio from the baseline value of 0.7 to 0.61. The efficiency becomes higher than the baseline value when the velocity ratio smaller than 0.57. This implies that the turbine performance is improved under high loading conditions so that more flow energy will be absorbed near

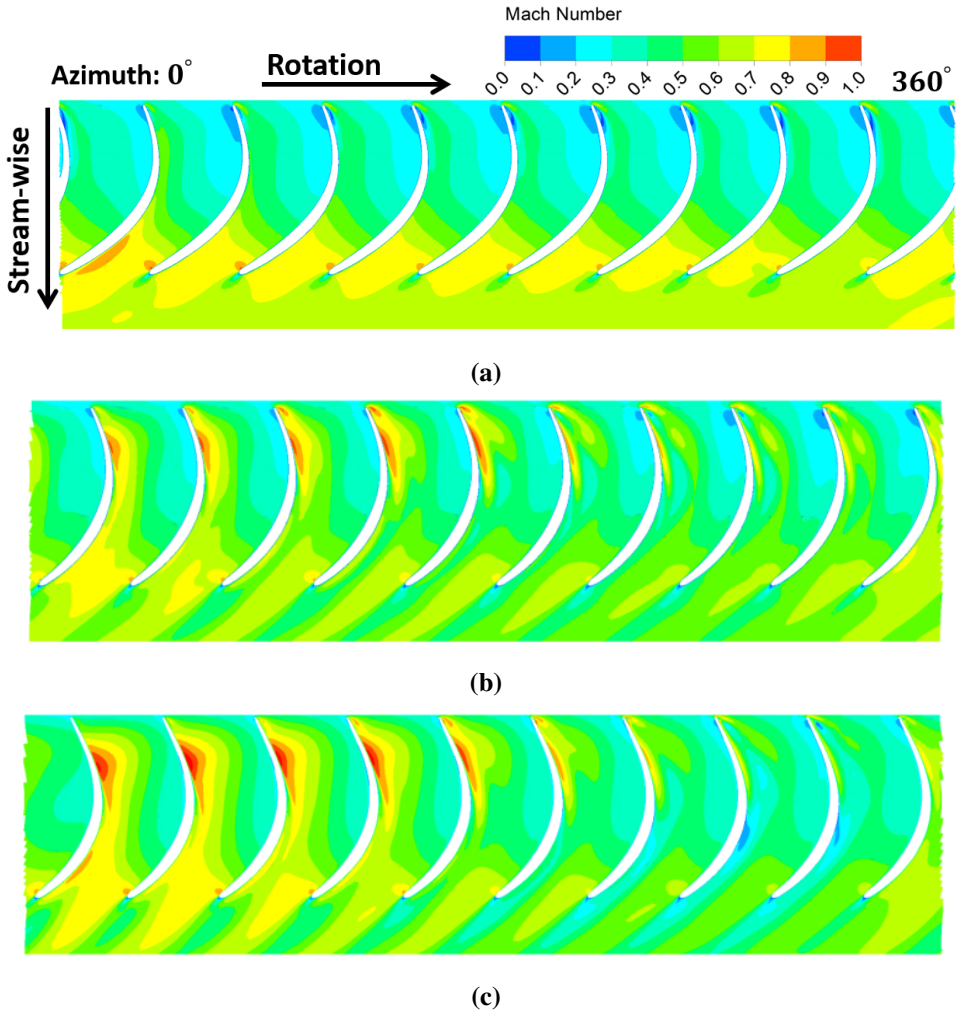

Figure. 7.23 Velocity flow filed in the blade passage at the midspan of (a) baseline (b) GA optimized (c) KS optimized turbine

the peak pulse regions. However, the new designs show the deterioration of performance when it operates under low loading conditions. The peak efficiencies of KS and GA based designs are dropped by 4 pp and 4.5 pp respectively. The deterioration is even greater under extreme low loading conditions. This implies the mean turbine performance over a pulse is highly influenced by the magnitude of pulse. In other words, the new designs will have a better chance to extract more flow energy so that offset the worse off-design performance when it is subjected to the pulses of higher magnitude.

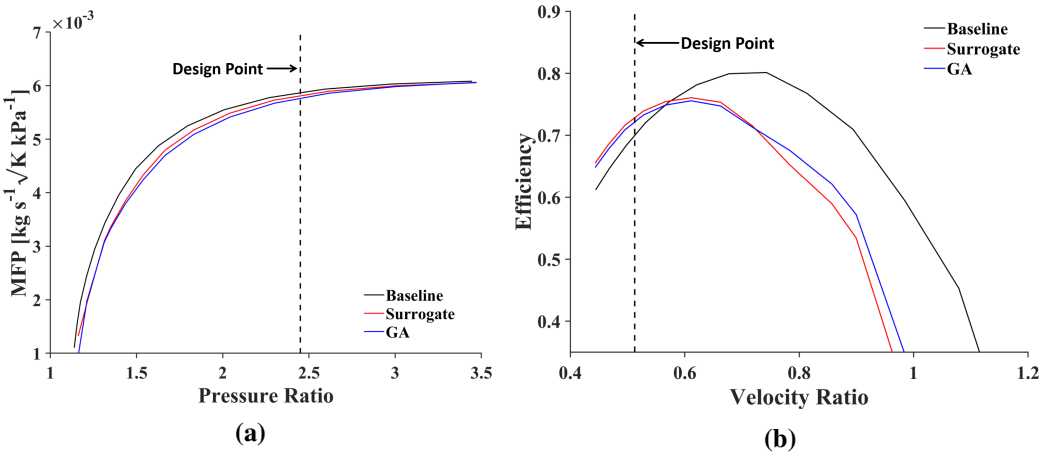

Figure. 7.24 Comparison of turbine performance between the optimized designs and the baseline (a) swallowing capacity characteristic (b) efficiency

This was tested by using the generic pulses, as shown in Fig. 7.25, which was modified based on the pulse profile that was taken from the exhaust pressure of a three-cylinder engine. The peak pressure of the pulse is modified from 2 bar to 4 bar so as to study the influence of the pulse magnitude on the turbine cycle-averaged performance. The quasi-steady assumption was applied for this analysis, where the turbine unsteady performance is assumed to be the same as the corresponding steady-state performance at any instantaneous of time. The energy generation during the pulse period was calculated as per Eq. 7.10, where the $\dot{W}_{isen}$ and $\eta(t)$ are the instantaneous isentropic power and the instantaneous efficiency respectively. Fig. 7.26 shows the influence of the peak pressure of the generic pulse on the energy generation compared with the baseline. Due to the higher efficiencies on the low velocity ratio regions, the optimized turbines have a better chance to increase the power generation at the peak of the pulse. The KS optimized turbine has a better performance when the peak pulse pressure is greater than 2.98 bar, whilst the value for the GA optimized turbine is 3.3 bar.

$$W = \int_{t=0}^{TT} \left[\dot{W}_{isen}(t) \cdot \eta(t)\right] dt \tag{7.10}$$

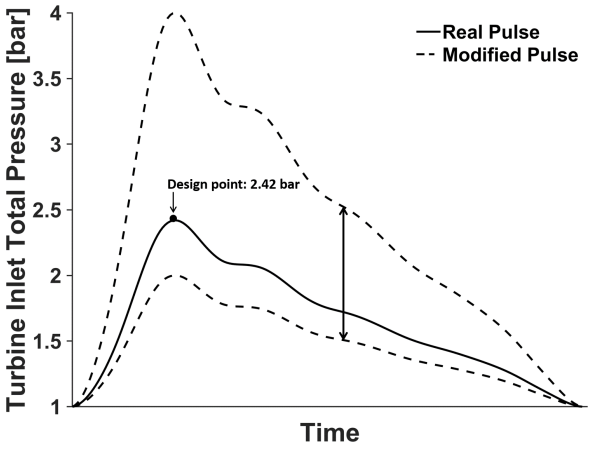

Figure. 7.25 Generic pulse used to simulate the mean turbine performance during one pulse

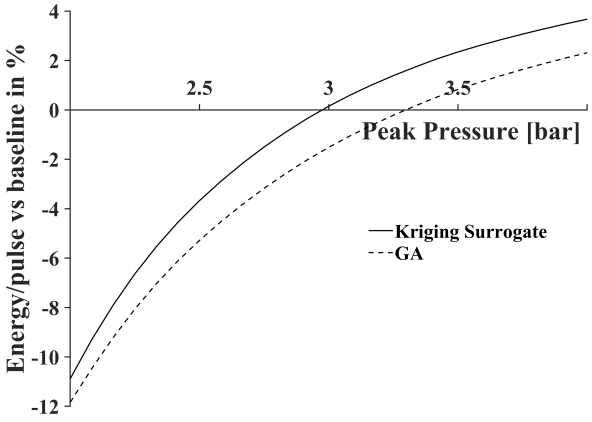

Figure. 7.26 Energy generation per pulse as a function of peak pulse pressure compared with baseline

7.2.5 Elementary Effectiveness Analysis

The optimization results produced a large database, containing about 1500 turbine designs. It is worthwhile to utilize the database study the influence of the turbine design variables on the turbine performance. A MATLAB SAFE toolbox developed by Pianosi et al. [169] is employed to perform the analysis. A screening method named elementary effects (EET) method used to measure the individual sensitivities. The EET method is based on the One-At-a-Time (OAT) method that only one variable is given a new value in each calculation. If one variable changes by the same amount (Δ) but causes the largest variation in the output, this variable will be considered to have the largest elementary effects. Consider a model with k independent variables $X_i,\ i = i,...,k$, in which the design space is constructed in the

k-dimensional cube. The cube is then discretized into a p-level grid, over which the variables can be sampled. The elementary effect of variable X_i is calculated as per Eq. 7.11, where p is the number of levels, Δ_i is a value in $\{1/(p-1), 2/(p-1), ..., 1-1/(p-1)\}$. Each OAT loop contains k+1 different designs, including a base element X_{base} and k different designs, in which only one variable X_i offsets corresponding base value by Δ_i, as shown in the OAT matrix Eq. 7.12.

Denoting r as the number of different OAT matrix, the mean elementary effects of X_i can be calculated as Eq. 7.13. The OAT method requires the overall number of design candidates to be $r(k+1)$, where r is 6500 and the overall number of design candidates is 91000 in this study. Latin Hypercube Sampling was used to generate the 6500 base candidates, and the rest were produced according to Eq. 7.12. The Kriging surrogate model was fitted by the database so as to perform the EET calculation. Note that the ineffective design candidates, which were assigned by the penalty equation, were screened out from the database since their results do not reflect the aerodynamic performance of the corresponding turbines.

$$EE(X_i) = \frac{f(X_1, X_2, ..., X_i + \Delta_i, ...X_k) - f(X_1, X_2, ..., X_k)}{\Delta_i} \tag{7.11}$$

$$
\begin{aligned}
X^r &= \begin{bmatrix} 0 \\ I_k \end{bmatrix} \Delta + X_{base} \\
&= \begin{bmatrix} 0 & 0 & 0 & \cdots & 0 \\ 1 & 0 & 0 & \cdots & 0 \\ 0 & 1 & 0 & \cdots & 0 \\ 0 & 0 & 1 & \cdots & 0 \\ \vdots & \vdots & \vdots & \ddots & \vdots \\ 0 & 0 & 0 & \cdots & 1 \end{bmatrix} \begin{bmatrix} \Delta_1 \\ \Delta_2 \\ \vdots \\ \Delta_i \\ \vdots \\ \Delta_k \end{bmatrix} + \begin{bmatrix} X_1 \\ X_2 \\ \vdots \\ X_i \\ \vdots \\ X_k \end{bmatrix}
\end{aligned} \tag{7.12}
$$

$$
\mu_{EE} = \frac{1}{r} \sum_{j=1}^{r} EE(X_i^j) \tag{7.13}
$$

In order to have confidence regarding the accuracy of the model prediction, the database was randomly split into two datasets. The first part is referred to the training dataset, containing 90% design candidates of the database, which was used to fit the surrogate model. The remaining datasets, named as the test dataset, were used to evaluate the model performance. Fig. 7.27 shows the model can perform satisfactory predictions, with the coefficient of determination (R^2) of 0.977 and root mean squared error of 3.96×10^{-3}. The accuracy is higher for the case that has higher efficiency, since there have more effective candidates fitted for the model.

The effectiveness of each variable normalised by the peak value is shown in Fig. 7.28. The most influential parameter is the tongue area factor K_{tongue}. This is in the expectation because this parameter influences the acceleration of the fluid across the volute thereby affecting the degree of reaction. The following four parameters after the K_{tongue} are related to the

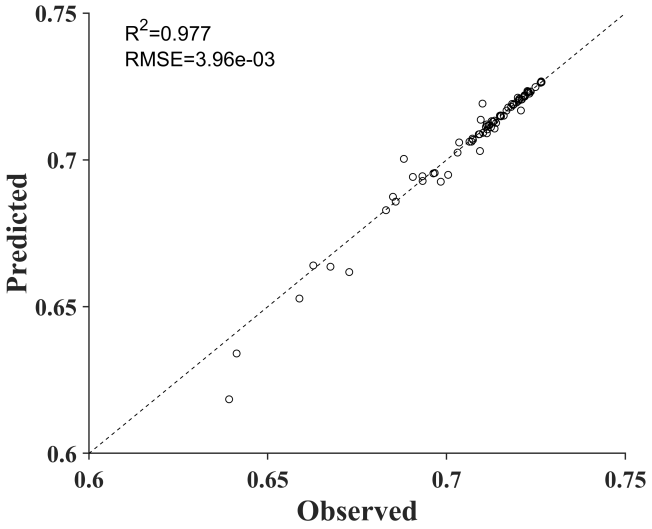

Figure. 7.27 Turbine efficiency prediction by the KS model, fitted by 90% of the datasets and tested by the remaining (10%) of the datasets

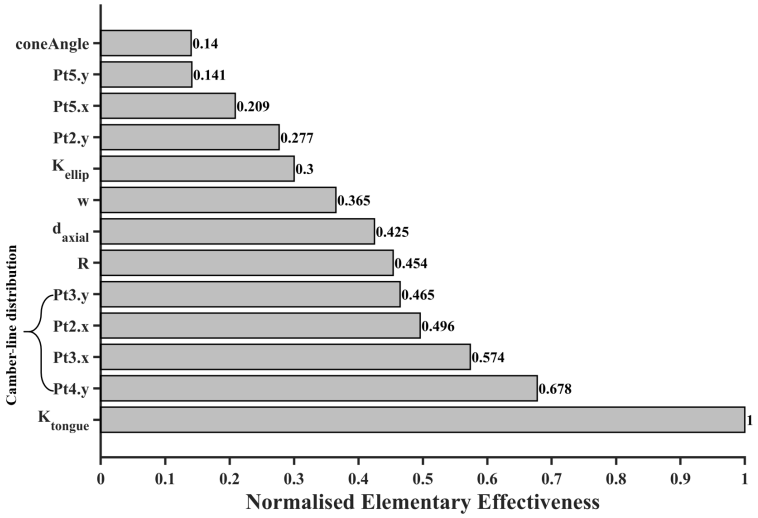

Figure. 7.28 Elementary effectiveness analysis of the turbine design variables

camber-line distribution, and their overall elementary effectiveness is more than twice of the K_{tongue}, implying the camber-line distribution of the blade plays a crucial role in the turbine performance.

CHAPTER 8

CONCLUSION

The main conclusion of the PhD study can be arranged in three sections based on the corresponding objectives as have explained in Section. 1.5.

8.1 Benefits of the Unsteady Mapping Approach

As is evident from the large body literature on the topic, the conventional way of mapping the characteristic map of turbocharger turbines using steady-state approach is not suitable for the purpose when deployed in 1D modelling software where there are large-amplitude flow pulses present. There is a combination of reasons why such maps tend to be inaccurate, but certainly include limited data range, poor or non-physical extrapolation, lack of negative efficiency, steady-frictional loss and the reliance on the quasi-steady assumption. With this in mind, this study has shown that it is possible to conceive of a new approach to mapping turbocharger turbine behaviour using *dynamic* measurements made during a single pulse. This approach has the following advantages:

1. It creates a very broad range of data that is only achievable in steady-state using a turbine dynamometer. However, since this data is created during a pulse, a standard compressor loading is all that is needed, greatly simplifying the test arrangement and setup.
2. It gives access to information during the negative efficiency phase of the pulse that is not possible to measure with steady-state mapping. This has shown to be especially

important during low frequency pulses or during cylinder deactivation. This negative efficiency period is created where the energy in the rotating inertia of the turbocharger is being dissipated into the exhaust stream (wind-milling).

3. The uses of a compressor as a loading device means that turbine power is partially calculated from the compressor thereby including mechanical efficiency (friction) into the turbine efficiency data. This means that the turbine map already contains reliable information on the dynamic changes in mechanical friction during a pulse.
4. Any differences in turbine efficiency that may be due to the unsteady fluid dynamics within the turbine will be captured since the map is generated from the most realistic flow behaviour. It is well known that efficiency multipliers are often applied to turbine maps in an industrial setting once it becomes clear from engine testing that the prediction based on steady-state maps overestimates the power delivered to the compressor.

According to the assessment of negative turbine power, it found the percentage of negative power has a negative correlation with pulse frequencies, and the magnitude is higher when engine adopts cylinder deactivations. The maximum negative work portion can reach to approximately 15% in three cylinder mode under 19.7 Hz pulses, and up to 17.8% in two cylinder model under 25.8 Hz pulses. However, the negative portion is negligible when the pulse frequency over 50 Hz, corresponding to 2000 rpm engine speed of a three cylinder engine. The proposed turbocharger model showed the ability to predict negative turbine power. By using the negative efficiency in the turbine map, the simulation results showed a clear improvement in terms of turbine speed and compressor power prediction. For the 20 Hz case, if the negative efficiency is not taken into account, the error of mean speed prediction will be increased by approximately 3%. As a consequence, the error of compressor power prediction is increased by approximately 7.9%. Moreover, if the steady-state data for

simulations is used directly, it may result in even larger errors. Thus, this clearly demonstrates the superiority of the proposed unsteady mapping methodology.

Literature findings showed that the turbine can operate at a negative power under low load conditions, but few of them analysed the influence of negative turbine power in turbocharger simulations. This probably due to the difficulties of using unsteady turbine maps in simulations as well as the inability of entering negative efficiencies in the turbine block provided by the commercial 1D codes. It is clear from this work that if the negative power is not considered in low frequency pulses, it will introduce sources of error in turbocharged engine simulations.

The main contribution of this work is the proposal to use unsteady data to help inform turbine maps. This approach in combination with a robust fitting strategy informed from physically based models of the turbine should address many of the shortcomings in the current industry-wide method of steady-state mapping on gas stand.

8.2 Advantages of the Unsteady Optimization Approach

This thesis presents a novel method of optimizing a mixed-flow turbine rotor under pulsating flow conditions. The objective of the optimization is to maximize turbine efficiency (energy-weighted) and work output for a specific pulse period.

Seven design variables that define the rotor cone angle, axial location, and camber-line distributions were considered during the optimization process. Design constraints were applied to ensure the maximum variation of turbine swallowing characteristic is constrained within $\pm$ 5%. In order to reduce the number of design parameters without sacrificing the variety of blade shapes, the blade angles were defined in the *theta* criteria. To reduce the internal stress due to the rotation, all blade layers are remained in the same camber-line angle distributions from the leading edge to the trailing edge. The unsteady optimization

was conducted under 50 Hz pulses. The time-step was chosen as corresponding to $10^{\cdot\circ}$ of rotation. Single point steady-state optimization was also conducted at the peak pulse point in order to compare the optimized results against unsteady optimization.

The optimized designs were validated by using the full-rotor sliding-mesh approach. The simplified model, namely the single-passage and frozen rotor approach, can produce comparable results as the complex model. The cycle-averaged performance between them is generally lower than 2%. Regarding the instantaneous performance, the largest deviation occurs when the pulsation energy reaches the maximum value.

The optimal design with respect to the maximum efficiency (known as $Max.\overline{\eta}_r$) during a pulse was obtained from unsteady optimizations, with a performance benefit 0.66 percentage points. The optimal design produced by steady-state optimization (known as $Opt.Steady$) has a comparable averaged efficiency during the unsteady simulation, but shows performance deterioration at off-design conditions when the velocity ratio greater than 0.66. Although the $Max.\overline{\eta}_r$ candidate also shows efficiency reduction when the velocity ratio greater than 0.7, it preserves the most low-loading performance noticed by the small difference compared with baseline.

Regarding the maximum energy output, the optimal design was also produced from the unsteady optimization (known as $Max.W_r$) with a performance gain of 5.42%. The major reason for turbine power increment was found to be the increased turbine swallowing capacities. From the flow field analysis, it is found that the suction side produces most of the losses. The efficiency improvement of the three optimized designs could be attributed to a better flow incidence near the shroud.

From the blade loading analysis, the performance gains were found to be the result of better blade loading distribution in the midspan at stream-wise locations between 0.2-0.6. However, All these three optimized designs show worse blade loadings in the hub at the stream-wise

locations between 0-0.2, especially the *Opt.Steady* candidate, where negative blade loading was observed at OP. B, as shown in Fig. 7.12.

Although the steady-state optimized blade produced higher efficiency at the peak pulse point, its worse performance under medium to low loading conditions offset the overall performance under unsteady flow conditions. The unsteady optimization method takes into account a broader range of operating conditions, thus more likely to produce a design that suits better to pulsating flow condition. Note that only 199 different candidates generated from unsteady optimization produces a better result than 961 different candidates generated from steady-state optimization. One interesting approach that would seek to better represent the pulse without the need to run a fully unsteady transient boundary condition is to apply a series of steady-state points beyond just the condition at the peak of the pulse. By applying appropriate weightings to these in the optimization, it may be possible to obtain the benefits of a fully unsteady optimization whilst being substantially quicker.

8.3 Superiorities of the Novel Global Optimization Method

This study has utilized a novel optimization method based on the Kriging surrogate model to optimize a mixed flow turbine, aiming at maximizing the turbine efficiency at a design point corresponding to the peak of a pulse. The optimization method takes advantage of a specific search pattern to avoid the solution to be trapped in the local minima, and shows an overall improvement compared with a conventional GA. Thirteen design parameters were used to define the geometric features of the turbine. Among them, six volute design parameters were used to control the aspect ratio, intake area, exit area, and the circumferential distribution of the cross-sectional area. Seven rotor parameters were utilized to modify the cone angle, blade axial location, and the camber-line angle distribution. In order to be consistent with the previous matching between the engine and the turbocharger, a penalty function was used to

have the new design to maintain a similar swallowing capacity characteristic as the baseline, with the maximum difference controlled within 2.5% at the design point.

The proposed optimization algorithm increased the turbine efficiency by 3.65 pp at the design point whilst the GA reached 3 pp after the same number of function evaluations (750). The novel global search algorithm also has achieved a higher rate in finding the global optimized design than the GA.

The optimal velocity ratio of both optimized turbines was shifted from 0.7 to 0.61, implying the turbine operates better in the higher loading conditions. The optimized turbine shows a smaller flow area of the volute, which has an impact on the flow acceleration within the stator stage, thereby shifting the degree of reactions to a lower level. The improvement of turbine performance was mainly attributed to the smaller production of exit losses. Besides, the blade loading characteristic was improved between the 0.2-0.4 stream-wise location.

The tongue to wheel distance was found to have an impact on the flow field upstream of the rotor, in which the smaller tongue to wheel distance will produce a greater adverse pressure gradient near the tongue and secondary fluctuations of the flow velocities, resulting in a larger deviation from the free vortex assumption. The sensitivity of the design variables on the turbine performance has been studied, based on the elementary effects method. It is found that the tongue area is the most influential parameter, whilst the parameters altogether to define camber-line distributions that play crucial effects on the turbine performance.

Since the optimization was only focused on the single operating point, the optimized designs show performance deteriorations when it works under low loading conditions. The quasi-steady simulation indicates the KS optimized turbine only performs better under the pulses that have a peak pressure above 3 bar. This can be improved by the aforementioned unsteady optimization, and this will be addressed in the future study.

8.4 Summary, contributions and impacts

Section. 2.5 summaries the conventional difficulties of mapping and optimizing the turbine under pulsating flow conditions, mainly including,

1. Few literatures studied the effects of negative efficiency on turbocharger performance.
2. The unsteady mechanical efficiency can be fluctuating and far from the steady-state condition, which increases the uncertainties in the 1D modelling.
3. The conventional physical extrapolation models fail to predict the negative efficiency.
4. It is conventional to optimize a turbine blade based on a single design point, but no study sought to optimize the design of turbine rotor whilst explicitly taking into account the full range conditions during an exhaust pulse.
5. It is normal to optimize a single component of the turbine (either volute or rotor), few researches sought to optimize the whole stage of turbine simultaneously.
6. Few researches studied different optimization algorithms on the turbine optimization problem in order to achieve a global optimized design.

This PhD research work proposed feasible solutions to the address the aforementioned difficulties. A new turbine mapping method has been developed, which can use unsteady experimental data to create a turbine performance map. This method does not require corrections of mechanical losses, and reduces the extrapolation errors, thereby improving the model predictions in the 1D simulations. This study also proposed a novel physical turbine extrapolation model, based on the modification of previous research work, where a nozzle model was used to predict the turbine swallowing capacity characteristics, and a mean-line model can predict the efficiency, including the negative efficiency.

An unsteady optimization method was proposed and shown that it can produce a higher cycle-averaged efficiency over a pulse and better off-design performance, whilst the single point optimization can achieve higher efficiency at the design point. Additionally, an optimization

method using the Kriging surrogate model together with a global search method that has achieved a higher rate in finding the global optimized design than the genetic algorithm. Finally, the automated whole stage turbine design and optimization platform has been developed, which offers a guideline to turbomachinery designers when they aim for improving the fuel economy but without significantly affecting the original matching between engine and turbocharger.

REFERENCES

[1] Pablo Fajardo. *Methodology for the Numerical Characterization of a Radial Turbine under Steady and Pulsating Flow*. PhD thesis, Universidad Politécnica de Valencia, Spain, 2012.

[2] IEA. CO_2 emission from fuel combustion highlights. Technical report, International Energy Agency, 2017.

[3] ICCT. CO_2 emissions from new passenger cars in the EU: Car manufacturers' performance in 2016. Technical report, The International Council on Clean Transportation, 2017.

[4] Automotive Council UK. Powertrain (internal combustion engine) technology, 2013. https://www.automotivecouncil.co.uk/wp-content/uploads/sites/13/2013/09/Powertrain.jpg, Last accessed on 6/2/2019.

[5] Bo Hu, James WG Turner, Sam Akehurst, Chris Brace, and Colin Copeland. Observations on and potential trends for mechanically supercharging a downsized passenger car engine: a review. *Proceedings of the Institution of Mechanical Engineers, Part D: Journal of Automobile Engineering*, 231(4):435–456, 2017.

[6] A Meghani, J Allen, JWG Turner, A Popplewell, DJ Marshall, JS Hoyle, S McBroom, R Urista, and M Bazyn. Effects of charging system variability on the performance and fuel economy of a supercharged spark-ignition engine. Technical report, SAE Technical Paper, 2015.

[7] Dominique Petitjean, Luciano Bernardini, Chris Middlemass, and SM Shahed. Advanced gasoline engine turbocharging technology for fuel economy improvements. Technical report, SAE Technical Paper, 2004.

[8] SM Shahed and Karl-Heinz Bauer. Parametric studies of the impact of turbocharging on gasoline engine downsizing. *SAE International Journal of Engines*, 2(1):1347–1358, 2009.

[9] MJ McAllister and DJ Buckley. Future gasoline engine downsizing technologies-co2 improvements and engine design considerations. In *ImechE Internal Combustion Engines Conference*, pages 19–26, 2009.

[10] N. Watson and M. S. Janota. *Turbocharging the internal combustion engine*. MacMillan, 1986.

[11] MH Padzillah, S Rajoo, and RF Martinez-Botas. A detailed comparison on the influence of flow unsteadiness between the vaned and vaneless mixed-flow turbocharger turbine. *Journal of Engineering for Gas Turbines and Power*, 140(4):042601, 2018.

[12] N Karamanis, RF Martinez-Botas, and CC Su. Mixed flow turbines: Inlet and exit flow under steady and pulsating conditions. *Journal of turbomachinery*, 123(2):359–371, 2001.

[13] Nick Baines and Oleg Dubitsky. A novel non-radial turbocharger turbine created using numerical optimisation. 2016.

[14] MH Padzillah, S Rajoo, and RF Martinez-Botas. Numerical assessment of unsteady flow effects on a nozzled turbocharger turbine. In *ASME Turbo Expo 2012: Turbine Technical Conference and Exposition*, pages 745–756. American Society of Mechanical Engineers, 2012.

[15] Srithar Rajoo and Ricardo Martinez-Botas. Mixed flow turbine research: A review. *Journal of Turbomachinery*, 130(4):044001, 2008.

[16] Nicholas C Baines. *Fundamentals of turbocharging*, volume 1. Concepts NREC White River Junction, Vermont, 2005.

[17] D Palfreyman and RF Martinez-Botas. Numerical study of the internal flow field characteristics in mixed flow turbines. In *ASME Turbo Expo 2002: Power for Land, Sea, and Air*, pages 455–472. American Society of Mechanical Engineers, 2002.

[18] FJ Wallace and GP Blair. The pulsating-flow performance of inward radial-flow turbines. In *ASME 1965 gas turbine conference and products show*, pages 1–19. American Society of Mechanical Engineers, 1965.

[19] RS Benson and KH Scrimshaw. Paper 23: An experimental investigation of non-steady flow in a radial gas turbine. In *Proceedings of the Institution of Mechanical Engineers, Conference Proceedings*, volume 180-10, pages 74–85. SAGE Publications Sage UK: London, England, 1965.

[20] H Kosuge, N Yamanaka, I Ariga, and I Watanabe. Performance of radial flow turbines under pulsating flow conditions. *Journal of Engineering for Power*, 98(1):53–59, 1976.

[21] Rowland S Benson. Nonsteady flow in a turbocharger nozzleless radial gas turbine. Technical report, SAE Technical Paper, 1974.

[22] NC Baines. Turbocharger turbine pulse flow performance and modeling-25 years on. In *9th International Conference on Turbochargers and Turbocharging, IMechE, 2010*, 2010.

[23] A Dale and N Watson. Vaneless radial turbocharger turbine performance. In *Proceedings of the Institution of Mechanical Engineers, 3rd International Conference on Turbocharging and Turbochargers, Paper*, number C110/86, 1986.

[24] X Shi, R Zhang, LG Yu, and CC Ma. Experimental investigation on the unsteady performance of automotive turbocharger turbine. *Experimental Techniques*, 38(6): 21–29, 2014.

[25] Aaron Costall, Ricardo F Martinez-Botas, and Dean Palfreyman. Detailed study of pulsating flow performance in a mixed flow turbocharger turbine. In *ASME Turbo Expo 2005: Power for Land, Sea, and Air*, pages 1415–1433. American Society of Mechanical Engineers, 2005.

[26] A Costall, S Rajoo, and RF Martinez-Botas. Modelling and experimental study of the unsteady effects and their significance for nozzleless and nozzled turbine performance. In *THIESEL Conference on Thermo and Fluid Dynamic Processes in Diesel Engines*, pages 537–553, 2006.

[27] Aaron Costall and Ricardo F Martinez-Botas. Fundamental characterization of turbocharger turbine unsteady flow behavior. In *ASME Turbo Expo 2007: Power for Land, Sea, and Air*, pages 1827–1839. American Society of Mechanical Engineers, 2007.

[28] Aaron W Costall, Robert M McDavid, Ricardo F Martinez-Botas, and Nicholas C Baines. Pulse performance modeling of a twin entry turbocharger turbine under full and unequal admission. In *ASME Turbo Expo 2009: Power for Land, Sea, and Air*, pages 1255–1266. American Society of Mechanical Engineers, 2009.

[29] JR Serrano, FJ Arnau, V Dolz, A Tiseira, and C Cervelló. A model of turbocharger radial turbines appropriate to be used in zero-and one-dimensional gas dynamics codes for internal combustion engines modelling. *Energy Conversion and Management*, 49 (12):3729–3745, 2008.

[30] M Capobianco and S Marelli. Experimental analysis of unsteady flow performance in an automotive turbocharger turbine fitted with a waste-gate valve. *Proceedings of the Institution of Mechanical Engineers, Part D: Journal of Automobile Engineering*, 225 (8):1087–1097, 2011.

[31] S Szymko, RF Martinez-Botas, and KR Pullen. Experimental evaluation of turbocharger turbine performance under pulsating flow conditions. In *ASME Turbo Expo 2005: Power for Land, Sea, and Air*, pages 1447–1457. American Society of Mechanical Engineers, 2005.

[32] JR Serrano, FJ Arnau, Pablo Fajardo, MA Reyes Belmonte, and Fabrice Vidal. Contribution to the modeling and understanding of cold pulsating flow influence in the efficiency of small radial turbines for turbochargers. *Journal of Engineering for Gas Turbines and Power*, 134(10):102701, 2012.

[33] HWDE Chen and DE Winterbone. A method to predict performance of vaneless radial turbines under steady and unsteady flow conditions. *IMechE Turbocharging and Turbochargers, Paper*, (C405/008):13–22, 1990.

[34] H Chen, I Hakeem, and RF Martinez-Botas. Modelling of a turbocharger turbine under pulsating inlet conditions. *Proceedings of the Institution of Mechanical Engineers, Part A: Journal of Power and Energy*, 210(5):397–408, 1996.

[35] Nicolaos Karamanis. *Inlet and exit flow characteristics of mixed flow turbines in advanced automotive turbocharging*. PhD thesis, Imperial College London (University of London), 2000.

[36] NC Baines, A Hajilouy-Benisi, and JH Yeo. The pulse flow performance and modelling of radial inflow turbines. In *Institution of Mechanical Engineers Conference Publications*, volume 6, pages 209–209. MEDICAL ENGINEERING PUBLICATIONS LTD, 1994.

[37] DE Winterbone and RJ Pearson. Turbocharger turbine performance under unsteady flow-a review of experimental results and proposed models. In *IMECHE CONFERENCE TRANSACTIONS*, volume 11, pages 193–208. MECHANICAL ENGINEERING PUBLICATIONS, 1998.

[38] Srithar Rajoo and RF Martinez-Botas. Unsteady effect in a nozzled turbocharger turbine. In *ASME Turbo Expo 2007: Power for Land, Sea, and Air*, pages 1159–1170. American Society of Mechanical Engineers, 2007.

[39] Silvia Marelli and Massimo Capobianco. Steady and pulsating flow efficiency of a waste-gated turbocharger radial flow turbine for automotive application. *Energy*, 36 (1):459–465, 2011.

[40] Fredrik Hellstrom and Laszlo Fuchs. Effects of inlet conditions on the turbine performance of a radial turbine. In *ASME Turbo Expo 2008: Power for Land, Sea, and Air*, pages 1985–2001. American Society of Mechanical Engineers, 2008.

[41] Fredrik Hellström and Laszlo Fuchs. Numerical computations of the pulsatile flow in a turbocharger with realistic inflow conditions from an exhaust manifold. In *ASME Turbo Expo 2009, Power for Land, Sea and Air*, 2009.

[42] Adrian Peter Dale. *Radial, vaneless, turbocharger turbine performance*. PhD thesis, Imperial College London, 1990.

[43] JH Yeo and NC Baines. Pulsating flow behaviour in a twin-entry vaneless radial-inflow turbine. imeche paper no. *C495*, 4, 1990.

[44] Colin Copeland, Peter Newton, Ricardo Martinez-Botas, and Martin Seiler. A comparison of pulsed flow timescales within a turbine stage. In *10th IMECHE International Conference on Turbochargers and Turbocharging*. University of Bath, 2012.

[45] I Hakeem, CC Su, A Costall, and RF Martinez-Botas. Effect of volute geometry on the steady and unsteady performance of mixed-flow turbines. *Proceedings of the Institution of Mechanical Engineers, Part A: Journal of Power and Energy*, 221(4): 535–549, 2007.

[46] Apostolos Pesiridis, Sotirios Lioutas, and Ricardo F Martinez-Botas. Integration of unsteady effects in the turbocharger design process. In *ASME Turbo Expo 2012: Turbine Technical Conference and Exposition*, pages 721–733. American Society of Mechanical Engineers, 2012.

[47] A Romagnoli, RF Martinez-Botas, and S Rajoo. Turbine performance studies for automotive turbochargers, part 1: Steady analysis. In *9th International Conference on Turbochargers and Turbocharging, Inst. of Mech. Eng., London*, 2010.

[48] Masanori Iwasaki, Nobuyuki Ikeya, Youichi Marutani, and Toshihiko Kitazawa. Comparison of turbocharger performance between steady flow and pulsating flow on engines. Technical report, SAE Technical Paper, 1994.

[49] Colin D Copeland, Ricardo Martinez-Botas, and Martin Seiler. Comparison between steady and unsteady double-entry turbine performance using the quasi-steady assumption. *Journal of Turbomachinery*, 133(3):031001, 2011.

[50] MGACG Capobianco, A Gambarotta, and G Cipolla. Influence of the pulsating flow operation on the turbine characteristics of a small internal combustion engine turbocharger. *IMechE Paper*, (C372/019), 1989.

[51] M Capobianco and A Gambarotta. Unsteady flow performance of turbocharger radial turbines. In *Proceeding of the Institute of Mechanical Engineers, Fourth International Conference of Turbocharging and Turbochargers*, pages 123–132, 1990.

[52] Zhanming Ding, Weilin Zhuge, Yangjun Zhang, Hua Chen, and Ricardo Martinez-Botas. Investigation on pulsating flow effect of a turbocharger turbine. In *ASME 2017 Fluids Engineering Division Summer Meeting*. American Society of Mechanical Engineers, 2017.

[53] Teng Cao, Liping Xu, Mingyang Yang, and Ricardo F Martinez-Botas. Radial turbine rotor response to pulsating inlet flows. *Journal of Turbomachinery*, 136(7):071003, 2014.

[54] N Karamanis and RF Martinez-Botas. Mixed-flow turbines for automotive turbochargers: steady and unsteady performance. *International Journal of Engine Research*, 3 (3):127–138, 2002.

[55] Srithar Rajoo, Alessandro Romagnoli, and Ricardo F Martinez-Botas. Unsteady performance analysis of a twin-entry variable geometry turbocharger turbine. *Energy*, 38(1):176–189, 2012.

[56] D Palfreyman and RF Martinez-Botas. The pulsating flow field in a mixed flow turbocharger turbine: an experimental and computational study. In *ASME turbo expo 2004: power for land, sea, and air*, pages 697–708. American Society of Mechanical Engineers, 2004.

[57] Fredrik Hellström. *Numerical computations of the unsteady flow in turbochargers*. PhD thesis, KTH, 2010.

[58] G Sieros, A Stamatis, and K Mathioudakis. Jet engine component maps for performance modeling and diagnosis. *Journal of Propulsion and Power*, 13(5):665–674, 1997.

[59] Marek Orkisz and Slawomir Stawarz. Modeling of turbine engine axial-flow compressor and turbine characteristics. *Journal of Propulsion and Power*, 16(2):336–339, 2000.

[60] Xiande Fang and Qiumin Dai. Modeling of turbine mass flow rate performances using the taylor expansion. *Applied Thermal Engineering*, 30(13):1824–1831, 2010.

[61] Lars Eriksson, Lars Nielsen, Jan Brugård, Johan Bergström, Fredrik Pettersson, and Per Andersson. Modeling of a turbocharged si engine. *Annual Reviews in Control*, 26 (1):129–137, 2002.

[62] J-P Jensen, AF Kristensen, Spencer C Sorenson, N Houbak, and E Hendricks. Mean value modeling of a small turbocharged diesel engine. Technical report, SAE Technical Paper, 1991.

[63] Xiande Fang, Qiumin Dai, Yanxin Yin, and Yu Xu. A compact and accurate empirical model for turbine mass flow characteristics. *Energy*, 35(12):4819–4823, 2010.

[64] T Gamma. Gt-suite-flow theory manual. *Gamma Technologies Inc*, 2017.

[65] F Payri, J Benajes, and M Reyes. Modelling of supercharger turbines in internal-combustion engines. *International journal of mechanical sciences*, 38(8-9):853–869, 1996.

[66] F Payri, JR Serrano, P Fajardo, MA Reyes-Belmonte, and R Gozalbo-Belles. A physically based methodology to extrapolate performance maps of radial turbines. *Energy Conversion and Management*, 55:149–163, 2012.

[67] Meng Soon Chiong, Srithar Rajoo, Alessandro Romagnoli, and Ricardo Martinez-Botas. Unsteady performance prediction of a single entry mixed flow turbine using 1-d gas dynamic code extended with meanline model. In *ASME turbo expo 2012: turbine technical conference and exposition*, pages 781–795. American Society of Mechanical Engineers, 2012.

[68] Meng Soon Chiong, Srithar Rajoo, Aaron W Costall, Wan Saiful-Islam Bin Wan Salim, Alessandro Romagnoli, and Ricardo F Martinez-Botas. Assessment of cycle averaged turbocharger maps through one dimensional and mean-line coupled codes. In *ASME Turbo Expo 2013: Turbine Technical Conference and Exposition*, pages V06CT40A026–V06CT40A026. American Society of Mechanical Engineers, 2013.

[69] software Ricardo. Wave user's manual. *Ricardo Inc*, 2009.

[70] Samuel M Futral and Charles A Wasserbauer. *Off-design performance prediction with experimental verification for a radial-inflow turbine: Samuel M. Futral Jr. and Charles A. Wasserbauer*. National Aeronautics and Space Administration, 1965.

[71] Carroll A Todd and Samuel M Futral. *A FORTRAN IV program to estimate the off-design performance of radial-inflow turbines*. National Aeronautics and Space Administration, 1969.

[72] Charles A Wasserbauer and Arthur J Glassman. Fortran program for predicting off-design performance of radial-inflow turbines. 1975.

[73] Peter L Meitner and Arthur J Glassman. Computer code for off-design performance analysis of radial-inflow turbines with rotor blade sweep. Technical report, NATIONAL AERONAUTICS AND SPACE ADMINISTRATION CLEVELAND OH LEWIS RESEARCH CENTER, 1983.

[74] Peter L Meitner and Arthur J Glassman. Off-design performance loss model for radial turbines with pivoting, variable-area stators. Technical report, NATIONAL AERONAUTICS AND SPACE ADMINISTRATION CLEVELAND OH LEWIS RESEARCH CENTER, 1980.

[75] Theodore Katsanis and William D McNally. Fortran program for calculating velocities and streamlines on the hub-shroud mid-channel flow surface of an axial-or mixed-flow turbomachine. 2: Programmer's manual. 1974.

[76] Theodore Katsanis and William D McNally. Revised fortran program for calculating velocities and streamlines on the hub-shroud midchannel stream surface of an axial-, radial-, or mixed-flow turbomachine or annular duct. 2: Programmer's manual. 1977.

[77] LJ Kastner and FS Bhinder. A method for predicting the performance of a centripetal gas turbine fitted with a nozzle-less volute casing. In *ASME 1975 International Gas Turbine Conference and Products Show*, pages V01BT02A003–V01BT02A003. American Society of Mechanical Engineers, 1975.

[78] A Whitfield and F.J. Wallace. Study of incidence loss models in radial and mixed-flow turbomachinery. *Proceedings of the Congress of Heat Fluid Flow in Steam and Gas Turbine Plant*, pages 122–132, 01 1973.

[79] A Romagnoli and R Martinez-Botas. Performance prediction of a nozzled and nozzleless mixed-flow turbine in steady conditions. *International Journal of Mechanical Sciences*, 53(8):557–574, 2011.

[80] M Abidat, M Hachemi, M K Hamidou, and N C Baines. Prediction of the steady and non-steady flow performance of a highly loaded mixed flow turbine. *Proceedings of the Institution of Mechanical Engineers, Part A: Journal of Power and Energy*, 212 (3):173–184, 1998. doi: 10.1243/0957650981536844.

[81] MS Chiong, S Rajoo, A Romagnoli, and RF Martinez-Botas. Single entry mixed flow turbine performance prediction with 1-d gas dynamic code coupled with mean line model. *Int. J. Gas Turbine, Propuls. Power Syst*, 4(2):8–16, 2012.

[82] MS Chiong, S Rajoo, RF Martinez-Botas, and AW Costall. Engine turbocharger performance prediction: One-dimensional modeling of a twin entry turbine. *Energy Conversion and Management*, 57:68–78, 2012.

[83] MS Chiong, S Rajoo, A Romagnoli, AW Costall, and RF Martinez-Botas. Integration of meanline and one-dimensional methods for prediction of pulsating performance of a turbocharger turbine. *Energy conversion and management*, 81:270–281, 2014.

[84] MS Chiong, S Rajoo, A Romagnoli, AW Costall, and RF Martinez-Botas. Non-adiabatic pressure loss boundary condition for modelling turbocharger turbine pulsating flow. *Energy Conversion and Management*, 93:267–281, 2015.

[85] Nikolaos Sakellaridis and Dimitrios Hountalas. Meanline modeling of radial turbine performance for turbocharger simulation and diagnostic applications. Technical report, SAE Technical Paper, 2013.

[86] JKW Lam, QDH Roberts, and GT McDonnell. Flow modelling of a turbocharger turbine under pulsating flow. In *7th International Conference on Turbochargers and Turbocharging, London, May*, volume 1415, page 18196, 2002.

[87] José Galindo, Pablo Fajardo, R Navarro, and LM García-Cuevas. Characterization of a radial turbocharger turbine in pulsating flow by means of cfd and its application to engine modeling. *Applied Energy*, 103:116–127, 2013.

[88] MH Padzillah, M Yang, W Zhuge, and RF Martinez-Botas. Numerical and experimental investigation of pulsating flow effect on a nozzled and nozzleless mixed flow turbine for an automotive turbocharger. In *ASME Turbo Expo 2014: Turbine Technical Conference and Exposition*, pages V02DT42A027–V02DT42A027. American Society of Mechanical Engineers, 2014.

[89] J Do Denton. Loss mechanisms in turbomachines. In *ASME 1993 International Gas Turbine and Aeroengine Congress and Exposition*, pages V002T14A001–V002T14A001. American Society of Mechanical Engineers, 1993.

[90] Torsten Palenschat, Peter Newton, Ricardo F Martinez-Botas, Markus Müller, and Johannes Leweux. 3-d computational loss analysis of an asymmetric volute twin-scroll turbocharger. In *ASME Turbo Expo 2017: Turbomachinery Technical Conference and Exposition*. American Society of Mechanical Engineers Digital Collection, 2017.

[91] P Newton, T Palenschat, R Martinez-Botas, and M Seiler. Entropy generation rate in a mixed flow turbine passage. In *International Gas Turbine Congress, Tokyo, Japan, Nov*, pages 15–20, 2015.

[92] Yingxian Xue, Mingyang Yang, Ricardo F Martinez-Botas, Bijie Yang, and Kangyao Deng. Unsteady performance of a mixed-flow turbine with nozzled twin-entry volute confronted by pulsating incoming flow. *Aerospace Science and Technology*, page 105485, 2019.

[93] Francisco Payri, Jose R Serrano, Pablo Olmeda, Arlington Paez, and Fabrice Vidal. Experimental methodology to characterize mechanical losses in small turbochargers. In *ASME Turbo Expo 2010: power for land, sea, and air*, pages 413–423. American Society of Mechanical Engineers, 2010.

[94] A Diango, C Perilhon, G Descombes, and E Danho. Application of exergy balances for the optimization of non-adiabatic small turbomachines operation. *Energy*, 36(5): 2924–2936, 2011.

[95] Constantine Arcoumanis. *Internal combustion engines*. Elsevier, 2012.

[96] Sameh Shaaban. *Experimental investigation and extended simulation of turbocharger non-adiabatic performance*. PhD thesis, Verlag nicht ermittelbar, 2004.

[97] José Ramón Serrano, Pablo Olmeda, Andrés Tiseira, Luis Miguel García-Cuevas, and Alain Lefebvre. Theoretical and experimental study of mechanical losses in automotive turbochargers. *Energy*, 55:888–898, 2013.

[98] M Deligant, P Podevin, and G Descombes. Cfd model for turbocharger journal bearing performances. *Applied Thermal Engineering*, 31(5):811–819, 2011.

[99] Jose Ramón Serrano, Pablo Olmeda, Andres Tiseira, Luis Miguel García-Cuevas, and Alain Lefebvre. Importance of mechanical losses modeling in the performance prediction of radial turbochargers under pulsating flow conditions. *SAE International Journal of Engines*, 6(2):729–738, 2013.

[100] Jan Macek and Oldřich Vítek. Simulation of pulsating flow unsteady operation of a turbocharger radial turbine. Technical report, SAE Technical Paper, 2008.

[101] Irebert Delgado and Margaret Proctor. Continued investigation of leakage and power loss test results for competing turbine engine seals. In *42nd AIAA/ASME/SAE/ASEE Joint Propulsion Conference & Exhibit*, page 4754, 2006.

[102] RF Martinez-Botas, KR Pullen, and F Shi. Numerical calculations of a turbine volute using a 3-d navier-stokes solver. In *ASME 1996 International Gas Turbine and Aeroengine Congress and Exhibition*. American Society of Mechanical Engineers Digital Collection, 1996.

[103] Mohamed Amine Meghnine, Mohammad Kamal Hamidou, and Mohammed Hamel. Influence of the volute cross-sectional shape on mixed inflow turbine performances. *Advances in Mechanical Engineering*, 9(7):1687814017708174, 2017.

[104] Mingyang Yang, Ricardo Martinez-Botas, Srithar Rajoo, Takao Yokoyama, and Seiichi Ibaraki. An investigation of volute cross-sectional shape on turbocharger turbine under pulsating conditions in internal combustion engine. *Energy Conversion and Management*, 105:167–177, 2015.

[105] Samuel Lee, Simon Barrans, Martyn Jupp, and Ambrose Nickson. The impact of volute aspect ratio on the performance of a mixed flow turbine. *Aerospace*, 4(4):56, 2017.

[106] Jan F Suhrmann, Dieter Peitsch, Marc Gugau, and Tom Heuer. On the effect of volute tongue design on radial turbine performance. In *ASME turbo expo 2012: Turbine technical conference and exposition*, pages 891–901. American Society of Mechanical Engineers Digital Collection, 2012.

[107] Tom Heuer, Marc Gugau, Achim Klein, and Paul Anschel. An analytical approach to support high cycle fatigue validation for turbocharger turbine stages. In *ASME Turbo Expo 2008: Power for Land, Sea, and Air*, pages 723–732. American Society of Mechanical Engineers Digital Collection, 2008.

[108] F Gu, A Engeda, and E Benisek. A comparative study of incompressible and compressible design approaches of radial inflow turbine volutes. *Proceedings of the Institution of Mechanical Engineers, Part A: Journal of Power and Energy*, 215(4):475–486, 2001.

[109] Arnold Whitfield and Nicholas C Baines. Design of radial turbomachines. 1990.

[110] Aman MI Bin Mamat and Ricardo F Martinez-Botas. Mean line flow model of steady and pulsating flow of a mixed-flow turbine turbocharger. In *ASME Turbo Expo 2010: Power for Land, Sea, and Air*, pages 2393–2404. American Society of Mechanical Engineers, 2010.

[111] Kiyarash Rahbar, Saad Mahmoud, Raya K Al-Dadah, and Nima Moazami. Parametric analysis and optimization of a small-scale radial turbine for organic rankine cycle. *Energy*, 83:696–711, 2015.

[112] Zheng Liu and Colin Copeland. New method for mapping radial turbines exposed to pulsating flows. *Energy*, 162:1205–1222, 2018.

[113] J Zhang, M Zangeneh, and P Eynon. A 3d inverse design based multidisciplinary optimization on the radial and mixed-inflow turbines for turbochargers. In *11th International Conference on Turbochargers and Turbocharging, London*, pages 399–410, 2014.

[114] MW Benner, SA Sjolander, and SH Moustapha. The influence of leading-edge geometry on secondary losses in a turbine cascade at the design incidence. *Journal of turbomachinery*, 126(2):277–287, 2004.

[115] Weihao Zhang, Zhengping Zou, and Jian Ye. Leading-edge redesign of a turbomachinery blade and its effect on aerodynamic performance. *Applied energy*, 93:655–667, 2012.

[116] T Leonard, S Spence, J Early, and D Filsinger. A numerical study of automotive turbocharger mixed flow turbine inlet geometry for off design performance. In *IOP Conference Series: Materials Science and Engineering*, volume 52, page 042012. IOP Publishing, 2013.

[117] H Chen and NC Baines. Analytical optimization design of radial and mixed flow turbines. *Proceedings of the Institution of Mechanical Engineers, Part A: Journal of Power and Energy*, 206(3):177–187, 1992.

[118] Uswah Khairuddin, Aaron W Costall, and Ricardo F Martinez-Botas. Influence of geometrical parameters on aerodynamic optimization of a mixed-flow turbocharger turbine. In *ASME Turbo Expo 2015: Turbine Technical Conference and Exposition*, pages V02CT42A002–V02CT42A002. American Society of Mechanical Engineers, 2015.

[119] K Rahbar, S Mahmoud, RK Al-Dadah, and N Moazami. One-dimensional and three-dimensional numerical optimization and comparison of single-stage supersonic and dual-stage transonic radial inflow turbines for the orc. In *ASME 2016 Power Conference collocated with the ASME 2016 10th International Conference on Energy Sustainability and the ASME 2016 14th International Conference on Fuel Cell Science, Engineering and Technology*, pages V001T08A017–V001T08A017. American Society of Mechanical Engineers, 2016.

[120] Ayad M Al Jubori, Raya Al-Dadah, and Saad Mahmoud. Performance enhancement of a small-scale organic rankine cycle radial-inflow turbine through multi-objective optimization algorithm. *Energy*, 131:297–311, 2017.

[121] Lasse Mueller, Zuheyr Alsalihi, and Tom Verstraete. Multidisciplinary optimization of a turbocharger radial turbine. *Journal of Turbomachinery*, 135(2):021022, 2013.

[122] Ying Zhao, Wenxi Lu, and Chuanning Xiao. A kriging surrogate model coupled in simulation–optimization approach for identifying release history of groundwater sources. *Journal of contaminant hydrology*, 185:51–60, 2016.

[123] Stefan Tüchler, Zhihang Chen, and Colin D Copeland. Multipoint shape optimisation of an automotive radial compressor using a coupled computational fluid dynamics and genetic algorithm approach. *Energy*, 165:543–561, 2018.

[124] Mohamed Amine Bouhlel, Nathalie Bartoli, Abdelkader Otsmane, and Joseph Morlier. Improving kriging surrogates of high-dimensional design models by partial least squares dimension reduction. *Structural and Multidisciplinary Optimization*, 53(5): 935–952, 2016.

[125] Maurice Joseph Zucrow and Joe D Hoffman. Gas dynamics. volume 2-multidimensional flow. *New York, John Wiley and Sons, Inc., 1977. 488 p.*, 1977.

[126] Rainer Zimmermann, Roland Baar, and Clemens Biet. Determination of the isentropic turbine efficiency due to adiabatic measurements and the validation of the conditions via a new criterion. *Proceedings of the Institution of Mechanical Engineers, Part C: Journal of Mechanical Engineering Science*, 232(24):4485–4494, 2018.

[127] Fredrik Westin and Hans-Erik Ångström. Calculation accuracy of pulsating flow through the turbine of si-engine turbochargers-part 1 calculations for choice of turbines with different flow characteristics. Technical report, SAE Technical Paper, 2005.

[128] Fredrik Westin and Hans-Erik Ångström. Calculation accuracy of pulsating flow through the turbine of si-engine turbochargers-part 2 measurements, simulation correlations and conclusions. *SAE transactions*, pages 1662–1684, 2005.

[129] Pablo Cesar Olmeda González, Andrés Omar Tiseira Izaguirre, Luis Miguel García-Cuevas González, and Alain Lefebvre. Importance of mechanical losses modeling in the performance prediction of radial turbochargers under pulsating flow conditions. In *SAE International Journal of Engines*, volume 6, pages 1–10. SAE International, 2013.

[130] Abraham Savitzky and Marcel JE Golay. Smoothing and differentiation of data by simplified least squares procedures. *Analytical chemistry*, 36(8):1627–1639, 1964.

[131] Ronald W Schafer. On the frequency-domain properties of savitzky-golay filters. In *Digital Signal Processing Workshop and IEEE Signal Processing Education Workshop (DSP/SPE), 2011 IEEE*, pages 54–59. IEEE, 2011.

[132] Petre Stoica, Randolph L Moses, et al. *Spectral analysis of signals*, volume 1. Pearson Prentice Hall Upper Saddle River, NJ, 2005.

[133] Duda Tomasz. *Turbocharger performance and surge definition on a steady flow turbocharger test stand*. PhD thesis, University of Bath, 2017.

[134] McCrometer. Mccrometer installation operation & maintenance manual. *McCrometer Inc*, 2017.

[135] Mingyang Yang, Kangyao Deng, Ricardo Martines-Botas, and Weilin Zhuge. An investigation on unsteadiness of a mixed-flow turbine under pulsating conditions. *Energy Conversion and Management*, 110:51–58, 2016.

[136] Qiyou Deng, RD Burke, Qingning Zhang, and Ludek Pohorelsky. A research on wastegated turbine performance under unsteady flow condition. *Journal of Engineering for Gas Turbines and Power*, 139(6):062603, 2017.

[137] Jean-Paul Zammit, Michael J McGhee, Paul J Shayler, and Ian Pegg. The influence of cylinder deactivation on the emissions and fuel economy of a four-cylinder direct-injection diesel engine. *Proceedings of the Institution of Mechanical Engineers, Part D: Journal of Automobile Engineering*, 228(2):206–217, 2014.

[138] Hermann Schlichting and Klaus Gersten. *Boundary-layer theory*. Springer, 2016.

[139] Henk Kaarle Versteeg and Weeratunge Malalasekera. *An introduction to computational fluid dynamics: the finite volume method*. Pearson education, 2007.

[140] F Moukalled, L Mangani, M Darwish, et al. The finite volume method in computational fluid dynamics. *An advanced introduction with OpenFoam® and Matlab®. Nueva York: Springer. Recuperado de http://www. gidropraktikum. narod. ru/Moukalled-et-al-FVM-OpenFOAM-Matlab. pdf*, 2016.

[141] Joseph Boussinesq. *Essai sur la théorie des eaux courantes*. Impr. nationale, 1877.

[142] François G Schmitt. About boussinesq's turbulent viscosity hypothesis: historical remarks and a direct evaluation of its validity. *Comptes Rendus Mécanique*, 335(9-10): 617–627, 2007.

[143] Brian Edward Launder and BI Sharma. Application of the energy-dissipation model of turbulence to the calculation of flow near a spinning disc. *Letters in heat and mass transfer*, 1(2):131–137, 1974.

[144] David C Wilcox et al. *Turbulence modeling for CFD*, volume 2. DCW industries La Canada, CA, 1998.

[145] Florian R Menter. Two-equation eddy-viscosity turbulence models for engineering applications. *AIAA journal*, 32(8):1598–1605, 1994.

[146] T Munk, D Kane, and DM Yebra. The effects of corrosion and fouling on the performance of ocean-going vessels: a naval architectural perspective. In *Advances in marine antifouling coatings and technologies*, pages 148–176. Elsevier, 2009.

[147] Marc Perlin, David R Dowling, and Steven L Ceccio. Freeman scholar review: passive and active skin-friction drag reduction in turbulent boundary layers. *Journal of Fluids Engineering*, 138(9):091104, 2016.

[148] Fluent Manual. Manual and user guide of fluent software. *Fluent Inc*, 597, 2005.

[149] CFX Ansys. Release 19.2: Ansys cfx-solver theory guide. ansys, 2018.

[150] Franklyn J Kelecy. Coupling momentum and continuity increases cfd robustness. *Ansys Advantage*, 2(2):49–51, 2008.

[151] Jose Ramon Serrano, Benjamin Pla, Ricardo Gozalbo, and Diego Ospina. Estimation of the extended turbine maps for a radial inflow turbine. Technical report, SAE Technical Paper, 2010.

[152] Cyril COUDERC, Pascal CHESSE, and David CHALET. Comparison of the prediction performances of different models of radial turbine under steady and unsteady flow conditions. *Scientific Bulletin, Automotive series, year XVII*, (21):2, 2011.

[153] Kiyarash Rahbar, Saad Mahmoud, and Raya K Al-Dadah. Mean-line modeling and cfd analysis of a miniature radial turbine for distributed power generation systems. *International Journal of Low-Carbon Technologies*, 11(2):157–168, 2016.

[154] Luca Da Lio, Giovanni Manente, and Andrea Lazzaretto. A mean-line model to predict the design efficiency of radial inflow turbines in organic rankine cycle (orc) systems. *Applied Energy*, 205:187–209, 2017.

[155] David Japikse, Nicholas Baines, et al. *Introduction to turbomachinery*. 1994.

[156] JD Stanitz. Some theoretical aerodynamic investigations of impellers in radial-and mixed flow centrifugal compressors. ASME, 1951.

[157] Alessandro Romagnoli. *Aerodynamic and thermal characterization of turbocharger turbines: experimental and computational evaluation*. PhD thesis, Department of Mechanical Engineering, Imperial College London, 2010.

[158] Daniel G Krige. A statistical approach to some basic mine valuation problems on the witwatersrand. *Journal of the Southern African Institute of Mining and Metallurgy*, 52 (6):119–139, 1951.

[159] Abdellatif Lghali. Surrogate based optimization using kriging based approximation. *VU BA paper*, 2012.

[160] B Gaspar, AP Teixeira, and C Guedes Soares. Assessment of the efficiency of kriging surrogate models for structural reliability analysis. *Probabilistic Engineering Mechanics*, 37:24–34, 2014.

[161] ZH Han. Kriging surrogate model and its application to design optimization: a review of recent progress. *Acta Aeronautica et Astronautica Sinica*, 37(11):3197–3225, 2016.

[162] Søren Nymand Lophaven, Hans Bruun Nielsen, and Jacob Søndergaard. Dace-a matlab kriging toolbox, version 2.0. 2002.

[163] Heinz Mühlenbein, M Schomisch, and Joachim Born. The parallel genetic algorithm as function optimizer. *Parallel computing*, 17(6-7):619–632, 1991.

[164] Colin D Copeland, Ricardo Martinez-Botas, and Martin Seiler. Unsteady performance of a double entry turbocharger turbine with a comparison to steady flow conditions. *Journal of Turbomachinery*, 134(2):021022, 2012.

[165] H Herwig and F Kock. Direct and indirect methods of calculating entropy generation rates in turbulent convective heat transfer problems. *Heat and mass transfer*, 43(3): 207–215, 2007.

[166] Peter Alan Davidson. *Turbulence: an introduction for scientists and engineers*. Oxford University Press, 2015.

[167] Nicholas Anton and William Wiberg. Aerodynamic design of a gas turbine rotor blade for the kth test turbine. *ISRN LUTMDN/TMHP–13/5284–SE*, 2013.

[168] Graham Cox. Challenges in the design of radial turbines for small gasoline engines. *PCA Engineers Limited, Lincoln, UK*, 2014.

[169] Francesca Pianosi, Fanny Sarrazin, and Thorsten Wagener. A matlab toolbox for global sensitivity analysis. *Environmental Modelling & Software*, 70:80–85, 2015.